Title
Molecular Choreography of Isomerization and Electron Transfer Using One and Two Dimensional Femtosecond Stimulated Raman Spectroscopy

Author
Hoffman, David Paul

Publication Date
2014

Peer reviewed|Thesis/dissertation

Molecular Choreography of Isomerization and Electron Transfer Using One and Two Dimensional Femtosecond Stimulated Raman Spectroscopy

by

David Paul Hoffman

A dissertation submitted in partial satisfaction of the
requirements for the degree of
Doctor of Philosophy

in

Chemistry

in the

Graduate Division

of the

University of California, Berkeley

Committee in charge:

Professor Richard A. Mathies, Chair
Professor Graham R. Fleming
Professor Joseph W. Orenstein

Spring 2014

Molecular Choreography of Isomerization and Electron Transfer Using One and Two Dimensional Femtosecond Stimulated Raman Spectroscopy

ABSTRACT

Molecular Choreography of Isomerization and Electron Transfer Using One and Two Dimensional Femtosecond Stimulated Raman Spectroscopy

by

David Paul Hoffman

Doctor of Philosophy in Chemistry

University of California, Berkeley

Professor Richard A. Mathies, Chair

Chemical reactions are defined by the change in the relative positions and bonding of nuclei in molecules. I have used femtosecond stimulated Raman spectroscopy (FSRS) to probe these transformations with structural specificity and high time precision revealing the mechanisms of two important classes of reactions; isomerization about an N=N bond and interfacial/intermolecular electron transfer.

Isomerization about a double bond is one of the simplest, yet most important, photochemical reactions. In contrast to carbon double bonds, nitrogen double bonds can react via two possible mechanisms; rotation or inversion. To determine which pathway is predominant, I studied an azobenzene derivative using both FSRS and impulsive stimulated Raman spectroscopy (ISRS). The FSRS experiments demonstrated that the photochemical reaction occurs concomitantly with the 700 fs non-radiative decay of the excited state; because no major change in N=N stretching frequency was measured, I surmised that the reaction proceeds through an inversion pathway. My subsequent ISRS experiments confirmed this hypothesis; I observed a highly displaced, low frequency, inversion-like mode, indicating that initial movement out of the Franck-Condon region proceeds along an inversion coordinate.

To probe which nuclear motions facilitate electron transfer and charge recombination, I used FSRS and the newly developed 2D-FSRS techniques to study two model systems, triphenylamine dyes bound to TiO_2 nanoparticles and a molecular charge transfer (CT) dimer. In the dye-nanoparticle system I discovered that charge separation persists much longer (> 100 ps) than previously thought by using the juxtaposition of the FSRS and transient absorption data to separate the dynamics of the dye from that of the injected electron. Additionally, I discovered that dye constructs with an added vinyl group were susceptible to quenching via isomerization. The CT dimer offered an opportunity to study a system in which charge recombination occurred on a shorter timescale (~10 ps). Here I found that impulsively excited coherent nuclear motion in the excited state survived for more than 5 ps. These long lived coherences enabled the performance of 2D-FSRS to identify the coupling and tuning modes of the conical intersection that connects the charge transfer excited state with the neutral ground state and therefore the nuclear motions responsible for

charge recombination. Furthermore, these data demonstrate that the photochemical reactivity is *not* mediated by phase-space randomization but rather by specific, coherent, nuclear trajectories.

In this thesis I have demonstrated the power and utility of FSRS in probing condensed phase chemical reaction dynamics and provided a glimpse of the capabilities of 2D-FSRS. In general, 2D-FSRS provides a direct measure of the anharmonic coupling that controls reactivity. Looking forward, higher time resolution (broader band) 2D-FSRS will open up a whole new approach for characterizing transition states and energy transfer processes.

To my family

For all their love and support

Contents

List of Figures

List of Tables

ACKNOWLEDGMENTS

Scientific progress is not made by individuals forging a path through the æther but rather by "dwarfs standing on the shoulders of giants." To know that this is true one only needs to look at the numerous names attached to most of the following chapters or the 232 references at the end of this thesis. There were many people who helped me on my journey to graduate school; Farhad Riahi, Rebecca J. Jackman, Christopher J. Barrett, Jane Frommer and Bradley J. Siwick. Here I attempt to thank the people that helped me the most during the preparation of my dissertation, though it is not and cannot be an exhaustive list.

First I must thank my dissertation advisor, Richard A. Mathies, for providing the necessary matériel and for convincing me that the most of my equipment requests were superfluous; he has taught me how to do much more with much less. Most importantly I thank him for never accepting my pleas of "it's not possible," because, with enough effort and ingenuity, it usually was. Rich also gave me the freedom, though not always intentionally, to pursue whatever project I wanted in whatever fashion I desired allowing me to experience life as a truly independent scientist.

I owe a debt of gratitude to the Mathies Group members who helped when I needed help and heard my complaints when I needed to complain. Mark Creelman, he taught me everything I know about keeping antique lasers running and running well and has been a good friend throughout. Ryan Leverenz, in an environment where "making it work" usually took precedence over durability he always new how to make it work and make it last. Jyotishman Dasgupta, the best postdoc during my tenure, he has an undying enthusiasm for science that I aspire to. Amy Twite, her constant supply of baked goods will be sorely missed. David Valley, always a good person with which to talk science. Daniel Dietze, he was the only lab mate to read this thesis in its entirety and check *every* equation in Chapter 2. Scott Ellis, he helped me avoid some logical errors. There are a few more alumni that must be mentioned; Renee Frontiera, Katelyn Spillane, Rosalie Tran, Chong Fang and Tomotsumi Fujisawa.

Friends outside of lab have done a great job helping me keep my sanity; Patrick Schaffer, Eric Sundstrom, Justin Lomont, Benjamin Caplins, Jessica Douglas and Olivia Lee. Of course I must thank my closest friends from high school; Joshua Krieger and Isaac Slavitt. Vacations back home would not have been complete without them. Most of all I thank them for always telling me that getting a PhD was a worthwhile endeavor.

Finally I must thank my close family for supporting me through all these hard and exciting years. My brother, Max, for always reminding me that my livelihood depends on the patronage of the Federal government. My father, Ross, for always encouraging my curiosity and insisting that I learn my times tables in the 3rd grade. My step-mother, Dorothy, who has always supported my decision to go to graduate school. Most importantly, I thank my wife, Frances, who has always been there for me and who can make me laugh like no one else.

Fool that I was to plunge with such unsanctioned phrensy into mysteries no man was meant to penetrate…

— H. P. Lovecraft, *Hypnos*

Chapter 1

Introduction

1.1 Understanding Chemical Reactions

Chemical species are defined by the relative location of and interactions between the atomic nuclei and electrons that constitute them. Chemical reactions transform one kind of matter into another by "simply" changing the location and bonding of matter's constituent atoms, releasing or consuming energy in the process. Chemical reactivity is key to the universe that surrounds us; to the materials, people, plants and animals that we interact with everyday. This thesis seeks to improve our understanding of *why* and *how* different molecular systems react; with specific focus on changes in molecular shape and the transfer of electrons from one species to another.

In the most general terms we can think of all of matter as a set of positively charged nuclei and negatively charged electrons interacting with each other. These interactions can be described by a many body potential energy function that depends on the relative positions and momenta of each particle in the system. To simplify this complex picture we frequently use the fact that the electrons are much lighter than the nuclei–the Born-Oppenheimer approximation–to separate their motion. When valid this approximation leads to potential energy surfaces defined in terms of the nuclear coordinates, and each surface corresponds to a particular quantum state of the electrons. The lowest energy electronic state is known as the ground state and any minima on it correspond to a stable nuclear configuration; a stable molecular species or set of species. Viewed through this lens, a chemical reaction is defined by the *path* the system takes from one ground state minimum to another. If we knew the "lay of the land" of the potential energy surface then we could predict not only the final stable species of a system but the path the system would take to get there. Predictive power eventually leads to control and a better understanding of reactivity could lead to precisely designed molecular systems which reliably turn simple reactants into complex products with few side reactions, much as nature has done through billions of years of evolution.

Even if we could measure and record the full potential energy surface for a system we would not want to do so. Consider a relatively small system like ethylene, which has 6 atoms.The potential energy surface for ethylene depends on 12 variables. Even if we only wanted to have 10 data points for each degree of freedom we would have to measure, and *record*, 10^{12} data points for just one electronic state! Every extra atom increases this number by *three* orders of magnitude. Such a Herculean task is clearly impossible. Moreover, it is unnecessary; many of these points would correspond to energetically inaccessible configurations or completely dissociated atoms. If we want to understand reactivity we really only need to map out the valleys–the minimum energy pathways–and their surrounding regions which connect the potential minima.

Mapping the geography of the potential energy surface requires that we are able to measure the nuclear configuration (molecular structure) and energy as a function of time. Many established experimental techniques–such as vibrational spectroscopy, x-ray diffraction, electron diffraction, NMR spectroscopy and mass spectrometry–excel at measuring static structures of molecules and solids. But there are two difficulties associated with measuring the structure of dynamic reacting systems; first, unstable structures–that is the structures along the path from reactant to product–are, by definition, short lived and second, in a given ensemble of reacting molecules some will be further along the reaction path than the others meaning the measured structure will be an average of the structures along the reaction coordinate. Both of these issues are closely intertwined and

have the same solution: femtochemistry.[1–3]

Femtochemistry is the study of light induced reactions with femtosecond time resolution. Many important chemical reactions are light induced, from the initial photochemical event that allows you to read this page[4] to the photo-initiated reduction of carbon dioxide that powers most life on this planet.[5] Photochemical reactions are initiated when a molecular system absorbs a photon, which changes the electronic state of the system and thus the nuclear potential energy surface. Now the initial nuclear configuration is no longer stable and the system's structure evolves in search of a new minimum. In some cases the system's evolution will take it to a nuclear configuration where two electronic surfaces come close together, the conical intersection,[6–8] near this point the system can hop to the other surface and continue its search for a minimum there.

Light initiated reactions offer a unique opportunity to overcome the challenges of observing short lived species and ensemble averaging. Advances in laser technology have made the production of few femtosecond duration light pulses routine,[9,10] and cutting edge technology has pushed the envelope into the attosecond regime.[11] In a typical experiment, one such pulse excites an ensemble of systems preparing a coherent population of excited systems. Generally, because the ground state has a narrow distribution of nuclear configurations the prepared excited state population will too.* Evolution of the ensemble is interrogated by a delayed probe pulse. If the pulses are short compared to the nuclear dynamics, progress along the reaction path corresponds directly to the time delay between the initiation (pump pulse) and the measurement (probe pulse). Furthermore, if the interaction between the system and the bath is weak over the timescale of the observation, the population will maintain coherence and ensemble averaging will not result in the average structure between reactants and products but a well defined structure at a specific point along the reaction path. In effect, if the nuclear dynamics are slow compared to the duration of the pump and probe pulses, the measurements correspond to "snapshots" of the structure along the reaction path.

In order to record the *structure* as a function of time we must find a way to correlate our measurements with nuclear configuration. One method is to directly diffract electrons[12] or x-rays[13] off our prepared system. The resulting patterns can be interpreted within the well established framework of crystallography. However, both methods suffer from severe drawbacks including poor time resolution and the inability to probe disordered condensed phase systems. Nature frequently works within the messy and chaotic realm of solutions, precluding diffraction techniques from being used. To probe more realistic models of reactions, different ultrafast methods are required.

One method that has found widespread use in particular is transient electronic spectroscopy, in particular transient absorption. The probe pulse, which is now in the visible regime, cannot probe nuclear structure *directly* but instead interrogates the electronic structure. When performed in the gas phase on simple systems it is easy to relate the electronic signature to structural evolution. Rose, Rosker, and Zewail's famous transient laser induced fluorescence (LIF) experiment on NaI[14] revealed an oscillatory pattern in the excited state transient absorption of the probe beam. It was clear that this modulation corresponded to an oscillation in the NaI bond length as that is the only

*Note that for large molecules with low frequency motions, which can be thermally populated at experimental temperatures, this is no longer true.

nuclear degree of freedom. They also found that the products, disassociated Na and I atoms, were produced in a pulsed fashion that matched the oscillatory frequency of the bond length. They had recorded a chemical reaction and they could determine the precise nuclear configuration of the transition state.

Zewail's experiment recorded everything we want to know about a chemical reaction. It measured the structure and energy as a function of time thereby measuring the potential energy surface. While this was a Nobel Prize worthy achievement, the outcome was not particularly unexpected: in a disassociation reaction of a diatomic molecule the reaction coordinate *must* be the extension of the internuclear distance. Moreover, the technique is not extensible to polyatomic systems. For polyatomic systems in the condensed phase it is no longer possible to say that a certain electronic spectroscopic change corresponds to a particular nuclear rearrangement. That is not to say that transient absorption has not been instrumental in extending our understanding of condensed phase reaction dynamics, because it has. But if we want to know what is happening structurally within a system we need a different type of spectroscopy.

Vibrational spectroscopy offers a way to discern molecular structure as a function of time without resorting to diffraction methods. Vibrational spectroscopy measures the energy of the system's normal modes of vibration (c.f. Section 2.2) which, with some knowledge of the relative bonding, can be related *directly* to the structure of the molecule. Thus, measuring the vibrational spectrum can be used to determine how the molecular structure changes as a function of time. By combining such a spectroscopy with transient absorption one can measure both the structure and energy as a function of time fulfilling the requirements necessary to measure the potential energy surface.

The most common type of time resolved vibrational spectroscopy is transient infrared absorption spectroscopy.[15] This variant is identical to its electronic cousin save for the center wavelength of the probe pulse which is generally around 2000 cm^{-1}. However, transient IR has three main drawbacks: first, it is difficult to generate and detect IR photons. The probe beam in many implementations only covers 100-200 cm^{-1} of the vibrational spectrum offering a limited window into the evolving structure. Second, IR wavelengths are strongly absorbed by common optical materials, such as quartz, and common solvents, such as water. Third, the limited bandwidth of the IR probe and the group velocity mismatch between it and the visible pump restricts the time resolution of the experiment to a few hundred femtoseconds at best. Considering that many systems have fundamental vibrational frequencies between 0 and 3000 cm^{-1} and that nuclear dynamics can occur during one period of vibration, i.e. 10 to 1000 fs, it is clear that a better technique is needed.

Our laboratory has developed a spectroscopy which we call femtosecond stimulated Raman spectroscopy, or FSRS. As a Raman technique, FSRS operates in the visible and near IR where broadband pulses are easy to generate and detect. Moreover, because FSRS is stimulated it can achieve better time resolution and signal-to-noise than competing techniques.[16–18] FSRS has been used to elucidate the ultrafast isomerization in rhodopsin,[19] and excited state proton transfer in GFP[20] among many other examples.[21–28] In each of these cases FSRS has been able to offer new insight into the structural evolution of systems during a chemical reaction. In particular, the studies of rhodopsin and GFP have shown how FSRS can track structural changes that happen faster than the vibrational dephasing time of the system, an unintuitive and unexpected result.

1.2 OUTLINE

My goal for this thesis is to improve our understanding of molecular reactivity. Chapter 2 furnishes the reader with a short review of the quantum mechanics, nonlinear optics and nonlinear optical spectroscopy necessary to understand the measurements and discussion in the rest of the thesis followed by a brief description of the instrumentation. Chapter 3 describes the main improvement I made to the instrument; implementing an etalon filter to generate the Raman pump beam. Etalon filters are just as simple to incorporate as dielectric notch filters but offer a number of advantages such as higher throughput, narrower bandwidths and an asymmetric pulse shape that increases the signal while concomitantly reducing the background.

Chapters 4 and 5 describe my investigation into the photoisomerization dynamics of an azobenzene derivative 4-nitro-4'-dimethylaminoazobenzene (NDAB). Azobenzenes are a class of chromophores which exhibit a light induced change from the *trans* to the *cis* form about an N=N bond. In contrast to stilbene and other C=C containing materials, azobenzenes have two possible pathways for isomerization: a stilbene-like rotation and an in-plane inversion. Much controversy surrounds the question of which pathway is dominant in this system.[24,29–48] However, both my FSRS data (Chapter 4) and my ISRS data (Chapter 5) support a model in which the primary motion out of the Franck-Condon region is inversional.

Chapter 6 presents a collaboration between our group and that of Prof. J. M. Fréchet wherein we probe the effect of structural perturbations on a prototypical dye sensitized solar cell system. We compared and contrasted the effect of these perturbations on the free dye in solution and bound to a semiconducting substrate. Two main discoveries resulted from this study; first, we found that the FSRS data was only sensitive to the dye but that the transient absorption was sensitive to the dye *and* the injected electron in the semiconducting nanoparticle. We were able to use this fact to distinguish their separate dynamics and show that the decay of the transient absorption does *not* correspond to recombination of the charge carriers. Second, we observed that the extended conjugation system (TPAC3) showed strong signs of isomerization after the absorption of a photon (connecting this study to that of NDAB) thereby indicating that photo-labile moieties must be avoided when designing spacers in photovoltaic materials.

Chapter 7 examines a different type of charge transfer system; a charge transfer (CT) complex between a donor, tetramethylbenzene (TMB), and an acceptor, tetracyanoquinodimethane (TCNQ). The first order kinetics of this experiment agreed almost exactly with those reported earlier by Fujisawa, Creelman, and Mathies:[49] charge is transferred almost immediately following photoexcitation after which the nascent contact-ion pair is stabilized by polar solvation and charge recombination occurs on the tens of picoseconds timescale. However, when we examined the high resolution data between -500 and 2500 fs we discovered that both the peak frequencies and intensities oscillated as a function of time. We determined that these oscillations where the result of a 5^{th} order nonlinear process (see Appendix E) meaning that their magnitudes could be directly related to the anharmonic coupling between the complex's normal modes. Interestingly, the coupling between a highly displaced, totally symmetric, low frequency mode and a non totally symmetric high frequency mode was particularly large. Using this fact we determined that the low frequency mode constitutes the tuning and the high frequency one the coupling mode for the conical intersection

between the charge transfer excited state and the neutral ground state.

I conclude with Chapter 8 which summarizes these results and discusses potential improvements to the technique. Three specific areas are considered; enhancing the signal-to-noise of the instrument, fully automating the data analysis, and improving the bandwidth of the 2D-FSRS experiment. Better signal-to-noise will allow the study of less Raman active species and the application of broadband stimulated Raman to microscopy or high throughput, label-free and multiplexed analysis. But even with improvement of the signal-to-noise, such techniques will be impossible without the development of automated baseline removal methods due to the sheer number of spectra produced. In Chapter 7 we showed the utility of 2D-FSRS but the number of cross-couplings we could observe was technically limited because of the relatively long actinic pump. A shorter actinic pulse would be able to impulsively excite *all* skeletal motions in the system revealing a complete map of the molecule's anharmonic couplings.

Chapter 2

Theory and Instrumentation

In order to understand the measurements reported in this thesis it is imperative to have a basic understanding of quantum mechanics in general and both linear and nonlinear spectroscopy and optics, in particular. While I make no attempt to provide a comprehensive review of these subjects, I hope that this chapter will serve as a refresher for the professional and a guide through the available literature for the novice. Important concepts and nomenclature are indicated with **bold face** font. Some comfort with physics in general and basic quantum mechanics in particular is assumed. My hope is that any person with some advanced undergraduate courses in mathematics and physics should be able to follow along well enough.

My goal is that by the end of this chapter the reader will understand *what* has been measured in this thesis, *why* we measured it and *how* we have performed the measurement.

2.1 A Short Review of Quantum Mechanics

In the early 20th century it was thought that other than a few oddities to be worked out, most of nature could be explained by Newton's Laws and Maxwell's equations on any size scale. However, a set of experiments measured light to have particle-like attributes[50] and electrons to have wave-like properties.[51] Out of these observations grew a new theory of matter on the microscopic scale, that of **Quantum Theory**, which postulates that all of nature may be described, completely, by a wave function. For particles, this function is localized in space and time, for waves it is spread out. This description of nature has allowed us to predict myriad phenomena with great accuracy, including completely non-classical ones such as tunneling.

There are a many text books that cover Quantum Theory at different levels of sophistication and approximation. Cohen-Tannoudji, Diu, and Laloë[52] provide an excellent reference at the intermediate level. For spectroscopists of all skill levels we heartily recommend the text by Fayer.[53] The reader is referred to these and other textbooks for a complete and thorough treatment of quantum theory.

To begin we introduce the reader to the concept of state space and the meaning of measurement in the context of microscopic matter.

2.1.1 State Space and the Nature of Quantum Measurement

We postulate the state of a physical system can be completely described by a **wave function**, denoted as a **ket**, $|\psi\rangle$, and that the set of all possible wave functions ($\{|\psi_i\rangle\}$) forms a basis for a Hilbert vector space, which we will refer to as **state space**. Hilbert spaces have a number of important properties such as closure, which means that the sum of any two members of a Hilbert space is another member of the same space; and they posses an **inner product**.

The inner (scalar) product between two kets, $|\psi\rangle$ and $|\phi\rangle$, is defined as

$$\lambda = \langle\phi|\psi\rangle \tag{2.1}$$

where the newly defined **bra**, denoted as $\langle\phi|$, is the complex conjugate of the ket, $|\phi\rangle$, i.e. $\langle\phi|=|\phi\rangle^\dagger$, and λ is a complex scalar. Implicitly this means that $\lambda^\dagger = \langle\psi|\phi\rangle$ where the dagger denotes complex

conjugation. We will assume that all kets are normalized, i.e. $\langle\phi|\phi\rangle = 1$, and that members of a basis set are orthogonal, $\langle\psi_i|\psi_j\rangle = \delta_{i,j}$.* **Operators** are objects of this Hilbert space which transform one state into another, i.e.

$$\mathscr{O}|\psi\rangle = |\phi\rangle \tag{2.2}$$

Operators will be denoted with capital script letters where possible or when this becomes cumbersome with "hats," ˆ. We can define an **eigenket** of an operator to have the following property

$$\mathscr{O}|\psi\rangle = \lambda_\psi|\psi\rangle \tag{2.3}$$

where λ_ψ is the eigenvalue of the operator $\mathscr{O}$ associated with the ket $|\psi\rangle$. Here the operator is said to be acting *to the right*. If we take the complex conjugate of the above equation we get

$$\langle\psi|\mathscr{O}^\dagger = \langle\psi|\lambda_\psi^\dagger \tag{2.4}$$

Now $\mathscr{O}^\dagger$ is said to be operating *to the left*. If $\lambda_\psi = \lambda_\psi^\dagger$, which means that λ_ψ is real, the operator is called **Hermitian**. With this definition and that of the inner product, it should be clear that the **outer product** of two kets, $|\phi\rangle\langle\psi|$, is also an operator.

The closure property of state space allows us to express a general state of the system in a basis that spans state space. Mathematically

$$|\phi\rangle = \sum a_i|\psi_i\rangle \tag{2.5}$$

By forming the inner product with a single basis ket we find that

$$\langle\psi_i|\phi\rangle = a_i \tag{2.6}$$

which means that we could write

$$|\phi\rangle = \sum|\psi_i\rangle\langle\psi_i|\phi\rangle \tag{2.7}$$

suggesting that

$$\mathscr{I} = \sum|\psi_i\rangle\langle\psi_i| \tag{2.8}$$

Where $\mathscr{I}$ is the identity operator and the above equation is known as the **completeness relation**, which holds as long as the set of $|\psi\rangle$ form a complete basis. Note that the normality of $|\psi\rangle$ means that $\sum|a_i|^2 = 1$. Equation 2.6 suggests the connection between kets and standard vectors. A ket may be expressed in particular basis by the ordered list of a_i's, i.e. a vector with components a_i. The a_i are frequently referred to as **expansion coefficients**.

Next we postulate that every experimental measurement corresponds to a quantum mechanical operator and that the observed outcome of that measurement will be one of the eigenvalues. Because such operators correspond to real measurements, which must have real outcomes, they must be Hermitian. Furthermore, it is postulated that after the measurement is performed the system will be in the state corresponding to the observed eigenvalue. Considering a system in state $|\phi\rangle$ and a

*$\delta_{i,j}$ is the Kronecker delta and is equal to 1 for $i = j$ and equal to 0 for $i \neq j$.

measurement corresponding to an operator $\mathscr{O}$ with eigenkets $|\psi_i\rangle$ and eigenvalues λ_i we define the **expectation value** of $\mathscr{O}$ as

$$\left\langle \mathscr{O}_\phi \right\rangle = \langle\phi|\mathscr{O}|\phi\rangle \tag{2.9}$$

where the subscript ϕ indicates that the expectation value is calculated with respect to state $|\phi\rangle$. In the future the state with which the expectation value is taken will be obvious and the subscript will be dropped. To see the meaning of the expectation value let us use the completeness relation to expand $|\phi\rangle$ in terms of the eigenkets of $\mathscr{O}$, $|\psi_i\rangle$,

$$\langle\mathscr{O}\rangle = \langle\phi|\Big(\sum|\psi_i\rangle\langle\psi_i|\Big)\,\mathscr{O}\,\Big(\sum|\psi_i\rangle\langle\psi_i|\Big)|\phi\rangle = \sum \lambda_{\psi_i}\,|a_i|^2 \tag{2.10}$$

which is the average of all of the operator's eigenvalues weighted by the magnitude squared of the expansion coefficients. This seems to conflict with our earlier assertion that the observed outcome of a measurement will be an eigenvalue.

To address this let us consider a simple thought experiment. Here our system is a linearly polarized photon. We want to measure the polarization direction of the photon and to do so we pass the photon through a linear polarizer whose optical axis is at an angle θ relative to that of the photon and attempt to detect the photon on the other side. We know, intuitively and experimentally, that such a measurement on a *single* photon can only have *one* outcome: either the photon is detected, or it is not. The state space description for this experiment is simple and is spanned by $|\hat{\imath}\rangle$, the polarization state of the photon, and $|\hat{\jmath}\rangle$, the orthogonal polarization state. Our measurement corresponds to an operator $\mathscr{P}$ that has a two eigenkets, $|\pi_+\rangle$ and $|\pi_-\rangle$ that correspond to "the photon is measured," eigenvalue of 1, or null, eigenvalue of 0. Mathematically

$$\begin{aligned}\mathscr{P}|\pi_+\rangle &= 1|\pi_+\rangle\\ \mathscr{P}|\pi_-\rangle &= 0|\pi_-\rangle\end{aligned} \tag{2.11}$$

$|\pi_\pm\rangle$ can be expressed in terms of our original basis as

$$\begin{aligned}|\pi_+\rangle &= \cos\theta|\hat{\imath}\rangle - \sin\theta|\hat{\jmath}\rangle\\ |\pi_-\rangle &= \sin\theta|\hat{\imath}\rangle + \cos\theta|\hat{\jmath}\rangle\end{aligned} \tag{2.12}$$

We can use this new basis to calculate the expectation value of our measurement considering our initial state is $|\hat{\imath}\rangle$

$$\langle\mathscr{P}\rangle = \langle\hat{\imath}|\mathscr{P}|\hat{\imath}\rangle = |\langle\pi_+|\hat{\imath}\rangle|^2 + |\langle\pi_-|\hat{\imath}\rangle|^2 = \cos^2\theta \tag{2.13}$$

which corresponds *exactly* to what we would measure in the classical case. We could rewrite this equation as

$$\langle\mathscr{P}\rangle = \lambda_+ P(+) + \lambda_- P(-) \tag{2.14}$$

where $\lambda_+ = 1$, $\lambda_- = 0$ and $P(\pm) = |\langle\pi_\pm|\hat{\imath}\rangle|^2$. Clearly, $P(\pm)$ is the *probability* of measuring the system in state $|\pi_\pm\rangle$ given that the system was prepared in $|\hat{\imath}\rangle$. This implies that we can interpret the wave function as the **probability amplitude** of finding the system in a given state. By taking the square of the inner product of our prepared state with one of the eigenstates of our measurement operator we can predict the probability of measuring that particular eigenvalue. The name of the expectation value should now be clear as it is the way to calculate the *expected value* of a large number of measurements.

2.1.2 Time-Evolution of Quantum Systems: the Schrödinger Equation

We have postulated that the wave function contains all knowable information about a system and we have shown how it can be used to predict the outcome of experiments. Even though we have defined the mathematics behind wave functions and operators we have yet to explain the physical theory that will allow us to determine the wave function for a given system and its evolution. To do this we turn to Schrödinger's famous equation

$$i\hbar\frac{\partial}{\partial t}|\psi\rangle = \mathscr{H}|\psi\rangle \tag{2.15}$$

which is postulated to describe the *complete* time evolution of the system. Here $\mathscr{H}$ is the Hamiltonian operator which is the quantum mechanical analog of the classical Hamiltonian. Therefore measurement of a system's energy corresponds to operating on its representative ket with $\mathscr{H}$. The eigenvalues of $\mathscr{H}$ are the total energies of the eigenstates.

If the eigenkets and eigenvalues of $\mathscr{H}$ can be found, which is a difficult task in and of itself for all but the simplest systems, and $\mathscr{H}$ is time-independent then eq. 2.15 yields a simple solution

$$|\psi(t)\rangle = \sum_i c_i e^{-\frac{i}{\hbar}E_i t}|\xi_i\rangle \tag{2.16}$$

Where $c_i = \langle\xi_i|\psi\rangle$ and E_i and $|\xi_i\rangle$ are the eigenenergies and eigenkets of $\mathscr{H}$, respectively. In other words,

$$\mathscr{H}|\xi_i\rangle = E_i|\xi_i\rangle \tag{2.17}$$

It should be clear that any expectation value taken with respect to the $|\xi_i\rangle$ will *not* evolve in time and thus the $|\xi_i\rangle$ are referred to as **stationary states**.

The mathematical description of quantum mechanics outlined above is called **the Schrödinger picture**. In it all of the time dependence is contained within the kets and the operators are time independent. Heisenberg put forward another description, called **the Heisenberg picture** in which all the dynamical information is contained within the *operators*. This leads to a new equation of motion

$$\frac{d}{dt}\mathscr{O}(t) = \frac{i}{\hbar}\big[\mathscr{H}, \mathscr{O}(t)\big] + \frac{\partial\mathscr{O}(t)}{\partial t} \tag{2.18}$$

The square bracket term is known as a **commutator** and is defined as

$$\big[\mathscr{A}, \mathscr{B}\big] = \mathscr{A}\mathscr{B} - \mathscr{B}\mathscr{A} \tag{2.19}$$

Operators $\mathscr{A}$ and $\mathscr{B}$ are said to **commute** if

$$\big[\mathscr{A}, \mathscr{B}\big] = 0 \tag{2.20}$$

Commutativity of operators implies that the measurements corresponding to the operators may be made one after the other without disturbing the state of the system. In other words, these operators have a common set of eigenkets. Measurements whose operators do *not* commute may not be

performed successively without significantly altering the state of the system, a fact that leads to the concept of **the uncertainty principle**, which will be stated here without proof:[53]

$$\left\langle \mathscr{A}^2 \right\rangle \left\langle \mathscr{B}^2 \right\rangle \geq \frac{1}{4} \langle \mathscr{C} \rangle^2 \tag{2.21}$$

where $[\mathscr{A}, \mathscr{B}] = i\mathscr{C}$. Position and momentum are famous examples of two observables that do not commute and it can be shown[53] that the corresponding uncertainty relation is

$$\Delta x \Delta p \geq \frac{\hbar}{2} \tag{2.22}$$

where Δx is the uncertainty in the position of the system and Δp is the uncertainty in its momentum.

2.1.3 Time-Dependent Perturbation Theory and the Light-Matter Interaction

All of the observations in this thesis are measurements of a system's response to light, or more accurately, the system and light interact with each other and we measure what effect this interaction has on the light. Here we develop a simple theory to predict the outcome of our measurements and in the next section we combine this theory with specific models for the matter.

In many cases it is possible to split the molecular Hamiltonian into a time-independent portion and a time-dependent part. Frequently the time-dependent part can be treated perturbatively and this type of perturbation theory forms the basis for most theoretical descriptions of spectroscopy. To develop this theory let us consider the following Hamiltonian

$$\mathscr{H}(t) = \mathscr{H}_0 + \mathscr{T}(t) \tag{2.23}$$

where $\mathscr{H}_0$ is completely solvable and time-independent, with eigenkets $|\xi_i\rangle$ and eigenenergies E_i. Because the $|\xi_i\rangle$ form a basis we can write $|\psi\rangle$ as

$$|\psi\rangle = \sum_i c_i |\Xi_i\rangle \tag{2.24}$$

where we have defined $|\Xi_i\rangle = e^{-\frac{i}{\hbar}E_i t}|\xi_i\rangle$. We can plug this solution back into eq. 2.15 to get

$$i\hbar \sum_i \dot{c}_i |\Xi_i\rangle + i\hbar \sum_i c_i |\dot{\Xi}_i\rangle = \sum_i c_i \mathscr{H}_0 |\Xi_i\rangle + \sum_i c_i \mathscr{T}(t) |\Xi_i\rangle \tag{2.25}$$

Note that a dot over a symbol indicates the time derivative of that symbol. The second term on the left and the first term on the right are equal to each other by definition. Left multiplying by $\langle \Xi_j |$ gives

$$i\hbar \dot{c}_j = \sum_i c_i \langle \Xi_j | \mathscr{T}(t) | \Xi_i \rangle \tag{2.26}$$

Up until this point we have not made any approximations. However, we are left with the equally daunting task of solving many coupled differential equations. There is hope though, if we assume

that the magnitude of $\mathscr{T}$ is small compared to $\mathscr{H}_0$ and that the system is initially prepared in only one eigenstate of $\mathscr{H}_0$, $|\xi_n\rangle$, then we can say

$$i\hbar\dot{c}_j = c_n\langle\xi_j|\mathscr{T}(t)|\xi_n\rangle e^{-i\omega_{jn}t} \tag{2.27}$$

where we have introduced the **transition frequency**, defined as

$$\omega_{jn} = \frac{E_j - E_n}{\hbar} \tag{2.28}$$

To connect this technique to spectroscopy we have to think about how an electric field interacts with a molecule. A molecule is a collection of positive (nuclei) and negative (electrons) charges. Charged particles interact with an electromagnetic field through the following potential

$$\mathbf{U} = q\Phi - \frac{q}{c}\mathbf{A}\cdot\mathbf{v} \tag{2.29}$$

where q is the charge of the particle, Φ is the scalar potential of the field, c is the speed of light, $\mathbf{A}$ is the vector potential of the field and $\mathbf{v}$ is the velocity of the particle. At this point we could realize that the length scale of the fields we commonly use in visible spectroscopy are much, much larger than the length scale of a typical system. For instance, we commonly use ~400 nm light to excite a molecule that is no larger than a few nm. We can use this separation of size scales to our advantage and assume that the field, at a given instant of time, is constant over the entire system. This is known as the **dipole approximation**. Furthermore, considering that the magnetic field's interaction with the system is in general much smaller than that of the electric field we can ignore it. With these two approximations it can be shown[52,53] that the point charge-field interaction becomes

$$\mathbf{U} = -q\frac{\mathbf{p}}{m}\cdot\boldsymbol{\mathcal{E}} \tag{2.30}$$

Where $\mathbf{p}$ is the momentum and m is the mass of the particle and $\boldsymbol{\mathcal{E}}$ is the electric field. If we continue to treat the field as classical but replace the molecular functions with their operator counterparts we obtain

$$\mathscr{T}(t) = -\frac{q}{m}\hat{\mathbf{p}}\cdot\boldsymbol{\mathcal{E}}(t) \tag{2.31}$$

Where we have equated $\mathbf{U}$ with the time dependent part of the quantum mechanical Hamiltonian, $\mathscr{T}(t)$, and we have introduced the quantum mechanical momentum operator $\hat{\mathbf{p}}$. It can be shown that $-i\hbar\hat{\mathbf{p}}/m = [\mathscr{H}_0, \hat{\mathbf{r}}]$, where $\hat{\mathbf{r}}$ is the quantum mechanical position operator. Making this substitution we can calculate the time-dependent probability amplitude associated with state j due to the time-dependent perturbation, via eq. 2.27, to be

$$\dot{c}_j = -\frac{c_n}{\hbar}\omega_{jn}q\langle\xi_j|\hat{\mathbf{r}}|\xi_n\rangle e^{-i\omega_{jn}t}\cdot\boldsymbol{\mathcal{E}}(t) \tag{2.32}$$

Note that the above equation needs to be solved for *all* the charge particles in a molecule, i.e. the *total* time-dependent Hamiltonian is actually

$$\mathscr{T}(t) = -\left(\sum_i \frac{q_i}{m_i}\hat{\mathbf{p}}_i\right)\cdot\boldsymbol{\mathcal{E}}(t) \tag{2.33}$$

where i runs over all charged particles and

$$\dot{c}_j = -\frac{c_n}{\hbar}\omega_{jn}e^{-i\omega_{jn}t}\left(\sum_i q_i\langle\xi_j|\hat{\mathbf{r}}_i|\xi_n\rangle\right)\cdot\boldsymbol{\mathcal{E}}(t) \tag{2.34}$$

We can write this as

$$\dot{c}_j = -\frac{c_n}{\hbar}\omega_{jn}e^{-i\omega_{jn}t}\hat{\boldsymbol{\mu}}_{jn}\cdot\boldsymbol{\mathcal{E}}(t) \tag{2.35}$$

where

$$\hat{\boldsymbol{\mu}}_{jn} = \langle\xi_j|\hat{\boldsymbol{\mu}}|\xi_n\rangle \tag{2.36}$$

is the **transition dipole moment** associated with the transition between state n and j. Here we have introduced the dipole moment operator

$$\hat{\boldsymbol{\mu}} = \sum_i q_i\hat{\mathbf{r}}_i = \mu_0\hat{\mathbf{r}} \tag{2.37}$$

where μ_0 is the dipole moment associated with the collection of charges and $\hat{\mathbf{r}}$ is the position operator along the dipole moment.

Without loss of generality let us consider a system whose dipole moment is aligned along an electric field oscillating with frequency ω. Now the time-rate of change of the probability amplitude that the system will be found in state j can be written as

$$\dot{c}_j = -\frac{c_n}{\hbar}\omega_{jn}\mathcal{E}_0\hat{\mu}_{jn}\left(e^{-i(\omega_{jn}-\omega)t} + e^{-i(\omega_{jn}+\omega)t}\right) \tag{2.38}$$

Before integrating this equation consider a situation when $\omega \approx \omega_{jn}$. In this case, the second term will oscillate at a frequency of ~2ω while the first will hardly oscillate at all. If the integral is over a large enough time interval the oscillations in the second term will average to zero. Neglecting the second term from hereon, as we will do, is referred to as the **rotating wave approximation**. Integrating yields:

$$c_j(t) = i\frac{c_n}{\hbar}\omega_{jn}\mathcal{E}_0\hat{\mu}_{jn}\frac{e^{-i(\omega_{jn}-\omega)t}-1}{\omega_{jn}-\omega} \tag{2.39}$$

where we have chosen our constant of integration such that $c_j(0) = 0$.

Now we can calculate the time-dependent *probability* of finding the system in state j given that it was initially in state n due to the influence of a classical oscillating electric field.

$$P_{jn}(t) = \left|c_j(t)\right|^2 = \frac{\omega_{jn}^2t^2}{4\hbar^2}I_0\hat{\mu}_{jn}^2\mathrm{sinc}^2\frac{\Delta\omega t}{2} \tag{2.40}$$

where $I_0 = |\mathcal{E}_0|^2$ is the intensity of the electric field and $\Delta\omega = \omega_{jn} - \omega$. Clearly the amount of transfer of population from initial state n to final state j per unit time–and keep in mind that this population is equivalent to the amount of energy being absorbed by the system–is directly controlled by the incident intensity, I_0, the resonance detuning, $\Delta\omega$, and the transition dipole moment, $\hat{\mu}_{jn}$. In the next section we see how to determine if $\hat{\mu}_{jn}$ is non-zero, that is whether or not the transition between states is allowed for a simple molecular model.

2.2 Molecular Spectroscopy

Molecular spectroscopy is covered beautifully at the basic level in the excellent text by Harris and Bertolucci.[54] For more advanced readers the canonical series by Herzberg[55–58] is recommended. McHale has written an excellent intermediate level text[59] which covers more modern topics in addition to the classics.

Spectroscopy, in its essence, is the act of using electromagnetic radiation to determine the nature of matter in microscopic detail. We showed above that a time varying electric field can couple to stationary states of a material system. For a general system composed of m electrons and n nuclei we have to solve the full Schrödinger equation for $3 \times (m + n)$ degrees of freedom. For more than a few select (i.e. small) systems such as the hydrogen atom and the $H_2{}^+$ molecule this problem quickly becomes intractable. However, there is some salvation to be had by using the separation of timescales implied by the difference in masses. There are four timescales that are important for molecular spectroscopy; translation of the center of mass, rotation of the system about its primary axes of inertia, internal motion of the nuclei (i.e. vibrations) and motion of the electrons (i.e. electronic states).

Consider an electron and a proton both having the same kinetic energy. Since $T = \frac{1}{2}mv^2$ this implies that for equal energies the electron is moving ~43 times faster. Such a large separation in speeds, which is much larger for heavier nuclei, suggests that nuclear motion may be separated from the electronic degrees of freedom, which is famously known as the **Born-Oppenheimer approximation** (BOA). In other words, we assume that the electrons are always at equilibrium with respect to the nuclear motion. While the BOA does break down, sometimes in fantastic fashion as will be discussed in Chapter 7, it can describe the vast majority of spectroscopy extremely well and therefore acts as the bedrock of molecular spectroscopy. As a result of the BOA the Hamiltonian of the system is separable into an electronic component and a nuclear component,

$$\mathscr{H} = \mathscr{H}_e(R) + \mathscr{H}_n \tag{2.41}$$

Where the electronic component depends *parametrically* on the nuclear coordinates. The parametric dependence means that the electronic wave function must be solved for each nuclear configuration. A separable Hamiltonian implies that the wave functions can be factorized, i.e.,

$$|\Psi\rangle = |\psi_e\rangle|\psi_n\rangle \tag{2.42}$$

which leads to the concept of a **potential energy surface** (PES) defined by $V_e(R) = \mathscr{H}_e(R)|\psi_e\rangle$. We can imagine the nuclear wave function evolving on a PES defined by the electrons. In cases where the nuclei are relatively heavy we can even approximate the motion on the PES as classical and this forms the basis for many semi-classical theories.

Within the BOA, the nuclear Hamiltonian is further separable into center of mass motions and internal motions. If we assume that the timescale of rotations is much larger than that for vibrations we can use the Rigid Rotor approximation to separate vibrations and rotations. Finally we have,

$$\mathscr{H} = \mathscr{H}_e(R) + \mathscr{H}_v + \mathscr{H}_r + \mathscr{H}_t \tag{2.43}$$

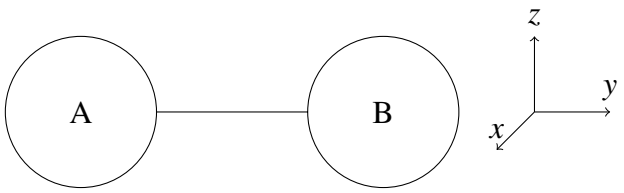

Figure 2.1: A simple diatomic molecule. Atoms A and B can be the same, a homonuclear diatomic, or different, a heteronuclear diatomic.

We are most interested in the internal motions of the system and will therefore be ignoring the translation of the center of mass for the rest of this thesis. This means that our wave function can now be written as,

$$|\Psi\rangle = |\psi_e\rangle|\psi_v\rangle|\psi_r\rangle \tag{2.44}$$

2.2.1 Diatomics

To gain a better understanding of how these approximations can lead to an intuitive understanding of molecular spectra let us begin with diatomics, see Figure 2.1. There are two classes of diatomic molecules; homonuclear, where both atoms are the same, e.g. H_2, N_2, O_2, etc.; and heteronuclear, where the atoms are different, e.g. NaCl, HCl, etc. Diatomics, while simple, illustrate the most important aspects of rotational, vibrational and electronic spectroscopies including selection rules.

Rotations

Diatomics have 6 nuclear degrees of freedom. Three are translations of the center of mass. Two are rotational degrees of freedom, one about z and the other about x. Rotation about y is not included because such a rotation has zero moment of inertia as the nuclei are assumed to be point masses. Furthermore both rotational motions are **degenerate**, meaning they have the same energy and character. Remember that even though we consider the nuclei to be moving much slower than the electrons the nuclei are still quantum particles and the rotational Hamiltonian is still,

$$\mathscr{H}_r = \frac{\hat{L}^2}{2I} \tag{2.45}$$

where $\hat{L}$ is the angular momentum operator and I is the moment of inertia. This potential is one of the canonical ones in physics and is known as the Rigid Rotor. The quantum mechanical Rigid Rotor has allowed energy of

$$E_J = \frac{J(J+1)\hbar^2}{2I} \tag{2.46}$$

where J is the rotational quantum number.

This would be a good time to introduce the concept of wavenumbers (cm^{-1}). Wavenumbers are a means of measuring energy, they are used frequently in vibrational and rotational spectroscopy as they have a convenient magnitude for both types of transitions; for instance a typical rotational

transition is on the order of a few wavenumbers and a typical vibrational transition is on the order of a few hundred to a few thousand wavenumbers.[†] For the rest of this chapter a tilde will indicate that a quantity is in wavenumbers. In this case the energy would be,

$$\widetilde{E}_J = \widetilde{B}_0 J(J+1) \tag{2.47}$$

where,

$$\widetilde{B}_0 = \frac{h}{8\pi^2 Ic} \tag{2.48}$$

The corresponding wave functions are spherical harmonics, $Y_J^M(\theta, \phi)$, see the references listed at the beginning of this section for more information.

Vibrations

After rotations we have one remaining nuclear degree of freedom, the internuclear distance, Q. In general the PES formed by the electrons is complicated; however, if we only assume small displacements from equilibrium we can Taylor expand $V_e(Q)$ about the equilibrium distance Q_0. The lowest order non-zero term of this expansion is the second order term because we can choose $V_e(Q_0) = 0$ and the first derivative is 0 by definition. This is known as the **Harmonic Oscillator Approximation**. A harmonic potential leads to an analytically solvable Hamiltonian and our energy levels (eigenvalues) are

$$\widetilde{E}_v = \left(v + \frac{1}{2}\right)\widetilde{\omega} \tag{2.49}$$

where $\widetilde{\omega}$ is the fundamental frequency in wavenumbers of the oscillator and v is the vibrational quantum number. Our wave functions are

$$\psi_v(Q) = \frac{1}{\sqrt{2^v v!}} \left(\frac{2\mu c\widetilde{\omega}}{\hbar}\right)^{\frac{1}{4}} \exp\left(-\frac{\pi\mu c\widetilde{\omega}Q^2}{\hbar}\right) H_v\left(\sqrt{\frac{2\pi c\mu\widetilde{\omega}}{\hbar}}Q\right) \tag{2.50}$$

where H_v are the Hermite polynomials and μ is the reduced mass of the molecule. Figure 2.2 presents a schematic harmonic potential energy surface and the probability densities of the harmonic oscillator wave functions, i.e. $P_v(Q) = |\langle\psi(Q)|\psi(Q)\rangle|^2 = |\langle\psi|Q\rangle\langle Q|\psi\rangle|^2$.

2.2.2 Spectroscopy

The previous sub-sections covered the different rotational and vibrational energy levels in a diatomic system. Now the question is: how do we measure these energy levels? As we saw above, molecular systems can absorb light, but not just any frequency. Equation 2.40 shows that if the light is incident on the system for an appreciable amount of time only energy that corresponds

[†]Of course large polyatomic species can have vibrational motions on the order of tens of wavenumbers and rotational motions that are fractions of a wavenumber. For these molecules the rotations can generally be treated classically as can some of the extremely low frequency vibrations.

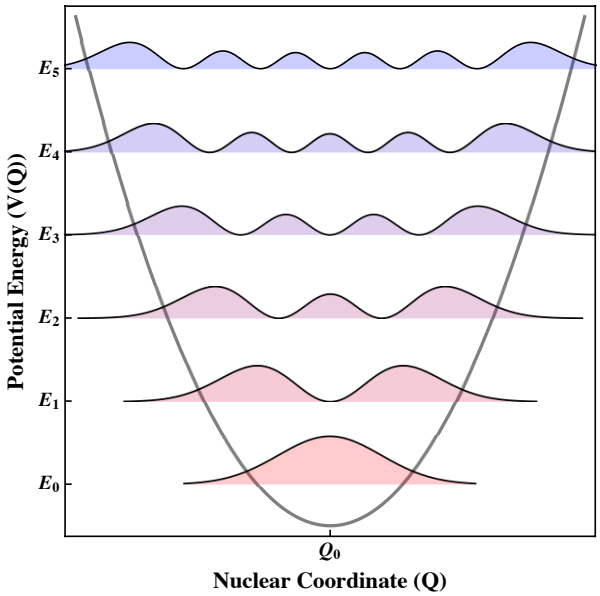

Figure 2.2: Harmonic oscillator potential and probability densities for the first six eigenstates. All energy levels are evenly spaced. Note that as the energy is increased the system is more likely to be found at the classical turning points.

to the difference in energy of two eigenstates of the molecular hamiltonian will be absorbed, i.e. $\Delta\omega = 0$. This is the **resonance condition**. However, this is not the only requirement that needs to be satisfied in order for photons to be absorbed, the other is that the transition dipole moment, eq. 2.36, must be non-zero. The requirements imposed by the transition dipole moment are known as **selection rules** and are a result of other physical properties of the system such as whether or not it has a dipole moment along a particular bond or not, the IR absorption selection rule. Selection rules can frequently be related to the symmetries of the states involved. Readers interested in the application of symmetry and group theory to spectroscopy are referred to Harris and Bertolucci's text[54] which provides the *best* starting point for a novice; more advanced readers will certainly want to consult Cotton's classic monograph.[60] Thus, if we were to record the transmission of light through the sample as a function of incident frequency, i.e. a spectrum, the resonances would tell us the energy levels (states) of the system and the intensity of the resonances would give us hints of the other properties of these energy levels (states).

Using our Born-Oppenheimer wave functions, the transition dipole moment, eq. 2.36, becomes

$$\langle\psi_{J'M'}|\langle\psi_{v'}|\langle\psi_{e'}|\hat{\boldsymbol{\mu}}|\psi_e\rangle|\psi_v\rangle|\psi_{JM}\rangle \tag{2.51}$$

Let us say that we are *not* changing electronic states, i.e. $e' = e$, then we can integrate out the electronic degrees of freedom, which gives

$$\langle\psi_{J'M'}|\langle\psi_{v'}|\hat{\boldsymbol{\mu}}^{(e)}|\psi_v\rangle|\psi_{JM}\rangle \tag{2.52}$$

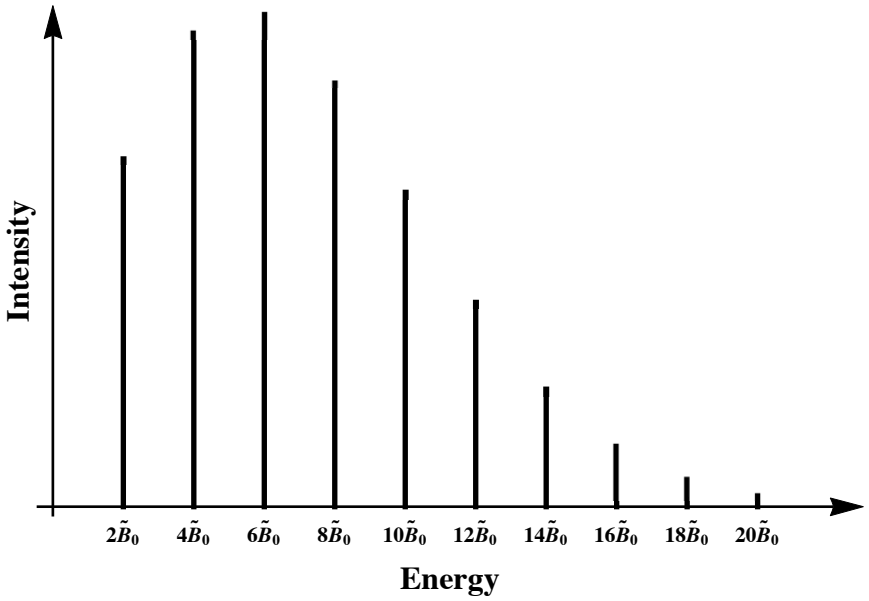

Figure 2.3: Theoretical rotational spectrum for a linear rigid rotor at finite temperature. Note that the rotational transitions are evenly spaced by $2\widetilde{B}_0$ which implies that the separation between eigenstates increases quadratically.

where $\hat{\boldsymbol{\mu}}^{(e)}$ is the dipole moment operator associated with electronic state e. Let us further assume that we are *not* changing vibrational states either, i.e. $v' = v$, then we can integrate out the vibrational degrees of freedom and we have,

$$\langle \psi_{J'M'} | \hat{\boldsymbol{\mu}}_0 | \psi_{JM} \rangle \tag{2.53}$$

where $\hat{\boldsymbol{\mu}}_0$ is the permanent dipole moment associated with vibrational state v and electronic state e, this is sometimes referred to as the vibronically averaged dipole moment.

With respect to these approximations the dipole moment becomes proportional to the vector connecting the two nuclei, i.e. $\boldsymbol{\mu_0} = \mu_0 \mathbf{Q}$. Using this result we can determine when eq. 2.53 is non-zero, in fact we get the same answer as for the Hydrogen atom, see references from Section 2.1, that is

$$\begin{aligned} \Delta J &= \pm 1 \\ \Delta M &= 0, \pm 1 \end{aligned} \tag{2.54}$$

Note that the molecule must have a permanent dipole moment ($\mu_0 \neq 0$) to have a pure rotational spectrum. Furthermore, the second selection rule, $\Delta M = 0, \pm 1$ only matters when the degeneracy amongst the M levels is lifted, as is the case when there is an external field. With this in hand we can calculate a pure rotational spectrum. The energy difference between adjacent states is

$$\Delta \widetilde{E}_{J,J+1} = 2\widetilde{B}_0(J+1) = \widetilde{\nu}_{J \to J+1} \tag{2.55}$$

Therefore, there will be resonances at each of these frequencies and the spectrum would look something like Figure 2.3. Note that each energy level has a degeneracy of $2J + 1$ associated with it.

Now let us examine what happens when there is a change in vibrational state as well, that is $v \neq v'$. Now we have,

$$\langle \psi_{J'M'} | \langle \psi_{v'} | \hat{\boldsymbol{\mu}}^{(e)} | \psi_v \rangle | \psi_{JM} \rangle = \langle \psi_{J'M'} | \hat{\boldsymbol{\mu}}_{v \to v'} | \psi_{JM} \rangle \tag{2.56}$$

where $\hat{\boldsymbol{\mu}}_{v \to v'}$ is the transition dipole moment operator associated with that vibrational transition. The dipole moment operator has some dependence on the nuclear coordinates, Q. Assuming the deviation from equilibrium is small we can expand $\hat{\boldsymbol{\mu}}^{(e)}$ in a Taylor series around the minimum internuclear distance Q_0,

$$\hat{\boldsymbol{\mu}}^{(e)}(Q) = \hat{\boldsymbol{\mu}}^{(e)}(Q_0) + \left.\frac{\partial \hat{\boldsymbol{\mu}}^{(e)}}{\partial Q}\right|_{Q=Q_0} \Delta Q + \cdots \tag{2.57}$$

Where ΔQ is the displacement from Q_0. Finally we have,

$$\begin{aligned} \hat{\boldsymbol{\mu}}_{v \to v'} = \langle \psi_{v'} | \hat{\boldsymbol{\mu}}^{(e)}(Q) | \psi_v \rangle &= \langle \psi_{v'} | \hat{\boldsymbol{\mu}}^{(e)}(Q_0) | \psi_v \rangle + \langle \psi_{v'} | \frac{\partial \hat{\boldsymbol{\mu}}^{(e)}}{\partial Q} \Delta Q | \psi_v \rangle \\ &= \hat{\boldsymbol{\mu}}^{(e)}(Q_0) \langle \psi_{v'} | \psi_v \rangle + \frac{\partial \hat{\boldsymbol{\mu}}^{(e)}}{\partial Q} \langle \psi_{v'} | \Delta Q | \psi_v \rangle \end{aligned} \tag{2.58}$$

The first term is zero if $v \neq v'$ and does not contribute to vibrational transitions. It can be shown[53] that $\langle \psi_{v'} | \Delta Q | \psi_v \rangle = 0$ if $\Delta v \neq \pm 1$. Therefore the second term is identically zero if $\Delta v \neq \pm 1$ or $\hat{\boldsymbol{\mu}}(Q)$ does not change with Q. That gives us two selection rules for seeing a vibrational transition:

1. The dipole moment must change with the vibration, $\frac{\partial \hat{\boldsymbol{\mu}}^{(e)}}{\partial Q} \neq 0$
2. The transition must be between adjacent vibrational states, $\Delta v = \pm 1$

Rule 2 was derived within the harmonic oscillator approximation and thus anharmonicities will relax the $\Delta v \pm 1$ selection rule. Of course, large deviations from Q_0 will not only lead to anharmonicities but also require that higher order terms be included in the expansion of eq. 2.58.

From this overview of rotational and vibrational selection rules it should be clear that it is possible to record a pure rotational spectrum but *not* a pure vibrational spectrum. Remember that if there is a vibrational transition then there will be a transition moment dipole ($\boldsymbol{\mu}_0$) that is non-zero and this will go on to operate on the rotational wave functions. Therefore, the *total* transition dipole moment will only be non-zero when there is a rotational transition as well. Figure 2.4 presents the infrared absorption spectrum of HCl which nicely illustrates these concepts. The energy of a pure vibrational transition is marked by the dotted line and a resonance at this energy is absent, as expected. The low energy side of the rotational fine-structure is called the P-Branch while the high side is called the R-Branch. Doublets are observed for each rotational transition due to the contribution of both naturally abundant chlorine isotopes ^{35}Cl and ^{37}Cl.

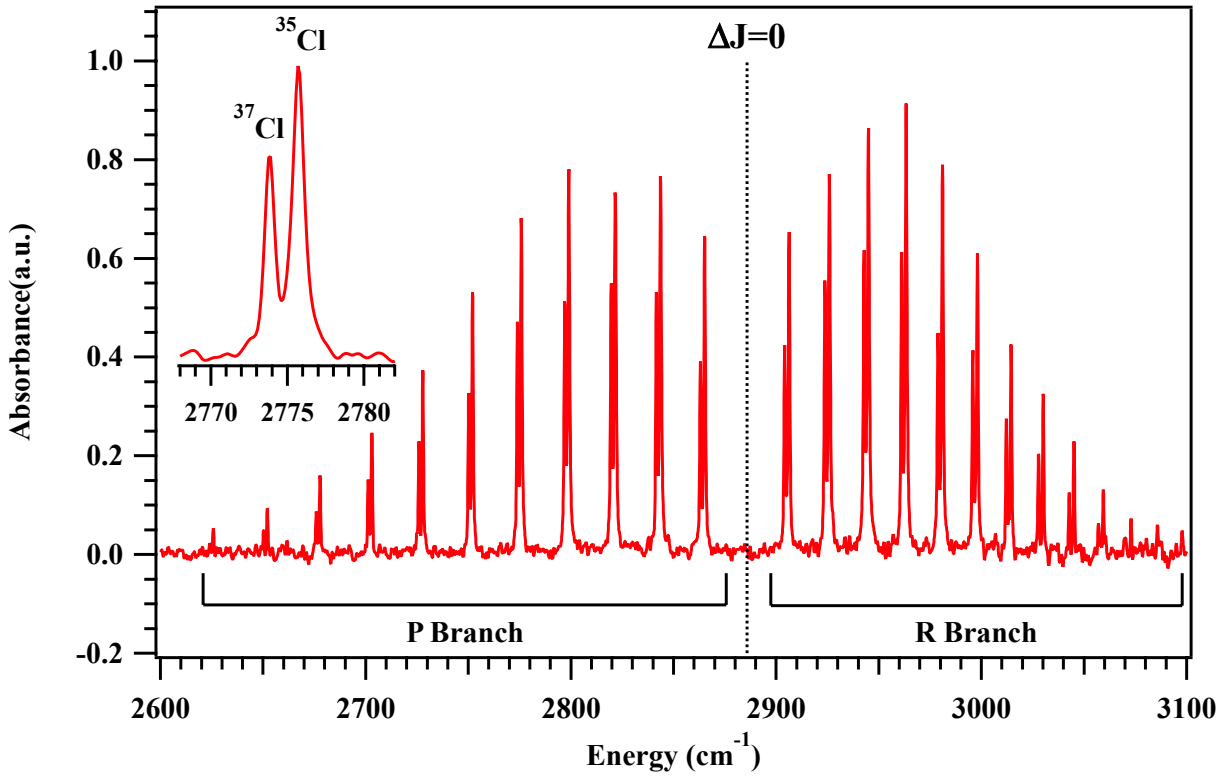

Figure 2.4: Rotational-vibrational infrared spectrum of HCl. Notice the absence of a resonance for $\Delta J = 0$ as expected. Notice the agreement of both rotational branches with Figure 2.3. The inset displays an expanded view of the $5 \rightarrow 4$ rotational transition which clearly shows the contributions from both naturally abundant chlorine isotopes. (*Data courtesy of David T. Valley.*)

Selection rules for electronic transitions, i.e. where $e' \neq e$, are calculated in an analogous manner to those of vibrational spectroscopy. The most salient difference here is that the rotational and vibrational wave functions of the excited state are *different* from the ground state. Going back to eq. 2.51 we see that the dipole moment operator, $\hat{\boldsymbol{\mu}}$, depends on *both* the nuclear and electronic degrees of freedom. Recall that the BOA rests on the fact that electronic motions occur much faster than nuclear motions. It seems reasonable, then, to assume that the nuclear dependence of the dipole operator can be ignored, i.e. $\hat{\boldsymbol{\mu}}(Q) \approx \hat{\boldsymbol{\mu}}(Q_0)$. This is known as the **Condon Approximation**, which leads to

$$\langle \psi^{e'}_{J'M'} | \psi^{e}_{JM} \rangle \langle \psi^{e'}_{v'} | \psi^{e}_{v} \rangle \langle \psi_{e'} | \hat{\boldsymbol{\mu}}(Q_0) | \psi_e \rangle \tag{2.59}$$

Where the electronic state of the vibrational and rotational wave functions has been made explicit. In general the evaluation of the electronic term is difficult, however, if the symmetry of the different electronic states are known (and there are a few ways to predict their character, such as molecular orbital theory) then an estimation of their "allowedness" is possible. One consequence of eq. 2.59 the importance of which cannot be stressed enough, is that the overall probability of the electronic transition is modulated by the overlap of the nuclear wave functions on the two electronic states.

This means that, in general, the most likely transition will *not* be from the ground vibrational state of electronic state e to the ground vibrational state of electronic state e'. This phenomenon is known as the **Franck-Condon Principle** and the bracket $\langle \psi_{v'}^{e'} | \psi_v^e \rangle$ is known as the **Franck-Condon Factor**.

Before moving on we should note that the spin states of the system have not been included in this discussion. For most main group elements, the Hamiltonian and resulting wave functions can be further factorized such that the electronic part now consists of the real space electronic degrees of freedom and the electronic spin degrees of freedom. Now both equations 2.51 and 2.59 will contain an extra term of $\langle \psi_{s'} | \psi_s \rangle$ which adds the additional selection rule of $\Delta s = 0$. As a consequence, light induced transitions between different spin states are formally forbidden.

Our current theory can adequately explain a fair amount of molecular spectroscopy. We can predict where we would expect to see absorption peaks and how intense they should be along with an explanation as to why the $0 \rightarrow 1$ vibrational transition is not allowed unless it is accompanied by a rotational transition. However, it is experimentally observed that the spacing between rotational levels depends on the vibrational level and vibrational overtone transitions can be measured, i.e. transitions of $0 \rightarrow 2$. Such observations suggest that our theoretical model is incomplete. To find an explanation for this shortcoming, let us consider the approximations we have made; one in particular should strike us as being especially egregious. Let us perform a thought experiment, picture two hydrogen atoms infinitely far apart from one another; there is no force between them. As we bring them closer together they begin to feel an attractive force due to dispersion effects. At a certain internuclear distance there is no force, the energy of the system is at a minimum. If we continue to push the atoms together the nuclei begin to repel each other, strongly. For small Q the potential increases sharply, for large Q the potential levels out to zero. Is this potential approximately harmonic? Clearly the answer is no!

A good empirical model for a diatomic PES is shown in Figure 2.5 and is known as the Morse potential. The equation for the Morse potential is,

$$V(Q) = D_e \left(1 - e^{-a\Delta Q}\right)^2 \tag{2.60}$$

The Schrödinger equation with this potential is exactly solvable and the allowed energy levels are,

$$\widetilde{E}_v = a\sqrt{\frac{\hbar \widetilde{D}_e}{\pi c \mu}}\left(v + \frac{1}{2}\right) - \frac{\hbar a^2}{4\pi c \mu}\left(v + \frac{1}{2}\right)^2 \tag{2.61}$$

It is immediately clear that there are a few major differences between the Morse and harmonic potentials:

1. The energy levels get closer together as v increases.
2. Overtones are now *allowed*
3. The average internuclear distance *increases* with increasing v as you can see in Figure 2.5

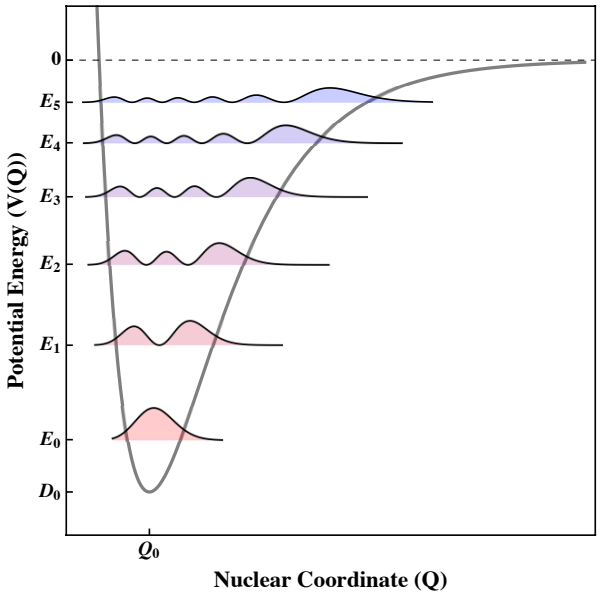

Figure 2.5: Morse potential with associated probability densities for the first six eigenstates. The probability densities have been magnified by a factor of 3 for clarity. Spacing between the energy levels decreases with increasing energy. Note that as the energy increases the system is more likely to be found at the far classical turning point in contrast with the harmonic oscillator.

The harmonic oscillator selection rule of $\Delta v = \pm 1$ is now void explaining the fact that overtones can be experimentally observed. Moreover, the irregular spacing of the energy levels explains why observed overtone bands occur at energies less than twice that of the fundamental, a prediction of the harmonic oscillator model.

Examining Figure 2.5 it is clear that the average internuclear distance $\langle Q \rangle$ increases with increasing v. If we again assume that vibrational motion is much faster than rotational motion then we see that the moment of inertia, I will depend parametrically on $\langle Q \rangle$ and hence the vibrational level. For a diatomic this effect can be taken into account empirically by modifying eq. 2.47 as follows

$$\widetilde{E}_J = \widetilde{B}_v J(J+1) \tag{2.62}$$

where,

$$\widetilde{B}_v = \widetilde{B}_e - \widetilde{\alpha}_e \left(v + \frac{1}{2} \right) \tag{2.63}$$

and $\widetilde{\alpha}_e$ is referred to as the *vibration-rotation coupling constant*.

2.2.3 Polyatomics

We have used diatomics to illustrate the basics of molecular spectroscopy, now we will generalize these concepts to polyatomic species. First let us consider how the nuclear degrees of freedom

Table 2.1: Comparison of the number and type of degrees of freedom for diatomic and polyatomic species.

	Diatomics	**Polyatomics**
Translational	3	3
Rotational	2	3
Vibrational	1	$3N-6$

increase with the number of nuclei (N), see Table 2.1. The number of rotational degrees of freedom only increases by one so we begin there.

Rotations

We know from classical mechanics[61] that the angular momentum of a rigid three dimensional body in an arbitrary cartesian coordinate system is

$$\mathbf{L} = \mathbf{I} \cdot \boldsymbol{\omega} \tag{2.64}$$

where $\boldsymbol{\omega}$ is the vector of rotational frequencies and $\mathbf{I}$ is the moment of inertia tensor defined as

$$\mathbf{I} = \begin{pmatrix} I_{xx} & I_{xy} & I_{xz} \\ I_{yx} & I_{yy} & I_{yz} \\ I_{zx} & I_{zy} & I_{zz} \end{pmatrix} \tag{2.65}$$

with

$$I_{jk} = \sum_i m_i \left(r_i^2 \delta_{jk} - j_i k_i \right) \tag{2.66}$$

where j and k are the coordinates with respect to the center of mass and δ is the Kronecker delta. As an example,

$$I_{xy} = -\sum_i m_i x_i y_i \tag{2.67}$$

There is a theorem of classical mechanics that says you can find three mutually perpendicular axes for which $\mathbf{I}$ is diagonal. This means that we can decouple the various angular momenta from each other allowing a solution of Schrödinger's equation. There is one caveat; at least two of the principle moments of inertia must be equal for the solutions to be analytical. Selection rules for spherical tops and prolate and oblate symmetric tops can be found in nearly any physical chemistry text book.

Vibrations

Now we move on to the $3N-6$ vibrational degrees of freedom. We will invoke the BOA again except that this time the electronic Hamiltonian depends on the $3N-6$ internal coordinates and

the resulting PES is a $3N-6$ dimensional surface. Nevertheless a minimum can still be found as evidenced by a stable, equilibrium, geometry and we can use a similar approach as before, namely expanding the potential in a Taylor series and truncating at second order

$$V(\mathbf{R}) = V(\mathbf{R}_0) + \nabla V(\mathbf{R}) \cdot \Delta\mathbf{R} + \frac{1}{2}\Delta\mathbf{R} \cdot H(V(\mathbf{R})) \cdot \Delta\mathbf{R} \tag{2.68}$$

where $\Delta\mathbf{R}$ is the displacement from $\mathbf{R}_0$ and H is called the Hessian which is the matrix of second derivatives of V, i.e.,

$$H = \begin{pmatrix} \frac{\partial^2 V}{\partial x_1^2} & \frac{\partial^2 V}{\partial x_1 \partial x_2} & \cdots & \frac{\partial^2 V}{\partial x_1 \partial x_n} \\ \frac{\partial^2 V}{\partial x_2 \partial x_1} & \frac{\partial^2 V}{\partial x_2^2} & \cdots & \frac{\partial^2 V}{\partial x_2 \partial x_n} \\ \vdots & \vdots & \ddots & \vdots \\ \frac{\partial^2 V}{\partial x_n \partial x_1} & \frac{\partial^2 V}{\partial x_n \partial x_2} & \cdots & \frac{\partial^2 V}{\partial x_n^2} \end{pmatrix} \tag{2.69}$$

and the x_i are the cartesian coordinates for each nuclei. The first two terms of 2.68 are identically zero by virtue of the fact that we have defined $V(\mathbf{R}_0)$ to be zero and that $\mathbf{R}_0$ is at the equilibrium geometry. This results in $3N-6$ coupled harmonic oscillator equations,

$$m_i \ddot{x}_i = -\sum_j k_{ij} x_j \tag{2.70}$$

where we have defined $k_{ij} = \partial^2 V / \partial x_i \partial x_j$ and the x_i represent displacements of coordinates from their equilibrium positions. If we switch to mass weighted coordinates we get,

$$\ddot{q}_i = -\sum_j b_{ij} k_j \tag{2.71}$$

where $q_i = \sqrt{m_i} x_i$ and $b_{ij} = k_{ij} / \sqrt{m_i m_j}$. This equation can be expressed in matrix form as,

$$\ddot{\mathbf{q}} = -B \cdot \mathbf{q} \tag{2.72}$$

If we can find a matrix D such that,

$$DBD^{-1} = \Lambda \tag{2.73}$$

where Λ is diagonal, then we can write, letting $D\mathbf{q} = \mathbf{Q}$,

$$\ddot{\mathbf{Q}} = -\Lambda \cdot \mathbf{Q} \tag{2.74}$$

Because Λ is diagonal this results in $3N-6$ *uncoupled* harmonic oscillators each with a fundamental frequency $\omega_i = \sqrt{\lambda_i}$ ($\lambda_i = \Lambda_{ii}$). We can solve Schrödingers equation for each of these uncoupled harmonic oscillators and this leads to the vibrational spectra we typically see: distinct peaks corresponding to the decoupled oscillators. These oscillators are called **normal modes of vibration** and the Q_i are called **normal coordinates**. The distinct feature of a normal mode is that the atoms involved all move with the same frequency and in straight lines. The interested reader is strongly encouraged to consult the work of Wilson, Decius, and Cross[62] which is considered to be the gold standard for normal mode analysis for molecules.

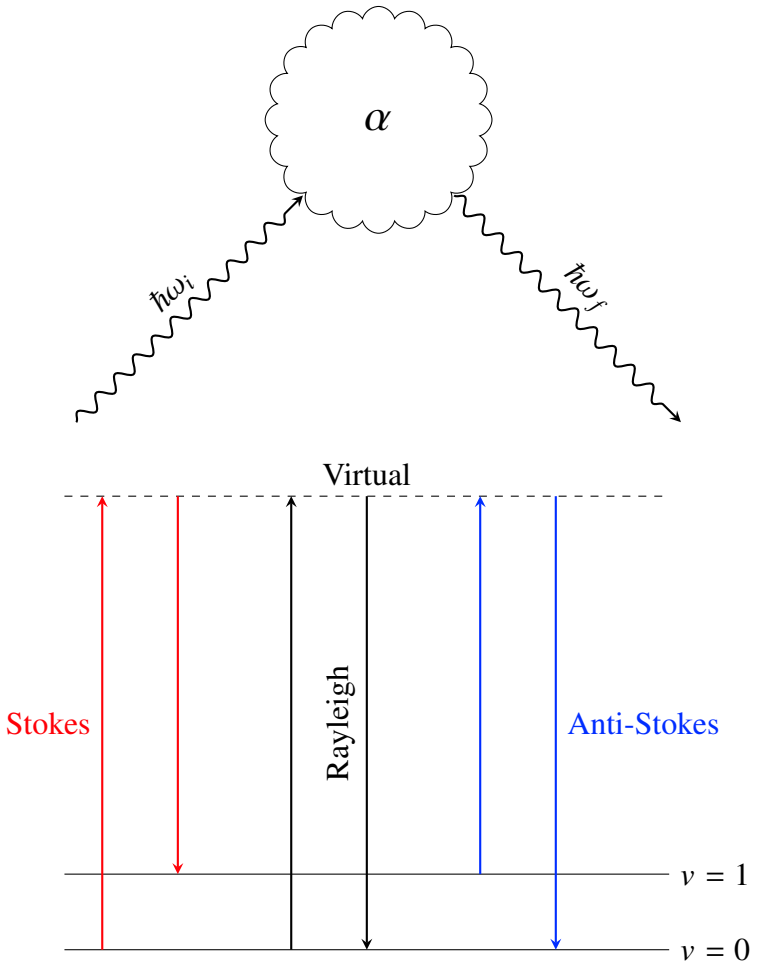

Figure 2.6: A schematic diagram of the Raman process (top) and the energy levels involved (bottom).

2.2.4 Off Resonance Raman Spectroscopy

Before moving on to the proper formal development of nonlinear spectroscopy it will be good to consider one type of nonlinear spectroscopy that most readers will be familiar with and that will be used frequently throughout this thesis; Raman spectroscopy. While regular off-resonance Raman spectroscopy may appear to be a linear spectroscopy because only one, real, light field is incident on the sample it is, in fact, a third order spectroscopy of the interaction with the vacuum field. In any case, it is useful to first form an intuitive understanding of the spectroscopy using the above development.

To begin our inquisition we can ask the question, what happens when monochromatic radiation is incident on a sample which has no resonances, electronic or nuclear, at the field's frequency? While the field cannot couple directly to a transition dipole moment, the electrons will still respond to the field and an electric field can *induce* a dipole in the molecule. This state, induced by the

electric field, is *not* an eigenstate of the molecular Hamiltonian and is often referred to as a **virtual state**. The induced dipole is related to the field through the polarizability,

$$\boldsymbol{\mu} = \boldsymbol{\alpha} \cdot \mathcal{E}(t) \tag{2.75}$$

Let us, for the moment, assume that the polarizability is a constant. In that case, the electric field, oscillating at frequency ω, will induce a dipole in the molecule that will also oscillate with the same frequency. Oscillating dipoles radiate light, in this case the scattered light would be of the same frequency and this is known as **Rayleigh Scattering**.

Now let us consider a vibrating molecule. In fact, any molecule *must* be vibrating because of the zero point energy of all its normal modes. If the molecular vibration affects the polarizability then it will modulate the frequency at which the induced dipole oscillates at and the scattered light will have a different frequency from the initial frequency. From conservation of energy we can see that energy is transferred from the electric field to that particular normal coordinate, increasing its vibrational quantum number by a certain amount.

In order to explain this phenomena properly we would need to use second order time-dependent perturbation theory. However, we can gain an intuitive idea of what makes a particular normal mode Raman active. To start, let us return to a diatomic system and expand the polarizability in terms of the internuclear distance Q about the equilibrium distance Q_0,

$$\alpha(Q) = \alpha(Q_0) + \frac{\partial \alpha}{\partial Q}\Delta Q + \cdots \tag{2.76}$$

Noting that $\mu \propto \alpha$ our transition moment integral will be proportional to,

$$\langle \psi_{v'} | \alpha | \psi_v \rangle = \langle \psi_{v'} | \alpha_0 | \psi_v \rangle + \frac{\partial \alpha}{\partial Q} \langle \psi_{v'} | \Delta Q | \psi_v \rangle \tag{2.77}$$

Again we find the same selection rule for a harmonic oscillator, $\Delta v = \pm 1$ but we see that the condition for Raman activity is that the *polarizability* must change with the vibration.

We should note that there are two possibilities for energy transfer, from the field to the molecule and from the molecule to the field. This leads to two spectra, the anti-Stokes spectrum where the scattered photons are *higher* in energy then the incident radiation and the Stokes spectrum where the scattered photons are at *lower* energies. In both cases we would expect resonances shifted from the Rayleigh line by the same amount. Note that the intensities on the anti-Stokes side provide information on the relative thermal excitation levels in the various normal modes.

2.3 Basics of Nonlinear Optics

Nonlinear optics and spectroscopy are closely intertwined fields. While the previous sections of this chapter have focused on the microscopic nature of matter and the following section will outline how nonlinear spectroscopy can offer new insights into this, it will be beneficial to take a brief step back into the macroscopic world. In this section we will cover some of the important concepts in

nonlinear optics and we will introduce terms common with nonlinear spectroscopy. Here we will see the effects of the nonlinear susceptibility of matter on the incident radiation field while in the next section we will see how that susceptibility is related to the internal quantum states of matter, their time evolution and their interaction with each other and the EM field. Many resources cover this subject in depth; the good student is encourage to read the texts of Shen[63], Mills[64] and Boyd[65].

There are two, equally valid, "lenses" through which to view the phenomenon of nonlinear optics. One is at the quantum, microscopic level in which individual photons interact with quantized matter. A fully quantum treatment is necessary to understand certain phenomena, including spontaneous emission. The other is at the macroscopic level where light is treated as an electromagnetic field and matter's only contribution is as a polarizable medium which couples to the field through its susceptibility, χ. In both cases, light and matter can interact with one another and exchange energy. If energy is imparted to or taken from the matter system the process is **non-parametric**; if after the process energy has only been exchanged between the EM fields then the process is **parametric**.

To avoid having to formally introduce and describe classical electromagnetic theory we will state the following as fact: an electric field can induce a polarization in a material, where the polarization is roughly defined as the dipole moment density of the medium and, conversely, a polarization can generate an electric field. For this thesis we will be ignoring the effect of magnetic fields.

A material's polarization is a function of the incident electric field. If the field is weak enough one can expand the polarization in orders of the field and truncate at low order. Note that in the most general treatment the fields and polarizations are vectors and the susceptibilities are tensors. In the interest of simplicity we will only consider them as scalars. Expanding the polarization P we find

$$P = P^{(0)} + P^{(1)} + P^{(2)} + P^{(3)} + \cdots \tag{2.78}$$

where each order of the polarization may be written as

$$P^{(n)} = \epsilon_0 \chi^{(n)} \mathcal{E}^n \tag{2.79}$$

Here $\mathcal{E}$ is the electric field and $\chi^{(n)}$ is the n^{th} order susceptibility which relates the incident field to the induced polarization. For the rest of this thesis the equilibrium polarization $P^{(0)}$ is assumed to be 0 and will be omitted. To see how higher orders of the polarization can lead to new wavelengths let's imagine that the electric field could be written as

$$\mathcal{E}(t) = \mathcal{E}_0 e^{-i\omega t} + c.c. \tag{2.80}$$

that is, the incident beam initially has one frequency component, ω. Our overall polarization would be, including only terms up to second order,

$$P(t) = \epsilon_0 \left(\chi^{(1)} \mathcal{E}_0 e^{-i\omega t} + \chi^{(2)} \mathcal{E}_0^2 e^{-i2\omega t} + c.c. \right) + 2\epsilon_0 \chi^{(2)} |\mathcal{E}_0|^2 \tag{2.81}$$

Remembering that an oscillating polarization will generate a field oscillating at the same frequency it is clear that the resulting field will contain a frequency component double that of the incident

one. This is referred to as second harmonic generation and was first observed by Franken et al.[66] in 1961. If we now imagine that the electric field could be written as

$$\mathcal{E}(t) = \mathcal{E}_0 \left(e^{-i\omega_1 t} + e^{-i\omega_2 t} \right) + c.c. \tag{2.82}$$

then the polarization would be

$$\begin{aligned} P(t) =& \epsilon_0 \left[\chi^{(1)} \mathcal{E}_0 \left(e^{-i\omega_1 t} + e^{-i\omega_2 t} + c.c. \right) + \chi^{(2)} \mathcal{E}_0^2 \left(e^{-i\omega_1 t} + e^{-i\omega_2 t} + c.c. \right)^2 \right] \\ =& 4\epsilon_0 \chi^{(2)} |\mathcal{E}_0|^2 + \left[\epsilon_0 \chi^{(1)} \mathcal{E}_0 \left(e^{-i\omega_1 t} + e^{-i\omega_2 t} \right) \right. \\ & \left. + \epsilon_0 \chi^{(2)} \mathcal{E}_0^2 \left(e^{-i2\omega_1 t} + 2e^{-i(\omega_1+\omega_2)t} + 2e^{-i(\omega_1-\omega_2)t} + e^{-i2\omega_2 t} \right) + c.c. \right] \end{aligned} \tag{2.83}$$

Now the emitted field not only has frequency components at the second harmonics of the input fields, as we saw above, but also the *sum* $(\omega_1 + \omega_2)$ and the *difference* $(\omega_1 - \omega_2)$ frequencies. One important fact about $\chi^{(2)}$ is that it is identically zero for media that are centrosymmetric, i.e. that have a center of inversion about which they are symmetric. This is true for all *even* ordered susceptibilities. For most materials the third order susceptibility is the first non-zero nonlinear susceptibility. The processes described above, related to the second order susceptibility, are known as three wave mixing because the two input fields and the signal, or output, field mix together and exchange energy. In general, any process associated with the $(n-1)^{\text{th}}$ order susceptibility is known as ***n* wave mixing**.

A plethora of phenomena can be attributed to the second and third order polarizations. From the above discussion we see that the second harmonic generation (SHG), sum frequency generation (SFG) and difference frequency generation (DFG) are all due to the second order nonlinear susceptibility, the non-collinear optical parametric amplifier discussed below uses both SHG and DFG. The third order susceptibility is responsible for third harmonic generation, self-focusing and self-phase modulation (which are two sides of the same coin).

One of the most important $\chi^{(3)}$ processes is known as **self-focusing**. For any media we can write the index of refraction as

$$n = n_0 + n_2 I \tag{2.84}$$

where n_0 is the regular, linear, index of refraction, I is the intensity of the EM field and

$$n_2 = \frac{3}{4n_0^2 \epsilon_0 c} \chi^{(3)} \tag{2.85}$$

Clearly, as the intensity of the beam is increased the index of refraction increases as well. This effect is known as the **optical Kerr effect** in relation to the well known static Kerr effect in which the index is modulated by a static electric field. Imagine that our incident beam is no longer a featureless plane wave, but has a Gaussian spatial intensity profile. Because of the Kerr effect the medium's index of refraction has a Gaussian profile now too. In effect, the beam has formed its own Gaussian lens! This is known as a **Kerr lens**. Of course this focuses the incoming beam

which necessarily increases its intensity, consequently increasing the power of the lens focusing the beam further and so on. This is self-focusing. At a certain point other nonlinear effects cause the beam to diffract and a filament is formed. Almost all modern ultrafast laser systems rely on this effect as it lies at the heart of **Kerr lens mode-locking**, **continuum generation** and **Kerr gating**.

2.3.1 Phase matching

One might be tempted to think that all nonlinear processes occur simultaneously, but this illusion is due to the fact that we have left the vectorial and tensorial nature of electromagnetic theory out of our discussion. Including the spatial dependence leads to a phenomenon known as **phase matching** in which only certain processes are allowed for a given system orientation.

To develop this concept we consider the spatial dependence of the fields during a nonlinear process. We can decompose our signal polarization into plane waves and focus on a single frequency and wave vector component, i.e.

$$P_s(z,t) = P_s(t)e^{-ik_s z - i\omega_s t} \tag{2.86}$$

where $P_s(t)$ is referred to as the envelope. It can be shown[65,67] that if the signal field's polarization envelope, $P_s(t)$ varies slowly compared to the frequency–the **slowly varying envelope approximation**–then the resulting intensity of the field after propagating through a length l of the medium is

$$I_s(t) \propto \text{sinc}^2\left(\frac{\Delta k l}{2}\right) \tag{2.87}$$

where $\Delta k = k_s - \sum k_i$ and the k_i are the wave vector's of the incoming fields. When the vectorial nature of the fields is taken into account we have $\Delta\mathbf{k} = \mathbf{k}_s - \sum \mathbf{k}_i$ and $\Delta\mathbf{k}$ known as the **phase mismatch**. If the length of propagation, l, is long then even a small mismatch will lead to zero signal intensity. Therefore it is desirable to reduce $\Delta\mathbf{k}$ to zero which is known as the **phase matching condition**. This principle is key to the operation of nonlinear optical components used in the instrumentation, described below. Phase matching is commonly achieved with a birefringent crystal and there are two common types for $\chi^{(2)}$ processes. In Type I phase matching the two incoming beams have the same polarization while in Type II the incoming beams are perpendicular to each other. Phase matching also allows the experimentalist to chose which signals he wants to amplify and which he wants to minimize.

2.3.2 Heterodyned detection

Before moving onto the theory of nonlinear spectroscopy it will be useful to introduce the concept of **heterodyned detection** as all the spectroscopies, with the exception of regular Raman, used in this thesis rely on this technique. Let us imagine that we are using weak pulses so that we can treat our spectroscopy in the perturbative limit. Because the incoming fields are weak the generated signal fields will be weak as well. In fact, as the order of the spectroscopy is increased the signal will necessarily become weaker and weaker as it will be a function of higher and higher orders of the field. We can try to detect this signal on it's own, but this will be experimentally difficult.

Another approach is to interfere this field with another, termed the **local oscillator**.[‡] Because most detectors can only detect the intensity of the field we have

$$I(t) = (E_{LO}(t) + E_s(t))^2 = E_{LO}(t)^2 + E_s(t)^2 + \mathrm{Re}\left(\bar{E}_{LO}(t)E_s(t)\right) \tag{2.88}$$

where the over bar indicates the complex conjugate. As we assumed the signal field was small to begin with we can assume that $E_s(t)^2$ is negligible. We can remove the contribution of $E_{LO}(t)^2$ by measuring it in the absence of the signal field. The technique is used in the recording of FSRS and ISRS spectra throughout this thesis.

2.4 Basics of Nonlinear Spectroscopy

In the previous section we were mostly concerned with matter's effect on the incident EM field. All we cared about was the value of the susceptibility. From this we could determine how efficiently energy could be transferred from one EM field to another. Here we are more interested in what that energy transfer between fields tells us about the susceptibility and therefore about the microscopic details of the medium. Clearly, these two subjects are closely tied together and the progress in nonlinear optics has been supplemented and supported by the progress in nonlinear spectroscopy and *vice versa*.

Many of the books cited in Section 2.3 have great chapters about spectroscopy. However, the most complete, comprehensive and self-contained treatment is that of Mukamel.[67]

So what, exactly, can χ tell us about the molecular details of the medium under study? Theoretically, everything. But first we need to expand on mathematical toolkit we built in Section 2.1.

2.4.1 Tools for Nonlinear Spectroscopy

The Time Evolution Operator and The Interaction Picture

Both the Heisenberg and Schrödinger pictures can be viewed as limiting cases of **the interaction picture** in which both operators and states have some time dependence. The interaction picture is particularly useful in application to time-dependent perturbation theory where the Hamiltonian can be split into an exactly solvable time *independent* part and a perturbative time dependent part.

Working in the Schrödinger picture, let us introduce the **time evolution operator** ($\mathscr{U}(t,t_0)$) defined as

$$|\psi(t)\rangle = \mathscr{U}(t,t_0)|\psi(t_0)\rangle \tag{2.89}$$

Plugging this into eq. 2.15 we find

$$i\hbar\frac{\partial}{\partial t}\mathscr{U}(t,t_0) = \mathscr{H}\mathscr{U}(t,t_0) \tag{2.90}$$

[‡]This terminology is a hold over from radio technology.

If $\mathscr{H}$ is independent of time then the above equation has a simple solution

$$\mathscr{U}(t,t_0) = e^{-\frac{i}{\hbar}\mathscr{H}(t-t_0)} \tag{2.91}$$

Considering again the Hamiltonian introduced in eq. 2.23, we can define the 0^{th} order time evolution operator using the above equation to be

$$\mathscr{U}_0(t,t_0) = e^{-\frac{i}{\hbar}\mathscr{H}_0(t-t_0)} \tag{2.92}$$

Now we are in a position to make the transformation to the interaction picture. We define $|\widetilde{\psi}\rangle$, the state vector in the interaction picture which is equivalent to $|\psi\rangle$ in the Schrödinger picture, to be

$$|\widetilde{\psi}\rangle = \mathscr{U}_0^{\dagger}(t,t_0)|\psi\rangle \tag{2.93}$$

We can calculate the time dependence of the interaction picture state to be

$$\begin{aligned} i\hbar\frac{\partial}{\partial t}|\widetilde{\psi}\rangle &= \left[i\hbar\frac{\partial}{\partial t}\mathscr{U}_0^{\dagger}(t,t_0)\right]|\psi\rangle + i\hbar\mathscr{U}_0^{\dagger}(t,t_0)\left[\frac{\partial}{\partial t}|\psi\rangle\right] \\ &= -\mathscr{U}_0^{\dagger}(t,t_0)\mathscr{H}_0|\psi\rangle + \mathscr{U}_0^{\dagger}(t,t_0)(\mathscr{H}_0 + \mathscr{T}(t))|\psi\rangle \\ &= \widetilde{\mathscr{T}}(t)|\widetilde{\psi}\rangle \end{aligned} \tag{2.94}$$

where we have used the fact that the time evolution operator is Hermitian and

$$\widetilde{\mathscr{T}}(t) = \mathscr{U}_0^{\dagger}(t,t_0)\mathscr{T}(t)\mathscr{U}_0(t,t_0) \tag{2.95}$$

The above equation suggests that we can write

$$i\hbar\frac{\partial}{\partial t}\widetilde{\mathscr{U}}(t,t_0) = \widetilde{\mathscr{T}}(t)\widetilde{\mathscr{U}}(t,t_0) \tag{2.96}$$

We can integrate this equation to yield

$$\widetilde{\mathscr{U}}(t,t_0) = 1 - \frac{i}{\hbar}\int_{t_0}^{t}\widetilde{\mathscr{T}}(t')\widetilde{\mathscr{U}}(t',t_0)dt' \tag{2.97}$$

Note that our complete time evolution operator, for the *entire* Hamiltonian may be written as

$$\mathscr{U}(t,t_0) = \mathscr{U}_0(t,t_0)\widetilde{\mathscr{U}}(t,t_0) = \mathscr{U}_0(t,t_0) - \frac{i}{\hbar}\int_{t_0}^{t}\mathscr{U}_0(t,t')\mathscr{T}(t')\mathscr{U}(t',t_0)dt' \tag{2.98}$$

where we have used the fact that $\mathscr{U}_0(t,t_0)\mathscr{U}_0^{\dagger}(t',t_0) = \mathscr{U}_0(t,t')$. So far no approximations have been used, but this equation has $\mathscr{U}(t,t_0)$ on both sides. We can solve it by splitting up the time interval into smaller parts and plugging eq. 2.98 iteratively into itself for each time slice. Furthermore, if the time dependent part of the Hamiltonian is weak, the time slices need not be small and only few terms must be kept. Before we can move on further to calculating the material's polarization under the influence of an external field it will be useful to introduce a new formalism.

The Density Operator

In many spectroscopic problems we will be performing measurements on ensembles of identical, non-interacting, quantum systems. To describe such a system we will introduce a new mathematical object, **the density operator**, defined as

$$\rho = \sum_i p_i |\psi_i\rangle\langle\psi_i| \tag{2.99}$$

where p_i describes the *statistical fraction* of systems in state $|\psi_i\rangle$. Of course, each $|\psi_i\rangle$ is a normalized quantum state. When all p_i except one are zero the density matrix is said to describe a **pure state** in all other cases it is describing a **mixed state**. The time evolution of the density matrix is easy to derive. To begin let us consider the time evolution of a pure state

$$\frac{\partial \rho}{\partial t} = \frac{\partial |\psi\rangle}{\partial t}\langle\psi| + |\psi\rangle\frac{\partial \langle\psi|}{\partial t} \tag{2.100}$$

Multiplying through by $i\hbar$ and using eq. 2.15 yields

$$i\hbar\frac{\partial \rho}{\partial t} = [\mathscr{H}, \rho] \tag{2.101}$$

Note that if $|\psi\rangle$ is an eigenket of $\mathscr{H}$ then $\dot{\rho} = 0$ and there is *no* time evolution of the density matrix, as expected. As we did with the wave function we can propagate the density matrix. The density operator equivalent of eq. 2.98 is

$$\rho(t) = \rho^{(0)}(t) - \frac{i}{\hbar}\int_{t_0}^{t} \mathscr{U}_0(t,t')[\mathscr{T}(t'), \rho(t')]\mathscr{U}_0^{\dagger}(t,t')dt' \tag{2.102}$$

where $\rho(t') = \mathscr{U}(t',t_0)\rho(t_0)\mathscr{U}^{\dagger}(t',t_0)$.

The density matrix can be expressed as a matrix with matrix elements of

$$\rho_{mn} = \langle m|\psi\rangle\langle\psi|n\rangle \tag{2.103}$$

where we have assumed that ρ is a pure state. Clearly there are two types of matrix elements, diagonal ones where $m = n$ and off diagonal ones where $m \neq n$. The interpretation of the diagonal ones is clear; $\rho_{nn} = |\langle n|\psi\rangle|^2$ is the probability that the system will be found in state $|n\rangle$. For this reason diagonal elements are known as **populations**. What about the off-diagonal elements? If the diagonal elements indicate the likelihood of finding the system in a particular state, then the off-diagonal elements indicate the probability of finding the system in a *coherent* superposition state between $|m\rangle$ and $|n\rangle$. For this reason the off diagonal elements are known as **coherences**. If the density matrix is expanded in terms of the Hamiltonian's eigenkets then the populations will be time independent and the coherences will oscillate at a frequency equal to the energy splitting between $|m\rangle$ and $|n\rangle$, i.e. ω_{mn}.

To see how expectation values are calculated using the density operator let us introduce an arbitrary set of basis kets $|\alpha\rangle$ and apply eq. 2.9 inserting the closure relation on both sides of the operator, $\mathscr{O}$

$$\langle\mathscr{O}\rangle = \langle\psi|\left(\sum_{\alpha'}|\alpha'\rangle\langle\alpha'|\right)\mathscr{O}\left(\sum_{\alpha}|\alpha\rangle\langle\alpha|\right)|\psi\rangle = \sum_{\alpha'}\sum_{\alpha}\langle\alpha|\psi\rangle\langle\psi|\alpha'\rangle\langle\alpha'|\mathscr{O}|\alpha\rangle \tag{2.104}$$

Noticing the density operator in the last equation and invoking the closure relation over α' gives

$$\langle\mathscr{O}\rangle = \sum_{\alpha}\langle\alpha|\rho\mathscr{O}|\alpha\rangle \tag{2.105}$$

If we were to express $\rho\mathscr{O}$ as a matrix then the above equation would be synonymous with taking the trace of this matrix. So we have

$$\langle\mathscr{O}\rangle = \mathrm{Tr}(\rho\mathscr{O}) \tag{2.106}$$

Now we can begin to see the utility in the density operator. For mixed systems each component of the density operator evolves separately from the other components and the expectation value of an operator is simply the average expectation value weighted by each p_i. In fact, we can average over (trace over), degrees of freedom of which we cannot, or do not want to, keep track

When we make a spectroscopic measurement, we are, in essence, measuring the material's polarization. A material's polarization is the response of the material to the external electric field. To make the connection between the macroscopic world and the microscopic one we can realize that we need to determine the *expectation value* of the material's response to the field. If the material can be thought of as a ensemble of N independent systems then we can use the density matrix formalism outlined above to calculate this response. As we determined earlier in Section 2.1 the material's response to an electric field (within the dipole approximation) is the expectation value of the dipole moment operator. That means that the macroscopic polarization can be written as, assuming the field is aligned with the dipole moment,

$$P(t) = N\,\langle\hat{\mu}\rangle = N\mathrm{Tr}(\rho(t)\hat{\mu}) \tag{2.107}$$

Moving forward the N will be implicit.

Our expansion of P in powers of the field $\mathcal{E}$ suggests that a similar tactic might work here and allow us to make a strong connection with the theory developed in the previous section. It might seem difficult to expand the trace in the above equation into powers of the electric field. It does not even appear in the equation! The key here is to realize that our interaction Hamiltonian, $\mathscr{T}(t)$ is equal to $-\hat{\mu}\mathcal{E}(t)$ and that if we had solved eq. 2.102 iteratively over an infinite number of time slices we would have found a solution of the form

$$\rho(t) = \sum_{n}^{\infty}\rho^{(n)}(t) \tag{2.108}$$

where the n^{th} term would be n time ordered integrals of n nested commutators and out of these n nested commutators would come n $\mathcal{E}$ terms multiplied together. In essence the $\rho^{(n)}$ term would

depend on the incident electric field to n^{th} order! Of course, the real functional form of $\rho^{(n)}$ is not so simple and some examples are in order.

First we note that from the above equation we can say that $P^{(n)} = \text{Tr}(\rho^{(n)}\hat{\mu})$. For the first order polarization we have one commutator and thus two terms

$$P^{(1)}(t) = \frac{i}{\hbar}\int_0^\infty d\tau_1 \mathcal{E}(t-\tau_1)\left\{\left\langle\hat{\mu}\left(\mathscr{U}_0(\tau_1,0)\hat{\mu}\rho(0)\right)\right\rangle - \left\langle\hat{\mu}\left(\rho(0)\hat{\mu}\mathscr{U}_0^\dagger(\tau_1,0)\right)\right\rangle\right\} \tag{2.109}$$

Note that we have switched from integrations over *actual* interaction times, t_i, to the intervals *between* interactions, τ_i.[§] These terms can be interpreted as follows. The system is initially in a state described by $\rho(0)$. At time $t = 0$, the system interacts with the field, this interaction can either occur on the ket side of the density operator, the first term, or the bra side, the second. Note that the second term is simply the complex conjugate of the first term and therefore contains no extra information. Following the interaction, the augmented ket or bra is propagated under the influence of the material Hamiltonian for a time period, τ_1. The expectation value of the polarization at time t is calculated by operating on the density matrix one more time, such that the bra and ket are found in the same state, and taking the trace. Note, that because the trace is invariant under cyclic permutation, the final dipole coupling may occur on *either* side of the density matrix. The integral over τ_1 ensures that we consider all possible intervals between the first interaction and the final dipole coupling.

Moving on to the second order we find that there are two nested commutators so we should have four terms

$$\begin{aligned} P^{(2)}(t) =& \frac{i}{\hbar}\int_0^\infty d\tau_2 \int_0^\infty d\tau_1 \mathcal{E}(t-\tau_2)\mathcal{E}(t-\tau_2-\tau_1) \\ &\times\Big\{\left\langle\hat{\mu}\left(\mathscr{U}_0(\tau_2,\tau_1)\hat{\mu}\mathscr{U}_0(\tau_1,0)\hat{\mu}\rho(0)\right)\right\rangle - \left\langle\hat{\mu}\left(\rho(0)\hat{\mu}\mathscr{U}_0^\dagger(\tau_1,0)\hat{\mu}\mathscr{U}_0^\dagger(\tau_2,\tau_1)\right)\right\rangle \\ &+\left\langle\hat{\mu}\left(\mathscr{U}_0(\tau_2,\tau_1)\hat{\mu}\rho(0)\hat{\mu}\mathscr{U}_0^\dagger(\tau_1,0)\right)\right\rangle - \left\langle\hat{\mu}\left(\mathscr{U}_0(\tau_1,0)\hat{\mu}\rho(0)\hat{\mu}\mathscr{U}_0^\dagger(\tau_2,\tau_1)\right)\right\rangle\Big\} \end{aligned} \tag{2.110}$$

In general the n^{th} order polarizability will have 2^n terms each with n dipole couplings but because half the terms are complex conjugates of the others only 2^{n-1} terms are independent. The first term above corresponds to the system's ket interacting once at $t = 0$ with the field, propagating for a time interval τ_1 before interacting again with the field (again on the ket side) and then propagating again for a time interval τ_2, the second term is complex conjugate of the first. In the third term, the first interaction is on the bra side after which the bra is propagated and then the second interaction is on the ket side after which the ket is propagated. The fourth term is, of course, the complex conjugate of the third.

Thus far the discussion has been kept as general as possible. However, we should note that once particular models for the electric field and molecular system are specified, the number of terms that strongly contribute to a particular signal are greatly reduced. For instance, all of the phase matching conditions described above still hold here as do the selection rules described in

[§]In explanation, $\tau_i = t_i - t_{i-1}$ and $t_0 \to 0$.

Section 2.2. It is also important to realize that while we have let our time intervals vary widely, i.e. the interactions can happen at any time as long as the time ordering is preserved, these are, in actuality, controlled by the experimenter. If one were able to create delta function pulses, and for many molecular phenomena a 20 fs Gaussian pulse may as well be represented by a delta function, then the integrals over the τ_i interval will be sharply truncated by any $\mathcal{E}$ term that depends on τ_i. When short pulses are used the τ_i become directly controllable by the experimentalist.

Next we will describe a diagrammatic technique introduced by Lee and Albrecht[68] for keeping track of the various nonlinear terms.

2.4.2 Diagrams for Representing n-Wave-Mixing

Clearly the mathematical formulas for describing the higher order density operator terms, and thus the higher order nonlinear polarizations, are cumbersome at best. Moreover they offer little, if any, physical insight into the processes occurring in the material system during both the interaction and propagation steps.

Consider again the dipole moment operator and its effect on a particular quantum state. Equation 2.36 shows that $\boldsymbol{\mu}$ can transform one molecular eigenstate into another. This means we can develop an intuitive, physically meaningful interpretation of each term in the density operator expansion. Take for instance the first term of the second order polarization; if we consider our initial density operator, $\rho(0)$, to represent a pure eigenstate of the molecular Hamiltonian then the action of the first dipole operator is to transform the ket to a new state creating a coherent superposition state. It is important to realize that this superposition is not collapsed until the final measurement is made, i.e. until the final dipole coupling occurs and the trace is taken. This state is then propagated under the influence of the molecular Hamiltonian for a time interval τ_1, the second dipole coupling again transforms the ket to a different state generating a new coherent superposition which evolves over time period τ_2. Each term in eq. 2.110 is referred to as a **nonlinear pathway** and this terminology should now be clear; each term represents a pathway through molecular state space mediated by the incoming electric field.

Albrecht ladder diagrams for all the possible three wave mixing ($\chi^{(2)}$) processes are depicted in Figure 2.7. Each diagram represents one of the pathways in eq. 2.110. Time is increasing along the horizontal axis from left to right. Energy is increasing along the vertical axis from bottom to top. Solid horizontal lines represent eigenstates of the medium's Hamiltonian ($\mathscr{H}$). Dashed lines indicate so-called virtual states. Virtual states arise due to implicit perturbations of the Hamiltonian or the explicit time-energy uncertainty principle. Solid arrows refer to ket side couplings while dashed arrows refer to the bra, wavy arrows correspond to the final dipole coupling involved in measuring the polarization of the sample. For the diagrams in Figure 2.7 it is tacitly assumed that we are modeling the quantum system as having only two real states. Of course, this need not be the case and diagrams will have to be drawn for each permutation of starting, intermediate and final state. Of course, experimental parameters, such as the duration and wave vectors of the incoming EM fields, and molecular realities, such as the resonance condition and selection rules outlined in Section 2.2, will restrict which pathways will contribute strongly to the observed signal. In Figure 2.7 we have assumed that each interaction with the field results in absorption (photon annihilation)

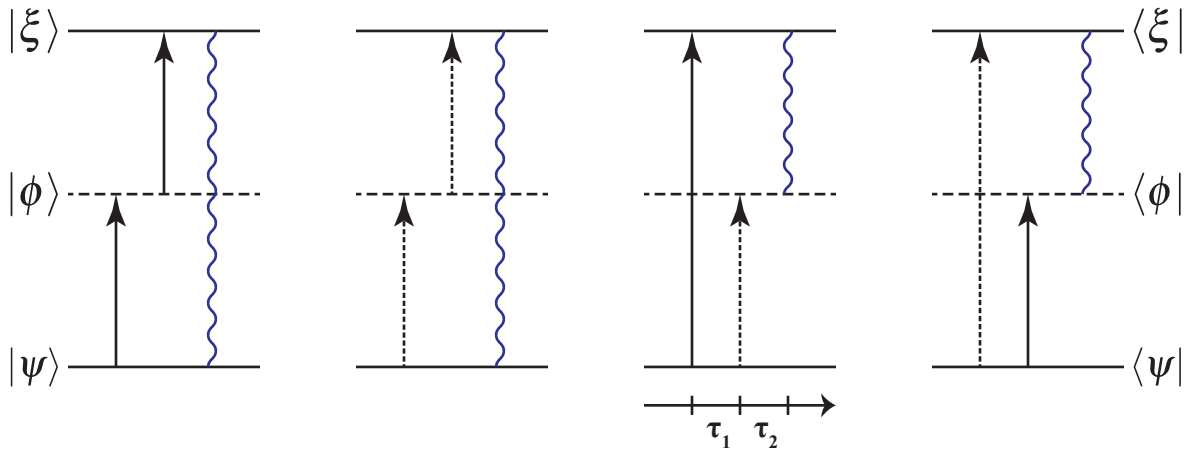

Figure 2.7: Albrecht energy ladder diagrams for the second order polarization, $P^{(2)}$.

while the final coupling is either absorptive or emissive depending on the required final state of the ket, i.e. that the final density matrix contain no coherences, i.e. all superpositions *must* be collapsed by the measurement. From the way we have drawn the pathways we can see that the first diagram represents sum-frequency generation (of which second harmonic generation is a limiting case), the third shows difference frequency generation and the second and fourth are unlikely to contribute strongly to a given signal as they require the absorption of a vacuum field photon.

2.4.3 Theory of Femtosecond Stimulated Raman Spectroscopy

To introduce the theory of Femtosecond Stimulated Raman spectroscopy (FSRS) we must introduce specific models for both the EM field and the medium. Because FSRS uses two beams, the EM field will consist of two components; a narrow band (long duration) Raman pump pulse and a broadband (short duration) Raman probe pulse. If the molecular Hamiltonian can be modeled in the Born-Oppenheimer Approximation then each dipole coupling will correspond to a change in electronic state and each propagation step will act on the nuclear wave function which will, in general, not be an eigenstate on this new electronic surface. A consequence of the BOA is that the system will have a set of well defined vibronic energy levels and, for the purposes of this subsection, we further assume that the pump and probe pulse frequencies are *off-resonance* with any of these vibronic transitions but their difference frequency corresponds to a difference in vibrational energy levels. Finally we assume that the initial density operator corresponds to pure ground state $|g\rangle$. Now we can draw a diagram representing the dominant term in the spectroscopy, which is presented in Figure 2.8.

A few important aspects of FSRS are illustrated by the diagram in Figure 2.8. The interval τ_1 is controlled by the relative durations of the pump and the probe. Because the probe is short this means that τ_1 must necessarily be small, a fact that will be important later. These first two inter-

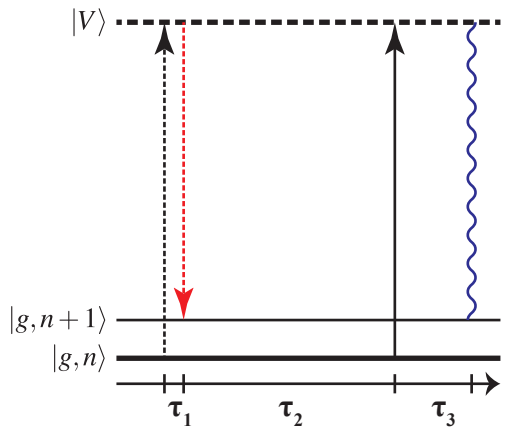

Figure 2.8: Albrecht ladder diagram for the dominant pathway in off-resonance ground state FSRS. Interactions with the Raman pump field are denoted by black arrows, interactions with the probe field by red arrows and the final dipole coupling by the blue wavy line.

actions generate a *vibrational* coherence in the ground electronic state, in this case $|g,n\rangle\langle g,n+1|$ which then evolves under the influence of the molecular Hamiltonian for a time period τ_2 before interacting *again* with the Raman pump generating an electronic coherence, $|V\rangle\langle g,n+1|$. After propagating for a time interval τ_3 the coherence is collapsed by the final dipole coupling and the signal field is generated. Importantly, τ_2 and τ_3 are not under experimental control; τ_2 is only limited by the lifetime of the *vibrational* coherence in the *ground* state and the duration of the Raman pump. If the Raman pump is long enough the entire vibrational coherence will be measured. Fourier transformation to the frequency domain will result in a sharp line centered at the vibrational transition frequency between the vibrational levels. On the other hand, τ_3 corresponds to the evolution of an *electronic* coherence which are generally short lived, so τ_3 will be short as well.

Raman and resonance Raman can also be well described by Figure 2.8, except in this case the real probe field is replaced by the vacuum field. Interaction with the vacuum field requires a fully quantum mechanical treatment of the system and field and is beyond the scope of this work. Keep in mind that this equivalence between Raman and FSRS breaks down when the system is not in the ground state and there are electronic resonances with either the pump or the probe, situations of this type are covered more fully in other works.[69–71] On the other hand, this correlation suggests that many of the Raman selection rules developed in Section 2.2 are relevant for FSRS.

The importance of a short duration probe cannot be overstated, it adds two important capabilities to FSRS over regular stimulated Raman. First, the broad bandwidth, a necessary condition of the short duration, allows many different vibrational transitions within the material system to be probed simultaneously. Second, the short duration means that we know precisely *when* the vibrational coherence was initiated. For the model system outlined above this second capability is of

limited utility because the density matrix is *not* evolving at the time the coherence is started. But, as will be discussed below in depth, if the density matrix contains time dependent populations or coherences, the precision enabled by the probe will be necessary to follow their evolution.

Another important aspect of FSRS is the phase-matching condition. Looking at Figure 2.8 we see that the phase matching condition reduces to $\mathbf{k}_s = -\mathbf{k}_{pu} + \mathbf{k}_{pr} + \mathbf{k}_{pu} = \mathbf{k}_{pr}$. Thus, the generated signal has the same wave vector as the probe field, which is referred to as **self-phase matched**. As a result, the FSRS signal is heterodyne detected against the probe which has advantages when off or pre-resonant but severe disadvantages when either the pump or probe is on resonance with an electronic transition; the second situation is particularly hard to avoid when probing excited states of large systems. To see the complication, think of a situation where the initially populated state $|g\rangle$ is no longer the ground state of the system but an intermediate. Here there are now *twelve* distinct pathways[71] that all have the appropriate phase matching condition and thus may contribute to the observed signal. Some pathways lead to broad background signals[70] or dispersive lineshapes.[69] Avoiding these pathways is one of the chief experimental concerns in FSRS.

For more information on the quantum, semiclassical and coupled wave descriptions of FSRS the interested reader is referred to the work of S.-Y. Lee and co-workers.[72–76]

2.4.4 Theory of Transient Absorption and Impulsive Stimulated Raman Spectroscopy

Here we consider a spectroscopy consisting of two short pulses with the signal detected along one of the pulse's wave vector. Both pulses are short duration, the one phase matched with the signal is termed the probe and the other the actinic pump. These restrictions lead to three active pathways, which are presented in Figure 2.9. Experimentally, the actinic pump is generally more intense than the probe. Note that the thick black lines denote the ground vibrational state of the i^{th} electronic state. The diagrams have been drawn such that a *vibrational* coherence is generated either in the n^{th} excited state, first two diagrams, or in the ground electronic state, $|g\rangle$, last diagram. Of course, the actinic pump will need to contain frequency components that connect both states. If such a breadth in frequencies is not present a vibrational coherence cannot be initiated. Next we will discuss the types of signals observed for three different time regimes.

First consider the case when Δt, which is equivalent to time period τ_2, is small. In this case interaction with the probe can occur during τ_1 and *electronic* coherences between $|n\rangle$ and $|m\rangle$ may be generated. The signals resulting from these coherences are generally known as the **coherent artifact** and are mostly treated as an unwanted, interfering, signal in this thesis.

Second, consider when the delay between pump and probe is larger than the electronic dephasing time but still on the order of the vibrational coherence time. Focusing on the last diagram in Figure 2.9 we see that a vibrational coherence is initiated on the ground state and is then probed after some delay Δt. Note the similarity between this diagram and that of Figure 2.8. In FSRS the probe is detected with a spectrograph, which is the experimental analog of performing a Fourier transform of the signal. This process is known as **impulsive Raman spectroscopy** and it contains precisely the same information as FSRS except that a spectrum must be recorded as a function of

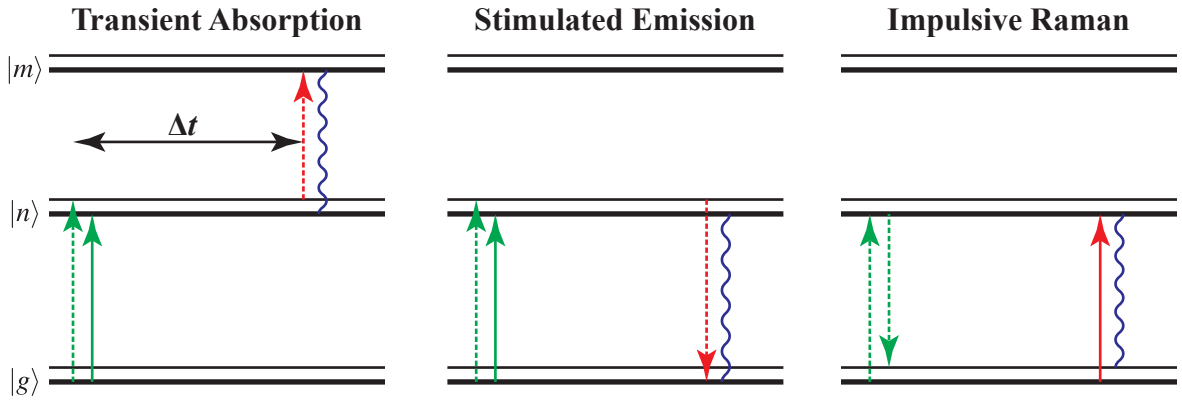

Figure 2.9: Albrecht ladder diagram for the dominants pathway in transient absorption spectroscopy. Interactions with the actinic pump field are denoted by green arrows, interactions with the probe field by red arrows and the final dipole coupling by the blue wavy line.

waiting time and then explicitly Fourier transformed. Note that vibrational coherences may also be generated on state $|n\rangle$ and thus the vibrational spectrum of the excited state measured. The main benefits of FSRS over impulsive Raman is that the Fourier transform is performed by the physical system, meaning that there is no *experimental* limit on the frequency range that may be probed beyond the bandwidth of the probe pulse. Furthermore, as the Fourier transform is performed for every set of pulses meaning the data acquisition time of FSRS is much less than that of ISRS.

Implicit in the diagrams of Figure 2.9 is the fact that the lines represent eigenstates of the molecular Hamiltonian and that there is no evolution during time period Δt. However, this means that we have to keep track of *all* the vibronic states in the system and the many vibrational coherences induced by the pump. We could, on the other hand, introduce the concept of the **wave packet** representation of the nuclear wave function. Here we will still keep track of the various electronic levels of the system but we will lump the coherent superposition of all the various nuclear states into a single time dependent, spatially localized, wave function. In this representation we can no longer distinguish between nuclear populations and coherences but we gain a much more intuitive understanding of the physics and we also simplify the computations for many-atom systems considerably. Of course, both the energy level and wave packet descriptions of nuclear motion are equally valid. However, just as one process may be simpler in the time or frequency domain, the wave packet description may be more or less useful depending on the circumstance.

To see how the wave packet representation works consider an arbitrary molecular system. If the system is stable it will necessarily have a well defined equilibrium geometry in the ground state. Invoking the harmonic approximation the system's ground state wave function will simply be a multidimensional Gaussian. This is our initial wave packet. Assuming the Condon approximation, discussed above, interaction with the actinic pump changes the electronic configuration

but leaves the nuclear coordinates unchanged, basically our wave packet's effective potential has been instantaneously changed to that of the excited state. On the excited state the wave packet is no longer an eigenstate and thus it will evolve when propagated by $\mathscr{U}$. If we wanted to represent this wave function in terms of vibronic stationary states we would have to find the Franck-Condon overlaps between the initial vibrational state and *all* the excited vibrational states.

Using the wave packet representation we can now consider the observed signals when Δt is large. Here our probing step is measuring the wave packet's evolution on the potential surface as a function of time through the changing energy difference between the $|n\rangle$ and $|m\rangle$ or $|g\rangle$ states. Unfortunately, this only tells us about the potential energy surfaces in relation to each other and not the absolute curvature of the state of interest.

FSRS is a vibrational spectroscopy and as such *directly* measures the local curvature of the PES. To convert FSRS to a time resolved technique we need only to add an actinic pump; in effect we are replacing the probe interaction in Figure 2.9 with the full diagram from Figure 2.8. Furthermore, if we consider Δt to be larger than the vibrational dephasing time we can simply consider time resolved FSRS to be a FSRS measurement performed on a non-stationary state that contains no coherences. With this we can map out the PES as the system evolves on it. Of course, we will not be able to map out the PES in its entirety but we will be guided, by the physical system itself, to measure the PES's salient features. Note that because we know *precisely* when the vibrational coherence is generated by action of the Raman pump and probe the, time precision of these interactions is well-defined

2.4.5 Theory of 2D-FSRS

Time resolved FSRS can be considered as a third order spectroscopy performed on a prepared, non-stationary, population when the separation between the actinic pump and the Raman probe pair is large. But this approximation breaks down, in some cases spectacularly, when the temporal separation between the actinic pump and Raman probe is short. For Δt on the order of the FWHM of the instrument response function the observed signal has large contributions from the coherent artifact except in this case the artifact is due to a full six-wave mixing process. Even when Δt is larger than the electronic dephasing time, the aforementioned approximation will fail such as when the nuclear response is large and fast, e.g. rhodopsin,[19,77] or large and oscillatory, e.g. GFP[20] and the TCNQ:TMB charge transfer dimer, discussed in Chapter 7). In fact, we expect that as laser technology improves in general, and FSRS with it, dispersive line shapes due to large structural changes during the vibrational dephasing time and oscillatory peaks due to anharmonic coupling will be observed in *all* condensed phase systems (c.f. Section 8.3).

For large and fast changes in the nuclear configuration, the heterodyned nature of FSRS becomes a clear feature of the technique. By being able to track the nuclear phase it is possible to "beat" the Fourier Uncertainty[16] and track nuclear changes that are faster than the vibrational dephasing times. The manifestation of this "victory" are clear negative dips in the spectra on the side of the peak to which it is shifting, e.g. in rhodopsin the HOOP modes in the 760-810 cm^{-1} region undergo a dramatic blue shift of nearly 100 cm^{-1} each and the result is a sharp negative dip to the blue. To reiterate, the key to understanding this "cheat," which other authors[16] have misun-

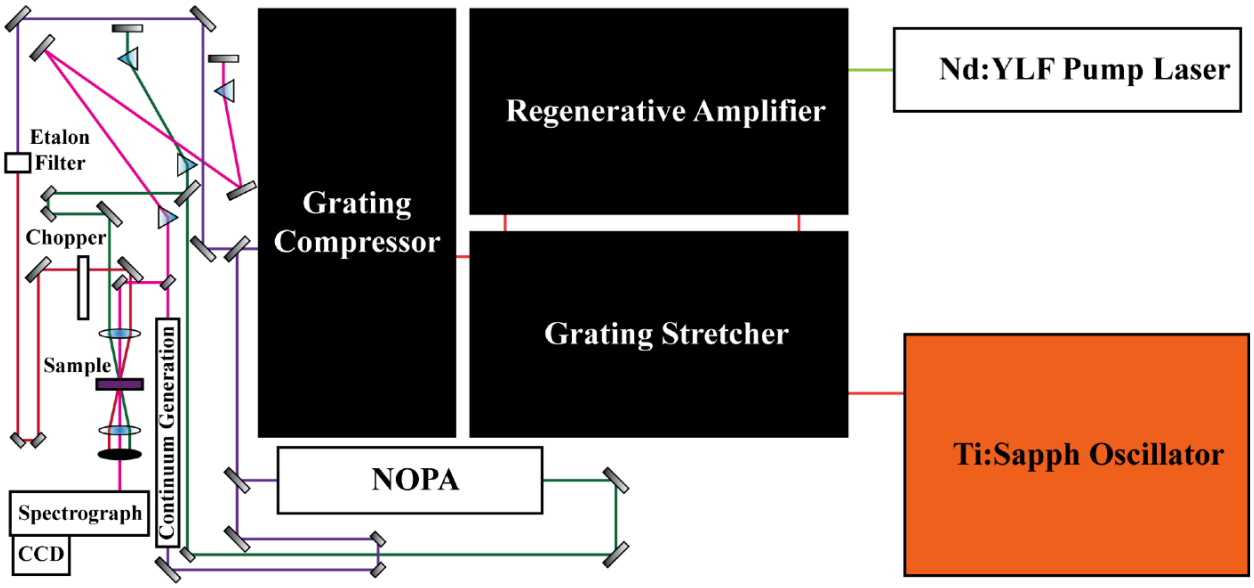

Figure 2.10: Block diagram of the Red Table showing the general layout of the instrument. The purple line traces the path of the fundamental, the green of the actinic, the magenta of the probe and the red of the Raman pump. The oscillator is described in Figure 2.11, the NOPA is described in Figure 2.12 and the etalon filter is described in Chapter 3. Continuum generation is identical to the seed formation in the NOPA. Notice the large foot print of the regenerative amplifier.

derstood, is the fact that the *resolution* is no better than it could be in the single pulse, picosecond time resolution, version of the experiment but here the phase of the Raman coherence is precisely controlled and measured. FSRS does *not* circumvent Heisenberg or Fourier Uncertainty, instead it makes them irrelevant, the manifestation of a true fifth order spectroscopy.

2.5 Brief Overview of the Instrumentation

The previous sections have explained what we are measuring and why. Now I will describe *how* the measurements are performed.

Most measurements in this thesis were made with three instruments: a resonance Raman spectrometer,[78] a tunable[79] FSR spectrometer and and a non-tunable[80] FSR spectrometer. The resonance Raman spectrometer is home built it is now considered a standard instrument and many varieties can be bought off-the-shelf. On the other hand, FSRS is a relatively new technique and our instrument is almost completely home built. As I have spent most of my time working on, maintaining and improving the non-tunable FSR spectrometer–which I will hereon refer to as the "Red Table"–it will be the focus of this section. Much of the design and many of the components of the Red Table are similar to the tunable instrument (the "Blue Table").

Figure 2.10 shows a block diagram of the Red Table which consists of three main components: a Ti:Sapphire oscillator which generates the femtosecond seed pulses, the amplifier which ampli-

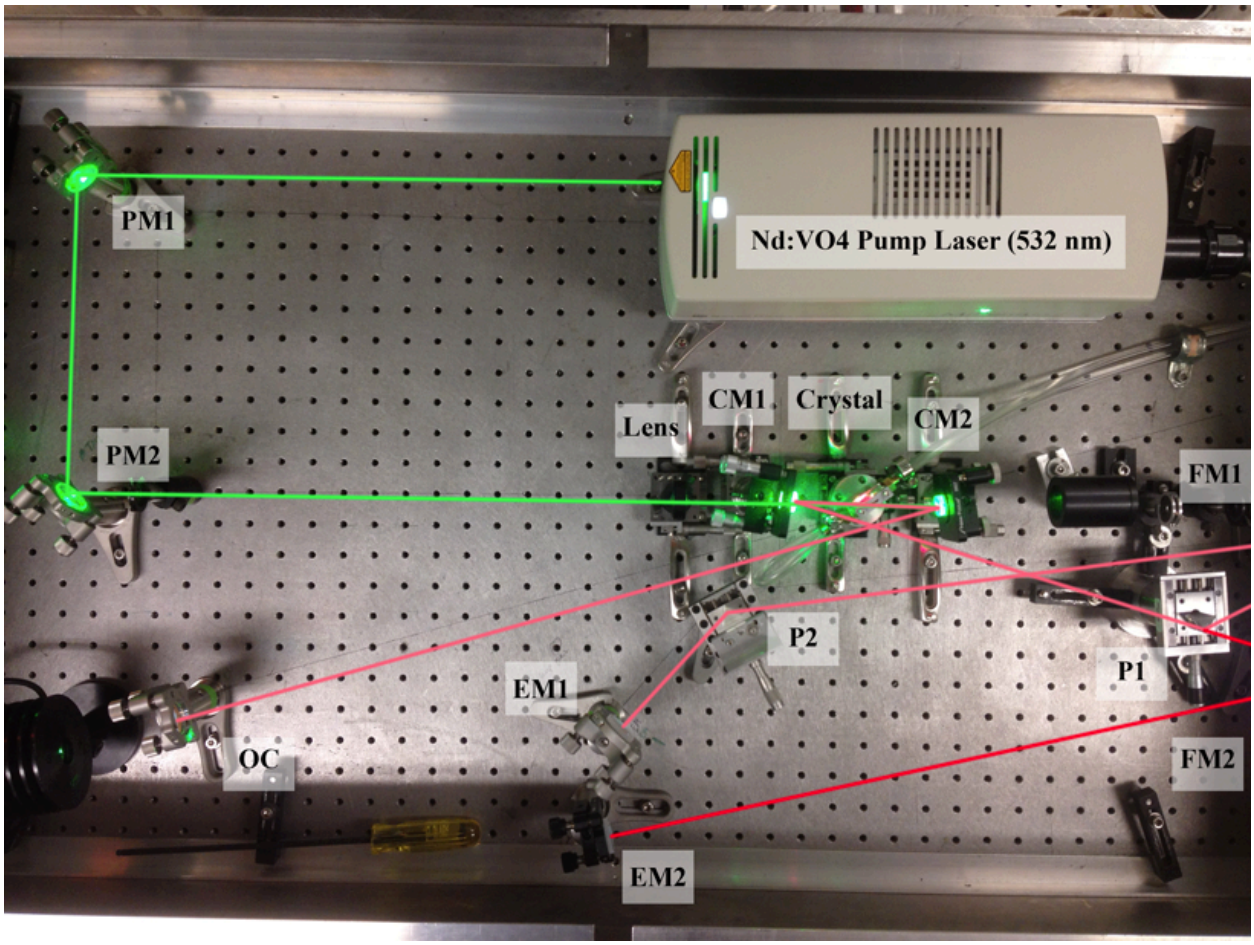

Figure 2.11: A schematic of the titanium sapphire oscillator on the Red Table labeled as follows: pump mirror (PM), lens, curved mirror (CM), crystal, folding mirror (FM), prism (P), end mirror (EM) and output coupler (OC). Note that the folding mirrors are outside the field of view. The green line traces the pump beam path, the pink line traces the mode-locked cavity and the red line shows the CW cavity. Note that the bread board in the picture has 1" spacing between the holes.

fies the pulses and the "open table" which includes all the optical components which transform the initially generated pulses into the ones used in FSRS; the actinic pump, the Raman pump and the Raman probe. In the rest of this section I will describe the components which I have improved the most, more details on the theory, operation and design of these and the other components can be found in ref. 81.

The oscillator's purpose is to generate a stable train of ultrashort pulses that will later be amplified. Because of Fourier uncertainty, the pulses must have a large bandwidth in order to have a short time duration. For Gaussian shaped pulses, which have the minimum Fourier uncertainty, the relation becomes $\Delta\nu\Delta t = 15$ ps cm^{-1}. This means that a 50 fs pulse *must* have at least 300 cm^{-1} of bandwidth. In order to generate pulses with the required bandwidth, the gain medium of

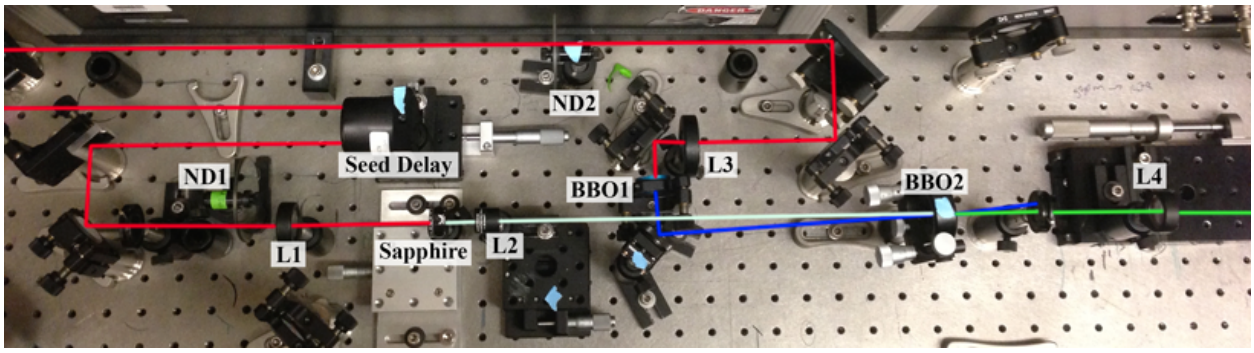

Figure 2.12: The non-collinear optical parametric amplifier (NOPA) on the Red Table labeled as follows: variable neutral density filter (ND), lens (L) and β-barium borate (BBO). The red line traces the input beam path, the blue line traces the pump beam, the white line indicates the seed beam and the green line shows the amplified beam. Note that the bread board in the picture has 1" spacing between the holes.

the oscillator needs to support as many **cavity modes** as possible. An optical cavity is defined by two end mirrors which form boundary conditions for the solutions of Maxwell's equations. In most cases the solutions are plane waves with wavelengths that are integral fractions of the cavity's length, these are the allowed cavity modes. Titanium sapphire is the ideal material for this purpose because of its vibrationally broadened energy levels which result in a gain bandwidth in excess of 3000 cm^{-1}.

In order to improve the performance of the system I rebuilt the oscillator, Figure 2.11 depicts the current design. Following this, reconstruction the overall stability of the system increased from a few hours to many days. The oscillator can be run either in continuous wave (CW) or mode-locked. Mode locking is covered well by Diels and Rudolph.[82] To run the oscillator as a CW laser the first prism (P1) is removed and mirrors FM2 and EM2 take the place of FM1 and EM1. The CW cavity is relatively simple, it consists of the gain medium, two curved mirrors set at each others conjugate focus, a folding mirror (FM2) an end mirror (EM2) and an output coupler (OC). The faces of the Ti:Sapphire crystal are cut at Brewster's angle and act as a polarization maintaining optic in the cavity. The mode-locking cavity is only slightly more complicated and introduces two prisms which compensate for the group velocity dispersion introduced by the crystal allowing for stable mode-locking of the laser. To activate mode-locking the following procedure is used. First, the CW cavity is perfectly aligned, then the prisms are introduced and the CW operation of of the mode-locking cavity is optimized. Following this the second curved mirror and the crystal positions are adjusted such that the CW cavity is de-optimized and the lasing mode is elongated vertically. This adjustment de-stabilizes the CW cavity while stabilizing the mode-locked cavity. To induce mode-locking the second prism (PM2) is perturbed briefly aligning the phases of all the cavity modes, generating an ultrashort pulse which self-stabilizes through Kerr lens mode-locking[82] creating a stable pulse train which is then aligned into the amplifier. Both cavities are collinearly pumped by a Nd:VO_4 laser that emits 3.5 W of 532 nm light.

The amplifier is a commercial system and as such will only be discussed briefly. It consists

of three modules; stretcher, regenerative amplifier and compressor. Because the input seed pulses are so short (~30 fs) they cannot be amplified directly as the resulting peak powers would damage the optics. Pulses are stretched first using a grating stretcher, the details of which can be found elsewhere.[83] Because the grating stretcher is composed solely of reflective, and not refractive, optics, the exact amount and nature of the chirp introduced into the pulse can be carefully controlled. Stretched pulses are directed to the amplifying module which consists of an isolator, to ensure that the amplified pulses can be redirected to the compressor, a pulse picker, which allows only one seed pulse into the regenerative amplifier's cavity at a time, and the cavity itself. The pulse picker also keeps the pulse in the cavity for an extended period of time allowing multiple passes through the energized gain medium before expelling it. The cavity design is very similar to that of the oscillator except the crystal is longer, in order to allow for more amplification, there are extra polarization maintaining optics in the form of Brewster's windows (which also play a role in the pulse picker), there are only three mirrors, two of them curved and no output coupler. After amplification the pulse is redirected to the compressor by the optical isolator and the chirp introduced by the stretcher is removed. Since the amplified compressed pulse is very intense, the compressor is also composed solely of reflective optics. Any refractive optic will add additional higher orders of chirp that are difficult to correct for and may cause self-focusing (see above) leading to damage. It should be noted that the bandwidth of the pulse is attenuated by the amplification process as discussed in other texts and so the output pulse of the amplifier is generally longer than the input pulse. By replacing damaged optics I increased the power, mode quality and stability greatly; the power was limited to 750 mW on a good day and is now 900 mW consistently, the mode used to have concentric rings and is now a smooth Gaussian and the system used to be stable for a maximum of 4 hours and now can perform consistently for over 24.

There are three main areas of the open table that I improved; I rebuilt the **non-collinear optical parametric amplifier** (NOPA), I improved the method of building prism compressors[84] and I replaced the grating filter with an etalon, the description and performance of which is the subject of Chapter 3.

The NOPA is a device which uses the second order nonlinear susceptibility of a medium (c.f. Section 2.3, in this case β-barium borate (BBO), to amplify select frequency components of a white light seed beam, see Figure 2.12 for a schematic. My design, depicted in Figure 2.12, is based on that of Cerullo and De Silvestri,[85] see Figure 18 of that reference and the discussion therein. Rebuilding the NOPA increased its stability from ~2 hrs to well over 24 and improved its bandwidth such that it can now produce pulses that could, in principle, be compressed to ~10 fs. Even so my improvement of the prism compressors is such that the probe pulse is now transform limited (~8 fs) and the overall instrument response function has been reduced by a factor of 4 and the probe chirp by nearly a factor of 20, see Figure 2.13. It is important to note that in the FSRS experiment the probe must be compressed, if this is not done some vibrational transitions maybe truncated more than others by the Raman pump. In fact, due to the asymmetric nature of the etalon-formed pump some peaks may be completely absent! Compression of the probe is not necessary for transient absorption as it can be corrected for *in silico*.[86] Finally, the improvement in stability means that the instrument can now detect changes on the order of 0.1 mOD with just a few seconds of averaging.

The Blue Table differs from the Red Table in that its Raman pump is tunable. The tunable Raman pump is generated by two extra NOPAs. Two of the NOPAs have a design similar to the one on the Red Table and the third is a specially designed narrow band one.[79] The broadband NOPA is spectral filtered with a grating filter and the resulting pulse is used to seed the narrow band NOPA. A portion of the amplifier fundamental is filtered in a separate grating filter and then doubled in a BBO to form the pump. Both the seed and the pump are combined in a second BBO to amplify the seed beam creating a powerful and tunable narrow bandwidth pulse for FSRS. The Blue Table was used for some of the experiments described in Chapter 4.

Detection of the FSRS and TA signals is similar for both instruments. In each case, all three beams are overlapped both spatially and temporally in the sample. The time delay between the Raman pump and probe is adjusted so that the ground state FSRS signal is maximal. The actinic pump delay is controlled by a computer. For ground state stimulated Raman measurements the actinic pump is blocked. The Raman pump is modulated by an optical chopper (ThorLabs, MC2000) at half the repetition rate of the laser and each probe pulse spectrum is recorded by a fast CCD (PIXIS, PI). Because the shot-to-shot fluctuations are low, a reference beam is unnecessary. The Raman gain is calculated as $\ln\left(\text{Probe}_{\text{Rpu On}}/\text{Probe}_{\text{Rpu Off}}\right)$. When performing ISRS experiments the chopper is moved to the actinic pump line to allow for maximum signal to noise in the TA. The TA is calculated as $-\log\left(\text{Probe}_{\text{Apu On}}/\text{Probe}_{\text{Apu Off}}\right)$. The Blue Table has two choppers and is able to collect one ground and excited state Raman spectrum as well as two TA spectra; one with and one without the Raman pump. However, this chopping scheme results in many more ground state Raman spectra than necessary being collected at the expense of the excited state spectra. For instance if one wants to collect spectra for 100 different values of Δt then the signal to noise of the excited state will be $1/10^{\text{th}}$ that of the ground state.

While I have been able to make major improvements to the Red Table further improvements in the signal to noise, to be discussed in Section 8.1, and pulse durations are possible. Simply replacing the actinic pump prism compressor with chirped mirrors should make 10 fs pulse durations feasible. In addition, a redesign of the NOPA that includes a module to compensate for the dispersion in the seed beam may allow for larger bandwidth pulses and therefore even shorter actinic pulse durations.

2.6 SUMMARY

I hope this chapter has clarified what we have measured, why we have measured it and how we have performed the measurement.

Technically, we are measuring the nonlinear susceptibility of the material system. The exact value of the susceptibility depends on to what order the field interacts with the medium. Within the harmonic approximation the resonances we observe are directly related the local curvature of the potential energy surface and thus the nuclear structure of the system. When we prepare a non-stationary state and probe it as it evolves we can learn how the structure of the system changes, or alternatively how the local curvature of the PES changes during the nuclear evolution. We want to

measure the PES because it completely determines molecular reactivity. To measure these spectra we have built a laser system that relies on the very nonlinear effects it is designed to probe.

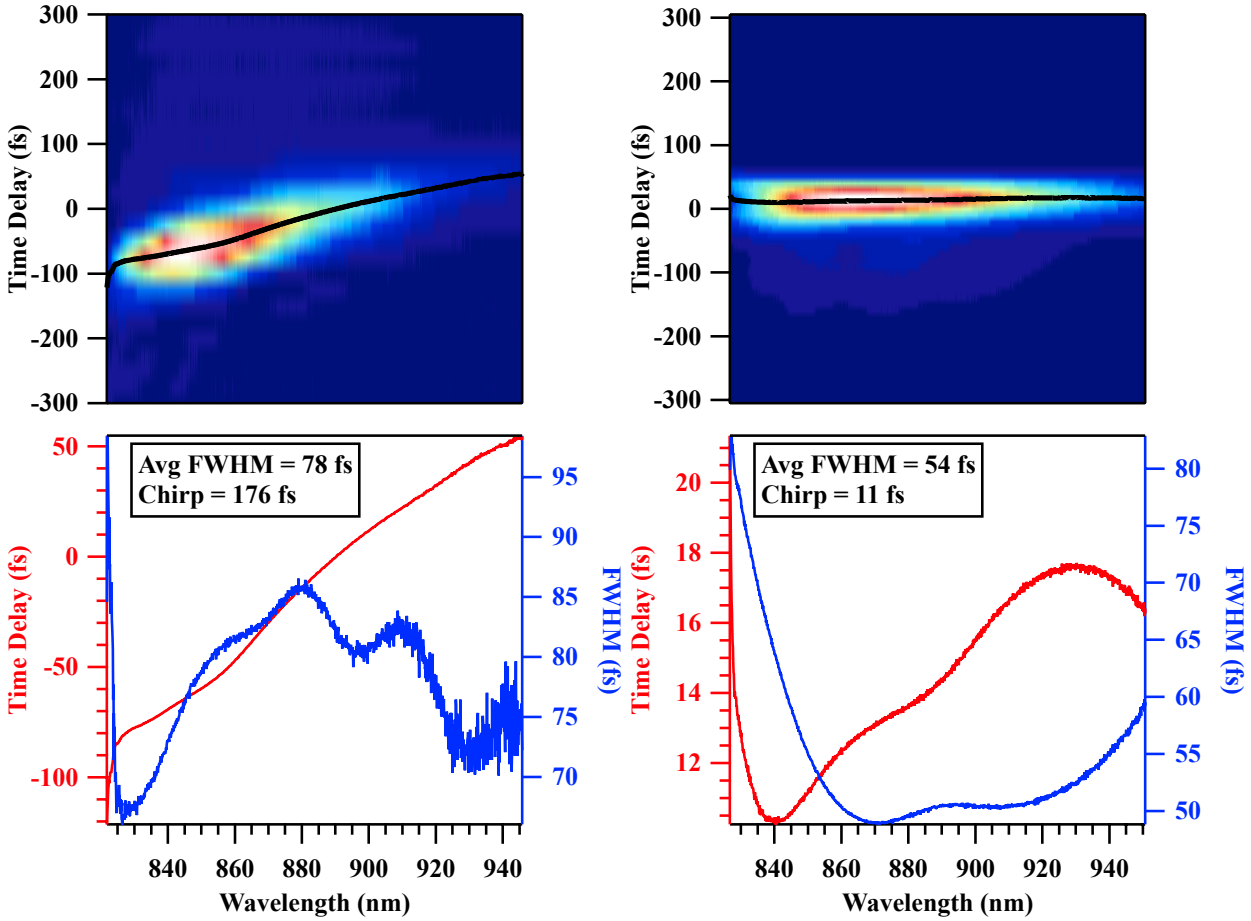

(a) Typical IRF before instrument improvements.

(b) Typical IRF after instrument improvements.

Figure 2.13: The response function of the Red Table as measured by frequency resolved cross-correlation of the actinic pump and probe using the Kerr gating method. The probe is dispersed and the actinic pump is acting as the gate. Each pixel is fit to a Gaussian function in order to extract the width and center which are plotted below in blue and red, respectively. A typical IRF from before the instrument improvement is shown on the left (Figure 2.13a) and that from after the improvement is shown on the right (Figure 2.13b). Note the nearly 25% improvement in the width, which relates mostly to the actinic pump and the nearly 20 fold improvement in the probe chirp.

Chapter 3

Optimally Shaped Narrowband Picosecond Pulses for Femtosecond Stimulated Raman Spectroscopy

3.1 Abstract

A comparison between a Fabry-Pérot etalon filter and a conventional grating filter for producing the picosecond (ps) Raman pump pulses for femtosecond stimulated Raman spectroscopy (FSRS) is presented. It is shown that for pulses of equal energy the etalon filter produces Raman signals twice as large as that of the grating filter while suppressing the electronically resonant background signal. The time asymmetric profile of the etalon-generated pulse is shown to be responsible for both of these observations. A theoretical discussion is presented which quantitatively supports this hypothesis. It is concluded that etalons are the ideal method for the generation of narrowband ps pulses for FSRS because of the optical simplicity, efficiency, improved FSRS intensity and reduced backgrounds.

3.2 Introduction

Narrowband picosecond (ps) pulses are crucial for coherent vibrational techniques such as coherent anti-Stokes Raman (CARS),[87,88] sum frequency generation (SFG),[89,90] and femtosecond stimulated Raman spectroscopy (FSRS).[21,80] In these spectroscopies, the narrowband ps pulse provides a well-defined virtual state energy resulting in well resolved vibrational spectra. Vibrational spectroscopy is particularly useful for studying chemical reaction dynamics as it probes reactive nuclear evolution with structural precision. In this endeavor, FSRS has three main advantages: simultaneous high time and frequency resolution,[17] effective rejection of fluorescence interference, and simple implementation.[80] Thus far, FSRS has been used to elucidate ultrafast structural dynamics in a number of diverse systems including photoswitches,[23,24] charge-transfer systems[26,91] and photoactivated proteins.[19,20,22] However, the convenient production of high power tunable ps pulses necessary to provide the Raman pump pulse in FSRS has been a consistent challenge.

In order to have synchronized broadband femtosecond and narrowband ps pulses, a portion of a femtosecond laser source is typically split and filtered. Common filtering techniques include grating filters and narrow band interference (NBI) filters.[80] However, each of these methods has intrinsic disadvantages: grating filters are inherently inefficient because, as illustrated in Figure 3.1, the beam must interact *twice* with a ruled diffraction grating. Additionally, the grating filter can adversely affect the laser beam's mode quality when the slit width is smaller than the input beam diameter. NBI filters are not broadly tunable, have large bandwidths and are susceptible to laser damage.

Fabry-Pérot etalons offer an attractive alternative filtering method for the generation of narrowband pulses and have been applied in SFG[89,90] and double resonance 2D-IR[92,93] spectroscopy. Etalons have not been previously used in FSRS but offer potential advantages; they have higher energy throughput than grating filters and narrower bandwidths than NBI filters while retaining tunability and durability. For example, the etalon described herein has a bandwidth of 2.8 cm^{-1}, an efficiency of 0.6% and a tuning range of 776-814 nm. Etalon filters also offer instrumental advantages; alignment consists of simply placing the optic in the beam path, the center wavelength of the etalon can be tuned by changing the angle of incidence[94] and the beam's mode quality is preserved

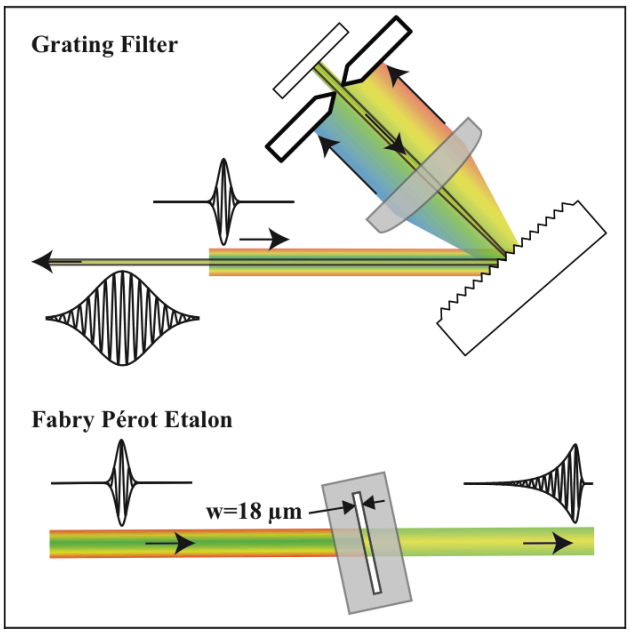

Figure 3.1: Schematics of the grating filter (top) and the etalon pulse shaper (bottom). Input and output pulse shapes are shown for both filters. The etalon device is optically simpler, more efficient and it provides improved beam quality compared to the grating filter.

regardless of its diameter. However, etalons are more expensive than the alternatives; therefore a critical examination of their utility is needed.

An additional, important, difference between etalon and grating or NBI filters is the resulting time domain pulse shape. Both grating and NBI filters create pulses that are symmetric in the time domain. The exact functional form depends on the nature of the individual filter; for narrow bandwidths, the resulting pulse is generally Gaussian. When the bandwidth of a Gaussian pulse is not sufficiently narrow, the resulting FSRS spectra are significantly broadened and the line-shapes are altered as well. In extreme cases the vibrational lines will take on "ringing" side wings.[95,96] On the other hand, etalons generate time asymmetric pulses (see Figure 3.1), a property that has been successfully used in SFG spectroscopy to suppress the non-vibrationally resonant background.[89] These pulses have a steep rise and an exponentially decaying tail meaning that while vibrational line-shapes may be broadened (the amount of which is determined by the bandwidth of the etalon) the vibrational lines will remain Lorentzian. It is also anticipated that the asymmetric etalon pulse profile will be advantageous for FSRS because it can reduce the electronically resonant non-linear background.

With these motivations, we investigated the use of etalon filters to produce the ps Raman pump pulse in FSRS. We accurately characterize the effect of the time delay between Raman pump and probe on signal characteristics for both the grating and etalon filters. A theoretical framework for modeling the etalon pulse and its role in the FSRS process, which quantitatively explains our results, is presented. Finally, we demonstrate the improvement in FSRS baselines by comparing

the excited state spectra of flavin adenine dinucleotide (FAD) when probed with the grating pulse versus the etalon pulse.

3.3 Materials and Methods

3.3.1 Femtosecond stimulated Raman

The laser system has been described in detail previously.[80] It consists of a home built Kerr lens mode-locked Ti:sapphire oscillator (30 fs 5.3 nJ/pulse, 91 MHz) that seeds a Ti:sapphire regenerative amplifier (B.M. Industries, Alpha 1000 US, 991 Hz, 70 fs, 0.91 mJ/pulse, λ_{max} = 790 nm) pumped by a Q-switched Nd:YLF (B.M. Industries, 621-D). A small portion of the fundamental is focused onto a 3 mm sapphire plate (ThorLabs) generating a broadband continuum which serves as the Stokes probe pulse in the FSRS process.[72] The probe pulse (8 fs, 5 nJ/pulse, λ_{max} = 883 nm) is subsequently compressed in the 820-945 nm region with a pair of BK7 equilateral dispersing prisms (CVI Melles Griot).[84] Approximately 200 μJ of the fundamental is used to pump a home-built noncolinear optical parametric amplifier (NOPA)[85] which generates the actinic pump pulse (30 fs, 150 nJ/pulse, λ_{max} = 475 nm). An F2 prism pair (ThorLabs) is used to compress the actinic pump.

The remaining ~690 μJ of the fundamental is used to generate the narrow bandwidth Raman pump. Traditionally, this has been done with a grating filter[97] consisting of a ruled diffraction grating blazed at 26.7° with 1200 groves/mm, a 200 mm fl cylindrical lens, an adjustable slit and a flat mirror. The bandwidth of the grating filter can be tuned by the slit width; however, the power is proportional to the bandwidth. When the bandwidth is set to ~2.8 cm^{-1} the maximum output pulse energy is ~0.7 μJ. Alternatively, we show here that a Fabry-Pérot etalon (TecOptics, Design #A6) can be used to produce the ps Raman pump pulse. This etalon has been designed with a reflectivity of 98.5 ± 0.5% and a spacing of 18.12 μm giving a free spectral range (FSR) of ~290 cm^{-1} and a finesse of ~100 resulting in a spectral bandwidth of ~2.8 cm^{-1}. The maximum output pulse energy for the etalon filter is ~2.3 μJ for the same input power. Input powers were measured immediately before the filters, however, the output powers were measured right before the sample. The measured absolute efficiency of the etalon is 0.6% which corresponds to a peak transmission of 44%. For different designs a sacrifice of some bandwidth will increase peak efficiency to ~85%.

All three beams are polarized parallel to the table and are spatially and temporally overlapped in the sample cell after being focused by a 100 mm fl achromatic lens. The instrument response function is measured in the sample cell in the relevant an aqueous buffer using the optical Kerr effect. After the sample, the probe beam is recollimated and directed to a spectrograph (Instruments SA, HR320) which disperses the beam onto a fast CCD (Princeton Instruments, PIXIS 100F). A phase locked chopper (Newport, 3501) blocks every other Raman pump pulse allowing a full Raman spectrum, calculated as $\ln(Probe_{\text{RPump On}}/Probe_{\text{RPump off}})$ to be collected for every two laser pulses. The delay between the actinic pump and the Raman pump/probe pulse pair is varied by a computer controlled delay stage (Nanomotion II, Melles Griot) while the delay between the Raman pump and probe is controlled with a manual micrometer. Initial data processing and instrument

control is performed by a custom LabVIEW program.[98]

3.3.2 Sample preparation

Spectral grade benzene (EMD, > 99.7%) was used as received. Measurements were performed in a 1 mm path length cell with 1.2 mm glass windows (Starna Cells, 21-G-1). A Raman pump energy of 0.7 μJ/pulse was used. The Raman shift axis was calibrated using benzene.

FAD (TCI America, > 94%) was used as received. FAD was dissolved in a 10 mM Tris, 50 mM NaCl buffer at pH = 8.0 forming a 2.2 mM solution which gives an optical density of 1 per 500 μm at 475 nm. The solution is flowed through a 500 μm path length cell with 200 μm quartz windows (Starna Cells, 48-Q-1-UTWA) from a 40 mL reservoir using a peristaltic pump at a rate sufficient to replenish the sample volume between consecutive laser pulses. A Raman pump energy of 1.5 μJ/pulse was used and the Raman shift was calibrated using cyclohexane.

3.4 Results

Figure 3.2(a) presents contour plots of the stimulated Raman signal of the 992 cm^{-1} mode of benzene as a function of Raman pump and probe delay for the grating filter (top, dashed) and the etalon filter (bottom, solid). The center traces show the signal amplitude as a function of delay, which mirrors the temporal profile of the pulses. In the case of the grating filter, the vibrational band is initially narrow and weak and then grows and broadens as the delay is increased. Increasing the delay further causes the line-shape to continue to broaden while the intensity decreases. Conversely, the signal resulting from the etalon filter increases sharply in intensity near a delay of zero and then decays exponentially; the width stays remarkably constant. Note that even though both pulses are ~0.7 μJ the maximum signal intensity for the etalon is nearly twice that for the grating filter.

Presented in Figure 3.2(b) are simulations of the signals shown in Figure 3.2(a) following the theory presented in refs. 72 and 97. To numerically generate the result of the etalon filter we explicitly simulated a transform limited pulse interacting with two highly reflective surfaces using eq. 3.1.[89,90]

$$E_{etalon}(\omega,t) = (1-R)\sum_{n=1}^{\infty} R^{2n+1} E_{laser}(\omega, t-(2n+1)\tau_{RT}) \tag{3.1}$$

Here ω is the carrier frequency, t is the time, R is the reflectivity of the etalon surfaces, τ_{RT} is the round trip time of the pulse in the cavity (τ_{RT} = (etalon spacing)/(speed of light)) and E_{laser} is defined as,

$$E_{laser}(\omega,t) = e^{-i\omega t} 16^{-(t/\sigma)^2} \tag{3.2}$$

where ω is the carrier frequency of the pulse, t is time and σ is the full width half maximum (FWHM) of the pulse in time. The Gaussian pulse resulting from the grating filter was modeled identically to that in refs. 72 and 97. The simulations quantitatively match the experiment when the model is parameterized as follows: the vibrational coherence time of the 992 cm^{-1} mode of

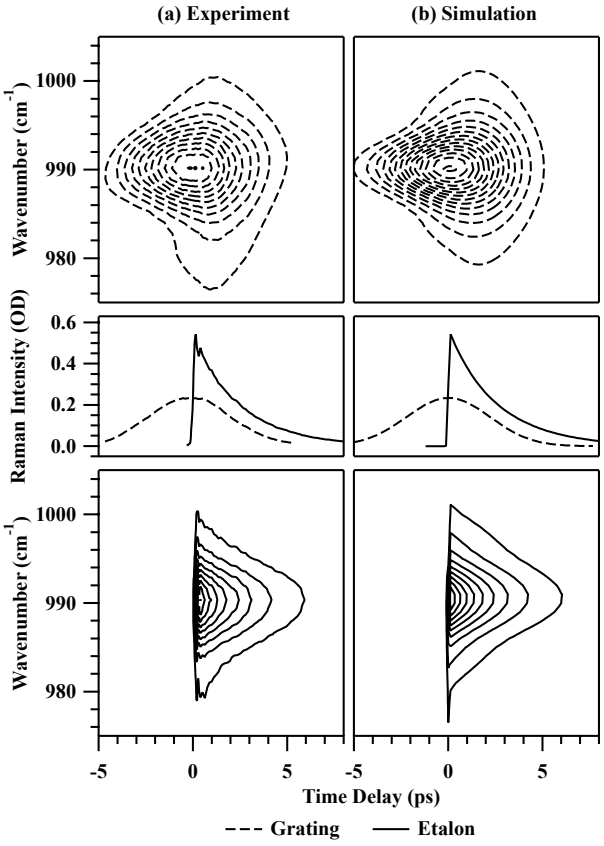

Figure 3.2: (a) Comparison of the effect of the time delay between the Raman pump and probe on the stimulated Raman signal of the 992 cm^{-1} mode of benzene. Contour plots of the stimulated Raman spectra are shown for the grating (top, dashed) and for the etalon (bottom, solid). The intensities of the 992 cm^{-1} peak are shown in the middle. The asymmetry in the grating filter data is due to the presence of a slight baseline. (b) Simulations of the data in (a) using the theory outlined in the text. Important model parameters are: vibrational FID, 2.2 ps; etalon reflectivity, 98.75%; etalon separation, 18.12 μm; FWHM of the electric field of the grating pump, 7 ps.

benzene is 2.2 ps, the etalon reflectivity (R) is 98.75%, the etalon spacing is 18.12 μm and the duration of the grating filter Raman pump electric field (*not* intensity) is 7 ps.

In order to evaluate the expected improvement in excited state baselines, transient stimulated Raman spectra of FAD were measured. The transient absorption of FAD is known to be strongly affected by the Raman pump when it is tuned to 795 nm[71] making FAD a challenging model system for this investigation. Figure 3.3 presents the transient stimulated Raman signal of FAD at 7.5 ps delay after excitation at 475 nm using the grating filter (dashed line) and the etalon filter (solid line). These results agree qualitatively with those of Weigel et al.[71] The etalon signal has been scaled by 0.45 so that the Raman features are the same magnitude, emphasizing the reduced baseline. Relative to total pump energy, the signal from the etalon is more than twice as intense as

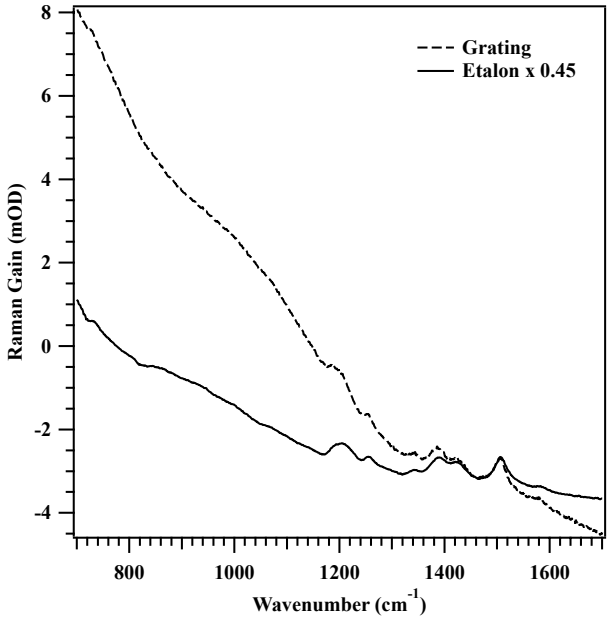

Figure 3.3: A comparison of the excited state Raman spectra of FAD at 7.5 ps delay taken with the grating (dashed) and the etalon (solid). The etalon spectrum has been scaled to that of the grating using the intensities of the FAD peaks in order to emphasize reduced baseline interference with the etalon.

that from the grating filter, in agreement with the results presented in Figure 3.2.

3.5 DISCUSSION

Optimally shaped narrow band ps pulses can be used to improve femtosecond stimulated Raman spectra. Proper tailoring of the Raman pump pulse results in a two-fold enhancement of the signal and a concomitant reduction in the background. Besides the intrinsic improvement in data quality, etalons are also much more simple to align and tune than grating filters while offering much narrower bandwidths and improved durability compared to NBI filters. Unlike grating filters, etalon filters maintain the laser beam's mode quality regardless of the beam diameter and have higher energy throughput.

Shaping the ps pulse to be asymmetric in time allows for nearly double the signal intensity per unit pulse energy, as shown in Figure 3.2. For asymmetric pulses, almost all of the pump photons contribute to the signal because they arrive at the sample at the same time or later than the stimulating probe pulse. On the other hand, nearly half of the pulse photons in symmetric pulses, such as those produced by grating or NBI filters, ineffectively arrive at the sample *before* the probe. Furthermore, the exponential shape of the etalon pulse mirrors the natural shape of the vibrational free-induction decay meaning that the resulting line shapes for homogeneously broadened vibrations remain Lorentzian and the width does not change with the time delay.

Another significant improvement, illustrated by the FAD data in Figure 3.3, is the reduction of excited state baselines. Because FSRS is a heterodyne technique it is susceptible to both resonant and non-resonant backgrounds. Properly removing baselines from FSRS data can be a challenging part of the data analysis. Although, some innovative experimental approaches have been developed to minimize baselines,[23] theses approaches are technically complex and ill-suited for some systems. The largest contribution to the background is the electronically resonant interaction of the Raman pump with the sample. For example, near a ground state resonance the Raman pump can create an excited state population. Alternatively, near an excited resonance the interaction can lead to a non-negligible dumping or promotion of the excited state population. These scenarios commonly result in a different absorption of the probe when the Raman pump is coincident. For a majority of systems the excited state absorption and stimulated emission cover the entire visible wavelength region and this *differential* absorption leads to broad featureless baselines in the Raman spectra. This effect can result in particularly complicated baselines when the Raman pump transfers a portion of the population to another excited state. Significant perturbation of the excited state population can also lead to unreliable kinetics.[71] Because these effects depend on the Raman pump they are directly correlated with the signal and therefore cannot be removed by conventional methods, such as signal averaging or increasing the excitation power. The time asymmetric pulse generated by the etalon minimizes the interaction of the Raman pump with the sample before the actual probing event thereby mitigating the perturbation of the system and reducing these unwanted background signals.

Finally, etalon filters can be incorporated into broadly tunable systems as long as the etalon's dielectric coating is sufficiently broadband and the FSR is large enough. Commercial amplifiers coupled with state of the art NOPAs provide sufficient power to produce multi-μJ tunable narrow band pulses with an etalon filter. The technical simplicity and improved power throughput compared with grating and NBI filters should reduce the barriers to implementing FSRS. While etalons are more expensive than conventional filters, the cost is relatively minor when compared to the femtosecond light source and the simplicity is advantageous for both new and experienced stimulated Raman spectroscopist.

Acknowledgments

Funding was provided by the Mathies Royalty fund.

Chapter 4

Photoexcited Structural Dynamics of an Azobenzene Analog 4-Nitro-4'-Dimethylamino-Azobenzene from Femtosecond Stimulated Raman

4.1 Abstract

Azobenzenes are used in many applications because of their robust and reversible light induced $trans \leftrightharpoons cis$ isomerization about the N=N bond, but the mechanism of this ultrafast reaction has not been conclusively defined. Addressing this problem we have used Femtosecond Stimulated Raman Spectroscopy (FSRS) to determine the structural transients in the $trans \rightarrow cis$ photoisomerization of the azobenzene derivative, 4-nitro-4'-dimethylamino-azobenzene (NDAB). Key marker modes, such as the 1570/1590 cm^{-1} NO_2 stretch and the 1630 cm^{-1} C–$N(Me)_2$ stretch, enable the separation and analysis of distinct *trans* and *cis* photoproduct dynamics revealing the 400 fs Franck-Condon relaxation, the 800 fs timescale of the *cis* product formation and the 2 ps emergence and 8 ps relaxation of the unsuccessful ground state *trans* species. Based on these observations, we propose a reaction mechanism, including initial dilation of the CNN bend later joined by quick movement along the CCNN, CNNC and NNCC torsional coordinates that constitutes a mixed inversion-rotation mechanism.

4.2 Introduction

Azobenzene's photoswitching capability has led to its use in molecular motors,[99] photoactive thin films[100,101] and storage media,[102] as well as novel applications where the azo moiety is inserted into a protein thereby allowing its activity to be modulated by light.[103] Azobenzene photoswitching is based on the wavelength dependent light induced $trans \leftrightharpoons cis$ isomerization about the N=N bond that changes the molecular shape.[101,104] Isomerization occurs after both S_1 and S_2 excitation though the quantum yields differ, an apparent violation of Kasha's rule. Even though azobenzenes are widely used and studied there remains considerable interest in determining the exact mechanism and time scale of the reaction for both fundamental and practical reasons.

Unlike its isoelectronic relative stilbene, azobenzene has *two* possible mechanistic pathways: stilbene-like rotation and/or inversion about one or both nitrogens. In an effort to explain azobenzene's violation of Kasha's rule,[105] Rau postulated that the difference in quantum yields was because each excited state leads to a distinct mechanism of isomerization. Based on studies of "locked" azobenzenes,[29,106] Rau concluded that the mechanism of isomerization is rotation after S_2 excitation and inversion after S_1 excitation. However, a recent consensus has formed among theorists that rotation is the dominant mechanism regardless of initial excitation.[41,42,44,45,47] Spectroscopically, the results are mixed: most ultrafast absorption experiments[107,108] have concluded that inversion is dominant in S_1 and rotation is preferred in S_2. A recent sub-picosecond fluorescence study[39] argued on the basis of anisotropy measurements that the mechanism of isomerization depends on the solvent properties; in ethylene glycol it is inversion and in hexane it is rotation. On the other hand, a time-resolved photoelectron experiment[38] supported by high-level calculations showed that inversion is dominant under all excitation conditions. Finally, it should be noted that most structural studies[37,40] have observed markers most consistent with inversion and Fujino, Arzhantsev, and Tahara[37,109] found that the reaction occurred in S_1 regardless of the excitation condition.

We have chosen to study an azobenzene derivative, 4-nitro-4'-dimethylamino-azobenzene (NDAB, Figure 4.1), for two reasons. First, NDAB is representative of a widely used sub-class of azobenzenes, the pseudostilbenes alternatively called push-pull substituted azobenzenes.[101] Formed by substituting the 4 and 4' positions alternatively with an electron donor and an electron acceptor, these derivatives have unique properties that make them technologically useful. For example, the *trans* $\pi \rightarrow \pi^*$ transition gains some charge transfer (CT) character, red shifts considerably to more accessible visible wavelengths and its absorption cross section increases substantially from ~400 to more than 30,000 $M^{-1}cm^{-1}$. This shift causes the *trans* and *cis* absorption spectra to significantly overlap allowing both species to be excited simultaneously. While this is disadvantageous for applications where discrete states are required, like optical storage, the constant isomerization from *trans* to *cis* and *vice versa* can be useful, e.g. to reversibly pattern thin films.[110] Secondly, because there is only one absorption band there should be only one reaction mechanism simplifying the interpretation. It is intuitive to assume that a difference in the electronic structure would have a large effect on the isomerization mechanism. However, calculations of the S_1 PES for azobenzene and azobenzene derivatives show they are very similar.[43] These calculations suggest that the rotational mechanism should be dominant in NDAB and authors of a recent femtosecond transient absorption study on a similar push-pull azobenzene[111] seem to agree. On the other hand, a study on yet another pseudo-stilbene[112] concluded that inversion was the main driver of the reaction. A qualification is that all the sub-picosecond transient data on NDAB have been electronic, i.e. transient absorption and fluorescence, which does *not* provide structural mechanistic data.

In an effort to provide new and structural data to this discussion we use the technique of Femtosecond Stimulated Raman Spectroscopy (FSRS),[21] with 10 cm^{-1} vibrational resolution and 25 fs temporal precision, to record structural snapshots of the NDAB reaction as it progresses. FSRS has recently been used to investigate the structural mechanisms of interfacial charge transfer,[113] isomerizations in phytochrome[22] and stilbene[23] and has revealed the importance of low frequency motions in facilitating the excited state intramolecular proton transfer in GFP.[20] Here we use FSRS to follow the structural dynamics of the photoexcited $trans \rightarrow cis$ reaction of NDAB enabling temporal structural characterization of the Franck-Condon relaxation and subsequent excited state dynamics followed by the formation of the initial *cis* and *trans* ground state photoproducts. These time resolved structural data reveal the intrinsic timescale and mechanism of the reaction.

4.3 Materials and Methods

4.3.1 Sample preparation

4-Nitro-4'-dimethylamino-azobenzene (NDAB, Figure 4.1) was obtained from TCI America (98%) and used as received. Samples were prepared by dissolving NDAB in dimethyl sulfoxide (DMSO, EMD Chemicals, 99.9%) or carbon tetrachloride (CCl_4, Sigma, 99.9+%) to obtain 1 OD per path length for the FSRS measurements; about 0.3 mM for the 1 mm path length cell (Starna Cells Inc., 48-Q-1) and 0.6 mM for 500 μm path length cell (Starna Cells Inc., 48-Q-0.5). Both cells have 1.25 mm thick quartz windows. For spontaneous Raman, experiments the sample was prepared

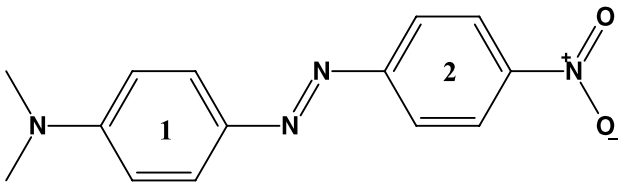

Figure 4.1: *trans* 4-nitro-4'-dimethylamino-azobenzene (NDAB)

to give ~0.08 OD per path length; about 16 μM for the 1.5 mm ID capillary used. In all cases the sample was circulated from a large sample reservoir (>5 mL) at a rate sufficient to ensure that each set of laser pulses encountered fresh sample, and in the case of the resonance Raman experiments that the photoalteration parameter was kept to less than 0.1. No change was observed in the absorption spectra of the samples after the measurements. In order to form the *cis* isomer, the CCl_4 solution reservoir and flow cell were illuminated with blue LEDs (λ_{max} = 470 nm, AND® Optoelectronics, AND190HBB) while the data were recorded.

4.3.2 Spontaneous Raman

Spectra were collected using the 496.5 nm line of an Ar^+ laser (Spectra Physics, Model 2020). A 50 mm fl lens focused the approximately 2 mW beam into the sample and the scattered light was detected by a liquid nitrogen cooled, back-illuminated CCD camera (Roper Scientific, LN/CCD-1100/PB) after passing through a subtractive dispersion double spectrograph (Spex, 1401). Spectra were calibrated using cyclohexane as a standard.

4.3.3 Femtosecond stimulated Raman spectroscopy

Two separate FSRS instruments were used both of which have been described in detail previously[80,114]. Briefly, the output of a Ti:sapphire regenerative amplifier (BMI, alpha/1000us for the 800 nm instrument[80] and Spectra Physics, Spitfire for the tunable instrument[114]) seeded by a home-built Kerr Lens Mode-locked Ti:sapphire oscillator is used to generate three pulses. The Raman probe pulse is created by focusing a small amount of the fundamental into a 3-mm thick sapphire window to generate a weak (7-10 nJ/pulse) broad band continuum pulse which is then compressed using a fused silica (for the NIR) or BK7 (for the visible) prism pair. The actinic pump pulse (0.3-0.4 μJ/pulse, λ_{max} = 500 nm) is generated by a non-collinear optical parametric amplifier (NOPA) and is compressed with a SF10 prism pair. In the 800 nm instrument the Raman pump pulse (2-4 μJ/pulse, 10 cm^{-1} FWHM, λ_{max} = 790 nm) is generated by spectrally filtering the fundamental with a custom built grating filter. In the tunable instrument the Raman pump pulse is formed by spectrally filtering the output of a second NOPA and using the resulting pulse to seed a narrow bandwidth NOPA resulting in 0.3-0.4 μJ, 20-30 cm^{-1} FWHM, pulses.[114]

All three beams, polarized parallel to the optical table, are focused into the sample by a 100 mm fl achromatic lens. An iris is used to spatially filter the Raman pump and actinic pump while the probe is recollimated by a second 100 mm fl lens and continues on to the detection

setup. The Raman pump and probe pulses remain overlapped in time for the duration of the experiment while actinic pump's time delay is varied by means of a computer controlled translation stage (Physik Instrumente, M-405.DG). The probe beam is dispersed by a spectrograph (Instruments SA, HR320 or Spex, 500M) and recorded by a CCD camera (Princeton Instruments, PIXIS 100F) which is capable of recording a full spectrum for each laser pulse. All spectra were calibrated using cyclohexane as a standard. A phase locked chopper (ThorLabs, MC2000) is used to chop the Raman pump beam at half the repetition rate of the amplifier and successive Raman-pump-on/Raman-pump-off spectra are collected. The Raman gain is calculated as Raman-pump-on÷Raman-pump-off on a shot-to-shot basis to mitigate the effect of fluctuations in the probe shape and/or energy. No reference beam is needed as the shot-to-shot fluctuations of the laser are less than 1%. The order in which different time delays were probed was randomized with ground state spectra taken intermittently by shuttering the actinic pump. Each spectrum is the result of averaging 3-6 sets of 4000 gain spectra (8000 raw spectra), each set takes 8 seconds to collect for a total acquisition time of 24-48 seconds per time point. Difference spectra shown have had the ground state and solvent signals removed after being normalized using the 670 cm^{-1} DMSO line as a reference correcting for both fluctuations in the Raman pump energy and any transient absorption; see Appendix B for more details on the data analysis, all of which was performed using IgorPro (WaveMetrics Inc.).

The instrument response function (IRF) was measured by optical Kerr effect cross correlation (data shown in Appendix B) between the actinic pump and Raman probe in the sample cell with only the solvent, DMSO, present. For the 800 nm instrument a typical IRF was Gaussian in shape with a FWHM of ~85 fs with a linear chirp of 70 fs across 840 to 920 nm spectral window. For the tunable instrument a typical IRF was Gaussian with a FWHM of ~120 fs with a linear chirp of about 70 fs in the 650 to 700 nm spectral window.

4.4 Results

Absorption spectra of NDAB in DMSO and CCl_4 are presented in Figure 4.2a. NDAB, like its parent molecule azobenzene, has two main absorption bands. The lower energy one, assigned to the $\pi \rightarrow \pi^*$/CT transition, is strongly allowed ($\epsilon = 33,100\ M^{-1}\ cm^{-1}$, in DMSO). This transition is expected have a large CT component as evidenced by NDAB's strong solvatochromism; its absorption maximum shifts from 452 nm in non-polar CCl_4 to 500 nm in DMSO. Like azobenzene, NDAB will isomerize after photoexcitation and form the meta-stable *cis* isomer. However, the lifetime of the *cis* isomer in polar solvents, like DMSO, is on the order of μs-ms, while in non-polar solvents, like CCl_4, it is on the order of minutes.[115] The *cis* isomer could not be formed in DMSO for long enough to obtain an absorption or Raman spectrum. In CCl_4 it was possible to obtain 60:40 mixture of *trans*:*cis* and the decomposed *cis*-NDAB absorption spectrum is also shown in Figure 4.2a. The $\pi \rightarrow \pi^*$/CT transition in *cis*-NDAB is red shifted relative to that of the *trans* isomer and is almost 40% broader with an extinction coefficient of only ~4000 $M^{-1}\ cm^{-1}$ at 490 nm.

Figure 4.2b presents illustrative stimulated Raman spectra of *cis* and *trans* NDAB excited at

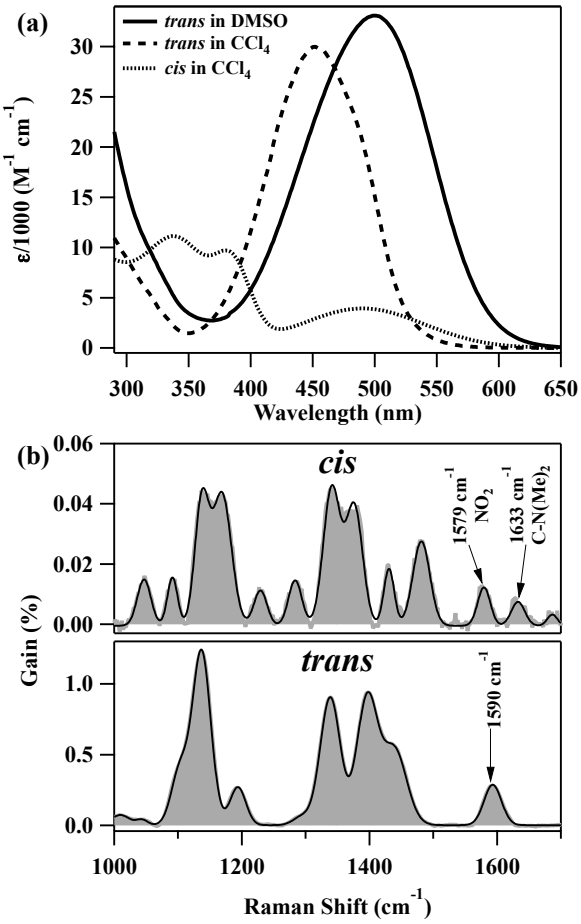

Figure 4.2: (a) Absorption spectra of NDAB in DMSO and CCl_4. The *cis* spectrum was obtained by irradiating the CCl_4 solution and then decomposing the data using the pure *trans* spectrum (see details in the Appendix B). (b) Steady state FSRS spectra of *cis* and *trans* NDAB in CCl_4, λ_{ex} = 568 nm. Fits to sums of Gaussians are indicated by the thin black line. The split of the ~1630 cm^{-1} NO_2 and the ~1580/1590 cm^{-1} C–$N(Me)_2$ stretching frequencies on going from *trans* to *cis* is diagnostic of isomerization.

568 nm. Because of its red shifted absorption the *cis* isomer has an absorption cross section that is nearly five fold that of the *trans* at 568 nm, so that its Raman spectrum is preferentially enhanced. Even with this enhancement the Raman cross sections of *cis*-NDAB are clearly much smaller than those of the *trans* isomer. The most salient difference between these two spectra is the increased splitting in the two modes near 1600 cm^{-1} on going from $trans \rightarrow cis$. This splitting will be used as an indicator for the isomerization.

Figure 4.3 presents a comparison of the spontaneous and stimulated Raman spectra of *trans* NDAB at high resolution. Detailed assignments of the mode character based on previous work[35,116] and DFT calculations at the B3LYP/6-311G++(d,p) level[117] are given in the Appendix B. Briefly,

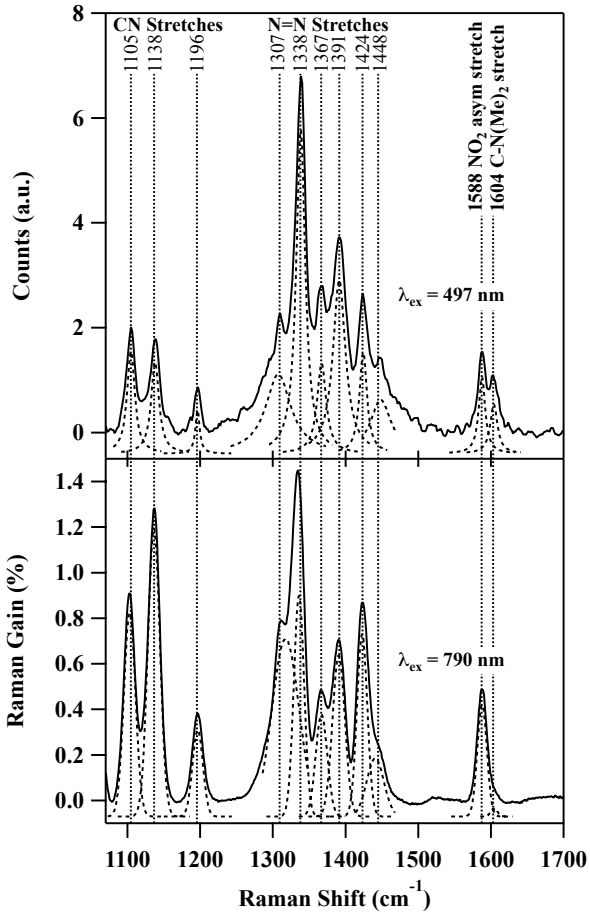

Figure 4.3: Raman spectra of *trans* NDAB in DMSO excited at 497 and 790 nm. The top trace was obtained with a spontaneous Raman spectrometer while the bottom trace was recorded with the 800 nm FSRS instrument. The experimental data are shown in black while the fits are shown with the dashed lines. The vertical dotted lines mark the peak positions.

the modes in the 1100-1200 cm^{-1} region are assigned to the CN stretches, those in between 1300 and 1500 cm^{-1} are N=N stretches, the 1588 cm^{-1} mode is the asymmetric NO_2 stretch mixed with some N=N and C=C stretching character, the 1604 cm^{-1} mode is the C–$N(Me)_2$ stretch mixed with C=C stretching character. On resonance, at 497 nm, both 1600 cm^{-1} modes are clearly visible and are of nearly equal intensity. At 790 nm excitation the intensity of the high frequency C–$N(Me)_2$ mode decreases drastically compared to the NO_2 mode.

4.4.1 FSRS EXCITED AT 625 NM

Figure 4.4 presents a subset of the transient Raman spectra of NDAB (λ_{ex} = 625 nm) collected in DMSO with time delays between 400 fs and 20 ps along with a ground state spectrum for reference.

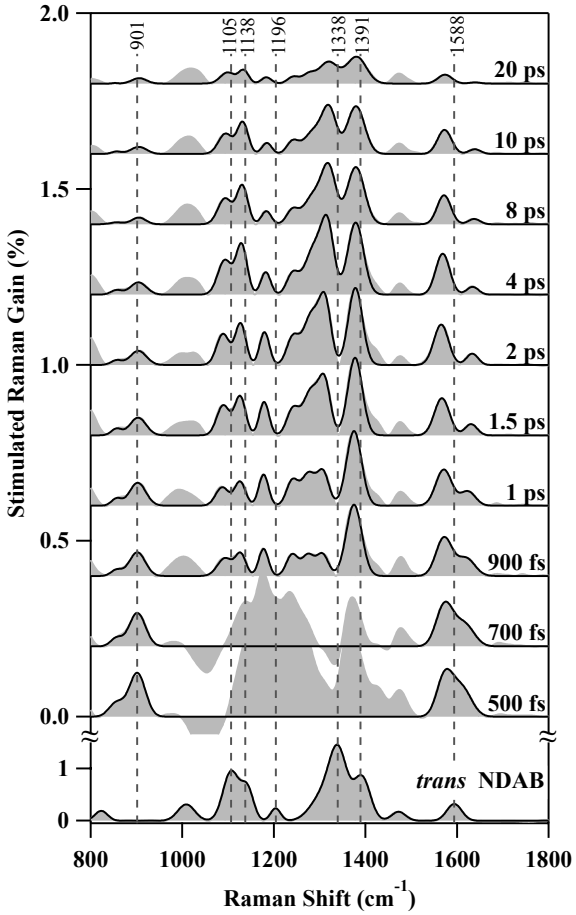

Figure 4.4: Time resolved FSRS spectra of NDAB in DMSO from 500 fs to 20 ps. The ground state NDAB and solvent signals have been removed. The ground state spectrum, taken under the same conditions as the excited state spectra, is shown for comparison. Fits to a sum of Gaussians are indicated by the thin black lines. Ground state peak positions are marked by the vertical dashed lines. The region between 1000 and 1500 cm^{-1} is obscured by RINE at times earlier than ~800 fs and the entire spectrum is obscured by RINE before 400 fs. λ_{ex} = 625 nm.

A Raman pump wavelength of 625 nm was chosen in an effort to be on resonance with S_1, as seen in the transient absorption of NDAB reported by Schmidt et al.[34] and Koller et al.[35], while not exciting the ground state with the Raman pump. Times earlier than 400 fs are obscured entirely by RINE[69]. By 2 ps the transient spectra are dominated by vibrationally excited *trans*-NDAB. These spectra have vibrational features that are red shifted by less than 1% from the ground state peaks while maintaining similar relative peak intensities. In addition two new bands are formed in the excited state both of which appear immediately following photoexcitation at 400 fs. The high frequency one near 1620 cm^{-1} can be assigned to an C–$N(Me)_2$ stretching mode. After about 1 ps it can be attributed solely to the *cis* isomer based on its final frequency of 1632 ± 6 cm^{-1}. The

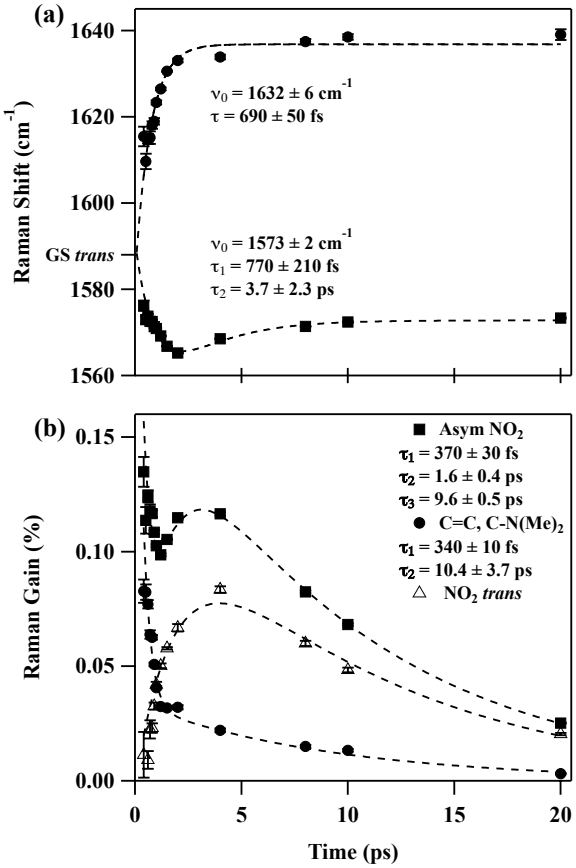

Figure 4.5: (a) Time evolution of the NO_2 and C–$N(Me)_2$ stretching band frequencies shown in Figure 4.4. Fits are shown with a dashed line. The high frequency band which is due solely to the *cis* isomer has been fit with a single exponential while the lower frequency band which has contributions from both isomers is fit with two exponentials of opposite phase. The fits are extrapolated back to zero time and coincide with the ground state NO_2 stretching frequency which is indicated on the axis. (b) The amplitudes of the *cis* and *trans* bands versus time. The trace labeled "*trans*" was obtained by subtracting the high frequency, *cis* only, band from the low frequency band after scaling by the ground state ratio of the two *cis* stretching modes near 1600 cm^{-1} shown in 4.2(b). λ_{ex} = 625 nm.

new feature near 900 cm^{-1} is much more difficult to assign as there are no experimentally observed or theoretically predicted peaks for ground state *trans* or *cis*-NDAB in this region; however, the kinetics of this peak are very similar to those of the 1620 cm^{-1} band and so it has also been assigned to the *cis* photoproduct.

Figure 4.5 presents kinetic traces of the center frequencies and the intensities of the NO_2 and C–$N(Me)_2$ peaks near 1600 cm^{-1}. Fits to exponential decays convoluted with the IRF are indicated by the dashed lines. The frequency evolution of the ~1620 cm^{-1} peak has been fit with a single exponential with a time constant of 690 ± 50 fs, while the amplitude has been fit with two compo-

nents having decay constants 340 ± 10 fs and 10.4 ± 3.7 ps. This peak can be assigned as due solely to the *cis* isomer for two reasons; first, its final frequency of 1632 cm^{-1} quantitatively matches the *cis* ground state peak frequency of 1633 cm^{-1}, secondly, the peak position evolves with a single time constant of ~800 fs which is similar to the excited state lifetime measured by transient absorption (data shown in Appendix B) and the lifetime reported in the literature by time-resolved fluorescence and absorption.[34,35] Thus the 1620 cm^{-1} peak does not exhibit any cooling dynamics on the ground state surface; this behavior is expected for the *cis* isomer because most of the excess energy is used up in driving the isomerization reaction.

The evolution of the red shifted ~1580 cm^{-1} *cis* peak is more complex but can be understood as follows. If the 1632 cm^{-1} peak is indeed due to the *cis* photoproduct then there should be an accompanying lower frequency NO_2 peak around 1572 cm^{-1}, cf. Figure 4.2b. Additionally, the *trans* photoproduct should be vibrationally excited leading to a slightly red shifted spectrum which would put the *trans*-NDAB NO_2 stretch at about 1580 cm^{-1}. Therefore the observed feature at 1580 cm^{-1} is most likely due to two overlapping vibrations from the two photoproducts each of which can be expected to have its own dynamics. To test this hypothesis, the intensity of the C–$N(Me)_2$ mode was scaled by about 1.5 – the ratio of the two ~1600 cm^{-1} peaks in the ground state *cis*-NDAB spectrum – and subtracted from intensity of the ~1580 cm^{-1} mode. The result is shown in Figure 4.5b as the △'s and clearly exhibits the kinetic trace of an intermediate. Thus the amplitude of the 1580 cm^{-1} peak was fit to the sum of an exponential decay and an exponential rise and decay of the same amplitude,

$$A_1 e^{-t/\tau_1} + A_2 \left(-e^{-t/\tau_2} + e^{-t/\tau_3}\right) \tag{4.1}$$

convoluted with the IRF. The extracted time constants are 370 ± 30 fs, 1.6 ± 0.4 ps and 9.6 ± 0.5 ps. The center frequency of the 1580 cm^{-1} peak has been fit with two exponential decays of opposite phase and different amplitudes with time constants 770 ± 210 fs and 3.7 ± 2.3 ps. The fact that the fast time constants of both the amplitude and frequency for the 1580 cm^{-1} peak are the *same* as the corresponding ones for the 1632 cm^{-1} peak supports the hypothesis that the 1580 cm^{-1} peak is in fact two overlapping peaks due to the *cis* and *trans* isomers.

4.4.2 FSRS excited at 790 nm

Figure 4.6 presents selected transient Raman spectra of NDAB (λ_{ex} = 790 nm) in DMSO with time delays between 100 fs and 20 ps. A wavelength of 790 nm was chosen to avoid any excited state resonance conditions and thus the RINE that affected the data in Figure 4.4. There are seven main peaks of interest, the NO_2 peak near 1600 cm^{-1}, the two N=N peaks near 1370 cm^{-1} and the four CN peaks between 1100 and 1200 cm^{-1}. All the peaks in the transient spectra correspond to ground state bands except for the CN stretch near 1110 cm^{-1} which will be discussed below.

Figure 4.7 presents the kinetic traces of the intensities and center frequencies of the (a) NO_2 mode, (b) N=N modes and (c) the 1110 cm^{-1} CN mode. The kinetics in Figure 4.7a are very similar to the 1580 cm^{-1} mode dynamics shown in Figure 4.5; all of the extracted time constants are the same, thus the dynamics are not affected by the change in resonance condition. At this wavelength the high frequency C–$N(Me)_2$ stretching frequency, assigned solely to the *cis* photoproduct, is not

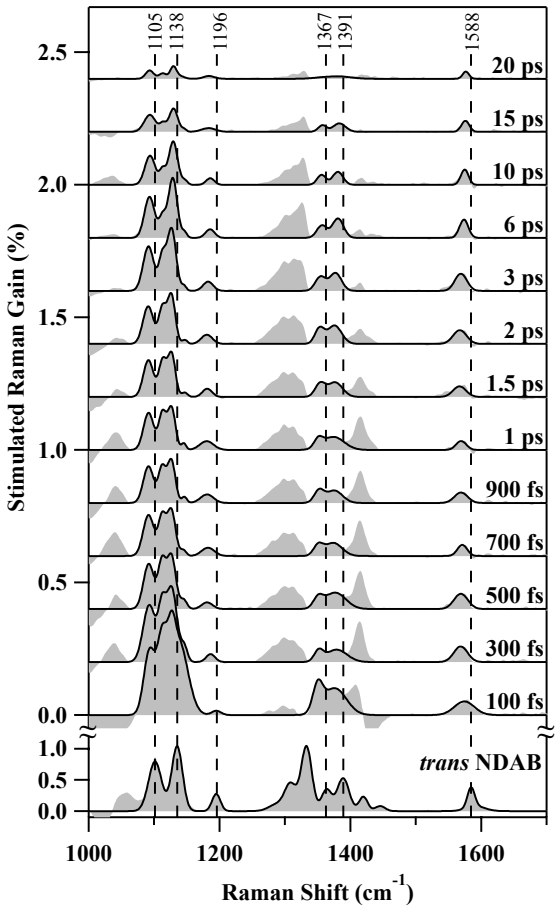

Figure 4.6: Time resolved FSRS spectra of NDAB in DMSO from 100 fs to 20 ps. A spectrum of the *trans* ground state is shown for reference. The spectra have had the ground state NDAB and solvent signals removed and have been offset for clarity. The ground state spectrum, taken under the same conditions as the excited state spectra, is shown for comparison. Fits to a sum of Gaussians are indicated by the thin black lines. Ground state peak positions are marked by the vertical dashed lines. λ_{ex} = 790 nm.

seen. This is not surprising because the *cis* isomer has small Raman cross sections even under pre-resonance conditions that weaken further at 790 nm as evidenced by the smaller amplitude of the initial decay component of the intensity. Furthermore, the high frequency C–N(Me)$_2$ mode is very weak in the *trans* isomer at λ_{ex} = 790 nm, see Figure 4.3b, and DFT calculations suggest that this is true for the *cis* isomer as well.

Figure 4.7b presents the N=N stretching mode kinetics. The amplitude response is quantitatively similar and the frequency response qualitatively similar to the NO_2 mode indicating that both dynamics result from the same process. The CN stretches, other than the 1110 cm^{-1} mode, have kinetics that follow a similar pattern to the NO_2 and N=N stretching modes and are not shown.

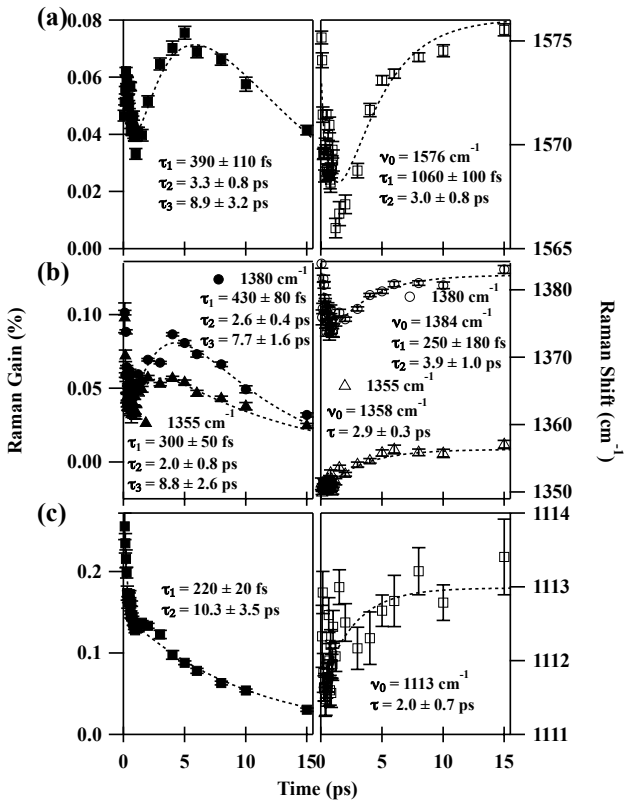

Figure 4.7: Time evolution of the (a) NO_2, (b) N=N and (c) CN stretching bands. Amplitudes (left) are shown with filled and frequencies (right) with empty markers. The 1110 cm^{-1} CN stretching mode has qualitatively different amplitude and frequency kinetics from the other bands indicating that it is due to the *cis* photoproduct. λ_{ex} = 790 nm.

Figure 4.7c shows the frequency and amplitude kinetics of the ~1110 cm^{-1} mode attributed to the *cis* photoproduct. The amplitude kinetic trace is a biphasic decay with τ_1 = 220 ± 20 fs and τ_2 = 10.3 ± 3.5 ps. The center frequency blue shifts slightly (2 cm^{-1}) with a time constant of 2.0 ± 0.7 ps. The amplitude time constants are consistent with those extracted for the 1632 cm^{-1} pure *cis* peak observed at λ_{ex} = 625 nm, suggesting that this peak is also due to the *cis* photoproduct.

4.5 Discussion

Time resolved structural data on the NDAB azobenzene derivative shed new light on the pathway of the photoexcited $trans \rightarrow cis$ isomerization. The Franck-Condon (FC) decay of the photoexcited *trans* isomer is identified, the bifurcation into separate *trans*/*cis* pathways on the excited state is revealed, and the subsequent relaxation is quantified. These temporally and structurally resolved observations allow us to propose a mechanism for the sequence of structural changes in

the $trans \rightarrow cis$ isomerization process for NDAB. This mechanism involves four different time regimes; each one revealing a different microscopic detail of the photoexcited reaction.

The shortest decay component, $\tau_1 = 400 \pm 80$ fs, due to fast FC decay is interesting because it has not been observed in previous studies on NDAB[34,35] or on similar push-pull azobenzenes.[111,112] Instead these earlier studies found a faster, ~100 fs, time constant which was not observed here; this discrepancy is likely because of the limited time resolution of our experiment and/or RINE interference. That being said, a similar time constant to τ_1 has been observed in earlier studies on the parent molecule, azobenzene.[38,39,109,118] In our work, τ_1 is observed in the amplitude kinetic traces for *all* modes at both excitation wavelengths. Furthermore, the RINE obscuring the early time excited state spectra taken when $\lambda_{ex} = 625$ nm decays at approximately the same rate. RINE[69] is an interfering process that leads to intense dispersive line shapes at ground state frequencies. As shown by McCamant, Kukura, and Mathies[69] the decay time of the RINE features is directly related to the movement of the excited state wave packet out of the FC region. Therefore, τ_1 is the time it takes for the photoexcited molecule to leave the FC region. This interpretation is consistent with the analysis of azobenzene's time-resolved fluorescence performed by Chang et al.[39]

The second time constant, $\tau_2 = 700 \pm 100$ fs, is specific to the formation of the *cis* photoproduct. This decay component is associated with three peaks in the FSRS spectra with $\lambda_{ex} = 625$ nm: ~900, ~1580 and ~1620 cm^{-1}. Of these, the C–$N(Me)_2$ stretch at 1632 cm^{-1} can be conclusively and uniquely assigned to the *cis* photoproduct after ~800 fs based on a comparison with the ground state *cis* spectrum. This mode decays to its final frequency, marking the end of the isomerization, with a time constant of τ_2. Considering that τ_2 is nearly the same as the S_1 lifetime, as measured by transient absorption and fluorescence,[34,35] we conclude that the isomerization occurs concurrently with the excited state decay. The frequencies of the other two peaks seen at $\lambda_{ex} = 625$ nm also change with a time constant of τ_2 and are thus assigned to the *cis* photoproduct.

At $\lambda_{ex} = 790$ nm, most modes correspond directly to ground state peaks. The one exception is the CN mode that appears near 1110 cm^{-1} and has kinetics similar to the *cis* modes observed at $\lambda_{ex} = 625$ nm. The appearance of this novel intense CN stretching/bending mode with a unique frequency not found in the ground state could indicate a distortion about the CNN angle and/or the CNNC dihedral. Such a distortion should relax the selection rules thereby enhancing the Raman intensity. Of the two possible deformations, torsion of the CNNC dihedral is unsupported based on the fact that the N=N stretching frequencies never deviate more than 10 cm^{-1} from the ground state values (see Figure 4.7b), suggesting that the double bond and associated π-system remain intact. However it must be noted that the excited state olefinic stretching frequency increases in stilbene[23] even though rotation is the only possible isomerization mechanism.

The third time constant, $\tau_3 = 2.3 \pm 0.7$ ps, is related to the formation of the vibrationally excited ground state *trans* photoproduct based on the analysis of the NO_2 and C–$N(Me)_2$ peaks. In the conventional model of photoisomerization, the population bifurcates at the conical intersection (CI) which occurs at an excited state minimum and a ground state maximum. Based on this model the *trans* isomer is expected to appear as the excited state species decays, i.e. the decay of the transient absorption/fluorescence, but this is not the case, in fact $\tau_3 > 2\tau_2$. Furthermore, τ_3 does not change with Raman excitation wavelength meaning that slower appearance of the *trans* photoproduct is not due to a difference in resonance conditions. One explanation is that the reactive and unreactive

populations split on the excited state and reach the seam at different times. However, it is more likely that the ground state PES near the CI on the reactant side is unstructured and relatively flat meaning that the un-reactive population must dissipate its excess vibrational energy in order to return to the harmonic regime of ground state PES and generate sharp vibrational features. Thus, τ_3 is equivalent to the time the system takes to reach the harmonic ground state well from the S_1/S_0 CI.

Finally, $\tau_4 = 8 \pm 2$ ps a time constant that has been observed in most ultrafast studies of azobenzene or its derivatives and can be best explained in terms of vibrational cooling. Hamm, Ohline, and Zinth[36] and Fujino and Tahara[37] have explored this kinetic extensively for azobenzene. Koller et al.[35] also found this time constant in NDAB with both vibrational and electronic probing. The data presented here are consistent with this picture.

A possible model that integrates and explains all of these observations is presented in Figure 4.8. To begin the reaction, an actinic pulse generates a population on the excited state surface. Under the influence of this new potential the population leaves the FC region within 400 fs evolving primarily along the CNN bending coordinate (ϕ_{CNN} in Figure 4.8) thus breaking the symmetry about the NN double bond while leaving the π-system and N=N bond strength mostly intact. This structural dynamic is consistent with the appearance of a new intense CN stretching mode and the lack of a significant change in the N=N stretching frequencies. In 800 fs, the continuing dilation of ϕ_{CNN} brings the two phenyl groups closer together. In order to minimize this growing interaction, the molecule begins to distort along the CCNN/NNCC and the CNNC dihedral angles – represented collectively as T in Figure 4.8. During this time a seam is reached between the two surfaces and the population crosses to the ground state. A small fraction quickly completes the isomerization along the torsional (T) and bending (ϕ_{CNN}) coordinates, as indicated by the red line on the bottom of Figure 4.8, while the major portion backtracks along the CNN bending coordinate from the CI to the reactant well forming the vibrationally excited *trans* in 2-3 ps which cools within 6-10 ps to the initial *trans* reactant state completing the photo-cycle.

Previous experimental results partially support this mechanistic interpretation. Fujino and Tahara[37] also observed that there was no significant change in the N=N stretching frequency and interpreted it as evidence for maintained planarity during the reaction and thus an inversion mechanism. Resonance Raman studies on azobenzene[40] and NDAB[116] predicted the conserved strength of the N=N double bond and planarity of the molecule as a whole with the largest FC displacements occurring in the CNN bend and CN and NN stretches. In addition, previous experimenters have observed a time constant similar to τ_2 in multiple azobenzene systems[34,36,108,111] and assigned it to the S_1 lifetime. However, all of these studies used electronic probing and therefore have been unable to determine the reaction mechanism. An exception is the study by Chang et al.[39] who found that the fluorescence anisotropy decayed much faster in hexane than ethylene glycol leading the authors to surmise that the rotation pathway was dominant in hexane but the inversion pathway was dominant in ethylene glycol.

Since all the structural evidence[37,40,116] points to an inversion dominated mechanism for azobenzene isomerization, it is surprising that most current theoretical studies[41–44] show rotation to be the preferred or, in most cases, dominant mechanism. On the other hand, more recent semi-classical simulations[45,47] have acknowledged the likelihood of a mixed, rotation/inversion, mechanism. For

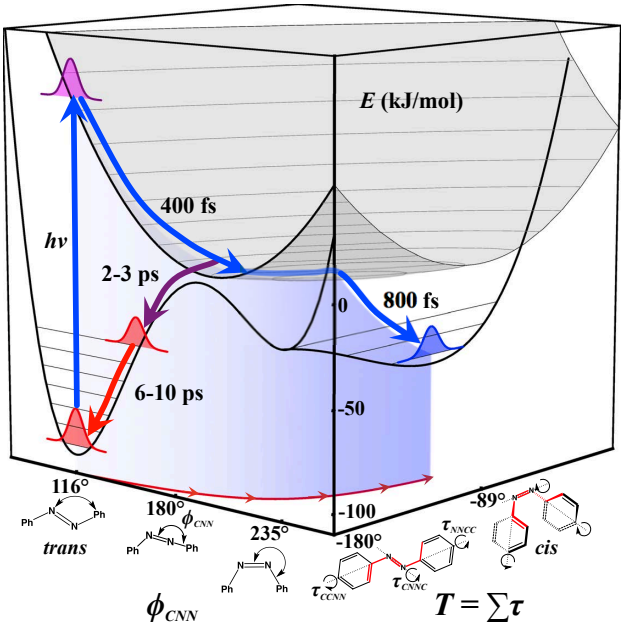

Figure 4.8: Schematic potential energy surface for the photoinitiated $trans \rightarrow cis$ isomerization of 4-nitro-4'-dimethylamino- azobenzene (NDAB). The bottom black curve represents the S_0 surface while the higher gray one represents the S_1 surface. The CNN bending coordinate is shown on the left of the figure and is represented by the CNN angle (ϕ_{CNN}). The collective torsional coordinate is shown on the right and is represented by the sum of the CCNN, CNNC and NNCC dihedral angles ($T = \tau_{CCNN} + \tau_{CNNC} + \tau_{NNCC}$). The hypothetical reaction coordinate is indicated by the red projection. The initially prepared wave packet quickly leaves the Franck Condon region, within 400 fs, through dilation of ϕ_{CNN}. Near the 180° point the population meets an S_1/S_0 seam and bifurcates. A small portion continues forward along the bending coordinate (ϕ_{CNN}) and a combination of phenyl torsional motions (T) to the *cis* product state effectively completing the reaction within 800 fs. The remainder moves back along ϕ_{CNN} and appears as vibrationally excited reactant on the ground state surface after 2-3 picoseconds. The hot ground state reactant continues to cool in the *trans* potential well for the next 6-10 picoseconds.

example, Tiberio et al.[45] found that at least 2/3 of their trajectories followed a mixed mechanism. The caveat being that the dividing line between "mixed" and "pure" is subjective, evidenced by the fact that approximately 30% of the trajectories counted as "pure" just reached the chosen dividing line. Furthermore, they have noted that for the "mixed" trajectories, torsion is followed by inversion, which is inconsistent with the data presented here. Even though the time scales used in the dynamical simulations were short, on the order of picoseconds, they were long enough for the reaction to be completed and the system to return to the ground state in all cases. Conversely, Conti, Garavelli, and Orlandi[44] found that while rotation was the minimum energy pathway (MEP), the PES they generated is relatively flat along the CNN bending coordinate meaning that an MD simulation with finite temperature and solvation effects may reveal that other slightly higher energy

CIs, including one with $\phi_{CNN} = 170°$, could contribute strongly, a possibility noted by the authors. Clearly, the gap between the experimental structural data and theory still stands to be closed.

In conclusion, we have detailed the photoreaction of an azobenzene derivative with the unprecedented structural and temporal resolution offered by FSRS. These capabilities have allowed the distinct evolution of both the reactive and un-reactive photoproducts to be experimentally separated and analyzed yielding two different time constants for the formation of the ground state *trans* and *cis* photoproducts. In addition, the appearance of a new CN stretching mode unique to the excited state with different intensity and frequency kinetics along with the preserved strength of the N=N bond suggests that the initial movement out of the FC region is along a low frequency CNN bending coordinate followed by collective CCNN, CNNC and NNCC torsional motions that effect isomerization. Finally, the reaction is quickly completed along these torsions and the CNN bend. These data provide a precise reaction time and and mechanism that will be a useful benchmark for testing future simulations.

Acknowledgements

Financial support was provided by the Mathies Royalty Fund and the Berkeley Fellowship for Graduate Study. DPH is indebted to Mark Creelman for his introduction to the FSRS instrumentation and thanks Kathy Durkin and Jamin Kraminsky of the Molecular Graphics and Computation Facility for assistance (NSF CHE-0840505).

Chapter 5

Low Frequency Resonant Impulsive Raman Modes Reveal Inversion Mechanism for Azobenzene

This was reprinted with permission from "Low Frequency Resonant Impulsive Raman Modes Reveal Inversion Mechanism for Azobenzene" by David P. Hoffman, Scott R. Ellis and Richard A. Mathies (2013)
The Journal of Physical Chemistry A **117**, 11472–11478.

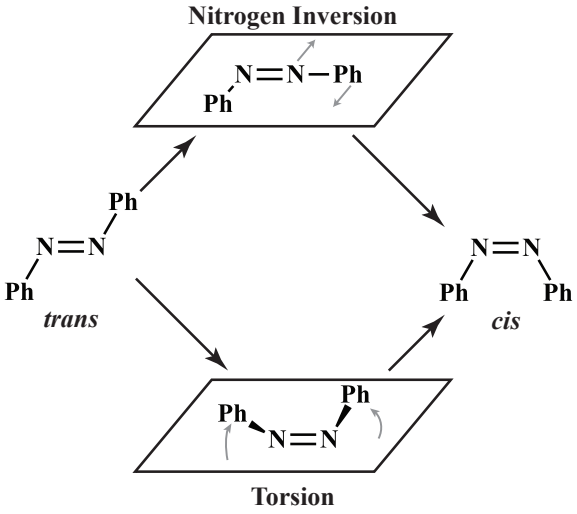

Figure 5.1: Two Canonical Isomerization Pathways Available to Azobenzene. The in-plane inversion mechanism linearizes the CNN bond while in the torsional mechanism the phenyl rings rotate out of the plane.

5.1 ABSTRACT

Azobenzenes are versatile photoswitches that find application in optical memory, light-driven motors, and molecular gating. Despite many studies, the molecular details of their light induced *trans* to *cis* isomerization are still debated. To inform this discussion we probed the low frequency skeletal motions in an azobenzene derivative, 4-nitro-4'-dimethylamino-azobenzene (NDAB), with resonant impulsive stimulated Raman spectroscopy (RISRS). Four previously unobserved modes at 14, 47, 150, and 201 cm^{-1} were found. Of these, the ~50 cm^{-1} inversion motion and the ~15 cm^{-1} torsional motion had particularly large intensities, suggesting that the excited state potential energy surface is steeply sloped along these coordinates in the Franck-Condon region. These data support a model in which NDAB isomerizes predominantly along a prompt inversion coordinate as well as a slower torsional motion that mitigates the phenyl-phenyl interactions on the pathway to the isomerized product.

5.2 INTRODUCTION

Azobenzenes are prototypical photoswitches based on the $trans \rightarrow cis$ photoisomerization about their N=N double bond.[101] Because of this photoinduced change in molecular shape, azobenzenes find many practical applications in information storage,[101,102] in molecular,[99] even macroscopic,[119] motors, and in imparting photosensitivity to molecular and biological systems allowing their study and control by optical means.[100,103,120–122] However, the precise mechanism underlying the $trans \rightarrow cis$ photoisomerzation is still intensely debated despite decades of both experimental[24,29–40] and theoretical[41–48] research.

Unlike stilbene,[123] the isomerization in azobenzene can involve motion along a combination of two orthogonal coordinates: a stilbene-like rotation about the central double bond or inversion about one of the nitrogen centers, see Figure 5.1. Azobenzene and its derivatives generally have excited state lifetimes in the subpicosecond regime and the reaction is thought to be significantly completed on the excited state surface. Many efforts have been made to determine the contribution of each of these two canonical mechanisms, especially ultrafast transient absorption studies in the visible[30–34] and IR regions.[35,36] Chang et al.[39] argued on the basis of dissimilar time-resolved emission anisotropies in solvents with different viscosities that azobenzene isomerized via inversion in viscous solvents and via rotation in nonviscous solvents. A time-resolved photoelectron spectroscopy study identified two nearly degenerate $\pi \rightarrow \pi^*$ states in *trans*-azobenzene and concluded, with the aid of electronic structure calculations, that the reaction proceeds by inversion.[38] Stuart and co-workers supported the inversion hypothesis with a resonance Raman (RR) study of azobenzene.[40] However, a resonant impulsive stimulated Raman spectroscopy (RISRS) study suggested that the reaction coordinate must be a more complex multidimensional combination of rotational and inversional coordinates.[33] In contrast, a recent femtosecond stimulated Raman spectroscopy (FSRS) study[24] of the 4-nitro-4'-dimethylamino-azobenzene derivative found no evidence of a weakened N=N bond and reasoned that the reaction coordinate must be primarily inversional.

The focus of this study, NDAB (Figure 5.2, top), belongs to the "push-pull" class of azobenzenes so-called because the electron-donating dimethylamino group on one end "pushes" electron density into the π system while the electron-withdrawing nitro group on the other "pulls" electron density out of it. The absorption spectrum of NDAB in DMSO, presented in Figure 5.2, shows that this alteration of the electronic structure strongly red shifts the $\pi \rightarrow \pi^*$ transition relative to that of azobenzene, which also gains charge transfer character as evidenced by its strong solvatochromism. In DMSO, this transition is centered at 500 nm and is 4,800 cm^{-1} wide. Push-pull azobenzenes, such as NDAB, are particularly important for light induced patterning of thin films[110] and also offer several experimental advantages such as a high extinction coefficient, a red-shifted absorption maximum and an extremely fast (μs-ms) $cis \rightarrow trans$ thermal reversion.

RISRS[124–132] of NDAB was chosen for this study because it allows one to experimentally determine the slope of the excited state potential energy surface (PES) in the Franck-Condon (FC) region, particularly along low-frequency normal modes. In the RISRS process, the actinic pump promotes a wave packet to the excited state which then evolves for some time before a second coupling brings it back to the ground state. Because the transient wave packet is no longer a vibrational eigenstate of the electronic ground state an oscillating ground state absorbance results, which can be most effectively probed where the ground state absorbance has the steepest slope, in this case at 547 nm.[127] Additionally, the excited state slope dictates the amount of wave packet distortion along a particular mode and thus the magnitude of its ground state oscillations. For reactions that are especially fast, the pathway out of the FC region provides a good indication of the entire reaction coordinate.[133] Previous authors have successfully used such data to investigate the early motions involved in the isomerization of *cis*-stilbene[134] and the retinal chromophore in bovine[133] and bacterial[127] rhodopsin. RR intensities of azobenzene have also been reported but with limited coverage of the important very low frequency modes.[40]

Here we focus on directly probing the large-scale low frequency skeletal motions that constitute

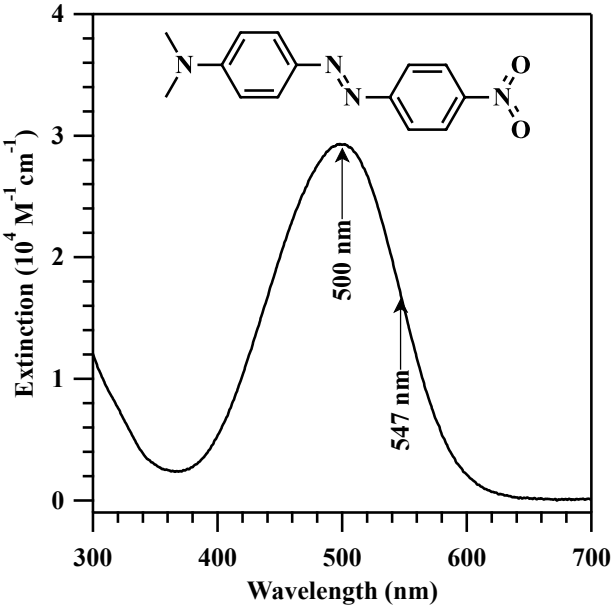

Figure 5.2: Structure of 4-nitro-4'-dimethylamino-azobenzene (NDAB) and absorption spectrum in DMSO. Arrows indicate the absorption maximum and where the slope of the absorption spectrum is greatest.

the excited state isomerization reaction coordinate in NDAB with RISRS. Two low frequency motions, assigned by electronic structure theory to the in-plane inversion and the out of plane phenyl torsion about the central CN bonds, are observed to have large intensities and consequently large excited state slopes in the FC region. These data suggest that initial motion out of the FC region is primarily along an inversion coordinate with additional, slight, phenyl torsional motions.

5.3 Materials and Methods

5.3.1 Sample Preparation

Solutions of NDAB (Tokyo Chemical Industry, > 98.0%) in dimethylsulfoxide (DMSO, EMD, 99.9%) were prepared at 3 and 0.03 mM for the Raman and RR, respectively, and at 0.47 mM for the RISRS experiments. For the spontaneous Raman experiments, the solutions were flowed through a 1.5 mm diameter capillary at a rate of ~2 mL/min using a peristaltic pump. For the RISR experiments, sample solutions were circulated through a 500 μm thick cell with 200 μm quartz windows (Starna Cells, 48-Q-0.5-UTWA) from a 40 mL sample reservoir.

5.3.2 Spontaneous Raman

The sample was excited with 6 mW at each of the following wavelengths: 456, 477, 488, 496, and 514 nm from an Ar^+ laser (Spectra Physics, 2020-05); 532 nm from a laser pointer; 647 nm from a Kr^+ laser (Spectra Physics, 2020-11); and 773 nm from a titanium sapphire laser (Lexel Lasers, 479). A photoalteration parameter of 0.06 was calculated assuming a photoisomerization quantum yield of 10% ($\Phi_{t\rightarrow c}$ = 0.10). Scattered intensity was collected in the 90° geometry using a double subtractive spectrograph (Spex, 1401). Spectra were imaged on a liquid-nitrogen-cooled CCD (Roper Scientific, LN/CCD 1100) and corrected for the wavelength dependent instrument response of the CCD and the self-absorption of the sample.

5.3.3 Resonant Impulsive Stimulated Raman

To generate the pump and probe pulses, the output of a Ti:sapphire regenerative amplifier ($\lambda_{\max}$ = 790, fwhm = 60 fs, 900 μJ/pulse, 990 Hz, B. M. Industries, alpha/1000us) was split into two beams. One beam was focused onto a 3 mm sapphire window (ThorLabs) generating a broadband continuum which was subsequently compressed with a prism compressor[84] using two 25 mm BK7 equilateral dispersing prisms (CVI Melles Griot). The separation between prisms was adjusted such that the chirp was minimal between 510 and 570 nm. A home-built noncolinear optical parametric amplifier (NOPA) was pumped with the rest of the fundamental. For the NOPA, a portion of the beam was doubled to 395 nm to form the pump while the remainder is used to generate a continuum seed. The pump and seed beams were combined in a BBO crystal (Red Optronics) cut for Type I phase matching forming the actinic pump (500 nm, fwhm = 400 cm^{-1}, 150 nJ/pulse). An F2 prism pair (ThorLabs) was used to compress the actinic pump.

The beams were polarized parallel to the table and simultaneously overlapped both spatially and temporally in the sample after being focused by a 100 mm fl achromatic lens (ThorLabs). The noncolinear geometry allowed the pump to be spatially filtered with an aperture after the sample. The probe was then recollimated and directed to a spectrograph (Instruments SA, HR320) which dispersed the beam onto a CCD detector (Princeton Instruments, PIXIS 100F). Phase-locked chopping of the actinic pump at half the repetition rate of the amplifier allowed for the collection of transient absorption (TA) spectra, which was calculated as $-\log(Probe_{\text{pump on}}/Probe_{\text{pump off}})$, without the need for an independent reference spectrum as probe fluctuations, shot-to-shot, were on the order of 1 mOD. The time delay between pump and probe was adjusted by a computer controlled delay stage (Melles Griot, Nanomotion II). Each individual transient absorption matrix consists of 426 time delays equally spaced by 20 fs. Time delays were averaged over 1000 laser pulses (500 TA spectra). A total of 28 matrices were collected and averaged for each data set. The wavelength axis was calibrated using a neon lamp as a standard. The instrument response function (IRF) was measured by the optical Kerr effect in the sample cell filled with the solvent (see Figure C.1 in Appendix C). Data collection is automated with LabVIEW (National Instruments).

5.3.4 Data Analysis

Transient absorption data were corrected for chirp using the IRF; the data at each wavelength were shifted in time by linear interpolation. Chirp corrected data were then integrated in the region of interest. Slowly varying population dynamics were removed by fitting the data after 200 fs to a sum of three exponentials using a trust-region Levenberg-Marquardt ordinary least-squares method. Residuals from the fit were modeled as the sum of damped cosinusoids using a linear prediction with singular value decomposition (LPSVD) algorithm[135–137] which recasts what is nominally a nonlinear least-squares problem into a linear one ensuring that the solution is globally optimum. All data analysis was performed using IGOR Pro 6.3 (Wavemetrics).[138]

5.3.5 Density Functional Theory (DFT)

Theoretical calculations were performed using standard DFT routines, the B3LYP functional, the 6-311++G(D,P) basis set, and the integral formalism variant polarizable continuum model to represent the solvent, DMSO, as implemented in the Gaussian 09 software package.[117]

5.4 Results

Figure 5.3 presents the dispersed TA of NDAB in DMSO in the 510-570 nm region after excitation at 500 nm with time delays from −500 to +4000 fs. At early times strong ground state bleaching is observable on the blue edge of the spectrum while slight transient absorption is visible on the red edge of the spectrum. The evolution of NDAB's TA in toluene[34] and DMSO[35] at low time resolution, with time delays out to tens of ps, has been analyzed in detail previously; our data agrees well with those earlier reports. However, here we focus on the previously unobserved impulsively excited coherent oscillations, which are clearly visible in Figure 5.3, particularly in the contour lines.

Figure 5.4, top, presents the time evolution of the band integral between 541 and 554 nm of the TA shown in Figure 5.3 (dotted line). Integration in this region ensures the highest possible signal-to-noise ratio for the coherent oscillations as it has been shown, both theoretically and experimentally,[127] that coherently excited ground state vibrations most strongly modulate the TA intensity where the ground state absorption spectrum has the greatest slope. Data earlier than 200 fs are strongly affected by cross phase modulation between the pump and probe, which can be seen as the sharp intense features around a delay of zero, and are therefore not included in the subsequent analysis. Slowly varying population dynamics are modeled as the sum of three exponential decays and a constant offset (solid line). Of the three exponentials included, the largest one corresponds to the bleach and the two smaller components correspond to the excited state decay. Previous authors[34,35] have found that the excited state signal decays with two or more components, depending on the study and the solvent. Presented in the bottom panel of Figure 5.4 are the residual oscillations after subtraction of the population dynamics (dotted line) which are modeled as a sum of eight exponentially damped cosinusoids (black line). Three of these components with frequencies of 394 ± 13, 347 ± 14, and 292 ± 10 cm^{-1} can be assigned to the solvent, DMSO, based

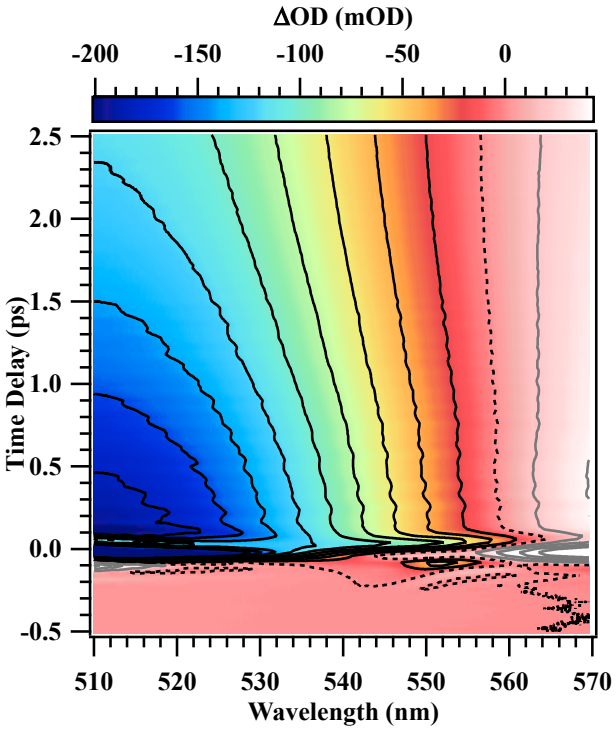

Figure 5.3: Contour plot of the transient absorption of NDAB in DMSO from −0.5 to +4 ps following excitation at 500 nm. Data have been corrected for chirp in the probe. Black lines indicate a negative ΔOD, gray lines indicate a positive ΔOD, and the dotted line indicates a ΔOD of zero. Coherent oscillations are clearly visible in the contour lines.

on data collected on the pure solvent (not shown) and comparison to literature values[139] of 382, 333, and 309 cm^{-1}. The residuals from the LPSVD fit are displayed below the oscillatory data as a second dotted line.

Figure 5.5 presents a comparison of the frequency domain representation of the RISRS signal (middle), the RR data using an excitation wavelength of 496 nm (top), and a theoretical calculation (bottom). RR features less than ~100 cm^{-1} are obscured by Rayleigh scattering. Complete RR data including the high frequency region, spectra at multiple wavelengths and a quantitative intensity analysis are available in Appendix C. The indicated uncertainties on the LPSVD model parameters are calculated as the Cramér-Rao bound.[137] The RR spectrum displays three modes below 250 cm^{-1}, a very weak one at 207 cm^{-1} and two strong bands at 179 and 156 cm^{-1}. Fits to Lorentzian line-shapes are shown as dotted lines. Similarly, the RISRS spectrum has strong bands at 201 ± 12 and 150 ± 20 cm^{-1}. Interestingly, the RISRS data does not precisely mirror the RR data as would be expected from theory. In particular, the relative intensities of the ~150 and ~200 cm^{-1} mode in the RR spectrum are the reverse of those in the RISR spectrum. Attempts to model three modes in this region, in either the time or frequency domains, failed to improve agreement with the RR data and resulted in a sharp increase in the uncertainty associated with the model

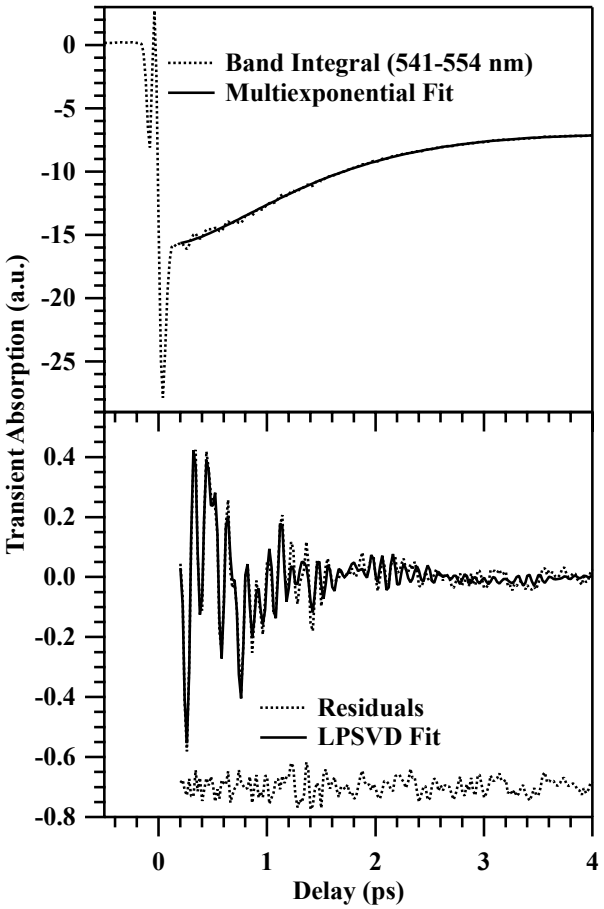

Figure 5.4: Band integral from 541 to 554 nm of the TA in Figure 5.3 is shown at the top as the dotted line. A multiexponential fit after a delay of 200 fs is shown as the solid line. Residuals are shown in the bottom panel as the dotted line along with the LPSVD fit which is shown as the solid line. A second dotted line below shows the residuals of the LPSVD fit.

parameters. In addition, due to the lack of Rayleigh interference in the time-domain measurements, two additional modes, one at 47 ± 11 and another at 14 ± 12 cm^{-1}, are only visible in the RISRS data. The position and intensity of the ~15 cm^{-1} mode are extremely sensitive to how the population dynamics are modeled; however, this mode is present regardless of the method of analysis. Black arrows indicated the correspondence between the DFT calculations and the experimental data. Note that while the calculated intensities are indicative of which modes have large polarizabilities, no resonance effects are included in the calculation. Therefore, these assignments are based on a combination of frequency and intensity.

Figure 5.6 presents the calculated normal motions associated with the observed low frequency modes.* The lowest frequency, ~15 cm^{-1}, motion corresponds to an out of plane twist of the phenyl

*An animated version is available online at http://pubs.acs.org/doi/suppl/10.1021/jp408470a/suppl_file/

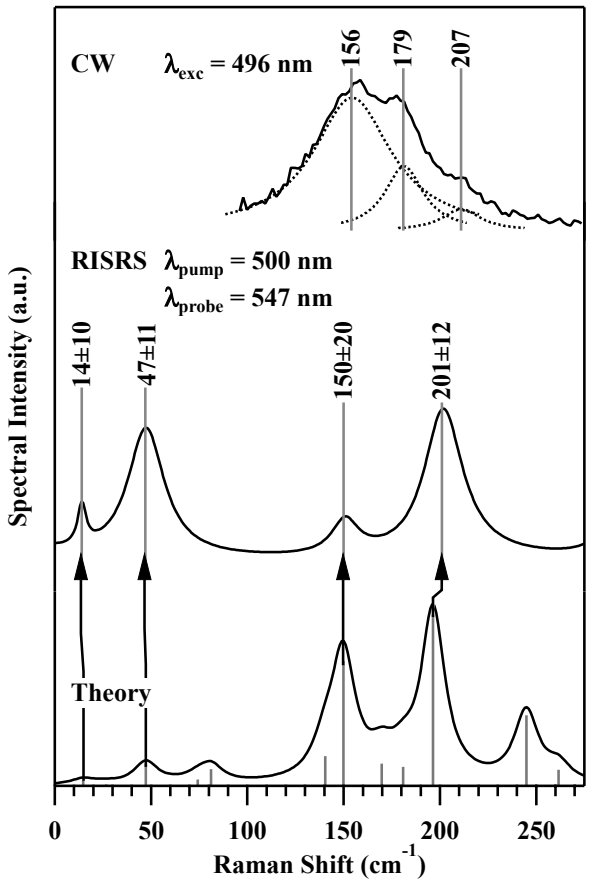

Figure 5.5: Comparison of the RISRS data in the frequency domain reconstructed from the LPSVD fit (middle) with the RR (top) and DFT calculations (bottom) at the B3LYP/6-311++G(D,P) level including a polarizable continuum model for the solvent, DMSO. Included with the RR data are dotted curves representing a fit to three peaks. There is good agreement between theory and the RISRS data, corresponding peaks are indicated by arrows. The discrepancy between the RISRS and the RR data is discussed in the text.

rings about the central C−N bonds. The ~50 cm^{-1} mode corresponds to an in-plane CNN bend of the entire molecule about the central C−N=N−C moiety. The two higher frequency motions are similar to each other and can be described as an in-plane compression of the molecule, with the two phenyl rings moving toward each other along parallel, nonintersecting, lines. The important difference between these modes and the ~50 cm^{-1} mode is that in the ~50 cm^{-1} mode the phenyl rings and the attached substituents move together in a sweeping motion while in the higher frequency motions the attached substituents move in the opposite direction of the phenyl rings.

jp408470a_si_002.mov.

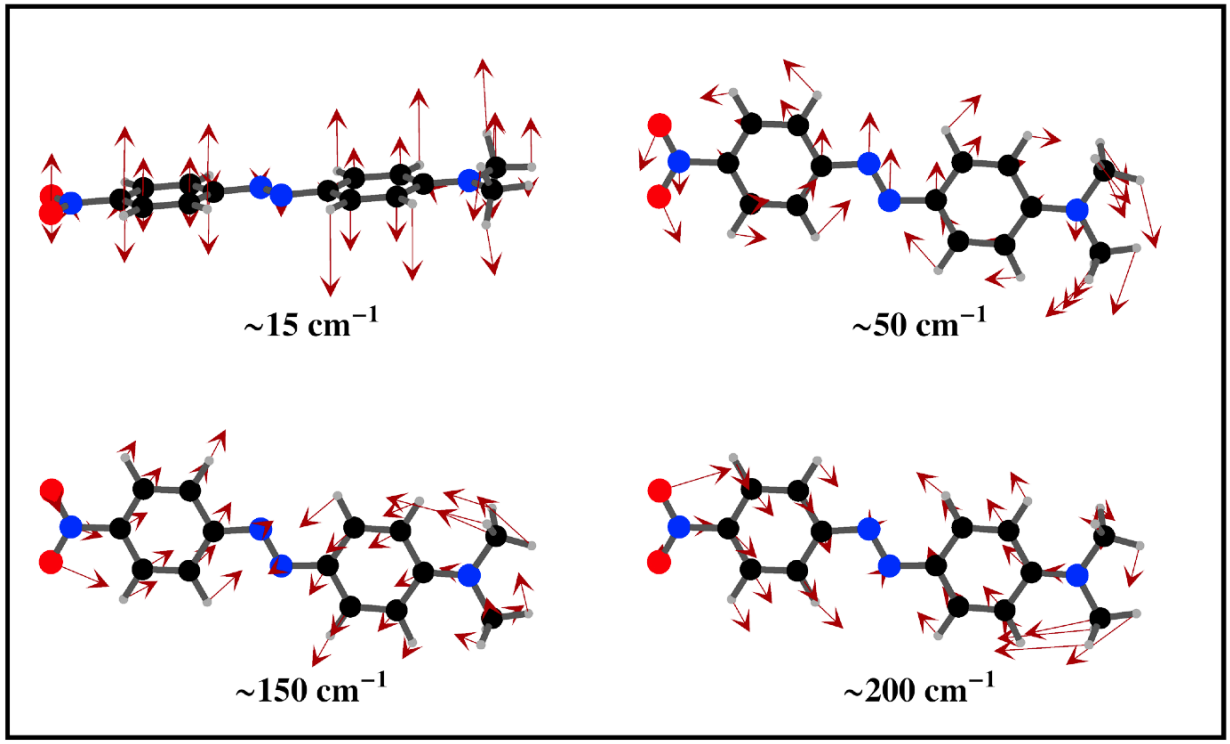

Figure 5.6: Character of the highly displaced normal modes detected by RISR. The ~50, ~150, and ~200 cm^{-1} modes are in-plane inversional motions of the phenyl rings. The ~15 cm^{-1} mode is a torsional motion of the phenyl rings about the central C–N bonds. The vectors denote mass weighted displacements.

5.5 Discussion

We have exploited the unique capabilities of RISRS to study the low frequency excited state dynamics in NDAB, an azobenzene analog. Four previously undetected low frequency normal motions were observed. An in-plane inversion mode at ~50 cm^{-1} has a particularly large intensity indicating that the excited state surface is steeply sloped along that coordinate. Combined with the lower frequency torsional band observed at ~15 cm^{-1}, these motions provide key information supporting a predominantly inversion pathway out of the FC region.

RISRS is theoretically similar to RR because in both cases the magnitude of the excited state slope in the FC region is the fundamental parameter that primarily determines the intensity of the ground state Raman[124,125,127,140] A high RR vibrational intensity implies a steep PES slope that produces significant evolution of the ground state nuclear wave packet $|i(t)\rangle$ when it is propagated on the excited state potential. The resulting overlap of $|i(t)\rangle$ with the final state of the Raman process $|f\rangle$ along a Raman-active mode results in the Raman intensity. For RR the propagation time of $|i(t)\rangle$ on the excited state is controlled only by the electronic dephasing time while for RISRS it also depends on the actinic pump duration. This difference is the reason that shorter pulses in

RISRS de-enhance low wavenumber modes and, in fact, a delta function pulse would result in no signal whatsoever within the Condon limit. Using effective linear response theory,[141,142] which is an approximation to the general third order response theory,[67] Kumar et al. have confirmed this effect showing that the amplitude of each impulsively excited ground state vibration depends on the width of the actinic pulse relative to the mode's frequency. RISRS intensities also depend on the actinic pump chirp.[131,143] For instance, a negatively chirped pump will enhance RISRS intensities; however, each frequency will be enhanced differently for a given amount of chirp. Actinic pump chirp may explain why the RR and RISRS intensities observed here do not agree exactly. It is also possible that excited state coherences are interfering with the measurement; however, such interference should be negligible in the probed region, which was chosen to maximize the ground state contributions. Disagreements between RR and RISRS data have been observed in myoglobin[129] and triiodide.[143] In the case of triiodide the 145 cm^{-1} antisymmetric stretching mode that is clearly observable in the RR spectrum is absent in the RISRS spectrum while for myoglobin the 304 cm^{-1} RR mode was red-shifted by ~20 cm^{-1} in the RISRS experiment. These differences are similar in magnitude to what is observed here for NDAB.

The observed ~50 cm^{-1} mode is associated with the normal motion depicted in the upper right-hand corner of Figure 5, which consists solely of an in-plane inversional motion of the phenyl rings and their attached substituents. We modeled the ~50 cm^{-1} mode using the dynamic wave packet theory developed for RR[140] by assuming that its absolute cross-section is approximately equal to 0.8 times the combined cross sections of the 156 and 179 cm^{-1} modes observed in the spontaneous Raman spectrum. Two different models for the excited state surface were used: a harmonic and a linear potential both of which predicted an FC slope of ~300 cm^{-1}, which is equivalent to a dimensionless displacement[140] of the harmonic ground and excited state minima (Δ) of 6 (see Appendix C for details). For reference, previous authors have modeled the five torsional modes of rhodopsin with ~200 cm^{-1} slopes[133] and the twist degree of freedom in *cis*-stilbene with a 785 cm^{-1} slope.[134] The fact that the ~50 cm^{-1} motion has a large slope and is relatively isolated leads us to believe that it constitutes the bulk of the reaction coordinate. Other motions may assist in leaving the FC region toward the conical intersection on the excited state but only in a limited fashion. It should be noted that the wave packet only propagates on the upper surface for the duration of the actinic pump, which in this case is ~60 fs; thus, our measurement of the excited state slope only directly probes the dynamics up to that time.

The ~15 cm^{-1} mode which is predicted to be a phenyl torsional motion (upper left panel of Figure 5.6) is also of reactive importance. It is important to note that this is not rotation about the N=N bond. Instead this mode consists of both phenyl rings twisting about central C−N bonds in opposite directions. In our earlier paper, we hypothesized that such motions must exist in order to alleviate the phenyl-phenyl interactions that occur at the end of the classical inversion mechanism.[24] These new data indicate that the torsional motion is initiated at the *beginning* of the reaction, concurrently with the start of the inversion. An animation is available online[†] which presents a view of NDAB propagated along the predicted excited state reaction coordinate, treating the 47 cm^{-1} mode as having a linear dissociative excited state slope of 282 and the 14 cm^{-1} mode as having a harmonic

[†]Video available at http://pubs.acs.org/doi/suppl/10.1021/jp408470a/suppl_file/jp408470a_si_003.mov

excited state surface with a frequency equal to the ground state and a Δ of 6. This video shows that the molecule approaches a distorted *cis*-like structure within the ~700 fs excited state lifetime of the molecule.

Our proposed mechanism differs from a building consensus in the theoretical community that azobenzene isomerizes through a torsional motion about the nitrogen double bond.[41–48] Normal modes corresponding to these proposed motions are observed in the RR spectrum of NDAB in dioxane at 281 and 319 cm^{-1} (see Appendix C) but the estimated Δ's are less than 0.25. Furthermore, no such modes were observed in the RR study[40] of azobenzene, indicating very small displacements along these modes. Thus we find little experimental evidence to support the rotational hypothesis. It will be interesting to see whether theory can accurately reproduce the experimental FC slopes for the phenyl rotational and inversional modes reported here.

In conclusion, we have used the low frequency Raman intensities revealed by RISRS to deduce the initial low frequency motion that makes up the excited state *trans* to *cis* photoisomerization reaction coordinate in NDAB. Because we are looking at ground state coherences, the RISRS intensities indicate how far the excited state wave packet moves along a particular coordinate while the actinic pump is incident on the sample, in this case ~60 fs. Because the ~50 cm^{-1} inversion-like mode has a particularly large slope in the FC region as indicated by its large RISRS intensity, we believe it forms the major component of the reaction coordinate. We also observed a lower frequency motion corresponding to the phenyl groups twisting out of plane; this motion is necessary to alleviate the phenyl-phenyl interactions in the nascent *cis* isomer. Finally, we find no evidence for the theoretically proposed stilbene-like torsion about the central N=N bond. These data add to a growing body of experimental evidence[24,37,39] that NDAB and other azobenzenes photoisomerize in the condensed phase via an inversion mechanism. Furthermore, this result illustrates the vital importance of multidimensional probing of low frequency motion for understanding condensed phase molecular reactions.

Acknowledgments

Funding was provided by the Mathies Royalty Fund. DFT calculations were performed with the support of the National Science Foundation grants CHE-0233882 and CHE-0840505. We thank David Valley for his programming help and Anne Myers Kelley for her resonance Raman intensity analysis code.

Chapter 6

Electron Transfer Dynamics of Triphenylamine Dyes Bound to TiO_2 Nanoparticles from Femtosecond Stimulated Raman Spectroscopy

6.1 Abstract

Interfacial electron transfer between sensitizers and semiconducting nanoparticles is a crucial yet poorly understood process. To address this problem, we have used transient absorption (TA) and femtosecond stimulated Raman spectroscopy (FSRS) to investigate the photoexcited dynamics of a series of triphenylamine-coumarin dye/TiO_2 conjugates. The TA decay is multiexponential, spanning time scales from 100 fs to 100 ps, while the characteristic transient Raman spectrum of the radical cation decays biexponentially with a dominant 3 ps component. To explain these observations, we propose a model in which the decay of the TA is due to hot electrons migrating from surface trap states to the conduction band of TiO_2 while the decay of the Raman signature is due to internal conversion of the dye molecule. Furthermore, the S_1 Raman spectrum of TPAC3, a dye wherein a vinyl group separates the triphenylamine and coumarin moieties, is similar to the S_1 Raman spectrum of *trans*-stilbene; we conclude that their S_1 potential energy surfaces and reactivity are also similar. This correlation suggests that dyes containing vinyl linkers undergo photoisomerization that competes with electron injection.

6.2 Introduction

Photoexcited electron transfer across an organic/inorganic interface is a crucial, efficiency-determining step in many important processes such as photocatalytic water splitting[144] and dye-sensitized photocurrent generation.[145] In all cases, a light-absorbing dye is used to "sensitize" an inexpensive semiconductor such as titanium dioxide. This strategy allows for the generation of reactive conduction band electrons with visible light, thereby exploiting a significant part of the solar spectrum. These processes for generating reactive electrons have been intensely studied with particular attention to both photochemical pathways and material properties that lead to efficient photoexcited electron transfer. To date, there are several key aspects of these processes that remain unknown. For example, the rate and yield of the direct recombination of photogenerated electrons and molecular cations at the interface are unclear, and the effects of the dye binding modality and conjugation length on charge separation are poorly understood.

If the energy level alignment between the dye and TiO_2 is appropriate, population of the S_1 state of the dye via photoexcitation will lead to subsequent electron injection, presumably into the conduction band of the TiO_2, though it has been suggested that surface trap states could also be involved.[146] Electrons in the conduction band are then available for further reactions or, in the case of dye-sensitized solar cells (DSSCs), collection at an electrode. Two criteria must be met to maximize the yield of the downstream reactions: first, injection efficiency must be maximal, and second, the lifetime of injected electrons in the conduction band must be as long as possible, which means that the efficiency of the reverse reaction (i.e., recombination)[147] must be minimal. In order to design systems that meet both of these criteria, a mechanistic understanding of both electron injection and recombination is necessary.

In general, electron injection occurs on the ultrafast time scale, while recombination can occur on a multitude of time scales ranging from picoseconds to microseconds. In the case of ruthenium

and other metal-containing dyes, injection from the singlet state occurs in ~100 fs and injection from the triplet state is on the order of picoseconds.[148] On the other hand, for metal-free dyes, the injection step is on the order of 10 fs or less and has nearly 100% transfer efficiency.[149–152] Thus, most studies of metal-free systems have focused on the recombination of the injected electrons and molecular cations.

Transient absorption (TA) spectroscopy[148,151–158] has been the method of choice for measuring ultrafast kinetics of photoexcited interfacial electron transfer (ET). Most,[152–156] but not all,[151] reports have concluded that the multiexponential (picoseconds-microseconds) decay observed in the TA is due to the recombination of electrons and holes, meaning that the recombination rate, and therefore the overall efficiency of charge separation, can be predicted. To obtain less ambiguous information on ruthenium- and iron-based dyes, the Lian group has performed a series of studies combining visible and, more species-specific, mid-IR TA.[148,158,159] However, experiments probing both the photoexcited electronic and structural dynamics have yet to be conducted on systems with metal-free dyes.

Organic dyes often contain linked donor and acceptor moieties to broaden their absorption in the visible region, and they are bound to the semiconductor surface through coordinating, acidic functional groups. Of all the dyes synthesized thus far, those containing triphenylamine (TPA) have been the most promising, achieving up to 8% power conversion efficiency in photovoltaics.[160] However, the effect that dye structure has on ET is still not fully understood. It is hypothesized that placing the hole localizing TPA moiety farther from the semiconductor surface may help keep charge carriers separate, thereby slowing down recombination. Additionally, the binding group can influence electron injection and recombination; She et al.[158] found that ruthenium dyes using phosphonic acid binding groups to bind to TiO_2 displayed slower injection than those bound through carboxylic acids.

To interrogate the interfacial ET in TPA-dye-sensitized particles with structural specificity, we use femtosecond stimulated Raman spectroscopy (FSRS) in conjunction with concurrent NIR (830-940 nm) TA.[21] FSRS has the unique ability to provide Raman vibrational spectra with femtosecond time resolution over a broad bandwidth. For example, FSRS has been used to probe the multidimensional reaction coordinate of green fluorescent protein[20] and to elucidate the ultrafast structural mechanisms of isomerization in azobenzene[24] and stilbene.[23] More recently, FSRS was used to study charge transfer between coumarin 343 and TiO_2[113] and within donor-acceptor molecules.[91,161]

In this report, we use FSRS to study the dye/semiconductor interface exploring the effect of different binding moieties and conjugation lengths on interfacial ET and the internal relaxation processes of both the dye and the nanoparticle. Discrepancies between the TA kinetics and the vibrational dynamics of the dye cation suggest that an alternative interpretation of the TA decays of these systems is necessary. Furthermore, the observed excited state structures for extended conjugation systems reveal an unexpected loss mechanism via photoisomerization of the dye.

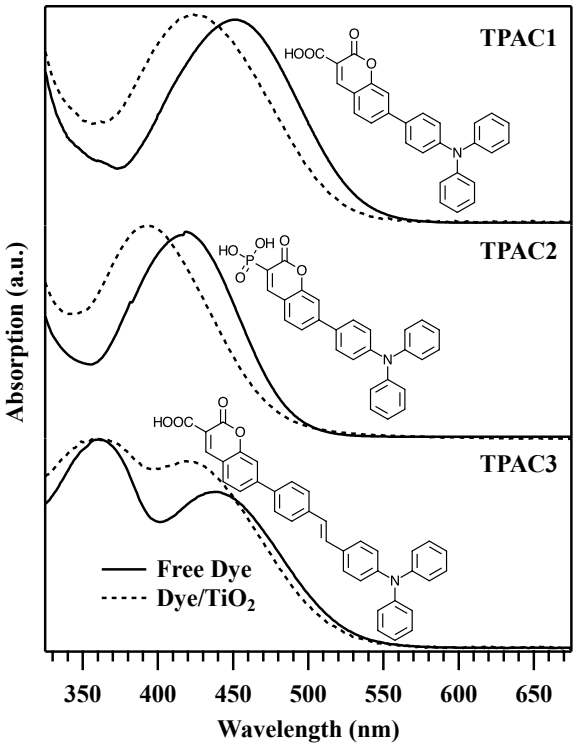

Figure 6.1: Structures and steady-state absorption spectra of TPAC1 (top), TPAC2 (middle), and TPAC3 (bottom) for both free dye (solid lines) and dye-nanoparticle conjugate (dotted lines) samples.

6.3 Materials and Methods

6.3.1 Sample Preparation

The detailed synthetic routes, preparation procedures, and characterization of the triphenyl-amine-coumarin dyes (TPACs, depicted in Figure 6.1), nanoparticles, and conjugates can be found in Appendix D and are thus only briefly summarized here.

The coumarin portion of the TPACs was synthesized from 4-bromosalicylaldehyde and diethylmalonate or triethyl phosphonoacetate via the Perkin reaction for TPAC1/3 and TPAC2, respectively. The triphenylamine was stannylated to enable subsequent Pd-catalyzed Stille cross-coupling with the bromo-functionalized coumarin fragments to provide the ester-protected TPAC1 and TPAC2. For TPAC3, the vinylphenyl linker was added to the triphenylamine using a previously reported Wittig olefination procedure.[162] The ester-protected TPAC3 was synthesized in a similar manner to TPAC1 and TPAC2 via Stille cross-coupling of the stannylated triphenylamine vinylphenyl fragment to the bromo-functionalized coumarin. Cleavage of the respective ester protecting groups provided the target acidic TPACs. Anatase titania particles were synthesized by base hydrolysis of titanium(IV) isopropoxide in methanol and characterized by transmission elec-

tron microscopy (TEM). The titania nanoparticles ($d = 89 \pm 16$ nm) were functionalized using a standard mass transfer technique; particles were suspended in a 10 mg/mL dye solution (5:1 $CHCl_3$:MeOH) with a 90-fold excess of the dye and heated at 50° C for 16 h. The conjugates were then repeatedly washed with a $CHCl_3$/MeOH mixture to remove residual free dye molecules. Final samples were prepared by resuspending the conjugates in $CHCl_3$ for photophysical studies.

^{1}H and ^{13}C NMR spectra were obtained in chloroform-d, unless otherwise noted, with a Bruker AVB-400, AV-500, or AV-600 instrument. ^{13}C NMR spectra were measured with a proton-decoupling pulse program. Chemical shifts (ppm) were calibrated to the residual peak of the deuterated solvent. Data from high-resolution mass spectrometry (HRMS) using electrospray ionization (ESI) were obtained by the UC Berkeley QB3 mass spectrometry facility. Elemental analysis (CHN) was performed by the UC Berkeley microanalysis laboratory.

6.3.2 Femtosecond Stimulated Raman Spectroscopy

FSRS measurements were carried out on samples of the TPAC dyes and their conjugates in $CHCl_3$ with optical densities ranging from 0.45 to 2 per mm at 395 nm. The sample was agitated throughout the measurement in a 1 mm cuvette (Starna Cells, 21-G-1) using a small piece of stainless steel wire (diameter = 0.018 in.) as a stir bar inside the cuvette and a magnet attached to a dc motor as the actuator.

The FSRS instrument has been described in detail elsewhere.[80] Briefly, a regenerative Ti:sapphire amplifier (BMI, alpha/1000us) with a repetition rate of 1 kHz generates 900 μJ pulses at 790 nm with a duration of 60 fs. This beam is split to generate the three pulses necessary for FSRS. The actinic pulse (λ_{max} = 395 nm, 80-150 nJ/pulse) is generated by frequency doubling the laser fundamental in a 1 mm BBO crystal. The Raman pulse (λ_{max} = 790 nm, 10 cm^{-1} fwhm, 0.1-2 μJ/pulse) is generated by spectrally filtering the laser fundamental with a grating filter. The continuum probe pulse (830-940 nm, ~10 nJ/pulse) is generated by focusing a small portion of the laser fundamental into a 3 mm thick sapphire plate followed by compression in an F2 prism pair. The three pulses, all polarized parallel to the table, are focused in a planar noncollinear geometry into the sample using a 100 mm focal length achromatic doublet. Parallel polarization allowed for the highest signal-to-noise ratio. Because of the comparative nature of this study and the size of the nanoparticles used, rotational reorientation is not expected to significantly alter our results and conclusions. After passing through the sample, the actinic and Raman pulses are spatially filtered by an aperture, while the probe is recollimated with a 100 mm lens and dispersed by a spectrograph (Instruments SA, HR320) onto a front-illuminated CCD (Princeton Instruments, PIXIS 100F) synchronized to the amplifier such that each pulse can be recorded separately. Phase-locked chopping of the Raman pulse at half the repetition rate of the amplifier allows for collection of Raman spectra without the need for a reference spectrum, as probe fluctuations are minimal (< 1%) on a shot-to-shot basis. Time-resolved FSRS spectra were collected by varying the time delay between the actinic pulse and the Raman/probe pulse pair using a computer controlled delay stage (Melles Griot, Nanomotion II). Ground-state spectra are obtained by intermittently shuttering the actinic pump. Each reported spectrum is the average of 20,000-120,000 individual spectra (40,000-240,000 laser shots). Data collection is automated with LabVIEW.

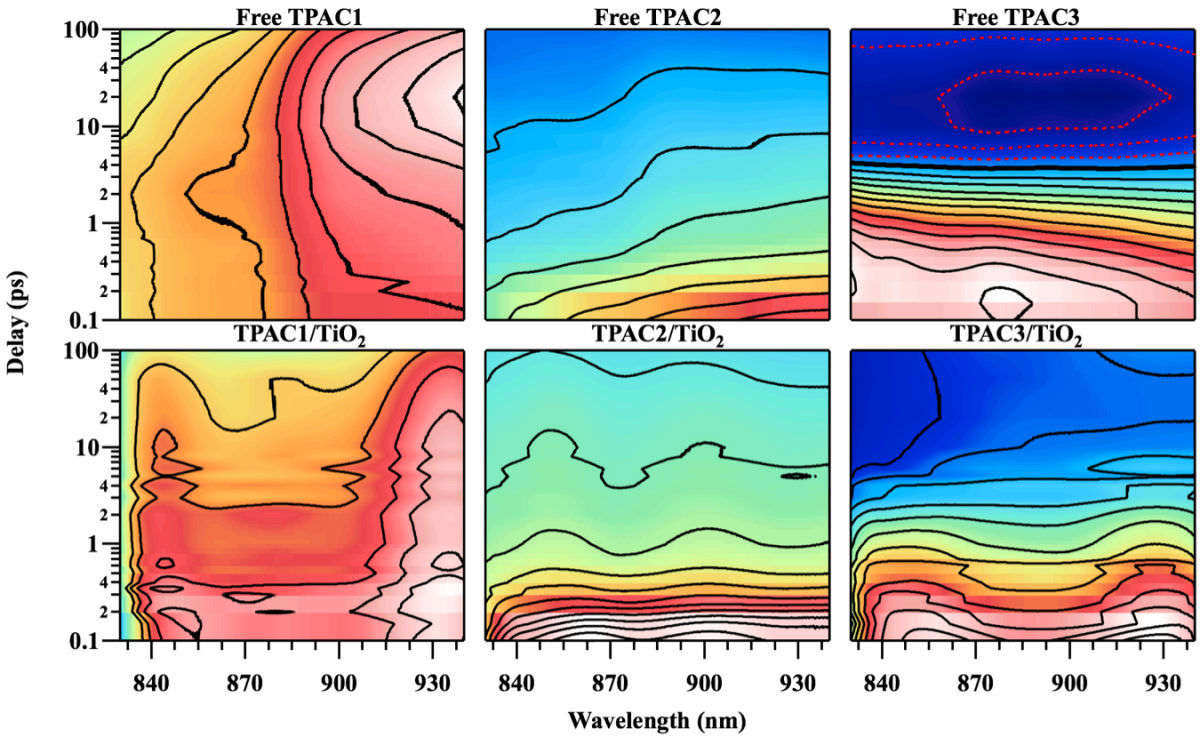

Figure 6.2: Contour plots of the transient absorption of the free (upper plots) and conjugated (lower plots) TPAC1 (left plots), TPAC2 (center plots), and TPAC3 (right plots). Thin solid lines indicate positive ΔOD, thick lines indicate a ΔOD of zero, and dotted lines indicate a negative ΔOD.

Transient difference Raman spectra have had the ground state and solvent signals removed after being normalized using the 669 cm^{-1} peak of $CHCl_3$ as an internal reference to correct for both fluctuations in the Raman pump energy and the sample's transient absorption. The energy axis was calibrated using cyclohexane as a standard. The instrument response function (IRF) was measured using the optical Kerr effect between the actinic and probe pulses in $CHCl_3$ in the sample cell; a typical value for the IRF was 140 fs fwhm. Example measurements are presented in Figure D.1.

6.4 Results

Absorption spectra of all dyes, both free and bound to TiO_2 nanoparticles, in chloroform are presented in Figure 6.1 along with their respective structures. TPAC1 and TPAC2 exhibit a single large absorption peak, assigned to a charge transfer (CT) transition that blue-shifts upon conjugation to the TiO_2 surface. The absorption spectrum of TPAC3 exhibits two peaks: the lower energy band is assigned to the CT transition, and the higher energy band is assigned to a delocalized $\pi \rightarrow \pi^*$ transition on the basis of DFT calculations at the B3LYP/6-311G++(d,p) level.[117] In contrast to the effect of titania conjugation on TPAC1 and TPAC2, the absorption spectrum of the TPAC3-TiO_2 conjugates broadens but does not blue-shift appreciably. This result is in agreement with

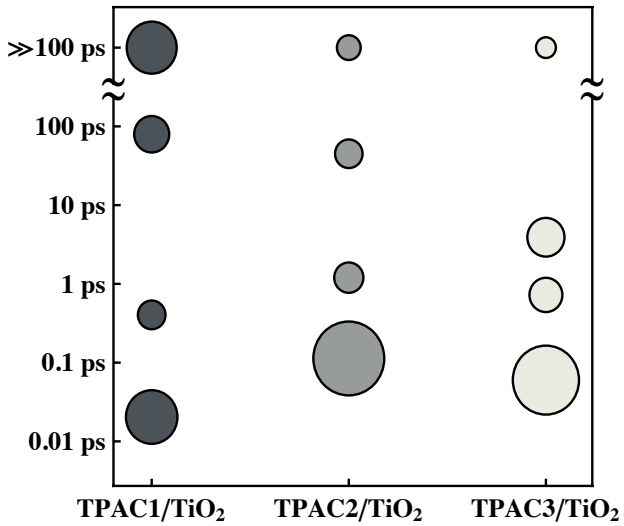

Figure 6.3: Summary of the TPAC/TiO_2 absorption transients integrated between 830 and 940 nm. The data are well modeled by a four-component exponential decay with the longest component fit as a constant offset. The vertical position of each bubble represents the time constant while the area represents the fractional amplitude of that decay component. See the text for details on the analysis and Figure D.2 for numerical data and fits.

previously reported spectra from structurally similar dyes.[154,156]

Presented in Figure 6.2 are the dispersed transient absorption (TA) spectra between 830 and 940 nm for the free dyes (top) and the bound dyes (bottom). Solid contour lines indicate positive ΔOD, thick lines indicate a ΔOD of zero, and red dashed lines indicate negative ΔOD. The TA of TPAC1 in this region is dominated by a single broad band that grows in at $\lambda > 930$ nm and blue-shifts slightly on the ~10 ps time scale. This band then decays in hundreds of picoseconds while simultaneously red-shifting. In contrast, the TA of bound TPAC1 has no rising component and displays two bands, one on either side of the observed region. Neither peak shifts appreciably. For TPAC2, the TA is dominated by a single decaying band. Upon binding, this band shifts to shorter wavelengths and splits into two barely discernible bands centered at ~855 and ~900 nm. Notably, the TA of TPAC3 changes from being absorptive early and emissive later to being always absorptive upon binding to TiO_2. It has been shown for TiO_2 thin films[163,164] that valence band electrons excited directly to the conduction band and to surface trap states absorb in this region. Other reports have assumed that electrons injected from photoexcited sensitizers into titania nanoparticles have similar spectral properties.[153–156] However, it is possible that the radical cation of the dye absorbs in this region as well, making unambiguous interpretation of the TA difficult.

In order to simplify the analysis of the TA and comparisons with previous reports,[153–156] the TAs of the conjugated dyes were integrated between 830 and 940 nm, and the resulting transients were fit to the sum of four exponentials convoluted with a Gaussian instrument response function of the appropriate width. The results of these fits, presented in Figure D.2, are summarized in Figure 6.3 as a bubble chart, where the center and area of each bubble indicate the time constant and

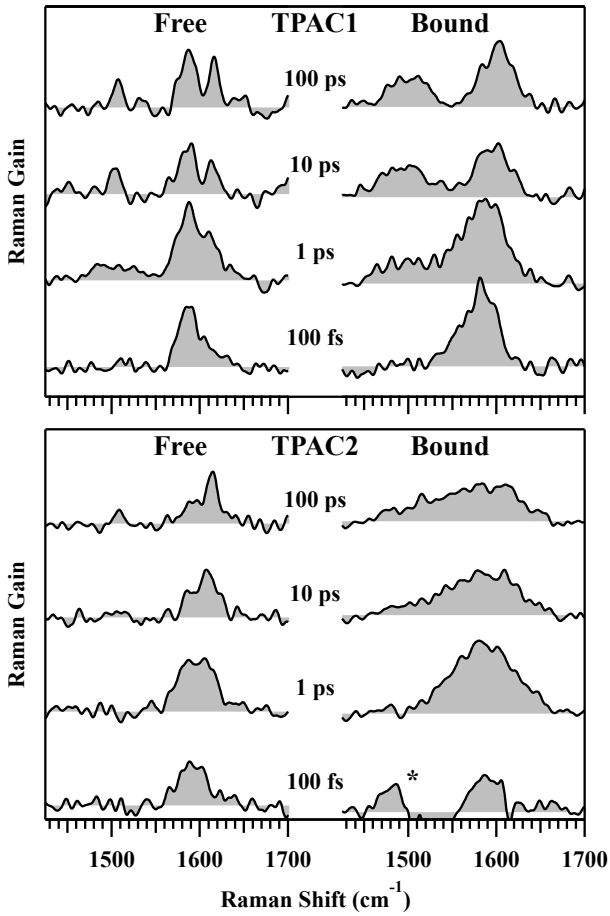

Figure 6.4: Transient stimulated Raman spectra of TPAC1 (top) and TPAC2 (bottom) in $CHCl_3$ at selected time delays. Free dye spectra are shown on the left, and conjugated dye spectra are shown on the right. For all spectra there is a delocalized C=C stretching mode located at ~1590 cm^{-1}. For the TPAC1/TiO_2 and TPAC2/TiO_2 samples there is another intense delocalized C=C mode located at ~1500 and ~1520 cm^{-1}, respectively. The asterisk marks the time-dependent solvent artifact due to impulsive excitation by the actinic pump.

fractional amplitude, respectively, of that decay component. TPAC1 has the slowest overall decay; the fast component, τ_1, constitutes a small portion of the decay when compared to the other dyes, and the second largest component (35%) is the slowest ($\tau_{long} \gg 100$ ps). Conversely, TPAC3 has the fastest and most complete decay; τ_1 is the largest component (60%), and τ_{long} only comprises 5% of the total intensity decay. Furthermore, τ_3 of TPAC3 is an order of magnitude shorter than that of the other dyes. TPAC2 exhibits a fast decay as well; τ_1 makes up 70% and τ_{long} 8% of the total decay.

Figure 6.4 presents selected transient stimulated Raman spectra of free and bound TPAC1 and TPAC2 in $CHCl_3$ (complete data are presented in Figures D.3/D.4 and D.5/D.6, respectively). All

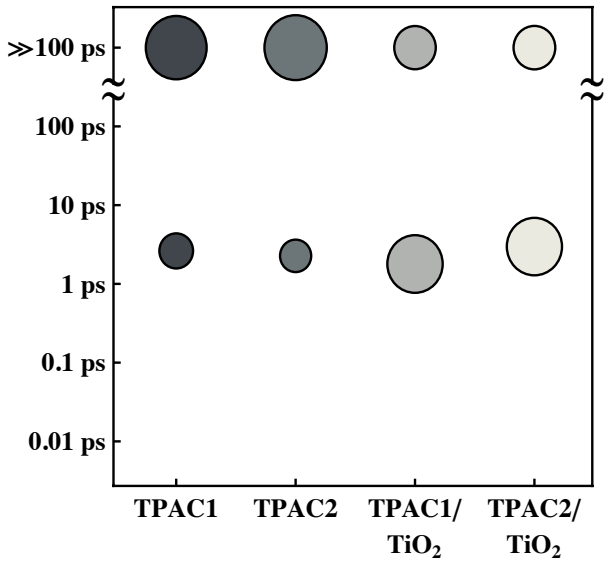

Figure 6.5: Summary of the intensity transients of the ~1590 cm^{-1} mode of TPAC1 and TPAC2 for both the free dyes and the conjugated dyes. In all four samples, the kinetics of the 1590 cm^{-1} mode are well described by an exponential function with two time constants: ~2.5 ps and one much greater than 100 ps. The vertical positions and areas of the bubbles represent the time constant and fractional amplitude of that decay component, respectively. See the text for details on the analysis and Figure D.8 for numerical data and fits.

spectra display an intense Raman mode near ~1590 cm^{-1}, which can be assigned to a delocalized C=C stretching motion along the conjugated backbone of the molecule. In the case of TPAC1, this stretching mode splits into two separate modes at longer times. Such behavior was not observed in the other samples, likely due to the fact that the free TPAC1 data were taken at a higher resolution than the others. Upon binding to the TiO_2 surface, a new transient appears in the 1500-1520 cm^{-1} region of the TPAC1 and TPAC2 spectra. Based on DFT calculations[117] of the radical cation, this mode can be assigned to another delocalized C=C stretching motion while the mode at 1590 cm^{-1} retains the same character as in the neutral molecule. A comparison of the observed spectra of the TPAC1 and TPAC2 conjugates at 100 ps and the predicted radical cation spectra is presented in Figure D.7.

In all instances the intensity of the ~1590 cm^{-1} mode can be well modeled by a biexponential decay (raw data and fits are available in Figure D.8). Model parameters are presented as a bubble chart in Figure 6.5. The shorter, accurately determined time constant is roughly the same for all samples at ~2.5 ps. Strikingly, the long time component represents nearly 75% of the decay for the free dyes but only ~40% of the decay for the conjugates. A direct comparison between Figures 6.3 and 6.5 shows that the transient Raman kinetics share little similarity with those of the TA; the decay of the TA is dispersive, when modeled by a multiexponential decay the extracted time constants span at least 4 orders of magnitude, while the transient Raman is best modeled by a biexponential decay.

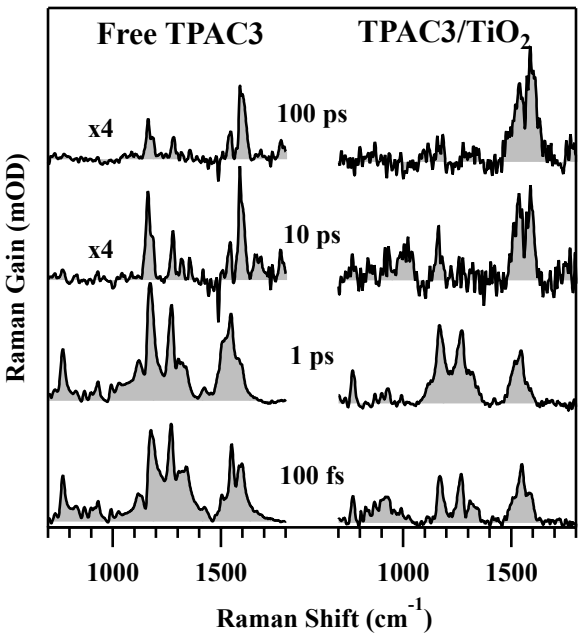

Figure 6.6: Transient Raman spectra of TPAC3 (left) and TPAC3/TiO_2 (right) at selected time delays. The band positions and intensities of the free and bound species are very similar.

Presented in Figure 6.6 are the transient Raman spectra of both free and bound TPAC3 in $CHCl_3$ (complete data are presented in Figures D.9/D.10). These spectra are rich in information containing many intense Raman modes over a wide range of frequencies. There is a notable similarity between the early time spectra for the free and bound dyes. While there appear to be slight differences at long times, the low signal-to-noise for the bound-dye samples makes baseline correction difficult, and therefore the significance of these deviations is hard to estimate. Noticeably, these spectra are nearly identical to those of photoexcited *trans*-stilbene.[23] A comparison of the S_1 Raman spectra of *trans*-stilbene[23] with free and bound TPAC3 3 ps after excitation is presented in Figure 6.7. Compared to the experiment performed by Weigel and Ernsting[23], our conditions are different: chloroform was used instead of hexane, probing was performed in the 830-940 nm region as opposed to the 605-695 nm region, and the sample was excited using a pulse centered at 395 nm versus one centered at 280 nm. Nevertheless, the band positions and intensities of photoexcited S_1 TPAC3 match those of photoexcited S_1*trans*-stilbene nearly quantitatively with two exceptions: a new peak in the TPAC3 spectra located at 766 cm^{-1} and a blue-shift of the olefinic CH deformation band to 1271 cm^{-1}. Other minor differences can be attributed to the higher resolution of the present experiment and different methods of baseline correction. In addition, the kinetic analysis of *trans*-stilbene[23] is consistent with those of both free and bound TPAC3, presented in Figure D.11. In brief, the intensities of the transient Raman bands as a function of time are best modeled by a short exponential rise and a picosecond exponential decay with a long time offset. Even though our analysis differs slightly from that performed by Weigel and Ernsting[23], the extracted

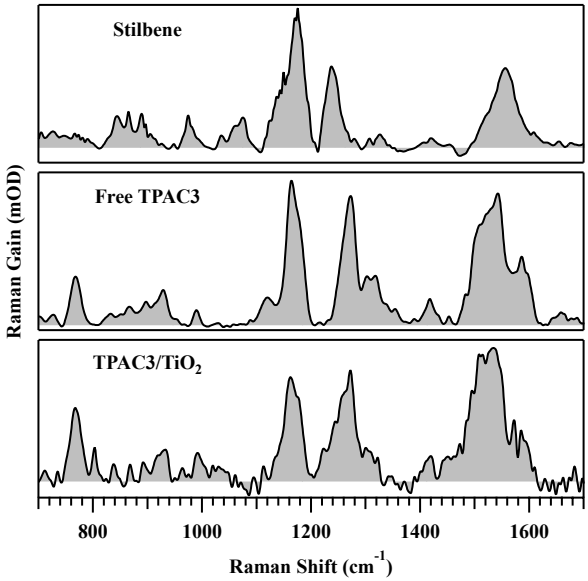

Figure 6.7: Comparison of the S_1 Raman spectra 3 ps after excitation of *trans*-stilbene in hexane, free TPAC3, and TPAC3 bound to TiO_2 in chloroform. Stilbene data were adapted from ref. 23.

time scales are comparable, 0.33 and 0.92 ps for *trans*-stilbene in hexane and 0.25 and 2 ps for TPAC3 in chloroform. The similarity between the excited-state potential energy surfaces (PESs) (as shown by the Raman spectra) and excited-state dynamics (as shown by the kinetic analyses) of *trans*-stilbene and TPAC3 suggests that they have similar photoreactivity-isomerization.

6.5 Discussion

Time-resolved vibrational and electronic data provide new information on the dynamics of electron transfer (ET) across a molecular/semiconductor interface. In overview, the vibrational data for TPAC1 and TPAC2 are inconsistent with the conventional interpretation of the TA, which directly relates the decay in the 830-940 nm region to the recombination of electrons and cations. The Raman kinetics of the radical cation are slower than and different in character from those of the TA, suggesting that the TA decay is reporting on another process. Additionally, the similarity between the excited state structure and ultrafast structural relaxation of TPAC3 with that of *trans*-stilbene suggests that isomerization of the vinyl linker competes *directly* with ET, reducing injection efficiency and photochemical stability for this system.

The analysis of the TA for dye-nanoparticle conjugates is difficult because it is hard to determine whether the signal is due to the dye, the nanoparticle, or the combined system. It has been shown[163,164] that surface trapped electrons, and to a much lesser extent bulk electrons, absorb in the region studied. However, as is evident in the top of Figure 6.2, the free TPAC dyes also absorb here. Previous reports[153–156,165] have assigned the TA decay in this region to the recombination of

electrons in TiO_2 with the molecular dye cations, assuming that the results for thin-film TiO_2[163,164] hold for nanoparticles. The dispersive nature of the decay was interpreted as being due to the heterogeneity of the particles' surface, leading to a distribution of recombination times.[153–156,165]

Comparing TPAC1 to TPAC2, we find that the TA decay is faster for TPAC2, a dye that binds to TiO_2 through a phosphonic acid instead of a carboxylic acid, than TPAC1. TPAC3, which has a longer π-conjugation length, exhibits a much faster decay than TPAC1. Within the previously outlined framework, these results would imply that the electron recombination rate should be fast for TPAC2 and faster for TPAC3. Therefore, the overall charge separation efficiencies of these two dyes are predicted to be lower than that of TPAC1.

In contrast, the evolution of the transient Raman spectra can be best described by a simpler set of two exponentials. For bound TPAC1 and TPAC2, the appearance of a new mode in the 1500-1520 cm^{-1} region of the long time spectra indicates the formation of the radical cation. If the TA decay was indeed related to the recombination of electrons and holes, then we would predict that a highly multiexponential evolution of the transient vibrational signal ranging from 100 fs to 100 ps should also be observed. We thus conclude that the TA decay is due to a process other than recombination, while the transient Raman tracks the oxidation state of the dye. If this interpretation is correct, it means that the recombination rates for both carboxylic and phosphonic acid bound dyes are much slower than 100 ps. The experimental time resolution of the present study was insufficient to determine the effect of different binding moieties on injection rates.

Unlike TPAC1 and TPAC2, the transient Raman spectra of TPAC3 show no clear evidence for the formation of the radical cation. However, the time-resolved vibrational spectra of the S_1 state of TPAC3 and of *trans*-stilbene[23] (see Figure 6.7) are very similar, indicating that the S_1 PESs, particularly in the region associated with the vinyl normal modes, of both species are nearly identical. This similarity is further supported by the approximate equivalence of the characteristic time scales for their spectral evolution: a 0.25 ps rise and 2 ps decay for TPAC3 and a 0.33 ps rise and 0.92 ps decay for *trans*-stilbene (see Figure D.11 and ref. 23, respectively). In *trans*-stilbene, this spectral evolution is due to vibrational cooling on the excited state and movement toward the S_1/S_0 conical intersection, which leads to isomerization. Because the shape of the PES determines chemical reactivity and because *trans*-stilbene and its derivatives are known to isomerize on the S_1 surface with up to 50% quantum yield,[166–168] these data suggest that TPAC3 also isomerizes. A previous scanning tunneling microscopy study[169] on triphenylamine- and ruthenium-based dyes presented cursory evidence that such isomerizations are possible. Similarly, it has been observed that the fraction of the *cis* isomer of an indoline-based dye sensitizer increased under irradiation[170] and that replacing a double bond with a nonisomerizing indene group increased DSSC efficiency by an average of 16%.[171] Furthermore, the high level of similarity between the transient Raman spectra and kinetics of TPAC3 and *trans*-stilbene suggests that the ultrafast structural relaxation of TPAC3 is dominated by the stilbene moiety and thus isomerization of the vinyl linker. It is likely that this process competes *directly* with charge separation, thereby reducing the efficiency and stability of the molecular dye responsible for electron injection. Vinyl linkers included in other dyes[145,151,153–156,172–174] are likely susceptible to this side reaction as well.

The vibrational data support a model for the TPAC dyes with slow electron recombination. This model is in agreement with studies on ruthenium-based dyes that have shown slow electron

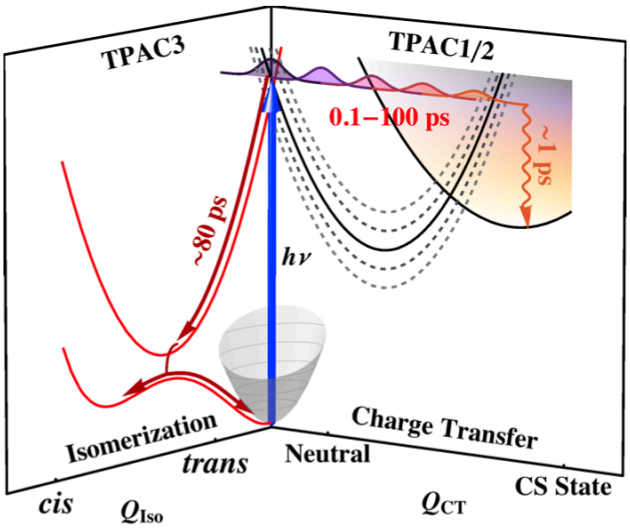

Figure 6.8: Schematic potential energy diagram showing the various processes occurring during and after electron injection from the dye to the nanoparticle. Absorption of a photon excites the system directly to a charge injection (CI) state formed from the LUMO of the dye and a surface trap state, shown as dashed lines on the right. The injection process leaves the electron with enough excess energy to be transferred into the charge-separated (CS) state, shown as the shaded curve. The CS state is one in which the dye has been formally oxidized and the electron resides in the conduction band (CB) of the titania. Heterogeneity in trap state energy levels leads to a variety of transfer rates resulting in dispersive kinetics. After transferring, the hot electron quickly internally converts to the bottom of the CS state. During this evolution the radical cation reorganizes along its internal degrees of freedom within ~2.5 ps. TPAC3 has a unique nonradiative pathway shown at left which represents the photoinitiated *trans* to *cis* isomerization about the C=C bond. This new process competes directly with electron injection, lowering efficiency and decreasing the photostability of the dye.

injection (0.1-1 ps) and much slower recombination (picoseconds-microseconds), in addition to studies of direct band gap excitation of TiO_2 thin films.[163,164] Furthermore, a visible TA study of aminophenyl acid sensitizers attached to TiO_2 thin films[151] found no evidence for subnanosecond charge recombination. In the case of the TPAC dyes, the TA decay could be due to electrons hopping from various surface trap states to the conduction band. The high level of heterogeneity in location and energy of the surface states throughout the sample may explain the multiexponential character of the TA decay. Within this new framework, the transient Raman tracks initial structural relaxation of the oxidized dye while transient absorption monitors the relaxation of electrons within the semiconducting material.

A model summarizing these observations is presented in Figure 6.8. Conjugation of the dye to the TiO_2 surface causes the LUMO of the free dye to rehybridize with the nearest surface trap state of TiO_2, creating a charge injection (CI) state, as shown by each of the dashed lines. Excitation

to this state causes electron injection on the ~10 fs time scale.[149,150] Because the injection process leaves a large amount of excess energy with the electron,[147,175] the hot electron can be subsequently transferred into the charge separated (CS) state, shown as the shaded curve. The CS state is one in which the dye has been formally oxidized and the nanoparticle formally reduced with the electron in the TiO_2 conduction band (CB). After entering the CS state, the electron cools rapidly, within 1 ps, through electron-phonon interactions.[176,177] The decay of the TA is due to electrons leaving the CI states and entering the CS state. Heterogeneity in trap state energy, and thus CI state energy, leads to highly multiexponential, dispersive, TA kinetics. More complete information on the distribution of trap state energies would allow for more sophisticated modeling of the system's dynamics and thus the TA decay. During this evolution, which is shown on the right as the charge transfer (CT) coordinate (Q_{CT}), the radical cation reorganizes along its internal degrees of freedom within ~2.5 ps, as tracked by FSRS. For TPAC3, there is a unique nonradiative decay pathway that is shown as the isomerization coordinate (Q_{Iso}) on the left. This pathway competes directly with the electron injection pathway, thereby degrading efficiency and stability.

In conclusion, we have investigated ultrafast interfacial electron transfer within a series of triphenylamine/coumarin dye-TiO_2 conjugates using both femtosecond transient absorption and stimulated Raman. The vibrational data are inconsistent with the common analysis of the TA, necessitating a new hypothesis in which the decay of the TA is attributed to hot electrons moving from the initially populated surface trap states to the conduction band and the picosecond process monitored by FSRS is the internal relaxation of the radical cation. Finally, our results indicate that the use of vinyl linkers as a means to extend π-conjugation in organic dyes for sensitizing semiconductors is deleterious because it introduces photoisomerization as an undesirable quenching mechanism.

Acknowledgments

This work was supported the U.S. Department of Energy, Office of Basic Energy Sciences, Division of Materials Sciences and Engineering, under Contract DE-AC02-05CH11231 and in part by the Mathies Royalty fund. DFT calculations were carried out with the support of the National Science Foundation Grant CHE-0840505, and M.S.C. thanks the Camille and Henry Dreyfus Postdoctoral Program in Environmental Chemistry for a fellowship.

Chapter 7

Characterization of a Conical Intersection in a Charge Transfer Dimer with Two-Dimensional Time Resolved Stimulated Raman Spectroscopy

A manuscript of the same name by David P. Hoffman, Scott R. Ellis, and Richard A. Mathies has been submitted to *The Journal of Physical Chemistry A*.

7.1 Abstract

Photochemical reactions are mediated by conical intersections (CI), which are difficult to directly probe and characterize. To gain insight into CIs, two-dimensional femtosecond stimulated Raman spectroscopy (2D-FSRS) is used to examine a model excited-state charge transfer (CT) complex consisting of an electron donor, tetramethylbenzene (TMB), and an acceptor, tetracyanoquinodimethane (TCNQ). Following impulsive excitation, the excited state transient absorption reveals strong excited state wave packet motion along low frequency modes, in particular TCNQ's totally symmetric 323 cm^{-1} CCN bend, which persist for ~5 ps. These low frequency coherences modulate the intensity and peak frequencies of the excited state FSRS vibrational spectra. In particular, large magnitude oscillations at 323 cm^{-1} are observed in the peak frequency ($\Delta\omega$ = 2 cm^{-1}) and intensity (ΔOD = 1.5 mOD) of the non-totally symmetric 1271 cm^{-1} C=C rocking mode. The magnitude of these oscillations is analyzed to determine the first order anharmonic coupling between the high and low frequency degrees of freedom in the excited state. The anharmonic coupling between the totally symmetric 323 cm^{-1} and the non-totally symmetric 1271 cm^{-1} modes is estimated to be in excess of 100 cm^{-1}, strongly suggesting that they are the tuning and coupling modes, respectively, for the CI that connects the CT excited state to the neutral ground state and controls charge recombination internal conversion.

7.2 Introduction

Conical intersections (CIs)[6,7] are ubiquitous features of photochemical reactions but by their very nature they are difficult to observe and characterize. CIs occur when two Born-Oppenheimer (adiabatic) nuclear potential energy surfaces (PES) are degenerate in energy. At and near this point, the electronic and nuclear degrees of freedom are strongly coupled. Due to the high dimensionality of phase space and the double cone topology of CIs, the system will be effectively trapped on the lower surface once it has "hopped" from the upper one. This efficient, fast and irreversible internal conversion lies at the heart of many important classes of photochemical reactions such as isomerizations, electron transfer and proton transfer.[178] Given the importance of CIs for understanding photochemistry, methods that directly characterize the nuclear motions that couple the electronic states are needed.

Charge recombination following photoinduced charge transfer in organic materials is a specific type of reaction where CIs play a major role. The fluorescence of these systems is very weak or undetectable[179] suggesting that internal conversion to the ground state is fast and efficient. For many materials, such as those used in photovoltaics,[180] this recombination is undesirable. An understanding of which structural changes promote charge separation and impede recombination may allow for the rational design of superior materials.

The model system explored here consists of an electron donor, tetramethylbenzene (TMB), and an electron acceptor, tetracyanoquinodimethane (TCNQ). When combined in solution they form a π-stacked molecular charge transfer (CT) complex; upon absorption of a photon an electron is transferred from the HOMO of the TMB to the LUMO of the TCNQ. The electron is trans-

ferred back to the TMB in a 10 ps process concomitant with internal conversion to the ground state. Charge transfer complexes have been extensively studied with resonance Raman spectroscopy[179,181–187] which offers insight into which modes are initially excited and promote the photoinduced charge separation. Most efforts at probing the ultrafast kinetics following FC relaxation have relied on pump-probe electronic spectroscopy[188–190] but these techniques do not have the energy resolution needed to provide direct evidence as to the precise nuclear rearrangements that mediate charge recombination.

To obtain the structural information necessary to characterize the CI responsible for charge recombination, we have used femtosecond stimulated Raman spectroscopy (FSRS) to study the TMB:TCNQ CT complex. FSRS offers the unique ability to record vibrational structural changes that occur faster than the vibrational dephasing time.[16–19,191] FSRS has been applied to a diverse range of systems such as rhodopsin,[19] GFP,[20] azobenzene,[24] charge transfer systems[25–27,49] and many others.[21,23,28,71] Prompted by earlier observations of time dependent oscillations in the vibrational frequencies of GFP[20] we sought an electron transfer system that might exhibit similar modulations. The observation of such oscillations would provide "two-dimensional" data that reports on the anharmonic coupling between different normal modes. Such 2D experiments have been attempted previously on neat solvents but have been plagued by 3rd order cascades,[192–194] which we have mitigated in this work (see Appendix E for details).

In this report we exploit the novel capabilities of 2D-FSRS to measure the anharmonic coupling between the totally symmetric 323 cm^{-1} CCN bending mode and the non-totally symmetric 1271 cm^{-1} C=C rocking mode of the TCNQ in the TMB:TCNQ CT complex. Transient absorption and resonance Raman measurements reveal that the 323 cm^{-1} CCN bending mode is strongly impulsively excited upon electronic excitation and its coherent wave packet motion persists for ~5 ps. Interestingly, these large amplitude low frequency motions modulate the intensities and frequencies of the other excited state Raman peaks; in particular the intensity and frequency of the 1271 cm^{-1} mode. Using theory developed here and elsewhere[73,75,193,195] the amplitudes of these oscillations are directly related to the anharmonic coupling between modes. CIs are formed by two key modes: a totally symmetric tuning mode that tunes the energy gap between the two surfaces and a non-totally symmetric coupling mode that distorts the nuclear symmetry allowing the different symmetry electronic surfaces to cross. The large anharmonic coupling between the symmetric 323 cm^{-1} and the non-totally symmetric 1271 cm^{-1} modes strongly suggests that they are the tuning and coupling modes, respectively, defining the CI that mediates charge recombination in the TMB:TCNQ charge transfer complex.

7.3 Materials and Methods

7.3.1 Sample Preparation

7,7,8,8-Tetracyanoquinodimethane (TCNQ, 98%, TCI America), 1,2,4,5-tetramethylbenzene (TMB, 99%, Sigma-Aldrich) and dichloromethane (DCM, 99.9%, EMD) were used as received. Excess TMB was necessary to solubilize the TCNQ and achieve the desired optical density of 0.15

OD per 1.5 mm and 0.7 OD per 500 μm at 530 nm for the spontaneous Raman and femtosecond stimulated Raman experiments, respectively. For stimulated Raman measurements the CT complex was formed in a solution of ~1 M TMB and 0.02 M TCNQ and for the spontaneous Raman experiments a solution of 33 mM TMB and 33 mM TCNQ was used. Solutions were filtered through a 0.45 μm Teflon filter.

The radical anion of TCNQ was prepared according to literature procedures.[196] Briefly, TCNQ (1 mmol) and $KI_{(s)}$ (2.5 mmol) were added to 10 mL of acetonitrile (99.9%, EMD) with stirring for 20 minutes at room temperature. After drying, the $TCNQ^{-}K^{+}$ salt formed as a purple powder with 88% yield. The product was subsequently recrystallized from acetonitrile. Solutions of the anion in acetonitrile were prepared and spontaneous Raman and steady state absorption measurements were performed immediately because the radical anion is known to slowly react with oxygen. Acetonitrile was used because the $TCNQ^{-}K^{+}$ salt is not soluble in DCM.

7.3.2 Spontaneous Raman

Samples were circulated through a 1.5 mm capillary tube at 2 m/s using a peristaltic pump and irradiated with 10 mW of 413, 514 and 647 nm light. The parallel polarized scattering was collected in the standard 90° geometry and focused onto the entrance slit of a 2 meter Spex 1401 double spectrograph. Spectra were imaged on a liquid nitrogen cooled CCD (Roper Scientific LN/CCD 1100). Spectra were corrected for self-absorption effects and cyclohexane was used to calibrate the Raman shift.

7.3.3 Femtosecond Stimulated Raman

The instrument has been described in detail previously.[80] Briefly, ultrashort pulses are generated by a homebuilt Kerr lens mode-locked Ti:Sapphire oscillator (30 fs, 5.3 nJ/pulse, 91 MHz) that seeds a Ti:Sapphire regenerative amplifier (B.M. Industries, Alpha 1000 US, λ_{max} = 790 nm, 70 fs, 0.9 mJ/pulse, 991 Hz) pumped by Q-switched Nd:YLF (B.M. Industries, 621-D). The fundamental output is split into three pulses. The actinic pump (λ_{max} = 530 nm, 60 fs, 150 nJ/pulse) is generated with a homebuilt noncolinear optical parametric amplifier (NOPA) and compressed by an F2 prism pair (ThorLabs). A portion of the fundamental is spectrally filtered and temporally shaped by a Fabry-Perot etalon (TecOptics, design A6) forming the narrow band Raman pump pulse (λ_{max} = 795 nm, 100 nJ/pulse, FWHM = 2.8 cm^{-1}).[197] The probe pulse (8 fs, 5 nJ/pulse, λ_{max} = 883 nm) is produced by generating a continuum in a 3 mm thick sapphire plate followed by temporal compression in a BK7 prism pair. Both the Raman pump and probe pulses are polarized parallel to the table. For short delay experiments the actinic pump is polarized parallel to the Raman beams for maximum signal to noise while for long delay experiments it is polarized at the magic angle to mitigate the effects of rotational diffusion on the kinetics. All beams are focused into the sample and overlapped both spatially and temporally.

After the sample, the probe pulse is isolated, re-collimated and directed into a spectrograph which disperses the beam onto a fast CCD (Princeton Instruments, PIXIS 100F). A phase locked chopper (Newport, 3501) blocks every other Raman pump pulse, allowing the Raman gain to

be calculated, shot-to-shot, as $\ln(Probe_{\text{Raman pump on}}/Probe_{\text{Raman pump off}})$. The shot-to-shot fluctuations of the probe are less than 0.1% circumventing the need for a reference beam. A computerized delay stage controls the timing between the actinic pump and the Raman pulse pair. Ground state stimulated Raman spectra are collected by intermittently shuttering the actinic pump. Near IR transient absorption spectra are calculated as $-\log(Probe_{\text{Actinic pump on}}/Probe_{\text{Actinic pump off}})$. All data collection and initial data processing is performed with a custom LabVIEW program.[98]

7.3.4 Data Analysis

Raman spectra have had the solvent contributions removed after appropriate averaging. For the spontaneous data the baselines were removed manually. For the time resolved stimulated Raman spectra the peaks and baselines were fit simultaneously across the following spectral regions, 750-900 cm^{-1}, 900-1850 cm^{-1}, 2130-2910 cm^{-1} and 2870-3030 cm^{-1}. A cubic polynomial was used to model the baseline in all regions except for the last one where a constant offset was used. All peaks were modeled with a Lorenztian line-shape except for the 1194, 1388 and 1599 cm^{-1} transitions, which were modeled with a dispersive Lorentzian, eq. 7.1.

$$I(\nu) = \frac{A + B\nu}{1 + \nu^2} \tag{7.1}$$

Here A is the intensity of the real part, B is the intensity of the dispersive part and ν is defined by eq. 7.2.

$$\nu = \frac{\omega - \omega_0}{\Gamma/2} \tag{7.2}$$

Where ω is the frequency, ω_0 is the frequency of the vibrational transition and Γ is the full width at half maximum (FWHM). The baselines in the intermediate spectral regions were removed manually for presentation.

To analyze the oscillatory components in the transient absorption and Raman data the slowly varying, exponential, population dynamics were removed using standard non-linear curve fitting to the appropriate exponential decay. The residual oscillatory signal was subsequently analyzed using a linear prediction with singular value decomposition (LPSVD) algorithm,[135–137] which converts the normally non-linear least squares problem of fitting the data to a sum of damped cosinusoids into a linear one, ensuring that the global optimum is found. Extracted model parameters are then converted into a frequency domain spectrum.

All data analysis is performed in IGOR Pro using custom developed procedures.[138]

7.4 Results

7.4.1 Electronic Probing of Charge Transfer Dynamics

Figure 7.1 presents the ground state visible absorption spectra of TMB (dotted line), TCNQ (dashed line), the complex (shaded curve) and the chemically generated TCNQ anion (solid line). The

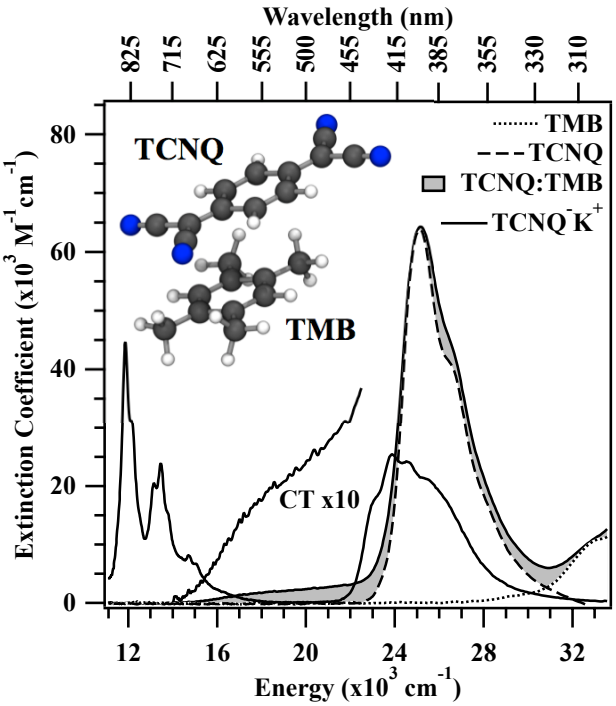

Figure 7.1: Absorption spectra of 7,7,8,8-tetracyanoquinodimethane (TCNQ, dashed, electron acceptor), 1,2,4,5-tetramethylbenzene (TMB, dotted, electron donor), the TMB:TCNQ complex (shaded) and the chemically generated TCNQ anion (TCNQ-K+, solid) in dichloromethane. The charge transfer band of the complex has been magnified by a factor of ten, for clarity. The inset shows the calculated C_1 complex structure.

TMB:TCNQ complex has a broad, featureless charge transfer (CT) absorption band in the 600-450 nm region. The CT transition is characterized by an intermolecular excitation from the HOMO of the TMB to the LUMO of the TCNQ. Binding properties of the complex in DCM were determined *via* the Benesi-Hildebrand method:[198] $K_{eq} = 0.25 \pm 0.03\ M^{-1}$, $\epsilon_{530} = 4300 \pm 400\ M^{-1}\ cm^{-1}$. When TCNQ is chemically reduced, the radical anion $TCNQ^{-}\cdot$ (solid line) shows an intense B_{1u} absorption band[199] with sharp vibronic features: $\lambda_{max} = 843$ nm, $\epsilon_{843} = 44000\ M^{-1}\ cm^{-1}$. Vibronic progressions due to the 323, 1271 and 1616 cm^{-1} modes are clearly visible. Two distinct stable intermolecular conformers, one with C_s symmetry (not shown) and the other with C_1 symmetry (inset of Figure 7.1), were identified with DFT calculations using the ωB97x-D functional and the 6-311++G(d,p) basis set.[117] When modeled in vacuum, the C_s conformer is about 80 cm^{-1} more stable than the C_1 conformer. However, time-dependent DFT calculations suggest that the lowest energy singlet transition of the C_s conformer is symmetry forbidden while that of the C_1 conformer has an oscillator strength 20 times greater. In addition, the ground state dipole moment of the C_1 conformer is predicted to be 3.5 fold that of the C_s conformer suggesting that with proper inclusion of polar solvation effects, the C_1 conformer should be lower energy. Thus while both conformers likely exist in the sample at room temperature it is probable that only the lower symmetry C_1

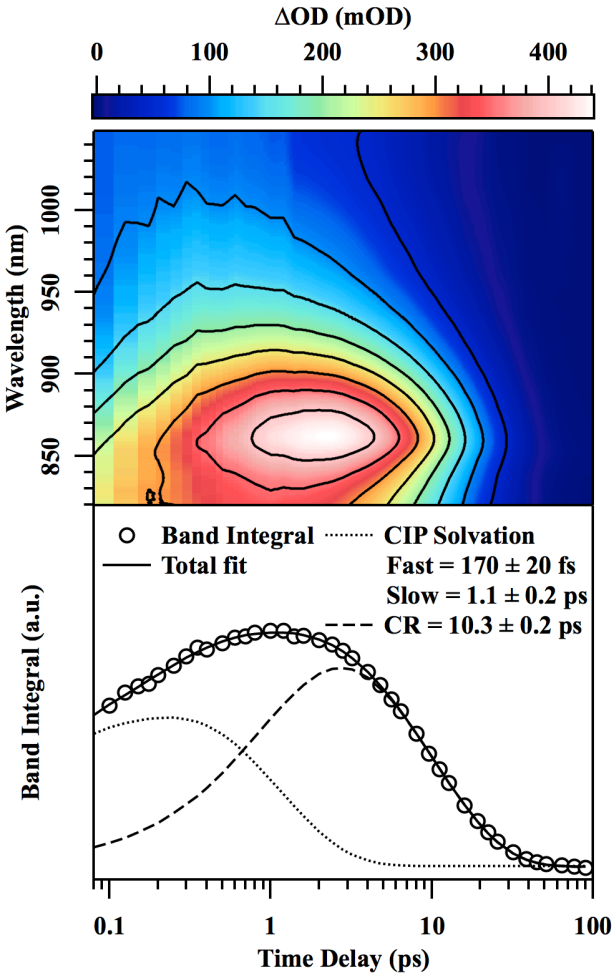

Figure 7.2: (Top) Dispersed transient absorption of the TMB:TCNQ complex from 0.05 to 90 ps in the 830-1450 nm region. The band integral over this region (circles) along with a three component exponential fit (solid line) is shown at the bottom. The two fast components (dotted line) correspond to polar solvation of the contact ion pair and the slow component (dashed line) is assigned to charge recombination.

conformer contributes to the excited state signal.

The dispersed transient absorption (TA) of the TNCQ:TMB complex over the 830-1450 nm region following excitation at 530 nm is presented at the top of Figure 7.2 with time delays from 50 fs to 90 ps on a logarithmic scale. An increase in absorbance and redshift in the maximum is observed at early times followed by a slight blue shift and a slow decay at longer times. The transient spectra are peaked around ~860 nm and the bandwidth and position are consistent with the ground state radical anion absorption albeit broadened and shifted to longer wavelengths. To simplify the subsequent analysis and remove the effect of spectral shifts, the TA was integrated over the entire probe window; the results are presented at the bottom of Figure 7.2 as open circles.

The band integral was best modeled by a three component exponential convoluted with a Gaussian instrument response function (IRF), solid line. Two of the components correspond to intensity increases and had time constants of 170 ± 20 fs and 1.1 ± 0.2 ps, respectively. Both decay constants quantitatively match the reported solvation times of coumarin 153 in DCM: 144 fs and 1.04 ps.[200] Due to this correspondence, these dynamics have been assigned to solvation of the nascent contact ion pair (CIP). The longest measured decay component has a time constant of 10.3 ± 0.2 ps and corresponds to the complete disappearance of the TA signal due to back electron transfer (i.e. charge recombination).

Figure 7.3(a) presents the dispersed TA of the complex in the 870-930 nm region following excitation at 530 nm from -500 to 2500 fs with 20 fs steps. Oscillations visible in the contour lines are due to coherent wave packet motion in the excited state. Oscillations due to impulsively excited *ground state* wave packets can be ruled out due to the large separation between the ground state and excited state absorption bands. To analyze these oscillations, the TA was integrated over the region of interest and the resulting band integral is presented in Figure 7.3(b) as the gray line. The 870-930 nm region was chosen because this is where the slopes of the transient spectra are steepest, which has been shown, both theoretically and experimentally, to give the highest signal to noise.[127] To extract the oscillatory signal, the slowly varying population decay was modeled by a three-component exponential decay convoluted with a Gaussian IRF, shown as the black line, and removed. The extracted oscillatory signal is shown as a gray line and the LPSVD[135–137] fit is shown as the black line in Figure 7.3(c). The residuals between the data and fit are shown as dots offset below.

Before conversion to the frequency domain, the magnitudes of the oscillatory signal are corrected for damping due to the finite duration of the pump and probe. Equation 7.3 displays the functional form of a damped oscillatory signal obtained in the limit of delta function pulses.

$$S(t) = e^{-t/\tau} \cos(\omega t)\theta(t) \tag{7.3}$$

Where τ is the dephasing time, ω is the angular frequency of oscillation, θ is the Heaviside step function and t is the delay between the actinic pump and the Raman probe. To model the effect of non-delta function pulses it is necessary to convolve eq. 7.3 with the Gaussian IRF. While there is no closed form solution for this convolution one does exist for an undamped sinusoid convoluted with a Gaussian; in this case the oscillatory magnitude is damped by the factor shown in eq. 7.4.

$$\exp\left(-\frac{1}{2}\sigma^2\omega^2\right) \tag{7.4}$$

Here σ is the standard deviation of the Gaussian IRF and ω is the angular frequency of the sinusoid. Numerical convolutions of eq. 7.3 with a Gaussian (see Appendix E) show a reduction in magnitude identical to eq. 7.4 as long as the delays chosen are longer than the full width at half maximum (FWHM) of the Gaussian function. Therefore, eq. 7.4 was used to scale all LPSVD magnitudes and FFT spectra before presentation.

Figure 7.3(d) presents the frequency domain representation of the LPSVD parameters (black line), an FFT of the raw data (gray line) and the low frequency resonance Raman (RR) spectrum

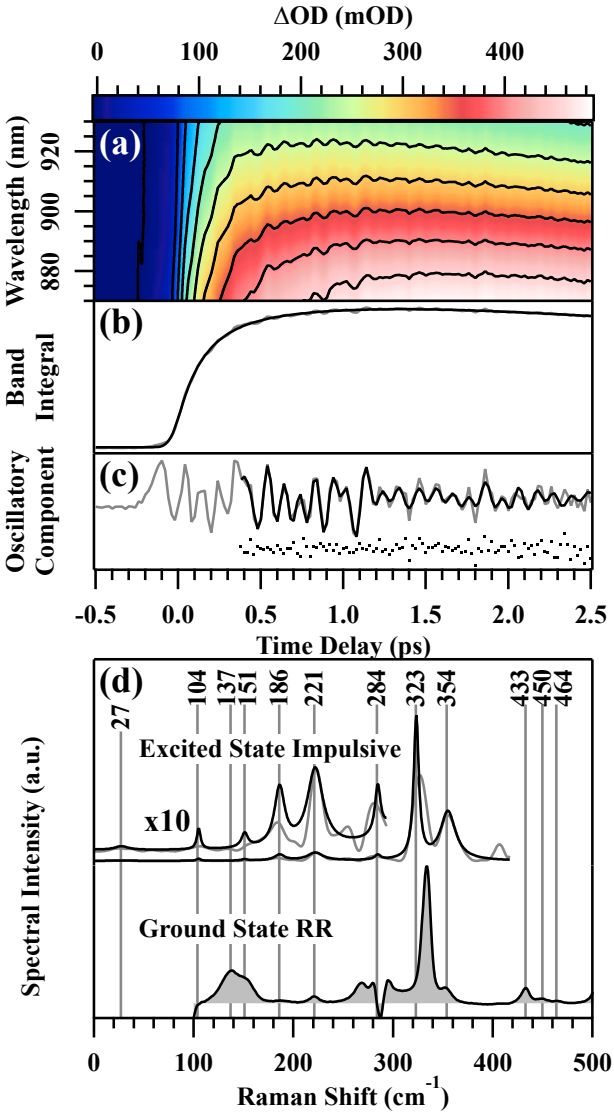

Figure 7.3: (a) Dispersed transient absorption of the TMB:TCNQ complex from -0.5 to 2.5 ps with 20 fs steps over the 870-930 nm region. (b) The integral of the TA over the region shown in (a) (gray line) along with a fit to a three-component exponential decay convoluted with a Gaussian instrument response function (black line). (c) The oscillatory component of (b) (gray line) is fit to eight exponentially decaying sinusoids using the LPSVD algorithm (black line). The residuals of the fit are shown as dots. (d) Frequency domain reconstruction of the LPSVD parameters (black line) and an FFT analysis of the oscillations in (c) (gray line) along with the low frequency resonance Raman spectrum of the complex acquired with 514 nm excitation (shaded). Magnitudes of the time domain data have been corrected for the finite duration of the pump and probe using eq. 7.4 as described in the text and data below 300 cm^{-1} has been magnified by a factor of ten for clarity. Frequencies of the LPSVD model are indicated.

of the TMB:TCNQ complex ground state taken with Raman excitation at 514 nm (shaded). Both of the time domain spectra have been scaled to correct for the effects of finite pulse widths, as described above. The LPSVD and FFT agree well with one another. A total of eight peaks are observed below 500 cm^{-1} in the RR and oscillatory TA data. Normal modes are assigned with the aid of DFT calculations and the literature[201–204] and complete descriptions, with respect to the axes and carbon numbering in Figure 7.4, can be found in Appendix E. One mode is highlighted here: the 323 (333) cm^{-1} mode, which can be described as an A_g CCN in-plane bend combined with $C_{2,4}$=$C_{3,5}$ stretches. The excited state impulsive and the ground state RR spectra are similar except for the slight shift in the 323 cm^{-1} mode and the large shift of the 137 cm^{-1} mode in the ground state to 104 cm^{-1} in the excited state.

7.4.2 Raman Spectroscopy of the Charge Transfer Excited State

Figure 7.4 presents the ground state RR spectra of (a) TMB, (b) the complex, (c) TCNQ and (d) the TCNQ anion along with (e) the excited state stimulated Raman spectrum of the complex 2 ps after excitation. Axes and carbon numbering used for mode characterizations are depicted in the upper right corner. Spectra of the anion and the excited state display a multitude of overtones and combination bands. Moreover, the striking similarity between spectra (d) and (e)–all frequencies are within 10 cm^{-1} of one another–indicates that the excited state of the complex can be accurately described as a transient biradical species, i.e. $TCNQ^{-}\cdot TMB^{+}\cdot$. No modes of the $TMB^{+}\cdot$ cation are observed in spectrum (e) because the Raman pump at 795 nm is strongly resonant with the $S_1 \rightarrow S_2$ excited state absorption band that is localized on TCNQ. While the spectra of the TCNQ monomer and excited state complex are similar, there is a consistent blue shift in modes that involve the benzene ring–at 722, 976 and 1616 cm^{-1}–and a large red shift in the 1388 cm^{-1} C_2=C_3 stretching mode upon reduction of the TNCQ. This observation is consistent with an extra electron being placed in the π^* anti-bonding orbital, which has a distinct node centered on the C_2=C_3 bond.

In Figure 7.4 there are eight fundamental vibrations above 500 cm^{-1} in the excited state spectrum which have A_g symmetry and are localized on the TCNQ. The 2198 cm^{-1} mode corresponds to a symmetric stretch of all CN groups. The 1616 cm^{-1} mode is a C_4=C_5 stretch on the benzene ring. The 1388 cm^{-1} mode is a C_2=C_3 stretching motion. The 1271 cm^{-1} motion is of B_{3g} symmetry and is an in-phase hydrogen rock coupled with C_2=C_3 rocking motion in which the $C_1C_2C_3$ and $C_2C_3C_4$ angles are alternately enlarged and compressed. The 1194 cm^{-1} mode is an in-phase hydrogen rock. The 1171 cm^{-1} mode is similar to the 1271 cm^{-1} mode but the carbon and hydrogen motions are more strongly coupled. The 976 cm^{-1} peak corresponds to a ring breathing coupled to a CCN bending motion. The 722 cm^{-1} mode is a ring compression motion along the *y* axis. The 616 cm^{-1} motion is a localized CCN bend.

Figure 7.5 presents excited state stimulated Raman spectra of the complex for selected time delays after actinic excitation along with a magnified ground state spectrum for reference. At each time delay the transient Raman spectrum was fit to a sum of Lorentzians and a baseline function. The peaks at 1194, 1388 and 1599 cm^{-1} are not purely positive and are modeled by a dispersive Lorentzian line shape. Dispersive lineshapes have been observed in FSRS before[69,71] and are due to resonant transitions through non-linear pathways other than RRS(I).[71,205,206] For long delays,

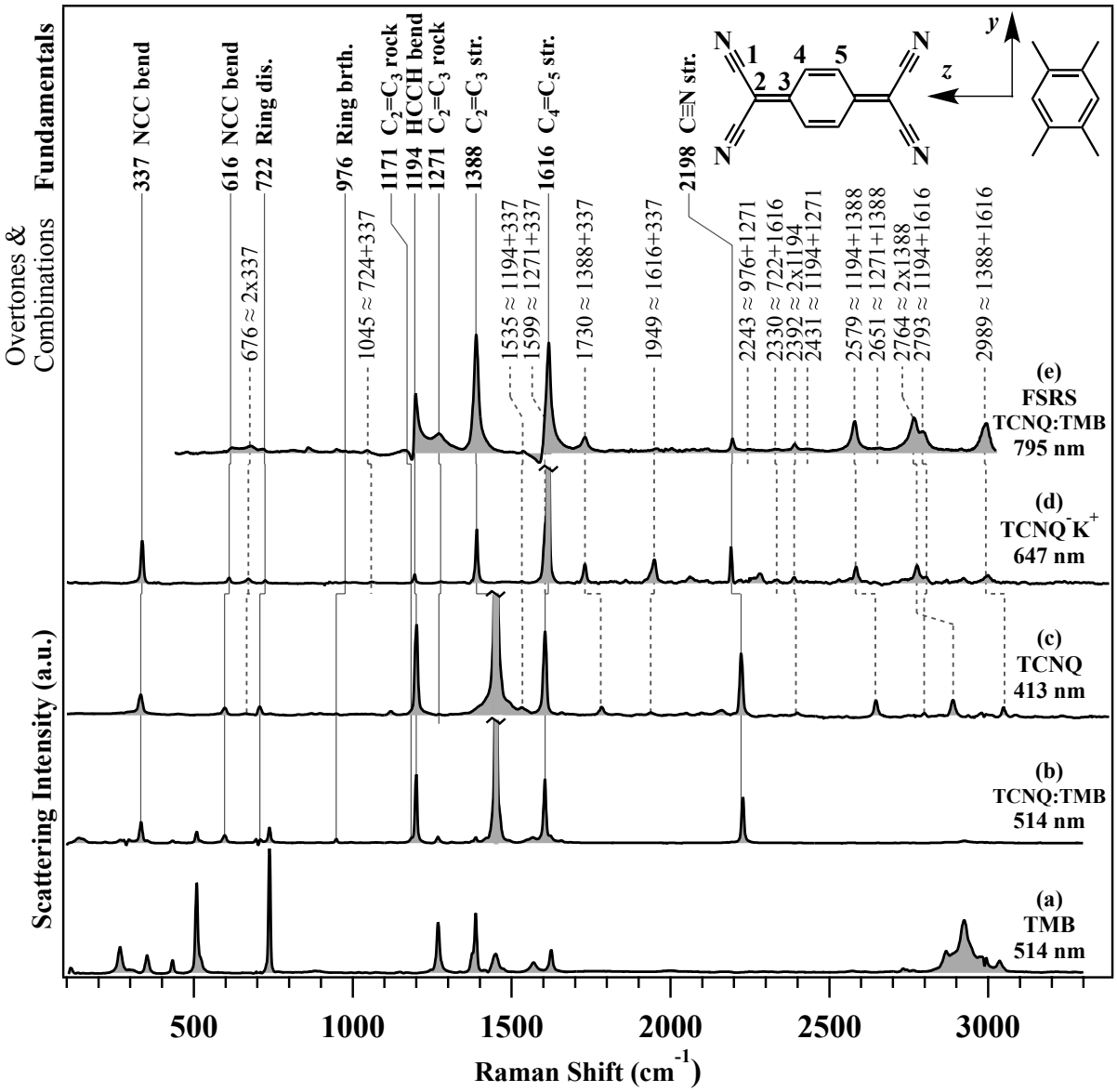

Figure 7.4: Spontaneous Raman spectra of (a) TMB with excitation at 514 nm, (b) the TMB:TCNQ charge transfer complex with excitation at 514 nm, (c) TCNQ with excitation at 405 nm and (d) the chemically generated TCNQ anion ($TCNQ^{-}K^{+}$) with excitation at 647 nm. (e) Excited state stimulated Raman spectrum of the TMB:TCNQ complex 2 ps after actinic excitation at 530 nm with Raman probing at 795 nm. Fundamental positions are marked by solid lines and overtone and combination bands are marked by dashed lines. Large peaks in (b), (c) and (d) have been truncated, as indicated, in order to make the weaker signals visible. Frequencies and assignments are listed at the top along with the structures of the monomers, the carbon numbering and the axes used to characterize the normal modes.

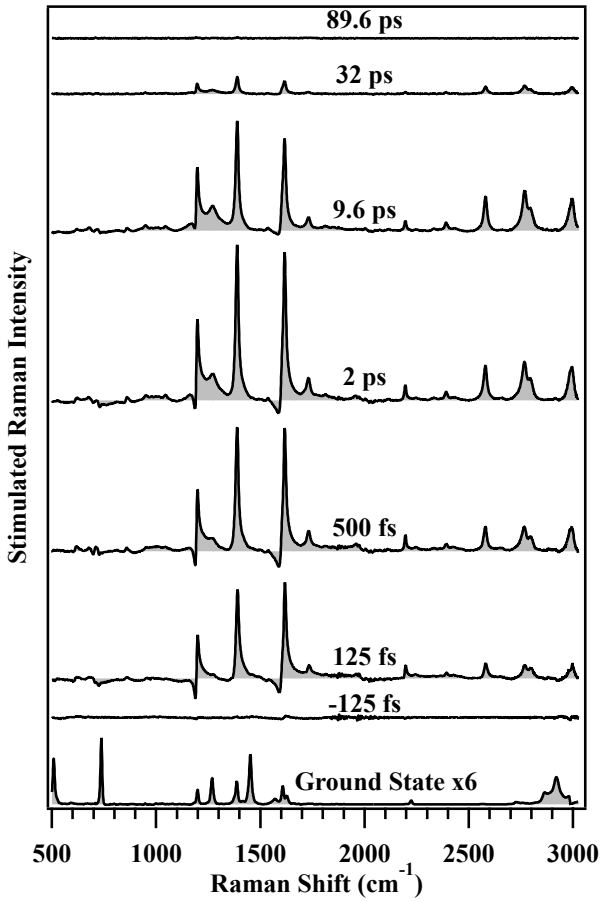

Figure 7.5: Stimulated Raman spectra of the TMB:TCNQ complex at selected time delays after excitation at 530 nm. Signals due to the solvent and residual ground state have been removed and the background has been corrected. The peak amplitudes increase at early times and then decrease in tandem with the TA, see Figure E.2. A magnified ground state spectrum is shown at the bottom for reference and contains large contributions from the TMB monomer.

the kinetics of the fitted amplitudes strongly mirror those of the TA, see Figure E.2. For the short delay data, taken with 20 fs time steps, the extracted center frequencies and amplitudes reveal more interesting dynamics.

7.4.3 OSCILLATORY EXCITED STATE RAMAN SIGNALS

Figure 7.6 presents three representative intensity-frequency trajectories for the 1271 (top), 1730 (middle) and 2431 (bottom) cm^{-1} modes. Data are displayed as colored tubes and projections of the peak position and the peak amplitude are shown on the bottom and back, respectively. High signal-to-noise oscillations are visible in both components for all three peaks with magnitudes of 2 cm^{-1} and 1.5 mOD for the 1271 cm^{-1} mode; 0.75 cm^{-1} and 2.1 mOD for the 1730 cm^{-1} mode; and 5

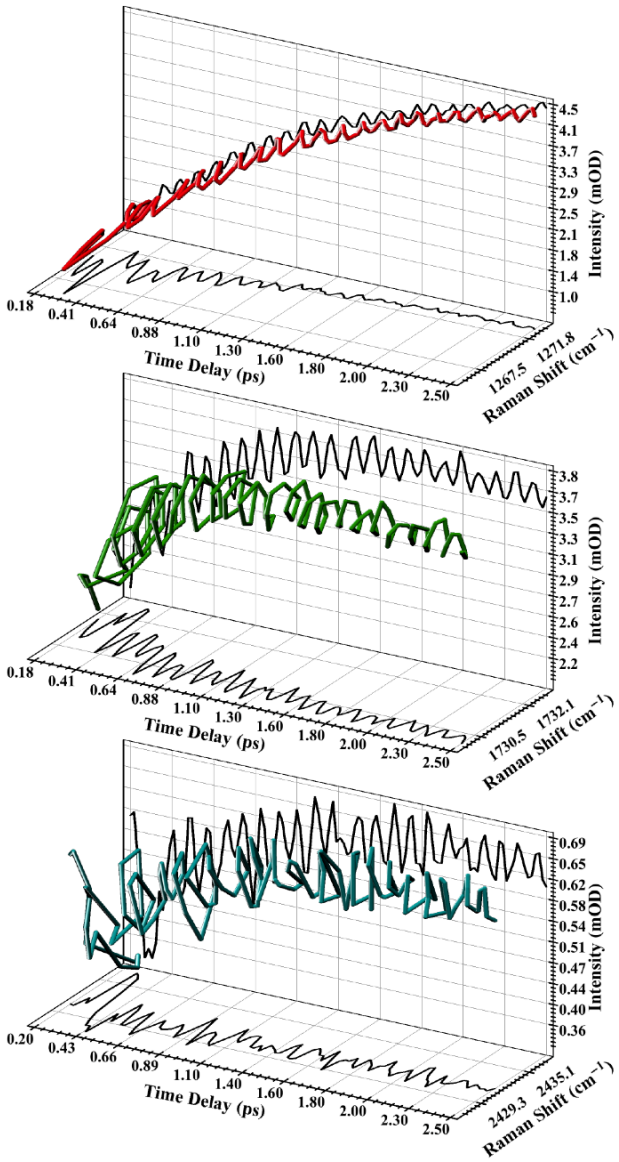

Figure 7.6: Intensity-frequency trajectories for three representative peaks; 1271 (top), 1730 (middle) and 2431 cm^{-1} (bottom). The amplitudes and peak positions are on the back and bottom axes, respectively. Oscillations in both amplitude and peak position are visible and their phase and frequency relation results in a corkscrew-like trajectory.

cm^{-1} and 0.05 mOD for the 2431 cm^{-1} mode. Note that all three trajectories evolve in a corkscrew pattern indicating that the peak amplitudes and centers both oscillate with the same frequencies and have a fixed $\pi/2$ phase relationship suggesting that they are modulated by the same underlying phenomenon. Stimulated Raman intensities may depend on many different parameters including the shape of *all* potential energy surfaces (PES) involved in the Raman process.[206] On the other

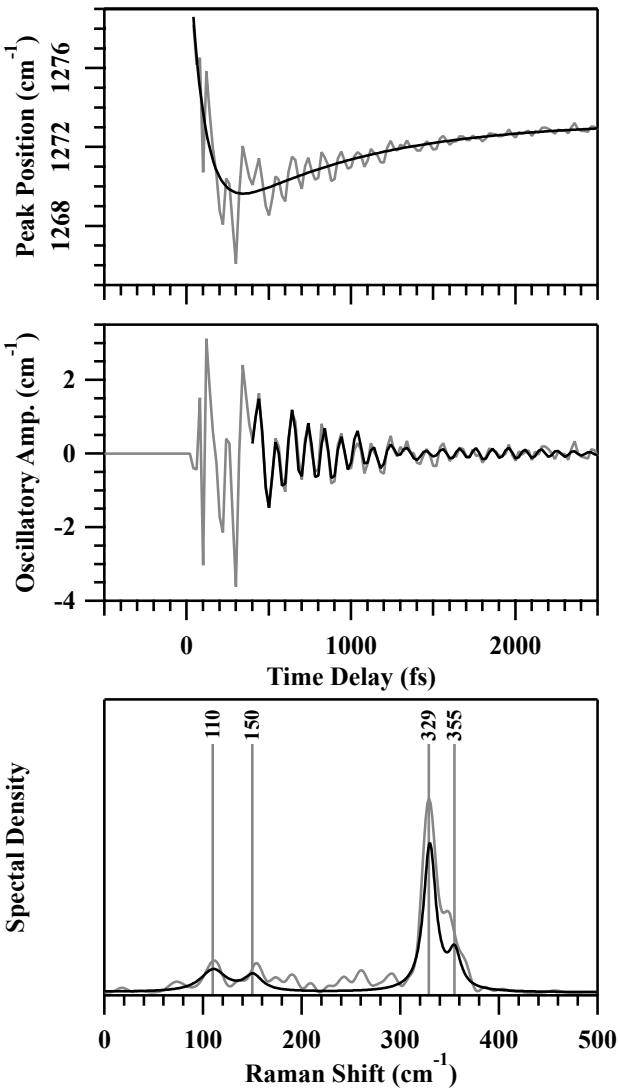

Figure 7.7: The extracted center frequency of the 1271 cm^{-1} peak as a function of time (top, gray line) along with a fit to an exponential decay (black line). The residual oscillatory component is shown in the middle (gray line) along with an LPSVD fit to four exponentially decaying cosinusoids (black line). A frequency domain reconstruction of the extracted model parameters is shown below (black line) along with an FFT analysis of the oscillatory component (gray line). These data have not been scaled by eqs. 7.4 or 7.9.

hand, peak frequencies are the direct measure of the curvature of the PES of interest. For this reason the rest of the discussion will focus on the temporal oscillations of the peak frequencies.

Analysis of the oscillatory peak frequencies followed the framework outlined for the oscillatory TA signal. First, the slowly varying population dynamics were removed after which the isolated oscillatory signal was modeled using the LPSVD algorithm. The data analysis steps for the 1271

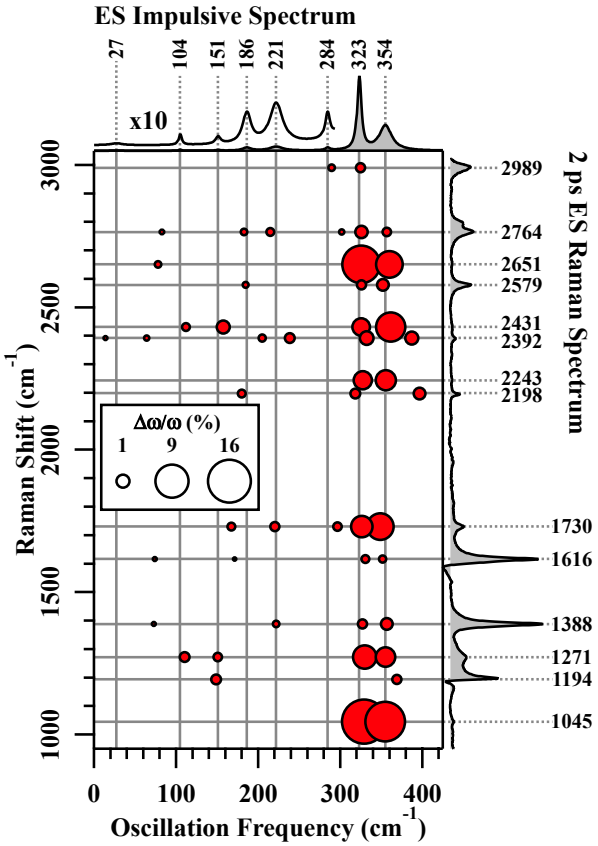

Figure 7.8: Correlations between the oscillatory peak centers measured with time resolved stimulated Raman and the impulsively excited low frequency vibrations measured by transient absorption of the TMB:TCNQ complex. Each circle's ordinate is locked to the center frequencies of the peaks in the excited state complex spectrum (2 ps after excitation). The abscissas are the measured frequency with which the peak centers oscillate and are *not* determined by the excited state impulsive data. The LPSVD reconstruction of the coherent TA oscillations is shown at the top. The areas of the circles indicate the relative magnitude of the oscillations with respect to the average FSRS peak position. These magnitudes have been corrected for the effects of the finite durations of the actinic pump and Raman probe and for the effect of averaging over the effective vibrational dephasing time. Note that the 1271 cm^{-1} mode, its overtones and combinations and those of the 323 cm^{-1} mode have large oscillatory magnitudes on the order of 10% (100 cm^{-1}).

cm^{-1} mode are demonstrated in Figure 7.7 (figures for the 1730 and 2431 cm^{-1} modes are presented in Appendix E). Again the LPSVD and FFT have excellent agreement and oscillatory components due to the 104, 151, 323 and 354 cm^{-1} modes are observed.

Figure 7.8 presents the extracted oscillatory parameters for all the peaks in the transient Raman spectra of the TMB:TCNQ complex. Each circle represents a detected oscillatory component and its abscissa, ordinate and size represent the frequency of oscillation, the position of the excited

state peak and the relative intrinsic magnitude of the oscillation with respect to the average center frequency, respectively. The excited state impulsive Raman spectrum from Figure 7.3(d) is shown along with vertical gray lines marking the peak centers for reference. The ordinates of the circle are fixed by definition to the peak positions of the transient Raman spectrum obtained 2 ps after excitation, which is shown at the right along with horizontal gray lines marking the peak positions, for reference.

The intrinsic magnitudes of the FSRS peak center frequency oscillations, shown in Figure 7.8, are significantly larger than the observed magnitudes, shown in Figure 7.7, because of the effect of finite pulse durations (discussed above) and averaging over the vibrational coherence dephasing time.* The damping due to the latter effect can be corrected for by calculating the average value of the instantaneous frequency as a function of actinic pump-Raman probe delay. The instantaneous frequency (defined as the derivative of the phase) of an oscillating high frequency mode modulated by a low frequency one can be modeled as

$$\frac{\partial \phi}{\partial t} = \omega(t) = \omega_{h,0} + Ae^{-t/\tau_{co}} \cos(\omega_l t) \tag{7.5}$$

where $\omega_{h,0}$ is the average center frequency of the high energy FSRS peak, ω_l is the frequency of the low energy normal mode causing the modulation, A is the intrinsic magnitude of the modulation and τ_{co} is the dephasing time of the impulsively excited low frequency vibrational coherence. In the limit of delta function pulses the dephasing of the Raman pump induced vibrational coherence can be modeled as

$$W(t) = e^{-t/\tau_{peak}} \tag{7.6}$$

where τ_{peak} is the dephasing time due to the Raman pump pulse shape and the intrinsic decay of the molecular system. With eqs. 7.5 and 7.6 the average change in frequency of the high frequency vibration becomes

$$\langle \Delta\omega(t) \rangle (\Delta t) = \frac{\int_0^\infty (\omega(t+\Delta t) - \omega_{h,0})\, W(t) \mathrm{d}t}{\int_0^\infty W(t) \mathrm{d}t} = \frac{Ae^{-\Delta t/\tau_{co}} \cos(\omega_l \Delta t - \alpha)}{\sqrt{\left(\omega_l \tau_{peak}\right)^2 + \left(\frac{\tau_{peak}}{\tau_{co}} + 1\right)^2}} \tag{7.7}$$

where Δt is the time delay between the actinic pump and the Raman pulse pair, t is the time between the initial and final field couplings which generate the vibrational coherence[21] and α is a phase shift defined in eq. 7.8.

$$\alpha = \arctan\left(\frac{-\omega_l}{\frac{1}{\tau_{peak}} + \frac{1}{\tau_{co}}}\right) \tag{7.8}$$

Equation 7.7 demonstrates that the FSRS center peak frequency will oscillate at frequency ω_l as a function of Δt but that observed magnitude of modulation will be strongly damped and the

*The observed vibrational coherence time is the convolution of the intrinsic molecular dephasing time and decay time of the Raman pump. In the frequency domain these linewidths are additive

observed phase will be different than the intrinsic phase. The intrinsic modulation magnitude may be obtained from experimentally observed parameters using eq. 7.9.

$$A = A_{obs}\sqrt{\left(\frac{2\nu_l}{\Gamma_{peak}}\right)^2 + \left(\frac{\Gamma_{co}}{\Gamma_{peak}} + 1\right)^2} \tag{7.9}$$

Here A_{obs} is the observed modulation magnitude, and we have replaced the dephasing times by the corresponding line widths ($\pi\Gamma = 1/\tau$) and the angular frequency with the regular frequency. All four of these parameters are readily available from the experiment and eq. 7.9 has been used to scale the magnitude data presented in Figure 7.8; Figure E.5 presents the raw data in the same format as Figure 7.8.

The 2D-FSRS plot in Figure 7.8 provides a direct measure of the large anharmonic couplings, some in excess of 100 cm^{-1}, between the low and high frequency degrees of freedom in the excited state CIP after the charge transfer reaction. In general, there is excellent agreement between the frequencies of the FSRS peak center oscillations and the TA oscillations. In particular, the 1271 cm^{-1} C_2=C_3 rocking mode is the only visible fundamental that displays significant (> 100 cm^{-1}) couplings to the 323 and 355 cm^{-1} modes, which are a CCN bend and an out-of-plane deformation of the TMB, respectively. As a consequence, combination tones of the 1271 cm^{-1} mode (the 2243, 2431 and 2651 cm^{-1} modes) also have large (> 100 cm^{-1}) magnitude oscillations. In addition, combination tones of the 323 cm^{-1} mode (the 1045 and 1730 cm^{-1} modes) are strongly modulated, which indirectly indicates a strong self-modulation of the 323 cm^{-1} mode. Previous results[23,71] have indicated that low frequency modes are often self-modulated. In addition, the 1271 cm^{-1} mode is the only observable fundamental to have detectable coupling to the 105 or 151 cm^{-1} modes, both of which involve deformations of the CCN angle. Interestingly, the weaker and broader Raman modes (Γ > 40 cm^{-1}) tend to have the largest couplings, with estimated intrinsic oscillatory magnitudes in excess of 100 cm^{-1}, to the low frequency degrees of freedom while the totally symmetric modes that are most Franck-Condon active (and have the most energy deposited into them during electronic excitation) have the smallest.

7.5 Discussion

Femtosecond stimulated Raman has been used to shed new light on the excited state dynamics, PES shape and charge recombination mechanism of the TMB:TCNQ charge transfer complex. Based on a comparison of the Raman spectra, the excited state structure of the acceptor, TCNQ, is identical to that of the chemically prepared radical anion and is formed almost immediately following photoexcitation. Solvent reorganization stabilizes the nascent CIP and charge recombination occurs in ~10 ps. At times earlier than 5 ps, while the excited state wave packet is still coherent and well defined, oscillations in both the transient absorption and the stimulated Raman frequencies and intensities corresponding to low frequency TCNQ and inter-dimer motions are observed. We have determined that the oscillations in the excited state Raman peak frequencies are the signature of a 5^{th} order process meaning that they are directly related to anharmonic couplings

between the low and high frequency modes, see Appendix E for more information. Using this implementation of 2D-FSRS we have characterized many cross couplings, some of which have intrinsic magnitudes that are estimated to be in excess of 100 cm^{-1}. These anharmonic couplings are of great value for understanding the mechanism of charge recombination (i.e. internal conversion) as discussed in more detail below.

Resonance Raman intensity data indicates which nuclear motions are strongly coupled to the initial photoinduced charge separation process.[179,181–187] Figure 7.4 shows that the 323 cm^{-1} CCN bending, 1194 cm^{-1} hydrogen rocking, 1388 cm^{-1} C_2=C_3 stretching and 1616 cm^{-1} C_4=C_5 stretching modes of TCNQ experience the largest geometry changes following electronic excitation. From Figure 7.5 we see that as early as 125 fs the excited state spectra look nearly identical to the chemically produced anion spectrum (Figure 7.4(d)). The growth kinetics of both the TA and the Raman quantitatively match those of polar solvation.[200] These results are very similar to those reported earlier[49] showing that the charge transfer occurs during the photoexcitation process and the subsequent solvent reorganization stabilizes the CIP. On the other hand, the 2D-FSRS data presented in Figure 7.8 offers new information on the structure and wave packet dynamics on the excited state PES and the resulting mechanism of the charge recombination reaction.

7.5.1 2D-FSRS Reveals Anharmonic Coupling

Two dimensional FSRS allows the direct measurement of anharmonic couplings between various modes on the reactive excited state surface. The intrinsic oscillatory magnitudes presented in Figure 7.8 may be related to the anharmonic coupling by eq. 7.10, the derivation of which can be found in Appendix E.

$$\frac{\Delta\omega(t)}{\omega_{h,0}} = \frac{\omega_h(t) - \omega_{h,0}}{\omega_{h,0}} = -\frac{1}{2}\chi\Delta\cos(\omega_l t) \tag{7.10}$$

Here ω_h is the measured frequency of the high frequency mode as a function of actinic pump-Raman probe delay, $\omega_{h,0}$ is the average frequency, ω_l is the frequency of the low energy mode, Δ is the dimensionless displacement of the excited state equilibrium geometry from the ground state equilibrium geometry along the low frequency normal coordinate and χ is the first order dimensionless anharmonic coupling between the low and high frequency degrees of freedom. Using eq. 7.10 anharmonic couplings may be determined *directly* from the size of the circles in Figure 7.8 together with the Δs of the low frequency modes, which can be extracted from the impulsive (Figure 7.3) or resonance Raman (Figure 7.4) data. Due to the nature of the TMB:TCNQ complex it is difficult to determine the complex concentration with high precision, limiting our ability to determine absolute Δs directly. However, we can estimate the Δ of the 323 cm^{-1} mode to be approximately 2, assuming that the TMB:TCNQ CN stretch has approximately the same Δ as that of the TCNE:HMB complex.[179,183,185] This indicates that the largest observed couplings, i.e. between the 323 and 1271 cm^{-1} modes, are on the order of 0.08 while the couplings between the 323 cm^{-1} mode and the rest of the fundamentals are on the order of 0.01. To put this into perspective the coupling between the C−Cl stretch and the CCl_3 bend in chloroform[193] and the intermolecular couplings in guanosine 5'-monophosphate[207] predicted by DFT are on the order of 0.03. Measured diagonal anharmonicities in diatomics are usually in the range of 0.01-0.02.

The observation that modes with weak broad lines in the excited state FSRS spectra couple strongly, while the Raman active modes do not, is crucial to understanding the vibrational dynamics. Inspection of the spectra in Figure 7.5 shows that the 1271 cm^{-1} mode is by far the broadest fundamental with a FWHM of ~55 cm^{-1}. A vibrational normal mode's breadth can be due to two underlying phenomena: heterogeneity of ground state conformations or intrinsically fast dephasing of the vibrational coherence. Heterogeneity leads to Gaussian broadening while fast dephasing retains solely Lorentzian character. As the 1271 cm^{-1} mode is Lorentzian (within experimental error) it is likely that its breadth is due to quick damping (~200 fs) of the vibrational coherence. Fast dephasing is, in general, a sign of strong coupling to other system or bath degrees of freedom. While the width of the mode can indicate whether or not it *is* strongly coupled, it cannot, in general, reveal to *which* other modes it is coupled. However, the 2D-FSRS data offers deep insight into the mode-specific coupling within this molecular complex revealing that the 1271 cm^{-1} C_2=C_3 rocking mode is strongly anharmonically coupled to the 323 cm^{-1} CCN bending and the 354 cm^{-1} TMB out of plane deformation modes.

The direct measurement of mode-specific anharmonic couplings in the excited state reveals the mechanism for the charge recombination internal conversion back to the neutral ground state. Figure 7.9 depicts a mechanism that involves a CI connecting the CT excited state with the ground state. At least two modes are necessary to form a CI: a totally symmetric (TS) mode that "tunes" the energy gap between the two states (known as the tuning mode) and a non-totally symmetric (NTS) mode that bridges the symmetry "gap" between them (known as the coupling mode). In Figure 7.9 the ground state is depicted as the gray surface while the CT state is shown in yellow. Both surfaces intersect at the CI, indicated by the green sphere. The TS degree of freedom is indicated by the black arrow and NTS by the magenta one. Slices of the PES along the NTS mode are shown in magenta. Note the large displacement between the tuning mode's equilibrium position on the ground and excited state. The subspace of all nuclear motion spanned by the TS and NTS modes is termed the branching space. In this space the degeneracy between the two electronic states is lifted, the two electronic surfaces do *not* touch, except at one point, the CI. However, at the CI (green sphere) the two electronic states are degenerate along *all* nuclear degrees of freedom.

In order to cross from the CT state to the ground state, the NTS mode must distort the molecular system to lower the electronic symmetry and couple the states but to do so it must gain some energy. However, the NTS mode is *not* vibrationally excited upon electronic excitation and because the potential is relatively harmonic in the FC region the wave function is initially *totally symmetric* (blue wave function). It is clear from Figure 7.9 that the adiabatic electronic surfaces in the branching space are *not* harmonic in the region about the CI. This anharmonicity allows energy to be transferred from the initially excited TS mode to the NTS mode,[208] as indicated by the change in the NTS wave function when moving along the red arrow from the FC region to the CI (red wave function). The coupling and tuning modes *must* be strongly coupled to each other and exchange energy if the system is to access the CI and internally convert to the ground state. This fact means that the data presented in Figure 8 and knowledge of the mode symmetry can be used to determine which excited state motions form a CI between the CT excited state and the neutral ground state. Only one pair of modes have the required coupling and symmetries; the totally symmetric 323 cm^{-1} CCN bending/ring stretching mode is the tuning mode and the non-totally symmetric 1271 cm^{-1}

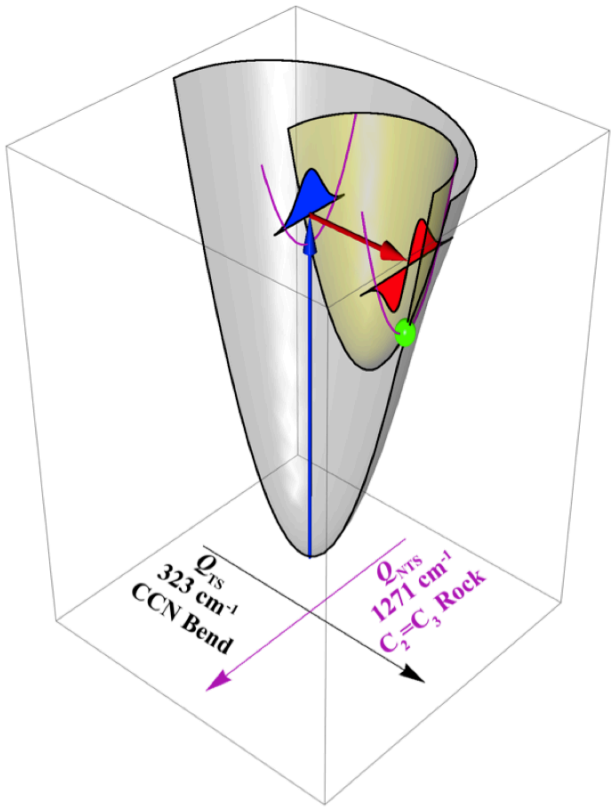

Figure 7.9: Schematic potential energy surfaces (PES) for the ground (gray) and charge transfer excited (yellow) states in terms of the totally symmetric (TS) tuning mode (black) and the non-totally symmetric (NTS) coupling mode (magenta). Vibrational wave functions for the coupling mode are shown both in the Franck-Condon region (blue) and near the conical intersection (red). Near the conical intersection (green sphere) the adiabatic potentials are no longer harmonic and energy can be transferred through the anharmonicity between the initially excited tuning mode to the coupling mode as indicated by the change in the NTS wave function. Such a transfer in energy is necessary to surmount the symmetry barrier between the ground and excited states.

C_2=C_3 rocking mode is the coupling mode that together define the branching space and drive the charge recombination internal conversion. Moreover, these assignments can be rationalized on the basis of molecular orbital theory; initially the TCNQ C_2=C_3 is at a 60° degree angle with respect to the TMB's z-axis, meaning that the lobes of the LUMO are skewed 60° degrees with respect to those of the HOMO. In order for radiationless charge recombination to occur these lobes must overlap well. For this to happen the C_2=C_3 bond must lengthen and the CCC angles must distort to better match TMB's benzene ring; this job is performed by the 323 cm^{-1} mode. Furthermore, the skew must be reduced; this distortion is achieved by the 1271 cm^{-1} mode.

7.5.2 Conclusions

Two-dimensional FSRS has been successfully implemented and used to measure multiple anharmonic couplings between the high and low frequency degrees of freedom in an excited state charge transfer complex. These multiple anharmonic couplings have been directly observed in the excited state of a condensed phase system. While most couplings are on the order of 10-15 cm^{-1}, some, in particular those between the 323 and the 1271 cm^{-1} modes, are nearly an order of magnitude larger indicating their importance for mechanistically relevant energy transfer. This observation combined with the fact that the 323 cm^{-1} CCN bending mode is totally symmetric and the 1271 cm^{-1} C_2=C_3 rocking mode is non-totally symmetric strongly suggests that these modes span the branching space of the conical intersection between the charge transfer excited state and the ground state thereby promoting the charge recombination reaction.

Another striking observation is that the vibrational spectra exhibit significant intensity and frequency oscillations that persist to at least 5 ps after excitation. This observation shows that the internal conversion process is mediated by localized wave packet dynamics rather than full phase space randomization. With modern laser systems and careful choice of resonance conditions it should be possible to probe the mode specific couplings between the all Raman active degrees of freedom in many more excited state systems. Furthermore, we predict that as more systems are studied it will become clear that *all* fast (< 10 ps) internal conversion processes are mediated by vibrationally coherent localized phase space evolutions. These coherences are a tool that can be leveraged by 2D-FSRS to characterize conical intersections in photoreactive systems. Our results suggest more generally that localized PES regions and specific early time coherent nuclear dynamics play a critical role in reactive internal conversion processes.

Acknowledgements

This work was supported by the Mathies Royalty Fund. DFT calculations were carried out with the support of the National Science Foundation Grant CHE-0840505. The authors thank David T. Valley and Philipp Kukura for illuminating discussions.

Chapter 8

Prospects

Throughout this thesis I have used vibrational spectroscopy, especially femtosecond stimulated Raman spectroscopy (FSRS), to study excited state reaction dynamics. I outlined some of the improvements I made to the instrument in Section 2.5 of Chapter 2 and Chapter 3 covered the innovative application of etalon filters to FSRS. In Chapters 4 and 5 I investigated the ultrafast isomerization of an azobenzene derivative using FSRS and ground state ISRS. Both spectroscopies supported the picture presented in Figure 4.8 in which the reaction from *trans* to *cis* occurs primarily along an inversion-like coordinate. Switching gears, I looked at ultrafast electron transfer from a dye to a semiconductor nanoparticle in Chapter 6. The results were surprising as the kinetics retrieved from the transient absorption data did not agree with those from the FSRS data suggesting that each was tracking a separate process. The high frequency of the vibrations made it clear that the FSRS data was tracking the structural evolution of the chromophore. On the other hand, the transient absorption had contributions from both the chromophore and the injected electron. These data demonstrate the powerful advantage FSRS has over conventional pump probe spectroscopy; the ability to separate the contribution of the molecular system from that of the bulk semiconductor. To gain a better understanding of electron transfer I moved on to study charge transfer dimers in Chapter 7. Here our overall results strongly mirrored those reported earlier by Fujisawa, Creelman, and Mathies;[49] the charge is transferred almost instantaneously after the absorption of a photon, the nascent contact ion pair is stabilized by polar solvation and charge recombination occurs on the tens of picoseconds timescale. However, close examination of the FSRS peak intensities and frequencies revealed interesting oscillatory dynamics. We were able to relate the oscillatory signals to mode-specific anharmonic couplings and use this insight to determine the coupling and tuning modes of the conical intersection between the charge transfer excited state and the neutral ground state. FSRS has proven itself to be the ideal tool for pump-probe experiments were it offers both information on the structural evolution of reactants to products and the ability to easily distinguish between different excited state species. However, we have just begun to scratch the surface of what FSRS is capable; in order to push forward we will need to improve FSRS such that 2D data can be readily acquired and analyzed.

FSRS is a relatively well established technique and, as far as nonlinear spectroscopies are concerned, it is easy: there are only three pulses and the signal is self-phase matched and self-heterodyned with the probe pulse. In fact, with a modern laser system only three optics need to be purchased to construct a FSR spectrometer; one BBO cut for SHG to form the actinic pump, one sapphire to generate the continuum and one etalon to form the Raman pump. Such a low barrier to entry has, and will hopefully continue to, encourage many researchers to apply this spectroscopy to myriad systems, as illustrated in Figure 8.1. But there are a few ways in which the spectroscopy could be greatly enhanced; improving the signal to noise, automating the data processing and improving the bandwidth of 2D-FSRS, as discussed below.

8.1 Extremely High SNR FSRS Instruments

Compared to spontaneous Raman scattering, FSRS has a roughly seven orders of magnitude improvement in the signal and the Red Table's sensitivity is on the order of 5×10^{-5} after 1 second of

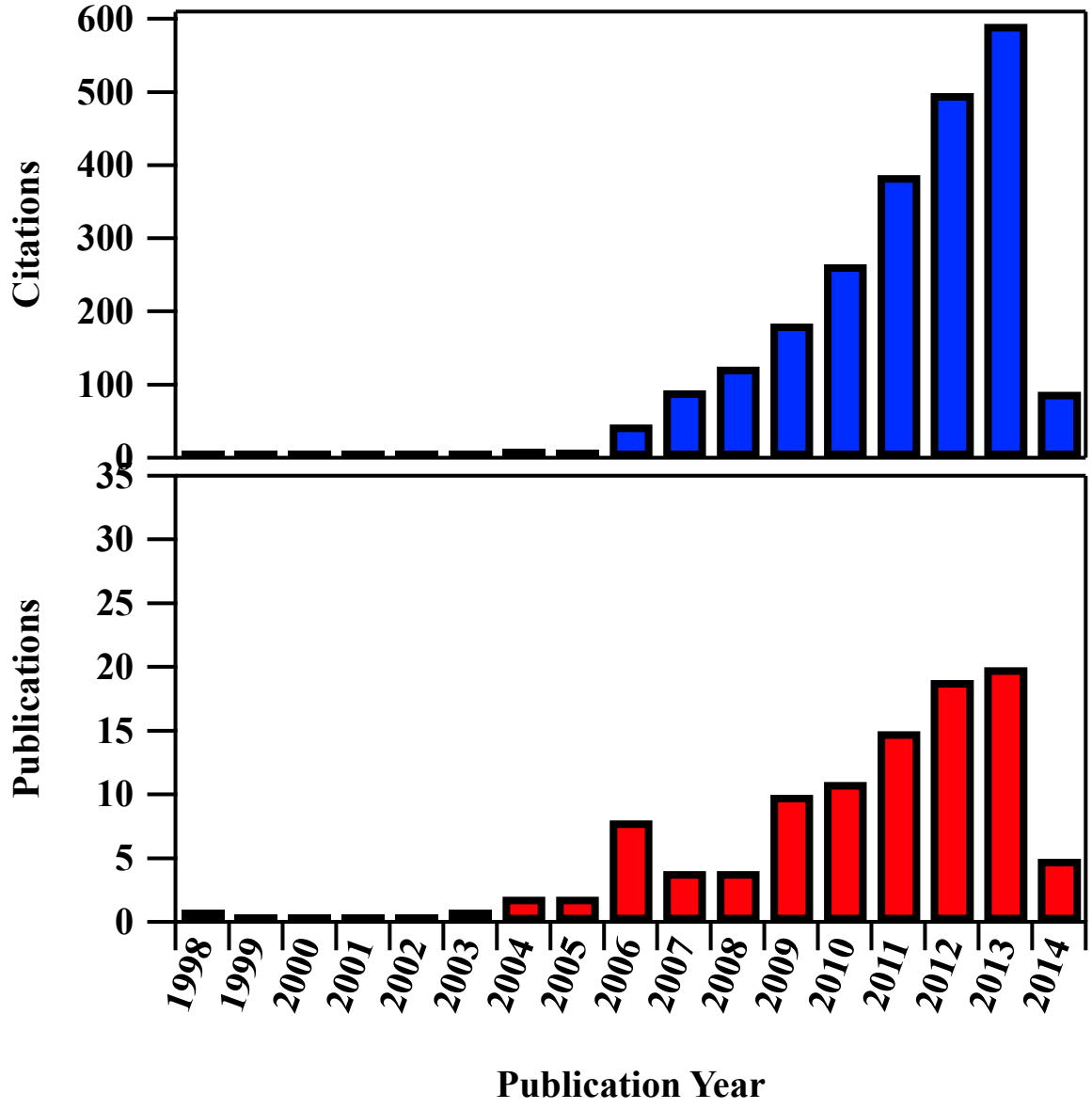

Figure 8.1: FSRS citations and publications. Data from Web of Science, search term `TITLE: ("stimulated Raman microscop*" OR "femtosecond stimulated Raman" OR "stimulated Raman scatter* microscop*")`.

averaging. This means that we can detect a change in the probe intensity of about 1 in 20,000 after 1 second which translates to a Raman gain of 50 μOD. Such performance is commonly reported for transient absorption instruments, see Dobryakov et al.[209] for example. The best sensitivities for stimulated Raman have been reported by SRS microscopists.[210–213] In many cases sensitivities of nearly 10^{-8}, 10 *nano* OD, are achieved with one second acquisition times; more than *three* orders

of magnitude better than our current FSR spectrometer.

Achieving these amazing sensitivities requires that the noise level be at the absolute minimum. When all other forms of noise have been suppressed one will always remain and is called **shot-noise**. Shot-noise is due to the quantum nature of light. In this limit Min et al.[211] have shown that the signal-to-noise ratio (SNR) of the stimulated Raman experiment can be expressed as

$$\text{SNR} = \alpha I_{pu} \sqrt{I_{pr}} \tag{8.1}$$

where α is a collection of constants related to the signal (αI_{pu} is the experimentally observed gain or modulation depth), I_{pu} is the intensity of the Raman pump and I_{pr} is the intensity of the Raman probe. If we assume that the maximum sensitivity of a SRS microscope corresponds to an SNR of 2 then the number of photons it measures per second is

$$I_{pr} = \left(\frac{2}{10^{-8}}\right)^2 = 4 \times 10^{16} \text{ photons/second} \tag{8.2}$$

More precisely, the microscope can measure 4×10^{16} photo*electrons*/second, which is close to the saturation limit for a standard photodiode.

Clearly, if FSRS is to reach these sensitivities it will need to simultaneously achieve two goals: shot noise limited detection and the ability to measure ~10^{16} photoelectrons per second.

Attaining shot-noise limited detection should not only be possible but relatively easy. Other than shot-noise the FSRS experiment is dominated by $1/f$ noise, which is characterized as having higher intensities at lower frequencies. The frequency here denotes the frequency of the measurement, for the Red Table this is 500 Hz. Intuitively this makes sense; imagine that we no longer collected spectra at 1 kHz but at 10 Hz. Now any fluctuations occurring on the 0.1 second time scale or less would cause the background probe shape to change and induce noise. Clearly, as the frequency of measurement is increasing there are fewer and fewer fluctuations that happen fast enough to perturb the Raman pump off *versus* on probe spectrum. Our laboratory has seen this effect upon moving to shot-to-shot detection. However, our current measurement frequency is limited by the repetition rate of the laser (1 kHz) and the speed of the camera (1 kHz). Faster lasers are common and oscillators with repetition rates up to 10 GHz are commercially available (microscopists frequently use 80-100 MHz sources). Unfortunately, multi-channeled detectors do not keep pace; the best have maximum frame rates of a few tens of kHz. That being said, 10-30 kHz may be fast enough to achieve nearly shot-noise limited performance.

Turning to the second question, we showed that SRS microscopists must measure at least 10^{16} photoelectrons per second to achieve sensitivities of 10^{-8}. An 11 mW, 800 nm beam will provide this number of photoelectrons assuming the detector is 90% efficient meaning that producing enough photons is not an issue. To put this into perspective let us consider the Red Table's current detector, the PIXIS 100F. The PIXIS operates at 1 kHz and has a full well capacity of about one million e^- per pixel corresponding to a saturation limit of 10^9 photoelectrons per second yielding a sensitivity of about 3×10^{-5} or 30 μOD, which is close to our measured sensitivities. Thus in order to significantly improve our signal to noise we need a detector capable of at least 1 kHz detection

but that has a full well capacity per pixel close to 10^{13}. Unfortunately, for array detectors these two properties are often at odds with one another. To the best of my knowledge no commercial detector exists that would allow for anything more than a five fold improvement over the PIXIS. Attaining 10^{-8} sensitivities will require big improvements in multi-channeled detectors.

8.2 Towards Automatic Data Processing

It is important to understand that the high signal to noise that the microscopists enjoy is for only a *single* frequency and that the previous discussion was an attempt to see if such sensitivities could be achieved with broadband detection. Microscopists also focus on well isolated peaks meaning they can largely ignore the contribution of nonlinear baselines to the overall noise. On the other hand, for broadband FSRS, where we are interested in recording the usually congested finger print region of the Raman spectrum, baselines are the single largest source of noise. Moreover, they are wholly systematic meaning that brute force averaging will *not* remove them. There are a few experimental methods for attenuating these baselines but most, such as the one described by Weigel and Ernsting[23], are difficult to implement and are not universally applicable. As described in Chapter 3, an etalon filter will mitigate but not fully remove the baseline. Any residual baseline has to be removed, in some instances it must be tediously done by hand. Baseline removal will have to be automated for high-throughput spectroscopy and hyper-spectral imaging.

A measured spectrum S can be represented as the sum of three distinct components; the signal, s, in which we are ultimately interested, the baseline, b which is essentially *low* frequency systematic noise and regular Gaussian distributed white noise (shot-noise), e. Formally,

$$S = s + b + e \tag{8.3}$$

One method used frequently throughout this thesis to solve this problem is to fit the data to a model where s is assumed to be a sum of line shape functions and the background a polynomial, usually of degree 3. Chapter 7 used this method very successfully, but the spectra were characterized by *huge* signals and a relatively weak and well behaved background. In cases were the spectra are congested and the baseline is more complicated this method fails, sometimes spectacularly. Another popular method is to choose points corresponding to the baseline by hand and interpolate a cubic spline through them, this was used in Chapter 4. If the points chosen for one spectrum are assumed to be valid for *all* spectra in a data set the manual labor will be sharply reduced. Of course, this assumes that the spectral features do not significantly change position as a function of time, which, as shown in Chapter 4, is not generally the case.

A model free, automated, way to determine b is desirable. Once b has been determined, more model specific analyses can be applied to s. A model free algorithm is necessary because it is *extremely* difficult to properly model the background as this component arises from many different and potentially unknown sources, both instrumental and phenomenological. Even if all of these sources could be incorporated it would be hard to generalize the analysis from one system to another. However, we do know *something* about the background in contrast to the signal, especially in FSRS; it is slowly varying. In concrete terms the typical Raman signal has a bandwidth of about

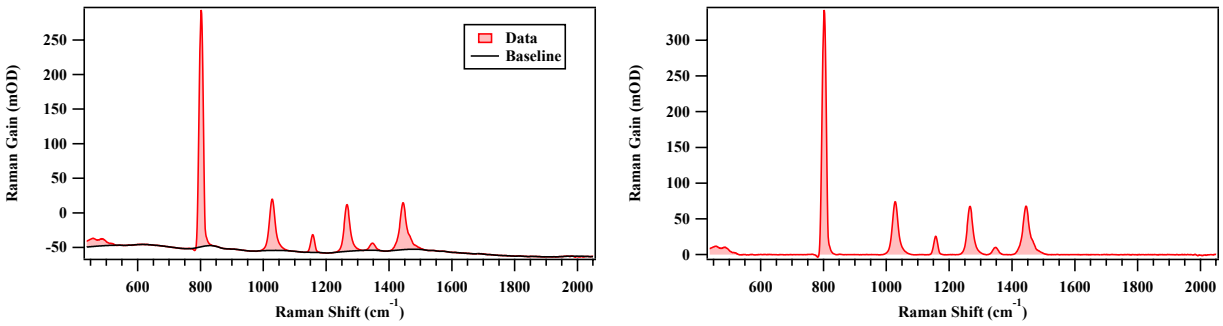

(a) Original data (red) and an algorithmically determined baseline (black).

(b) Data after subtraction of the baseline.

Figure 8.2: A FSRS spectrum of cyclohexane. Both types of noise are small, the signal is sharp and the baseline is easily identified and removed.

10 cm^{-1} while that of the background is larger than 200 cm^{-1}. There have been many attempts to use this fact to solve the baseline problem in the literature[214–223] and they can be broadly categorized as either derivative methods or filtering methods.

Derivative Methods

The idea behind the derivative methods is quite simple. If the background varies slowly so will its derivative. On the other hand, the signal varies quickly in a localized region meaning the derivative will only have large magnitudes near the signal, s. One can then choose a threshold and any points whose derivative is below that threshold is considered part of the baseline. What differentiates the many papers in this category are the methods for choosing this threshold and whether or not they are iterative.

Filtering Methods

Filtering methods work on basically the same principle, they capitalize on the difference in frequency between the signal and the noise. The problem is that its difficult to find the right space in which to represent the signal and design a filter that will effectively separate the signal from the background.

Application of the Derivative Method

Figures 8.2 and 8.3 present two examples on which the derivative method, as I have implemented it, works well. Figure 8.4 presents an example where it fails.

Figure 8.2 presents FSRS data of cyclohexane, which has high intensity, sharp peaks. As such the SNR is huge, for both types of noise, and the algorithm can easily separate the peaks from the

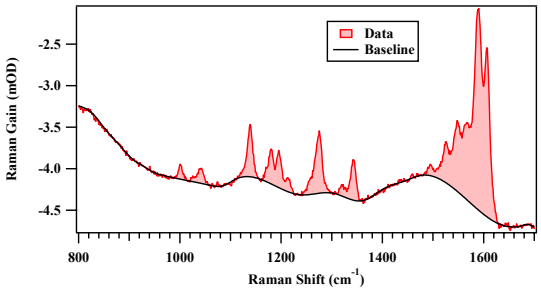

(a) Original data (red) and an algorithmically determined baseline (black).

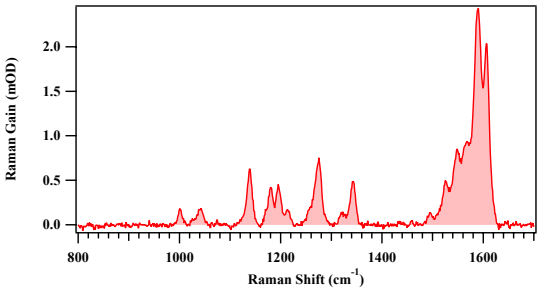

(b) Data after subtraction of the algorithmically drawn baseline.

Figure 8.3: Baseline removal for the ground state of TPAC1 using the derivative method. Even though the spectrum is much noisier than that presented in Figure 8.2 the algorithm has successfully identified the baseline.

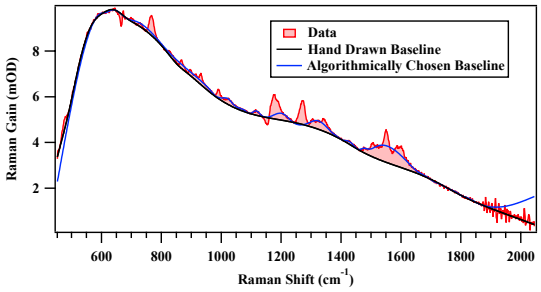

(a) Original data (red), a hand drawn baseline (black) and an algorithmically drawn baseline (blue).

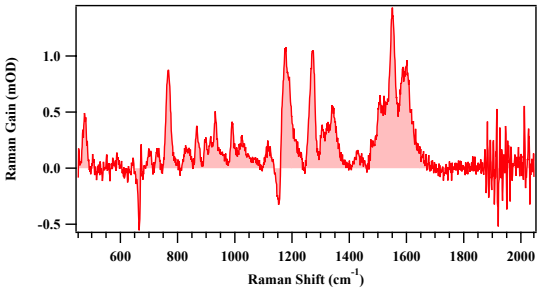

(b) Data after subtraction of the hand drawn baseline.

Figure 8.4: Baseline removal for the excited state of TPAC3. The baseline is relatively small and well behaved but the algorithm fails because of the closely packed peaks. A hand drawn baseline is included for reference (black).

baseline. Figure 8.3 presents a more difficult spectrum, that of the ground state of TPAC1 from Chapter 6. Both types of noise are larger, but the signal to baseline ratio is much smaller than for cyclohexane. Even so the derivative method works well.

Figure 8.4 presents the excited state spectra of TPAC3. In this case the baseline is easily discerned by the human eye and seems well behaved; i.e. the baseline noise is low. However, the peaks in this spectrum are broad and closely spaced, which leads the algorithm to erroneously choose points within the peak clusters as part of the baseline, this is an example for which current methods fail.

8.2.1 Optimization Methods

One method that has yet to be attempted is to use optimization methods to separate the signal from the noise. These methods are commonplace in the electrical engineering and computer science communities but are largely unknown within the physical sciences, to our detriment. For more information on optimizations in general and convex optimizations in particular see the work of Boyd and Vandenberghe.[224] To reformulate the baseline problem into an optimization problem we need to choose an appropriate objective function which when minimized or maximized will produce s, b and e. Once the objective function is chosen there are many available algorithms to choose from to optimize it and thus separate the signal from the noise.

The hardest part of any optimization problem is choosing the correct objective function. One promising objective function is given in eq. 8.4.[225] To find s, b and e we want to minimize our objective function, $f(s,b,e)$, subject to the constraint $S = s + b + e$.

$$f(s,b,e) = \lambda_1 \mathbf{smooth}(b) + \lambda_2 \mathbf{card}(s) + \frac{1}{2}\|e\|_F^2 \tag{8.4}$$

Here $\|e\|$ is the norm of the noise and protects against large outliers, $\mathbf{card}(s)$ is the number of non-zero entries in s (we want s to be only peaks, which means there should not be many of them) and finally $\mathbf{smooth}(b)$ is a function that relates to the smoothness of the baseline. Unfortunately, **card** is very difficult to optimize so we can replace it with its convex approximation the ℓ_1 norm instead.

There are many possible candidates for smooth(b), i.e. we could look at the Fourier transform of b and penalize entries based on their frequency. Alternatively, we could calculate the sum of the squares of the second derivative, i.e.

$$\int \left(\frac{\partial^2 y}{\partial x^2}\right)^2 dx \tag{8.5}$$

But how to choose λ_1 and λ_2 remains an open question. Future progress in this direction may hold the key to automating the most difficult part of FSRS data processing.

8.3 Broadband 2D-FSRS and Beyond

A great achievement of this thesis was the successful measurement of excited state anharmonicities in Chapter 7. These anharmonicities were used to reveal the modes integral in the conical intersection between the charge transfer excited state and the neutral ground state of a molecular dimer. More generally, the 2D-FSRS data allows one to map out the Born-Oppenheimer potential energy surface beyond the harmonic approximation. Apart from revealing the nature of conical intersections these data will be useful in determining the pathways for energy flow in molecules, particularly intramolecular vibrational energy redistribution (IVR) following photoexcitation. Fluorophores offer an excellent model system with which to investigate IVR using this method because they can be prepared in a non-stationary state on a long lived excited electronic surface that does not couple to the ground state through CIs.

Our understanding of what 2D-FSRS measures was greatly improved by the work presented in Chapter 7. It is interesting to revisit older work with this new perspective, specifically that of GFP.[20] Here the authors observed the modulation of the C=O stretch by a phenyl wagging motion. These were the only oscillations observed in this experiment, most likely a consequence of the poor time resolution. Even so the authors estimated an intrinsic oscillatory magnitude of 32 cm^{-1} after correcting for averaging over the vibrational dephasing time. But they did not correct for the finite instrument response time. Using the data provided in ref. 20 and the equations in Chapter 7 to correct for this leads to an estimated intrinsic oscillatory magnitude of nearly 70 cm^{-1}. If we were to interpret these results within the same framework as Chapter 7 then we could suggest, assuming C_s symmetry for the chromophore, that the non totally symmetric phenyl wagging mode acts as the coupling mode and the totally symmetric C=O stretch acts as the tuning mode for the conical intersection that mediates excited state proton transfer.

It would also be interesting to perform the 2D-FSRS experiment on azobenzene. In both Chapters 4 and 5 we demonstrated that the ~50 cm^{-1} inversion and ~15 cm^{-1} phenyl rotation modes played a big role in the isomerization reaction. Furthermore, we showed in Chapter 4 that the reaction is *coincident* with radiationless decay suggesting that the conical intersection mediates the photochemistry of azobenzene. However, *trans* azobenzene has C_{2h} symmetry and both the inversion and rotation modes are non-totally symmetric meaning that neither can act as the tuning mode. A proper 2D-FSRS experiment could reveal which totally symmetric mode acts as the tuning mode and which of these two low frequency modes acts as the coupling mode. However, it is likely that the molecule is *significantly* distorted by the time it reaches the conical intersection and this low symmetry configuration may make the distinction between coupling and tuning modes difficult. Nonetheless 2D-FSRS data on azobenzene will undoubtably improve our understanding of its photochemistry.

In order to improve the 2D-FSRS experiment it will be necessary to shorten the duration of the actinic pump pulse. Ideally we would want a delta function actinic pump and Raman probe so that couplings between *all* modes may be observed. While this is not possible, the Red table's NOPA already produces pulses that have enough bandwidth to be compressed to ~10 fs. Such compression could be readily achieved with chirped mirrors. A 10 fs pulse corresponds to a FWHM of 1472 cm^{-1} in frequency. Using eq. 7.4 from Chapter 7 we find that the intrinsic oscillatory magnitude of a 2000 cm^{-1} oscillation will only be damped by about 70% meaning its observation should still be feasible.

8.4 Conclusion

FSRS has proven itself to be a versatile technique. It is easy to implement and, when performed on slowly evolving systems off resonance, the data are easy to interpret. However, when the systems exhibit large structural evolutions on the ultrafast time scale, what was once a simple interpretation becomes more nuanced and less intuitive. This should not be a surprise as vibrational spectroscopy probes *bound* nuclear motions and large and fast structural evolution necessarily implies highly anharmonic or even unbound nuclear potential energy surfaces. In light of this we have slowly

realized that FSRS does *not* provide "structural snapshots" of evolving systems.[16,18,206] However, because of the well defined phase of the vibrational coherence imparted by the ultrashort probe pulse and the self heterodyned nature of the spectroscopy we can intuit dynamics that occur faster than the vibrational dephasing time. Large and fast nuclear dynamics can be roughly separated into two groups: irreversible and oscillatory. Beautiful experiments performed by Kukura et al.[19] clearly showed that irreversible nuclear motion on the 200 fs timescale could be resolved even with vibrational dephasing times more than three times slower, and I have shown in Chapter 7 that 100 fs oscillatory motions can be measured even when the vibrational dephasing time is on the order of picoseconds. These two types of measurements demonstrate that FSRS can help us understand nuclear dynamics beyond the Born-Oppenheimer approximation by directly probing CIs and providing experimental data to test dynamical predictions of anharmonic reactive surfaces. As such I believe that FSRS offers a new perspective on condensed phase reactions which will only be fully appreciated in the future.

Appendix A

Etalon Design Principles

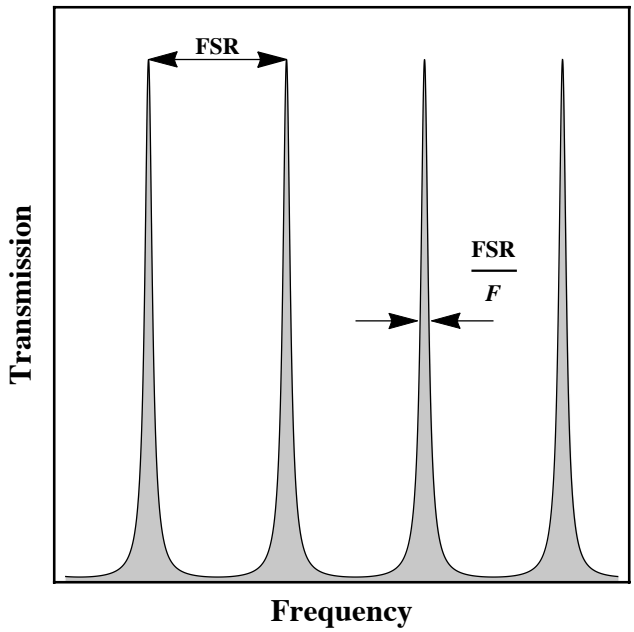

Figure A.1: An etalon's transmission as a function of incident frequency. Notice the periodically spaced approximately Lorenztian resonances.

Etalon's are simple pulse shaping devices. They are formed by two very flat, very reflective parallel surfaces placed in close proximity to one another. As described in Chapter 3 the input pulse bounces back and forth in the cavity interfering with itself and only wavelengths that are integer multiples of the cavity spacing are transmitted. More formally an etalon' s transmission follows eq. A.1.[94]

$$T(\nu) = \frac{1}{1 + \mathcal{F}^2 \sin^2\left(\frac{\pi\nu}{\mathrm{FSR}}\right)} \tag{A.1}$$

where $\mathcal{F}$ is the finesse of the etalon and FSR is the free spectral range of the etalon. The finesse is totally determined by the losses experienced by an EM field as it bounces back and forth between the mirrors and as such is primarily controlled by the reflectivity of the surfaces but is ultimately limited by imperfections and the overall quality of the cavity. On the other hand, the FSR is controlled by the spacing of the surfaces. Equation A.1 results in periodically spaced approximately Lorentzian line shapes each with a full width at half maximum (FWHM) that is roughly equal to FSR/$\mathcal{F}$, see Figure A.1. The free spectral range controls the spacing between the resonances, hence the name. Because the FSR depends on the separation of the surfaces it can be tuned by changing the angle of incidence of the input beam thereby changing the effective separation between the reflective surfaces; this operation will also shift the center frequency of a given resonance allowing the pass band of the filter to be tuned as well.

Intuitively, the FSR controls the intensity of the output pulses. If we assume a Gaussian shape for the intensity of our incident pulse in the frequency domain and that a transmission peak of the etalon is aligned with the maximum of the input pulse, then the ratio of the intensity of the pulse

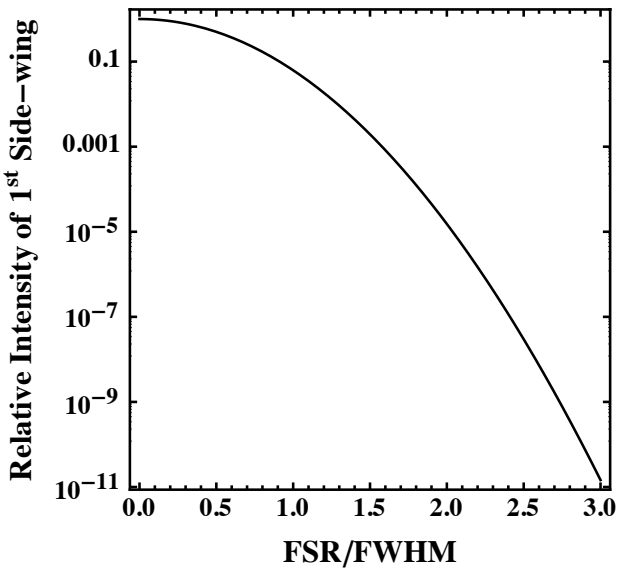

Figure A.2: The intensity of the first side-wing to the main pulse as a function of the ratio of the FSR to the FWHM. Notice that the intensity decreases drastically as the FSR is increased relative to the FWHM.

due to the neighboring etalon resonance–which is termed a "side-wing"–to the main output pulse is

$$\frac{I_{side}}{I_{main}} = 16^{-\left(\frac{\text{FSR}}{\text{FWHM}}\right)^2} \tag{A.2}$$

where FWHM is the bandwidth of the input pulse and FSR is the free spectral range of the etalon. Figure A.2 shows how the relative intensity of the side-wing to the main pulse varies with FSR/FWHM.

It is important to remember that the bandwidth, $\Delta\nu$, of the etalon's transmission bands increases linearly with FSR. Unfortunately, while it is possible to make spacers on the 10's of nm scale, giving FSR's in excess of 1,000 cm^{-1} it is not feasible to increase the finesse at the same pace. Therefore, there is a point where the increase in FSR makes the bandwidth unduly large resulting in poorly resolved Raman spectra. A good rule of thumb is to design the etalon such that its FSR is *twice* the FWHM of the input pulse. For example, for a pulse with a FWHM of 250 cm^{-1} (equivalent to a bandwidth limited ~60 fs pulse) and an etalon with an FSR of 500 cm^{-1} (corresponding to a distance of about 10 μm) the side-wings would be 65,536 times less intense than the main peak. Meaning that the signal to noise ratio would need to be in excess of 65536:1 in order to measure signals due to the side-wings.

Clearly, most of the energy loss in an etalon is simply due to the filtering process, see Figure A.3. Of course, there will be other losses associated with the specific optics but that will vary from manufacturer to manufacturer and with the other design and financial constraints. We can determine the transmission coefficient of the input pulse by calculating the transmitted intensity

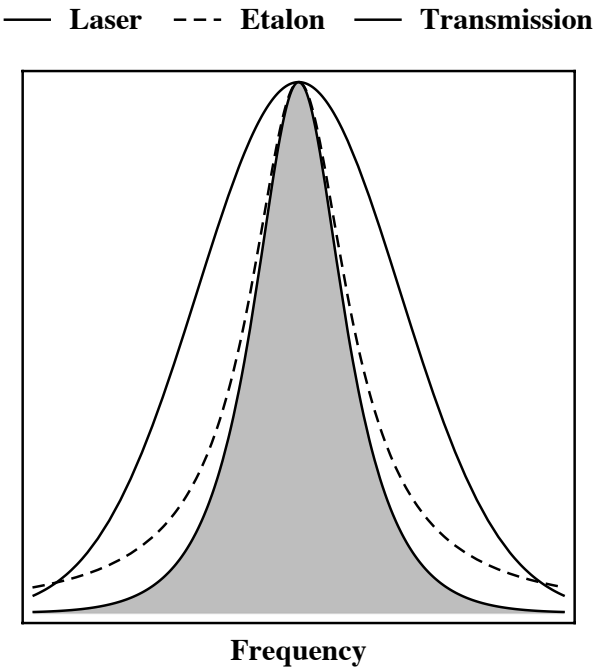

Figure A.3: The intensity profile of the input Gaussian pulse is shown in black, the transmission profile of the etalon in blue and the transmitted intensity of the output pulse in red. Note that the FWHM of the Gaussian pulse and etalon filter have been exaggerated for visualization.

and dividing it by the input intensity. In this case the input intensity as a function of frequency can be written as

$$I_{in}(\nu) = A \times 16^{-\left(\frac{\nu}{\Gamma_{in}}\right)^2} \tag{A.3}$$

Here $I_{in}(\nu)$ is a Gaussian function with a FWHM of Γ_{in}, A is the amplitude of the pulse and ν is the frequency. If we assume that the FSR of the etalon is much larger than Γ_{in} then the etalon's transmission function can be approximated as

$$T_{etalon} = \frac{\left(\frac{\Gamma_E}{2}\right)^2}{\nu^2 + \left(\frac{\Gamma_E}{2}\right)^2} \tag{A.4}$$

Here T_{etalon} is a Lorentzian with a FWHM of Γ_E. The intensity of the transmitted pulse is simply $I_{out}(\nu) = I_{in}(\nu)T_{etalon}(\nu)$ thus the transmission of the etalon can be calculated as

$$T = \frac{\int_{-\infty}^{\infty} I_{in}(\nu)T_{etalon}(\nu)d\nu}{\int_{-\infty}^{\infty} I_{in}(\nu)} = \frac{\pi^{3/2}\Gamma_E 2^{\frac{\Gamma_E^2}{\Gamma_{in}^2}-1}\,\mathrm{Erfc}\left(\frac{\sqrt{\ln 2}\Gamma_E}{\Gamma_{in}}\right)}{\sqrt{\ln 16}\Gamma_{in}} \tag{A.5}$$

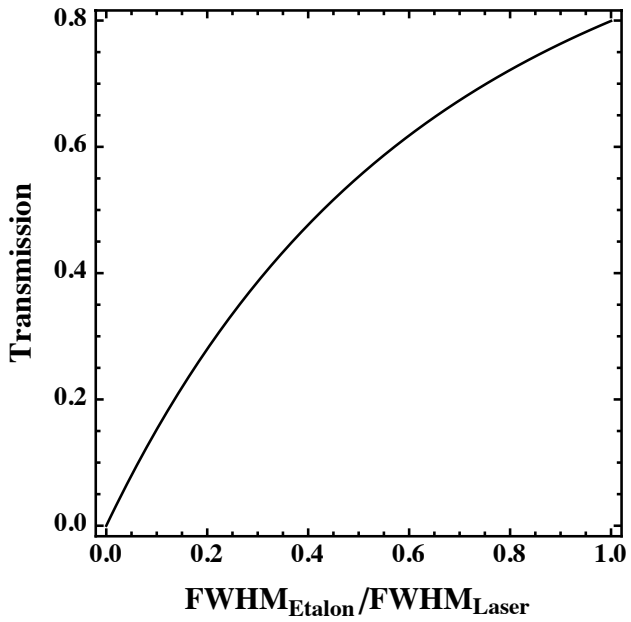

Figure A.4: The transmission of the etalon as a function of the ratio of the FWHM of the etalon to the FWHM of the input pulse.

We can write the transmission coefficient as a function of the ratio of the FWHM of the etalon to that of the laser pulse, i.e. $R = \Gamma_E/\Gamma_{in}$

$$T(R) = \frac{2^{R^2-1}\pi^{3/2}R \operatorname{Erfc}\left(\sqrt{\ln 2}R\right)}{\sqrt{\ln 16}} \tag{A.6}$$

For small values of R this reduces to

$$T(R) \approx \frac{\pi^{3/2}R}{2\sqrt{\ln 16}} \cong 1.67R \tag{A.7}$$

Figure A.4 shows how the transmission varies as a function of R. In general R will be on the order of 0.01 so the output pulse energy will be about 1-2% of the input energy.

Appendix B

Supporting Information for the Manuscript: Photoexcited Structural Dynamics of an Azobenzene Analog 4-Nitro-4'-Dimethylamino-Azobenzene from Femtosecond Stimulated Raman

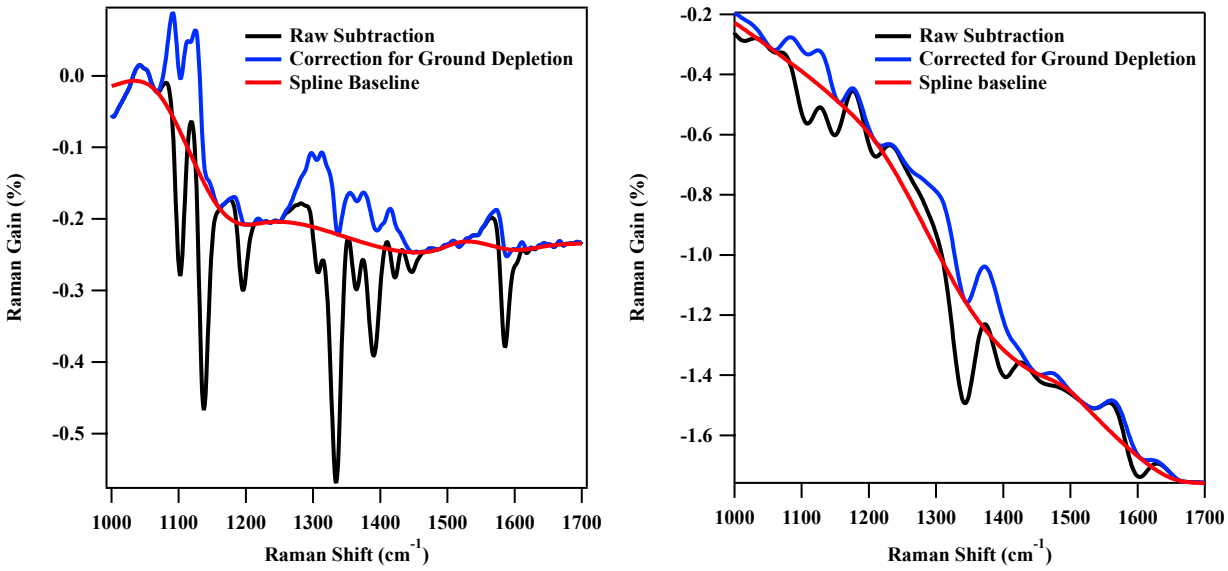

(a) Typical data from the 800 nm instrument

(b) Typical data from the tunable instrument

Figure B.1: Demonstrates the main steps to extract transient FSRS spectra from the raw data. Initial subtractions are shown in black, spectra after ground state compensation are shown in blue and the baselines are shown in red.

B.1 Data Analysis

After performing the appropriate averaging of the various spectra, i.e. transient, ground and solvent, the ground state spectrum is subtracted from each transient spectra. In order to correct for any long term fluctuations in the regenerative amplifier's output, the transient spectra were normalized to the ground state spectrum using the 670 cm^{-1} line of DMSO as an internal standard. Normalizing also helps correct for the transient absorption of the Raman pump by the excited state species. This effect is non-negligible for λ_{ex} = 625 nm.

Subtracting the ground state spectrum from the transient spectra effectively removes the solvent contributions but it over corrects for the ground state contribution. Figure B.1 presents representative spectra for both the 800 nm and tunable instruments, the black lines show the spectra after the initial subtraction. To account for the ground state depletion the pure ground state spectrum is added back to the raw subtraction until the ground state depletion is satisfactorily compensated for, shown as the blue lines in Figure B.1. In order to obtain the pure ground state spectrum the solvent signals were removed by subtraction, again normalizing to the ground state spectrum using the 670 cm^{-1} mode of DMSO. Any residual baseline was then removed and the final spectrum was fit to a sum of Gaussians. This fit was used as the "pure" spectrum to avoid adding noise to the transient spectra. Finally, the baselines were removed from the ground depletion corrected transient spectra by fitting a third order spline through points chosen as the baseline and subtracting this from the

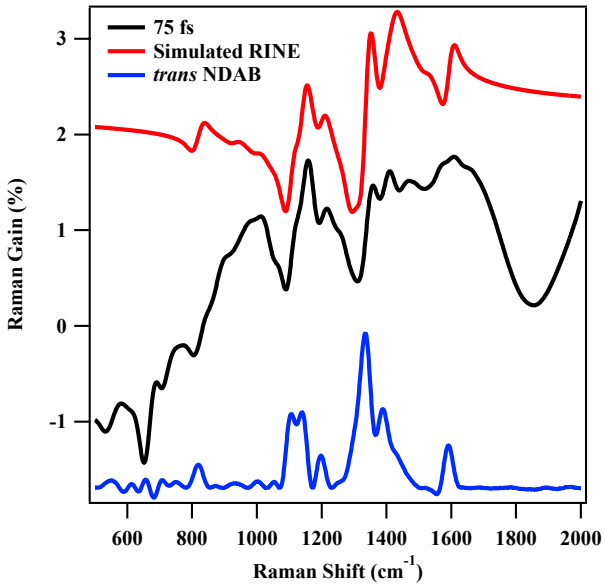

Figure B.2: Simulated RINE spectra compared with the experimentally recorded 75 fs raw difference spectrum and the ground state *trans* spectrum both recorded at λ_{ex} = 625 nm. The simulated RINE spectrum (generated as described in the text) almost exactly reproduces the experimentally observed 75 fs difference spectrum. Any differences can be attributed to underlying excited state transients, this is especially visible near 1600 cm^{-1}

spectra. The spline baseline is shown in red in Figure B.1.

B.2 RINE Simulations

As mentioned in the main text, the early time transients at λ_{ex} = 625 nm are dominated by RINE. In order to test this hypothesis a simulated RINE spectrum was generated and compared to the experimental spectra. Figure B.2 presents an example comparison in which shows the experimental ground state *trans* and excited state transient at a time delay of 75 fs with the Raman pump at 625 nm. The simulated RINE spectrum almost quantitatively matches the transient spectrum especially in the CN and NN stretching regions, strongly supporting the original hypothesis. It should be noted that the transient spectrum deviates significantly from the simulated one in the NO_2 and $C-N(Me)_2$ stretching region likely due to underlying excited state resonances.

As explained by McCamant, Kukura, and Mathies[69] RINE results when the Raman pump and probe interactions produce a vibrational coherence on the ground state surface. As such the appearance of the RINE spectrum is that of dispersive peaks centered at ground state frequencies. In their derivation McCamant, Kukura, and Mathies assumed that the Raman pump had an infinite duration and found that the resulting line-shape was that of a dispersive Lorentzian. Unfortunately, the Raman pump produced by the tunable instrument has a much shorter duration which was taken

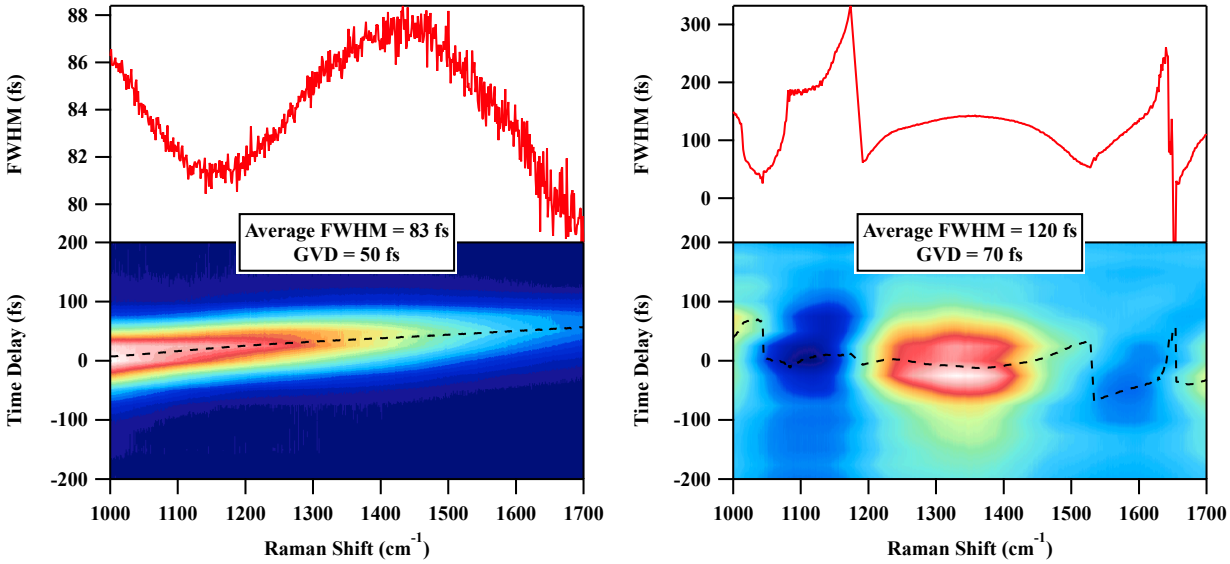

(a) λ_{Apu} = 500 nm, λ_{pr} = 857 – 912 nm

(b) λ_{Apu} = 500 nm, λ_{Rpr} = 667 – 700 nm

Figure B.3: Typical frequency resolved optical Kerr effect (OKE) cross correlation traces taken with (a) the 800 nm instrument and (b) the tunable instrument. The top trace shows how the FWHM varies with each pixel while the bottom contour shows the raw data with the position of t_0 indicated by the dotted line. Note that because of imperfections in the probe polarization and the analyzer used with the tunable instrument the OKE signal changes sign periodically leading to uncertainty in the position of t_0 and the FWHM at these pixels.

into account by modeling the line-shape as a convolution of a dispersive Lorentzian with a Gaussian. With this in mind, the ground state spectrum was analyzed and the widths, heights and center frequencies of the various vibrational resonances were extracted. Using this data, the simulated spectrum was generated by placing dispersive Lorentzians at each center frequency, scaled by the height and with a width proportional to the ground state width then the whole spectrum was convoluted with a Gaussian (FWHM of 30 cm^{-1}), this is the red line in Figure B.2.

B.3 Instrument Response Functions

Figure B.3a presents typical instrument response functions for both instruments.

B.4 Transient Absorption

Figure B.4 presents the transient absorption of *trans*-NDAB at two wavelengths. Data where recorded by modulating the actinic pump with an optical chopper (Perkin Elmer, Model 651)

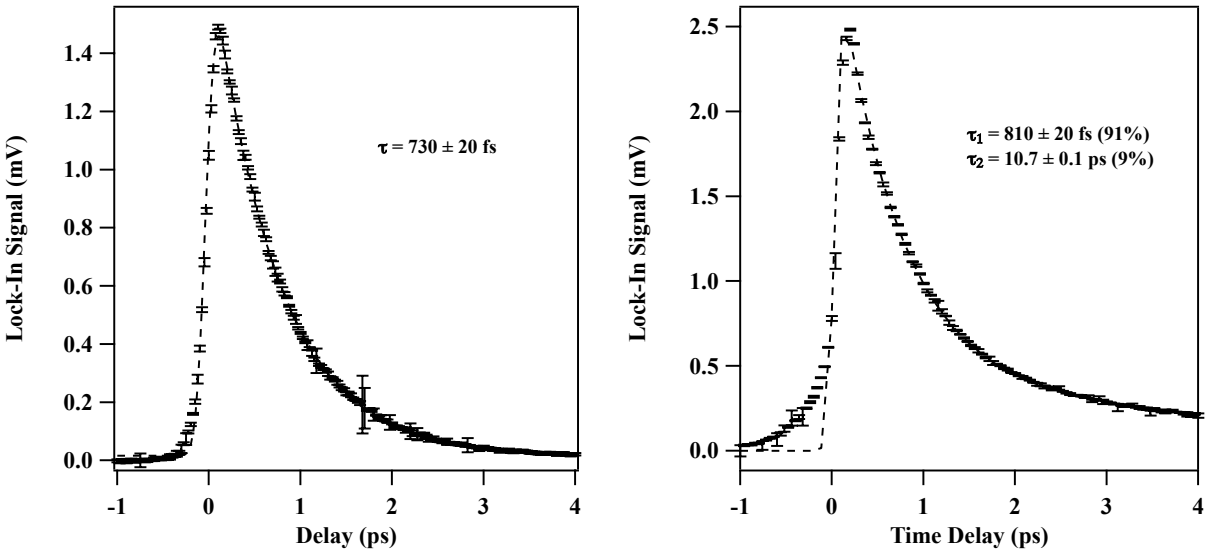

(a) Transient absorption at 790 nm

(b) Transient absorption at 625 nm

Figure B.4: Transient absorption of *trans*-NDAB excited at 500 nm. (a) Show the transient absorption at 790 nm and (b) shows the transient absorption at 625 nm. Note that the trace at 625 nm is bi-exponential; 625 nm is close enough to the ground state absorption that the effects of vibrational cooling are apparent.

and amplifying the output of a photodiode (ThorLabs, DET110) with a lock-in amplifier (Stanford Research Systems, SR830).

B.5 *cis* Absorption Spectrum

As mentioned in the main text the *cis* isomer of NDAB is short lived in polar solvents but has a lifetime on the order of 10-100 seconds in non-polar solvents. Complicating matters further is the fact that the absorption spectrum for the *cis* and *trans* isomers overlap substantially. Fortunately, because of the short lifetime of the *cis* isomer it was possible to record a pure *trans* spectrum after allowing the sample to dark adapt. In order to decompose the mixed spectrum, the acquisition of which is described in the main text, the spectrum was fit to a sum of Gaussians and a scaled pure *trans* spectrum. The initial positions and intensities of the Gaussians were suggested by TD-DFT calculations on the *cis* isomer, c.f. Figure B.5. The resulting *cis* spectrum was then divided by (1 − *trans* scale factor) to obtain a properly scaled spectrum, i.e. correcting for the concentration. The results of this procedure are presented in Figure 1(a) in the main text.

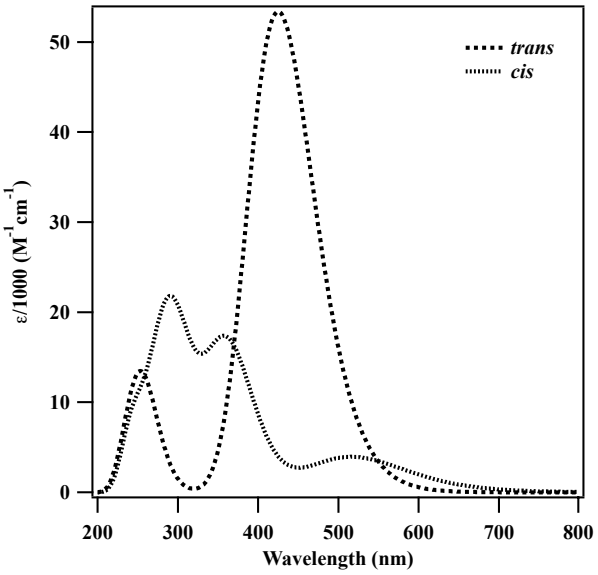

Figure B.5: Calculated absorption spectra of *trans* and *cis* NDAB in CCl_4 are shown. Calculations were performed using the TD-DFT formalism with the M06-2X functional and the 6-311++g(d,p) basis set, solvent effects were included by a Polarizable Continuum Model (PCM) using the integral equation formalism variant (IEFPCM) as implemented by the Gaussian 09 software package.[117]

B.6 Electronic Structure Calculations

In order to determine the character of the vibrational modes of NDAB, normal mode frequency calculations were performed using the DFT formalism at the B3LYP/6-311G++(d,p) level using the Gaussian 09 software package.[117] Because the calculation of IR intensities is much easier, and therefore more accurate, than calculating Raman intensities, coupled with the fact that NDAB is *not* centrosymmetric and therefore *not* subject to the mutual exclusion rule, the FTIR spectrum was used to assign the normal modes. Figure B.6 presents the calculated and experimental IR spectra demonstrating that the agreement between the theory and experiment is excellent. The normal mode characterizations based on this calculation are presented in Table B.1.

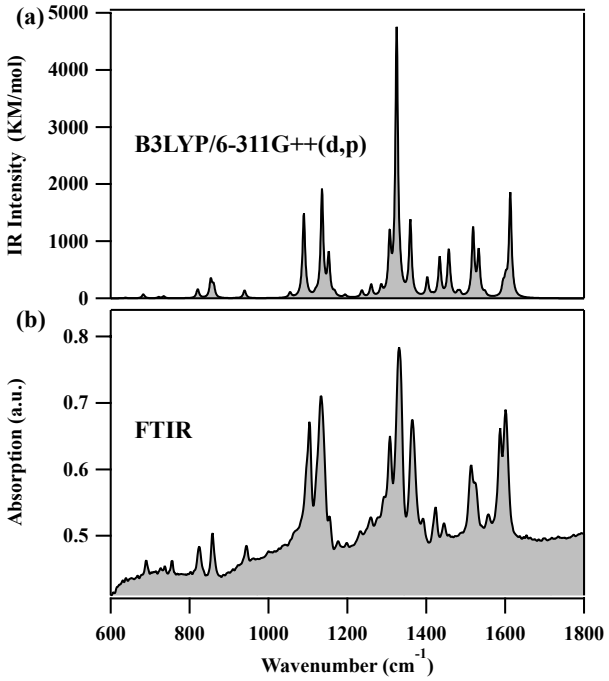

Figure B.6: (a) Calculated and (b) experimental (KBr pellet, Varian, Model 3100) IR absorption spectra of NDAB. The calculated spectrum has had its frequency axis scaled by 0.978.

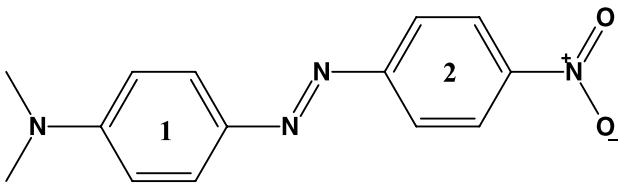

Figure B.7: *trans* 4-Nitro-4'-Dimethylaminoazobenzene (NDAB).

Table B.1: A summary of the normal mode frequencies and assignments of ground state *trans*-NDAB, included are the experimentally observed frequencies using three different vibrational spectroscopies. Ring numbering refers to Figure B.7. All numbers are in cm^{-1}.

Raman λ_{ex} = 497 nm	**FSRS** λ_{ex} = 790 nm	**FTIR**	**DFT** B3LYP 6-311g++(d,p)	**Mode Character**
1105	1103	1103	1114	H rock, ring 2 breathing, CN stretch
1138	1136	1132	1161	CN stretching (both), H rock both rings
1196	1197	1198	1221	CN stretches out of phase
—	—	1259	1288	CN stretches out of phase
1307	1317	1308	1337	C(ring 1)N=N bend, H rock ring 1
1338	1336	1331	1354	N=N stretch, NO_2 symmetric bend
1367	1367	1364	1390	N=N stretch, H in phase rock ring 1
1391	1390	1393	1434	Out of phase C=C stretches (either side of ring 2) and N=N stretch
1424	1423	1423	1466	N=N stretch and C=C stretches on either side of both rings out of phase
1448	1441	1445	1490	N=N stretch and C=C stretches on either side of both rings out of phase
1588	1588	1587	1637	NO_2 asymmetric stretch C=C stretches on ring 2, N=N stretch
1604	1604	1601	1649	C−$N(Me)_2$ stretch, C=C stretches ring 1, with a little methyl deformation

Appendix C

Supporting Information for the Manuscript: Low Frequency Resonant Impulsive Raman Modes Reveal Inversion Mechanism for Azobenzene

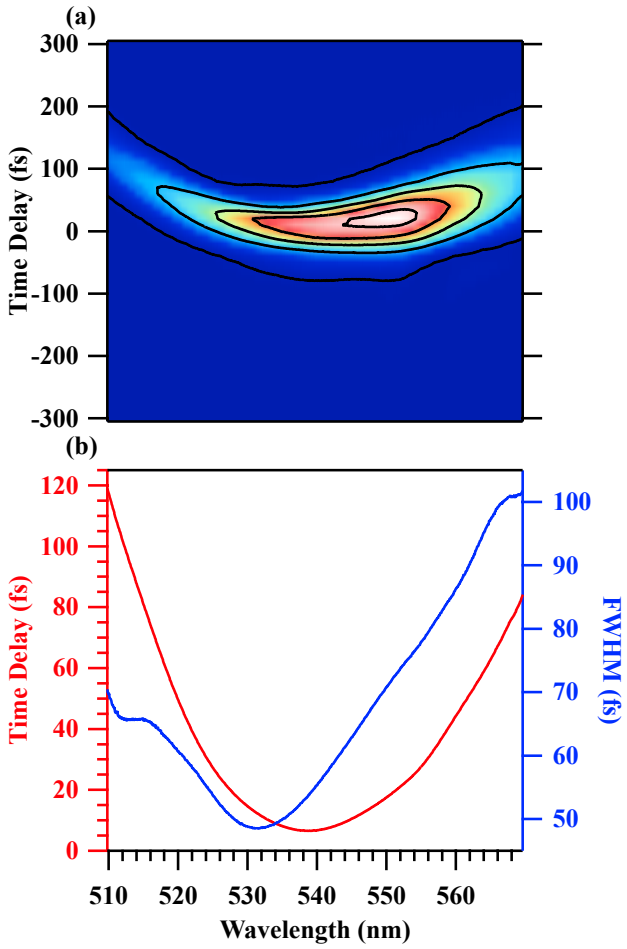

Figure C.1: (a) Frequency resolved cross correlation between the pump and the probe pulses measured by the optical Kerr effect in DMSO in the sample cell. (b) Extracted centers and FWHMs of Gaussian fits to the cross correlation profile at each wavelength.

C.1 Supplementary Data

Figure C.1(a) presents the frequency resolved cross-correlation of the probe gated by the pump as measured with the Kerr gating method in the sample cell with the solvent, DMSO, present. The time trace for each pixel was fit to a Gaussian model function and the extracted parameters–the position in red and the width in blue–are presented in Figure C.1(b).

Figure C.2 presents the resonance Raman spectrum of NDAB in dioxane between 120 and 350 cm^{-1}. Without solvent interference two bands at 281 and 319 cm^{-1} are clearly visible. These two bands, which are assigned to the nitrogen "pedal" motion described in the text, are estimated to have dimensionless displacements that are much smaller than the 47 cm^{-1} mode based on the short time approximation outlined below.

C.2 Video Generation

Video S1* is the animated analog of Figure 5.6 in the main text. It presents the four lowest frequency, resonance Raman active, vibrational modes. The animation was generated by displacing the molecule along the each normal coordinate in a sinusoidal pattern with a normalized frequency so that they all move at the same speed. Video S2† presents the molecule displaced along the two lowest frequency coordinates, which we believe make up the majority of the reaction coordinate, using eq. C.1 for the ~15 cm^{-1} mode and eq. C.2 for the ~50 cm^{-1} mode.

$$q(t) = \Delta(1 - \cos(\omega t)) \tag{C.1}$$

$$q(t) = \frac{\beta \omega t^2}{2\hbar} \tag{C.2}$$

Equation C.1 describes the movement of the center of a classical wave packet on a harmonic surface of frequency ω with a dimensionless displacement from the ground state minimum of Δ. Equation C.2 is similar to eq. C.1 except that the excited surface is linear with slope β, the ground state is still a harmonic surface with frequency of β.

C.3 Resonance Raman Data Analysis

Figure C.3 presents the differential cross-sections of three Raman intensity standards. Peak intensities were determined by fitting to Lorentzian lineshapes. The DMSO symmetric C=S stretch 667 cm^{-1} was used as an internal intensity standard in for the calculation of NDAB cross-sections. The differential cross-section of the 667 cm^{-1} band was first determined by comparison with the well characterized 992 cm^{-1} band of benzene as an external standard and fit to eq. C.3.[226]

$$\frac{\partial \sigma}{\partial \Omega}(\nu) = K \nu \nu_s^3 \left[\frac{\nu_e^2 + \nu^2}{\left(\nu_e^2 - \nu^2\right)^2} \right]^2 \tag{C.3}$$

Equation C.3 describes the frequency dependence of pre-resonant scattering, K is a scaling constant, ν is the excitation frequency, ν_s is the scattered frequency and ν_e is the approximate frequency of the lowest lying electronic state.

The absolute Raman cross-sections of NDAB were calculated using eq. C.4.

$$\sigma_{NDAB} = \frac{8\pi}{3} \left(\frac{1 + 2\rho}{1 + \rho} \right) \left[\left(\frac{\nu - \nu_{NDAB}}{\nu - \nu_{std}} \right)^3 \left(\frac{A_{NDAB}}{A_{std}} \right) \left(\frac{C_{std}}{C_{NDAB}} \right) \left(\frac{\partial \sigma_{std}}{\partial \Omega} \right) \right] \tag{C.4}$$

Where A is the area of the fit peaks, C is the concentration of solute and solvent, ν is the excitation frequency, $\nu - \nu_{NDAB}$ is the frequency of scattered photons, $\frac{\partial \sigma_{std}}{\partial \Omega}$ is the differential cross-section of the standard and ρ is the depolarization ratio of NDAB which was taken to be $1/3$.

*Video available at http://pubs.acs.org/doi/suppl/10.1021/jp408470a/suppl_file/jp408470a_si_002.mov

†Video available at http://pubs.acs.org/doi/suppl/10.1021/jp408470a/suppl_file/jp408470a_si_003.mov

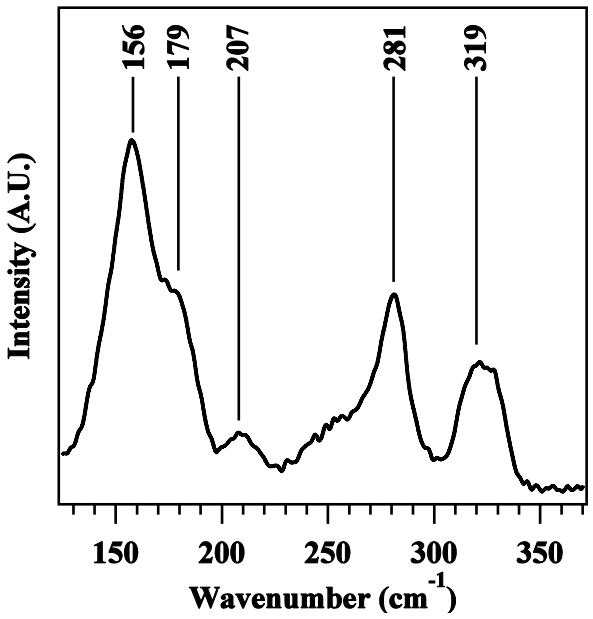

Figure C.2: Low frequency resonance Raman spectrum of NDAB excited at 514 nm in dioxane. The 281 and 319 cm^{-1} modes are unobstructed by solvent peaks.

Figure C.4 presents resonance Raman spectra of NDAB taken at 8 different excitation wavelengths. The resonance Raman spectra reveal interesting non-tuning resonances in the 920 cm^{-1} and 949 cm^{-1} modes. Similar resonance features at 927 and 985 cm^{-1} in *trans*-azobenzene have been implicated in vibronic coupling the 1^1B_u $\pi \rightarrow \pi^*$ to the state 1^1B_g $n \rightarrow \pi^*$ states.[227,228] We propose that these features may be better explained by rapid C_{2h} symmetry breaking on the $n \rightarrow \pi^*$ excited state. These features will be discussed in future work.

C.4 Resonance Raman Intensity Analysis

The absorption and Raman scattering cross-sections were modeled simultaneously using the time dependent wave packet formulation described by eqs. C.5 and C.6.[140]

$$\sigma_A = \frac{4\pi E_L e^2 M^2}{6\hbar^2 cn} 2\Re \left[\int_0^\infty \langle i|i(t)\rangle \exp\left(\frac{i(E_L+\epsilon_i)}{\hbar}\right) e^{-\Gamma t/\hbar} dt \right] \tag{C.5}$$

$$\sigma_R = \frac{8\pi E_s^3 E_L e^4 M^4}{9\hbar^6 c^4} \left| \int_0^\infty \langle f|i(t)\rangle \exp\left(\frac{i(E_L+\epsilon_i)}{\hbar}\right) e^{-\Gamma t/\hbar} dt \right|^2 \tag{C.6}$$

Where M is the transition dipole length, E_0 is the excitation energy, ϵ_i is the vibrational energy of the initial state and Γ is the damping factor, which is the time domain equivalent of the homogenous linewidth in the frequency domain. The cross-sections are determined by the multidimensional Franck-Condon (FC) overlaps of the ground state wave packet propagated by the excited state

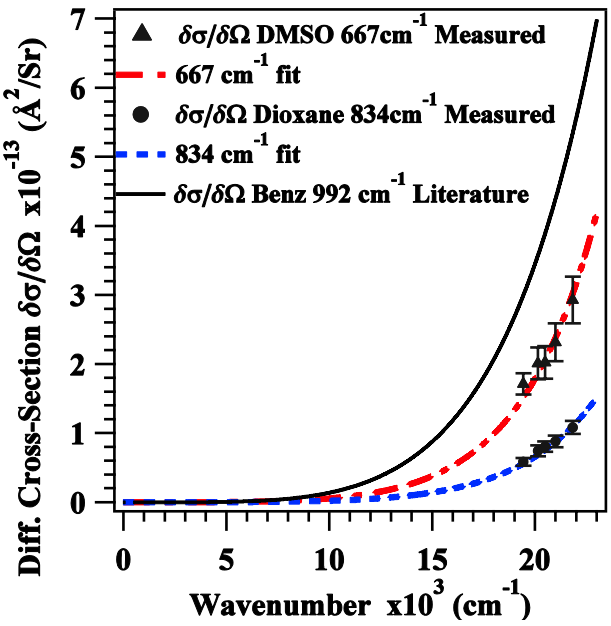

Figure C.3: Fits to eq. C.3 for three common solvents with the following parameters: DMSO: 667 cm^{-1}, $K = 47.9 \times 10^{-13}$Å^2/Sr, $\nu_e = 54{,}600 cm^{-1}$ Dioxane: 834 cm^{-1}, $K = 21.4 \times 10^{-13}$Å^2/Sr, $\nu_e = 56{,}200 cm^{-1}$ Benzene: 992 cm^{-1}, $K = 704 \times 10^{-13}$Å^2/Sr, $\nu_e = 80{,}000 cm^{-1}$

Hamiltonian, $|i(t)\rangle$. When the potential energy surfaces are approximated by separable harmonic surfaces with equal frequencies, the multidimensional overlaps can be expressed as follows:

$$\langle i|i(t)\rangle = \sum_{j=1}^{N} \exp\left[-\frac{\Delta_j}{\sqrt{2}}\left(1 - \exp(-i\omega_j t)\right)\right] \tag{C.7}$$

$$\langle f|i(t)\rangle_i = -\frac{\Delta_i}{\sqrt{2}}\left(e^{-i\omega_i t} - 1\right) \sum_{j=1}^{N} \exp\left[-\frac{\Delta_j}{\sqrt{2}}\left(1 - \exp(-i\omega_j t)\right)\right] \tag{C.8}$$

Where Δ is the dimensionless displacements of the ground and excited state potential harmonic minima. The predicted Δ's for each of the resonance Raman active modes are presented in Table C.1.

A comparison with previous work highlights the effect of including low frequency modes.[228] Low frequency modes carry the wave packet out of the FC active region irreversibly because by the time the low frequency component completes one period, the multidimensional overlap has dephased. As a consequence of short time dynamics the time dependent overlap can be Taylor expanded and truncated at the first order term. At this order the Raman cross-section becomes proportional to the square of the slope of the excited state potential energy surface, i.e. $\sigma_R \propto \Delta^2\omega^2$. This rough approximation indicates that low frequency modes may be highly displaced despite having a relatively small Raman cross-section while the same is less true for high frequency modes.

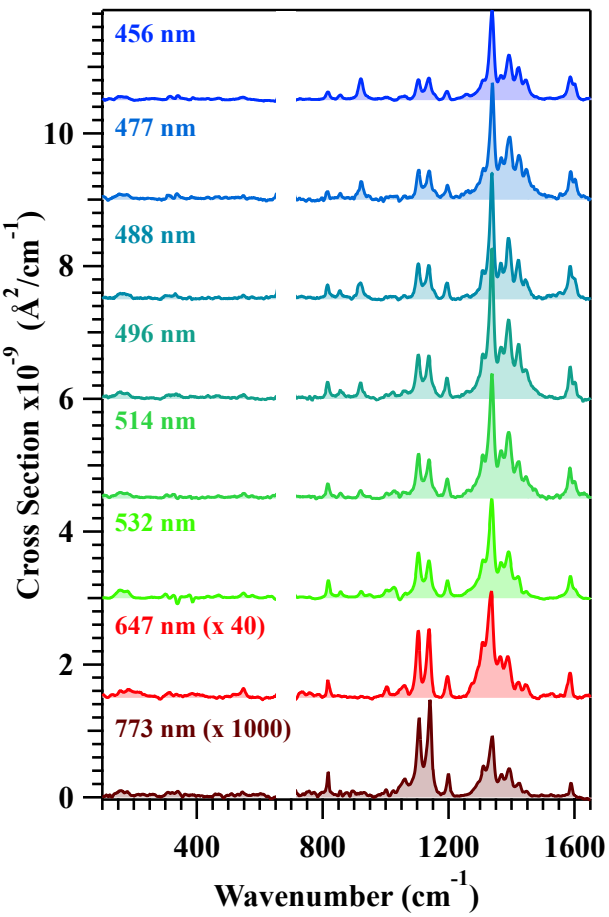

Figure C.4: Resonance Raman spectra of NDAB in DMSO with eight different excitation wavelengths. Spectra have been scaled such that the peak areas represent their absolute Raman cross-section. Solvent bands have been subtracted and regions of substantial solvent interference have been excluded for clarity.

Figure C.5 and C.6 present the measured and modeled absorption and Raman cross-sections, respectively. The 47 cm^{-1} mode's cross-section was estimated to be 0.8 times the combined cross-sections of the 156 and 179 cm^{-1} modes based on the RISRS results presented in the main text. The 47 cm^{-1} mode was modeled using both a harmonic and a linear dissociative excited state potential energy surface. Both models yielded a slope of ~300 cm^{-1} (equivalent to a harmonic Δ of ~6).

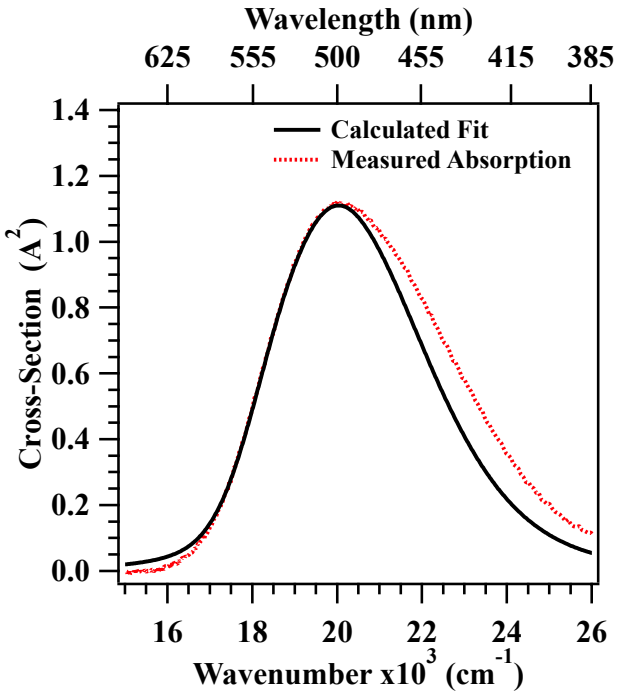

Figure C.5: Comparison of experimental and calculated absorption cross-section of NDAB modeled with the following parameters: $E_0 = 18{,}280$ cm^{-1}, $M = 2.04$ Å, $\Gamma = 380$ cm^{-1}, $\theta = 690$ cm^{-1}.

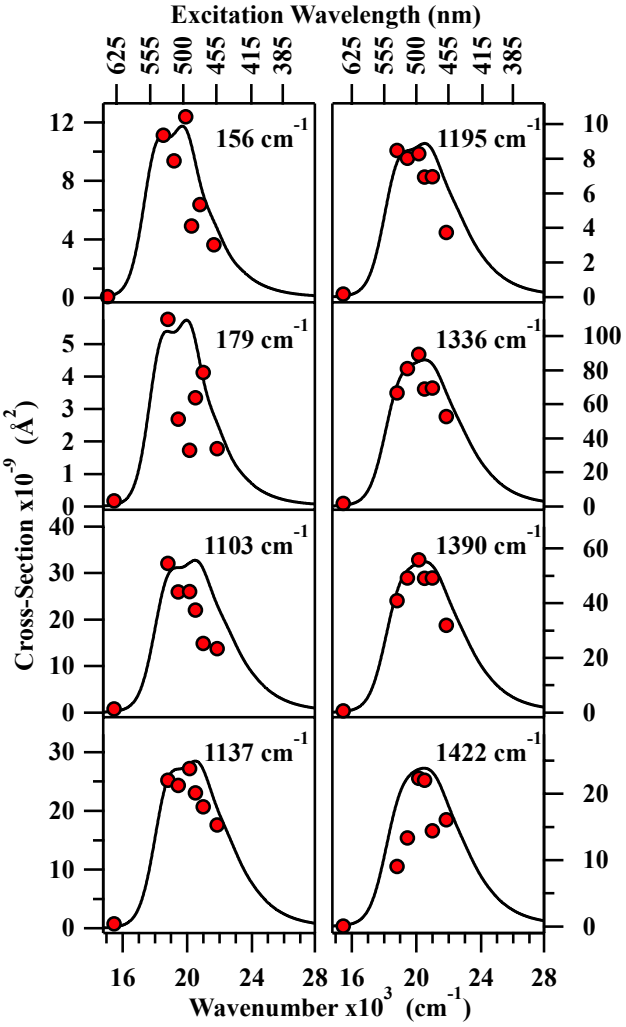

Figure C.6: Experimental cross-sections (red circles) with calculated Raman excitation profiles (black lines) for eight NDAB modes.

Table C.1: Resonant Raman active modes and dimensionless displacements as determined from time dependent wave packet modeling.

Shift (cm^{-1})	Δ
47	6.00
156	1.80
179	1.10
547	0.35
817	0.35
854	0.28
1103	0.57
1137	0.52
1195	0.28
1308	0.37
1336	0.80
1362	0.33
1390	0.62
1422	0.40
1445	0.40
1585	0.31
1598	0.20

Appendix D

Supporting Information for the Manuscript: Electron Transfer Dynamics of Triphenylamine Dyes Bound to TiO_2 Nanoparticles from Femtosecond Stimulated Raman Spectroscopy

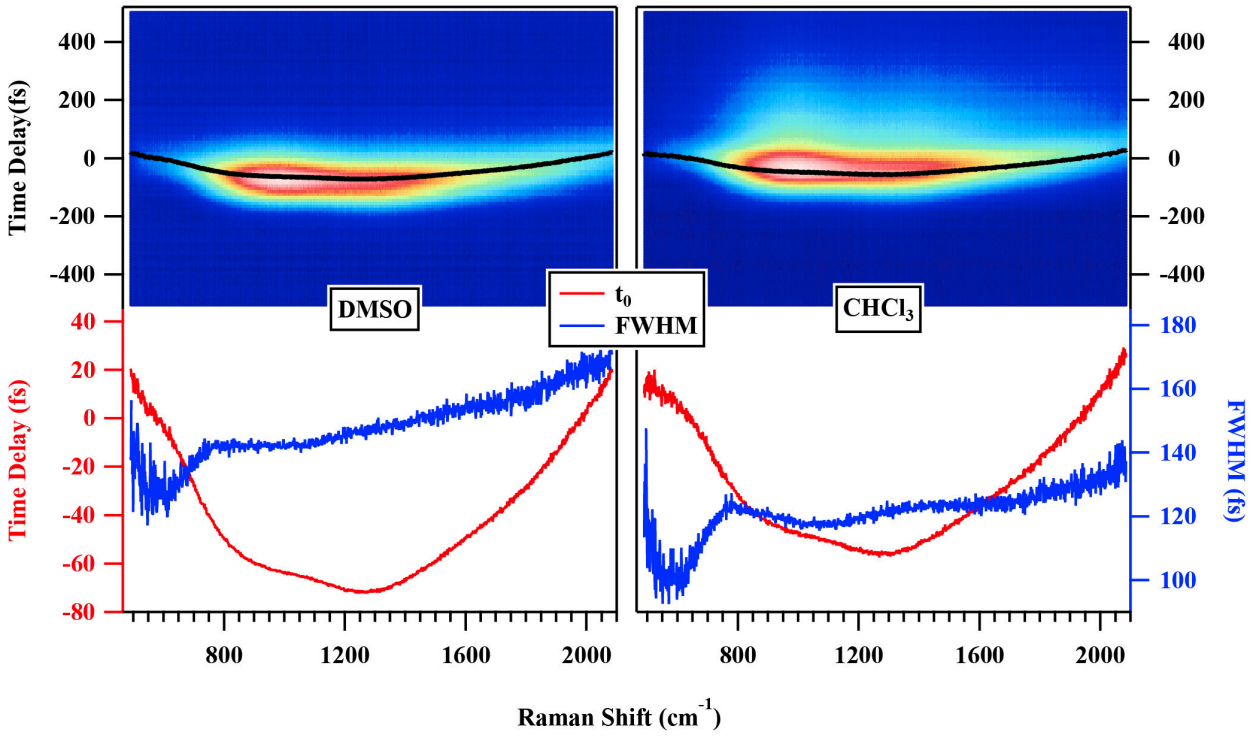

Figure D.1: Representative examples of dispersed cross correlations measured in the sample cell in DMSO (left) and $CHCl_3$ (right). The contour plots shown at the top are the raw data, and the traces shown on the bottom are the extracted instrument response function parameters, the center (red) and the full width at half maximum (FWHM, blue). For the DMSO data the IRF at each pixel was modeled as a single Gaussian function. On the other hand, the $CHCl_3$ data was modeled as the sum of a Gaussian component, for the instantaneous electronic response, and an exponential decay component, for the impulsively excited vibrations. These data were taken on the same day, one after the other.

D.1 Instrument Response Function

For each experiment the instrument response function (IRF) was measured using a Kerr gating method. The actinic pump and Raman probe were aligned into the sample cell. An analyzer was placed after the collimating lens and adjusted to extinguish as many probe photons as possible, then the polarization of the actinic pump was set to 45° relative to the probe. When the pump and probe are overlapped in time, the nonlinear birefringence induced by the pump rotates the polarization of the probe increasing the intensity recorded after the analyzer. The delay between pump and probe was varied with a computerized delay state, and the dispersed probe photons were recorded on the CCD. Presented in Figure D.1 are examples recorded in DMSO (left) and $CHCl_3$ (right). An advantage of this method is that the IRF is measured in the same sample cell and solvent used in the experiment.

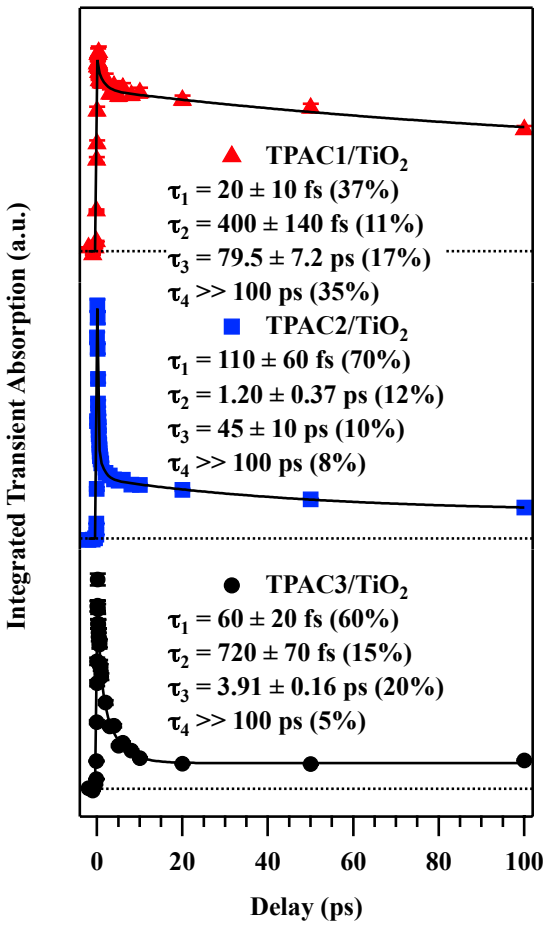

Figure D.2: Transient absorption integrated between 830 and 940 nm of TPAC1/TiO_2 (top), TPAC2/TiO_2 (middle) and TPAC3/TiO_2 (bottom) are shown as the markers. The dotted lines show zero. Multiexponential fits are shown as the black lines and the extracted time constants are shown in the legend.

In the case of DMSO, the IRF at each pixel (i.e. vertical slice in Figure D.1) can be accurately modeled as a Gaussian function indicating that the actinic pump is only interacting with the electronic degrees of freedom. On the other hand, for $CHCl_3$, the actinic pump can impulsively excite low frequency vibrational motions leading to an asymmetric IRF. This can be appropriately modeled by convoluting a Gaussian representing the IRF, with the sum of a delta function for the electronic component, and a decaying exponential for the vibrational component. Shown at the bottom of Figure D.1 are the extracted widths and center positions of the per-pixel IRFs. The similarity between those recorded in DMSO, which only has an instantaneous electronic response, and $CHCl_3$, which has an additional slow vibrational response, indicates that the modeling detailed above is appropriate.

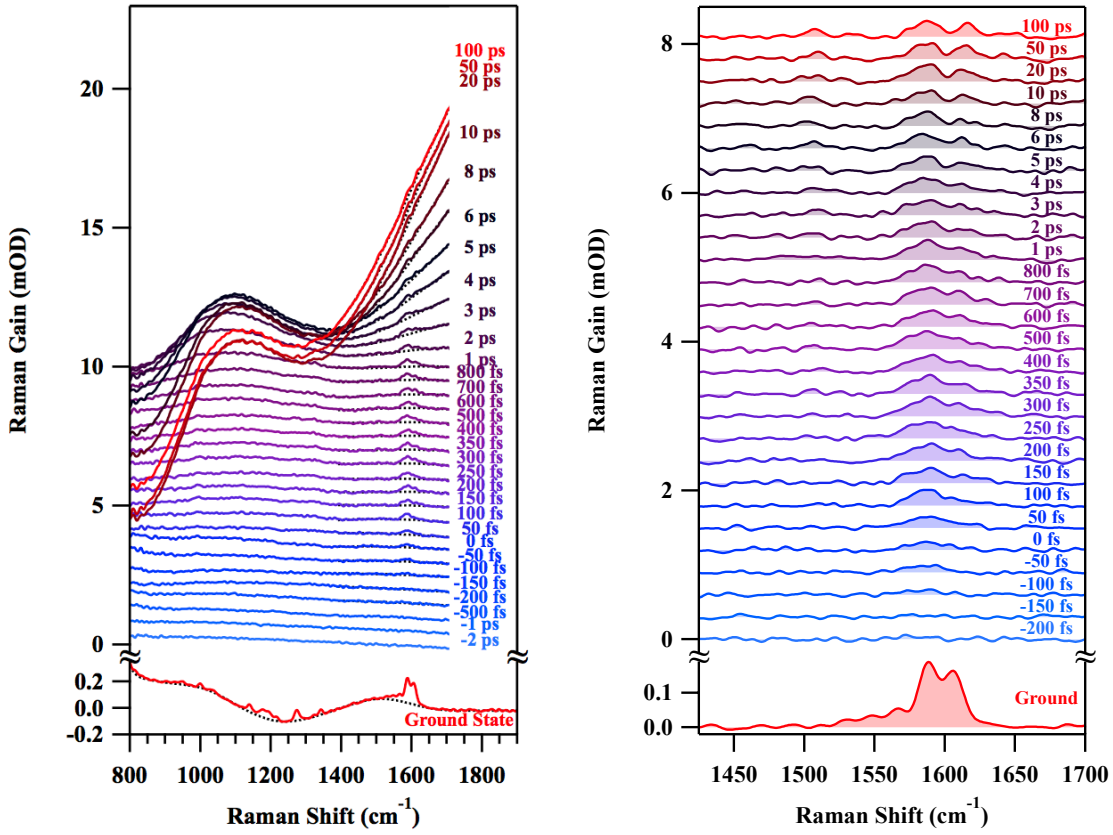

Figure D.3: Complete Raman spectra of TPAC1. Raw data is shown on the left, and baseline subtracted data is shown on the right. Traces have been offset for clarity. Baselines (dotted lines) for the excited state were estimated algorithmically by fitting the spectra to a model function consisting of one or more Gaussian peaks for the signal and a 3rd order polynomial for the baseline. Ground state baselines were generated by fitting a spline through hand chosen points.

D.2 Supplementary Data

Figure D.2 presents the time evolution of the integral of the transient absorption (TA) from 830-940 nm of the conjugated TPACs, shown in the bottom half of Figure 6.2 in Chapter 6. These decays were fit to the sum of three exponentials and a constant offset–used to model a very long time component–convoluted with the instrument response function. Algebraically,

$$TA(t) = S(t) \otimes \left(A_0 + \sum_{i=1}^{3} A_i e^{-t/\tau_i} \right) \tag{D.1}$$

and

$$\sum A_i = 1 \tag{D.2}$$

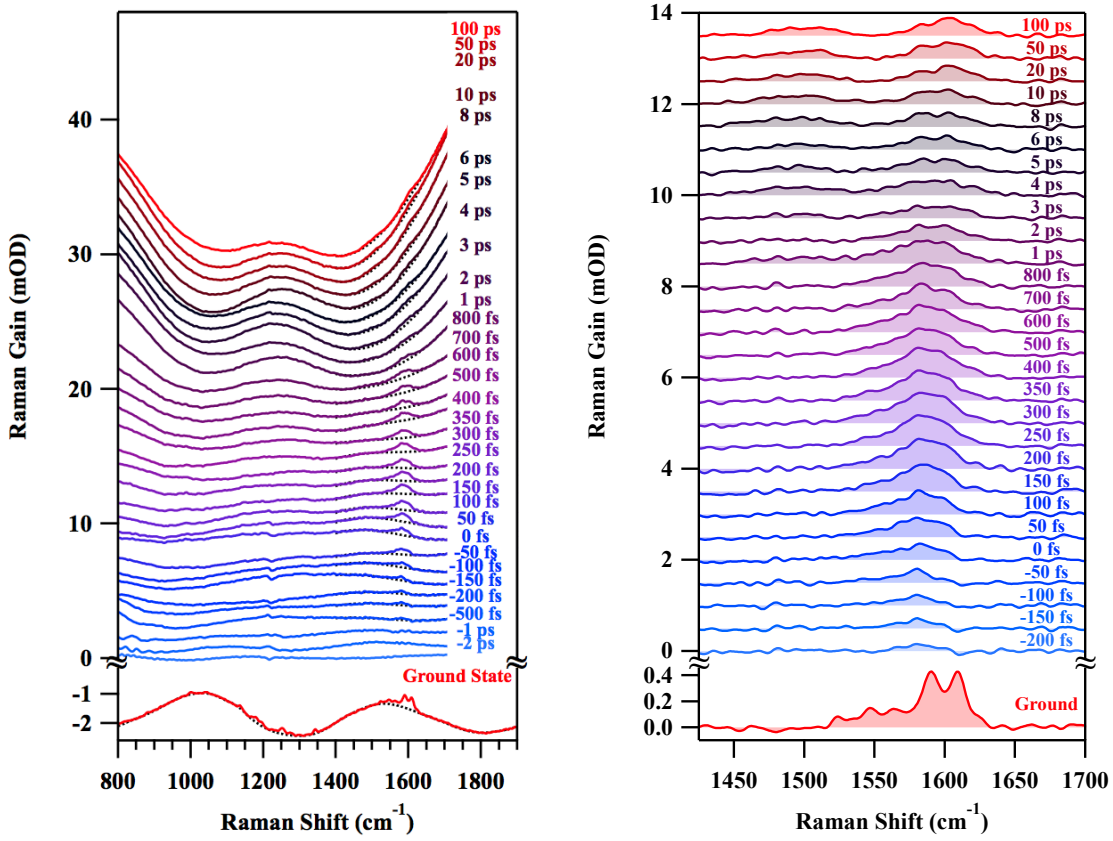

Figure D.4: Same as Figure D.3 but for conjugated TPAC1.

Where $TA(t)$ is the integral of the TA, $S(t)$ is the instrument response function, and A_i and τ_i represent the fractional amplitude and the time constant, respectively, of the i^{th} decay component. Fits are shown as solid black lines and the dotted lines indicate zero. The amplitudes and time constants are tabulated in Figure D.2 and depicted visually in Figure 6.3 of the main text.

Figure D.3 presents the raw (left) and baseline subtracted (right) data of TPAC1. Figures D.4, D.5 and D.6 are the corresponding figures for conjugated TPAC1, TPAC2 and conjugated TPAC2, respectively. The baselines (dotted lines) for the ground state spectra were estimated by and interpolating a spline through points manually chosen as belonging to the baseline, similar to previous studies.[20–22,24,49,229,230] On the other hand, the baselines of the excited state spectra were estimated by fitting a subregion of the spectra to one, in the case of the free dye samples, or two, in the case of the conjugates samples, Gaussian peaks for the signal and a third order polynomial for the baseline. This method has been previously used to analyze the FSRS spectra of 4-(Dimethylamino)benzonitrile.[25]

Presented in Figure D.7 is a comparison of the observed excited state Raman spectra 100 ps after excitation, shown in red, of conjugated TPAC1 (left) and TPAC2 (right) with the predicted spectra of the corresponding radical cation, shown in blue. Radical cation Raman cross sections, shown

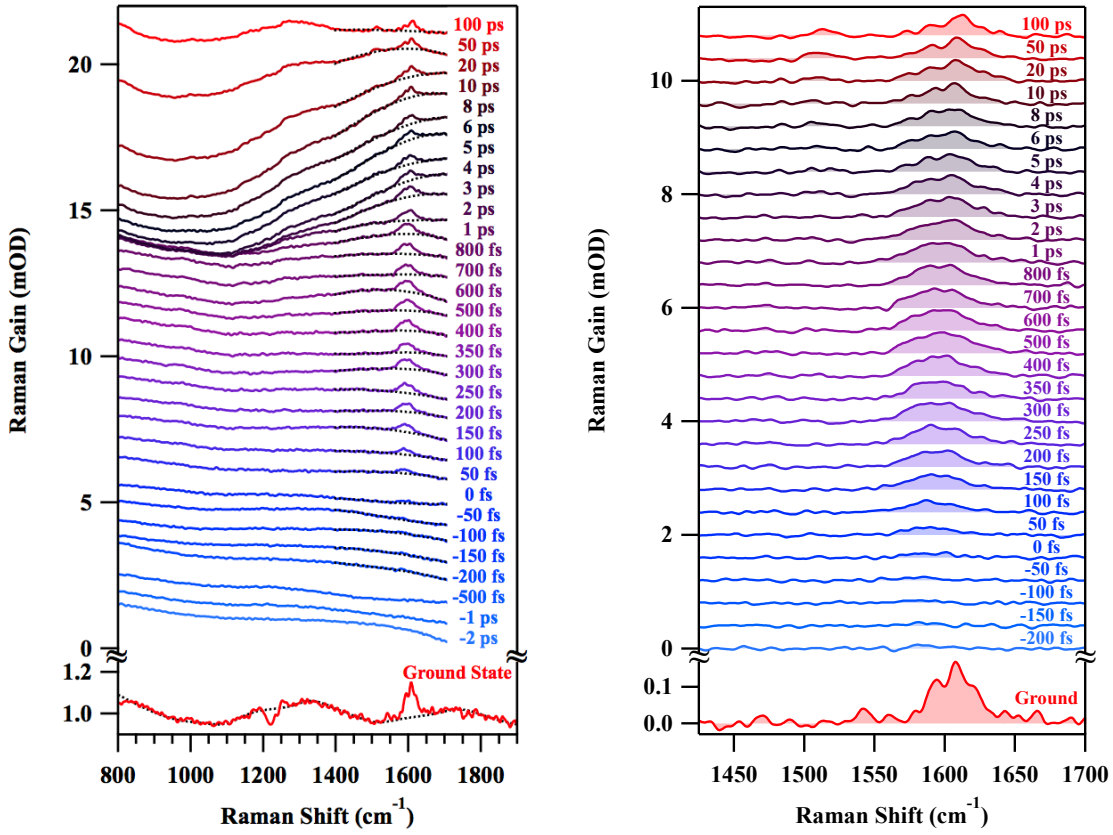

Figure D.5: Same as Figure D.3 but for TPAC2.

as the black sticks, were calculated using density functional theory (DFT) as implemented in the Gaussian 09 software package.[117] DFT calculations were performed at the B3LYP/6-311G++(D,P) level without symmetry restrictions on a pruned (99,590) grid. To aid the comparison, artificial spectra (blue curves) were generated using a 30 and 40 cm^{-1} FWHM Gaussian lineshape function for TPAC1 and TPAC2, respectively.

The amplitudes of the Raman peaks shown in Figures D.3-D.6 are presented in Figure D.8. These transients were fit to the sum of an exponential and a constant offset–used to model a very long time component–convoluted with the instrument response function. Algebraically,

$$I(t) = S(t) \otimes \left(A_0 + A_1 e^{-t/\tau}\right) \tag{D.3}$$

and

$$A_0 + A_1 = 1 \tag{D.4}$$

Where $I(t)$ is the intensity of the 1590 cm^{-1} mode, $S(t)$ is the instrument response function, A_0 is the amplitude of the long time constant (modeled as a constant offset) and A_1 is the fractional amplitude associated with the τ time constant. The amplitudes and time constants are tabulated in Figure D.8 and depicted visually in Figure 6.5 of Chapter 6.

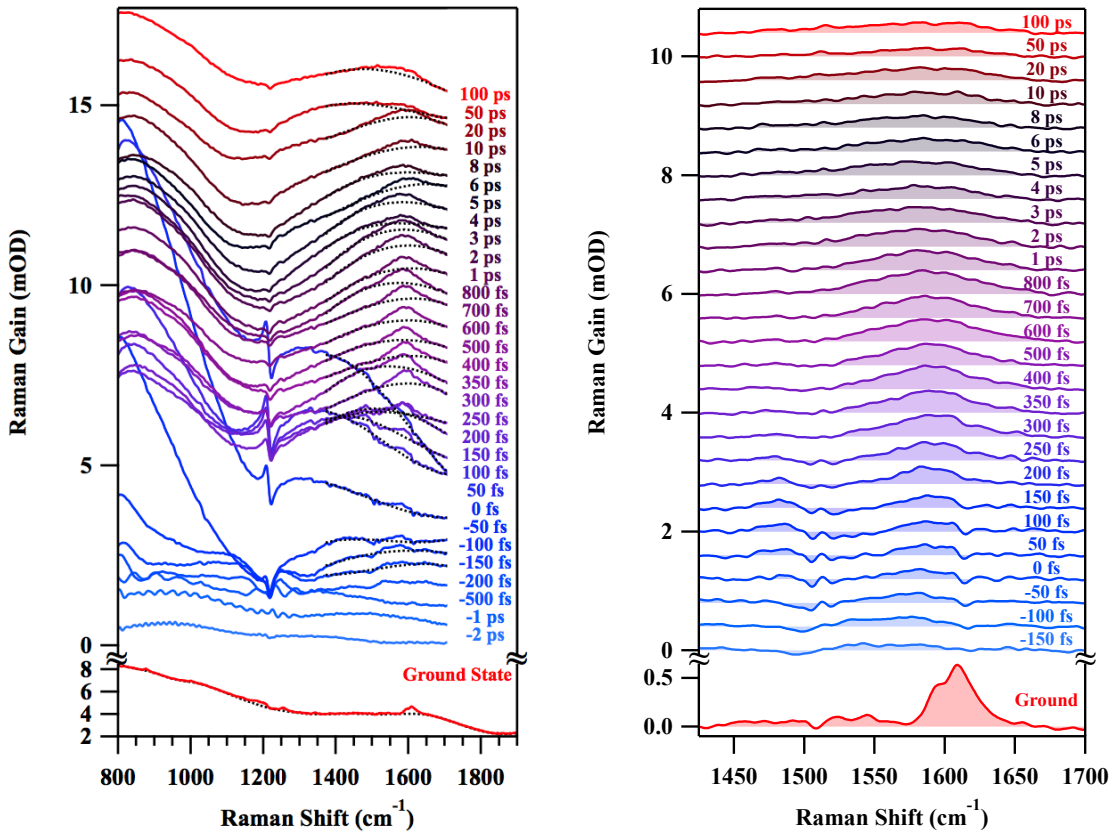

Figure D.6: Same as Figure D.3 but for conjugated TPAC2.

Figures D.9 and D.10 present the raw (left) and baseline subtracted (right) data of TPAC3 and conjugated TPAC3, respectively. In this case, the data were sufficiently complex that both the ground and excited state baselines, shown as dotted lines, were estimated using the manual method described previously.[20–22,24,49,229,230]

Figure D.11 presents the time evolution of the integral, from 700 to 1830 cm^{-1}, of the excited state Raman spectra of free and conjugated TPAC3. A similar analysis of photoexcited S1 trans-stilbene has been presented by Weigel and Ernsting[23] who found a 0.33 ps rise and 0.92 ps decay time. The analysis of TPAC3 yielded similar set of time constants of 0.25 and 2 ps. Note that in the analysis of trans-stilbene, the constant offset of the band integral was removed prior to analysis.

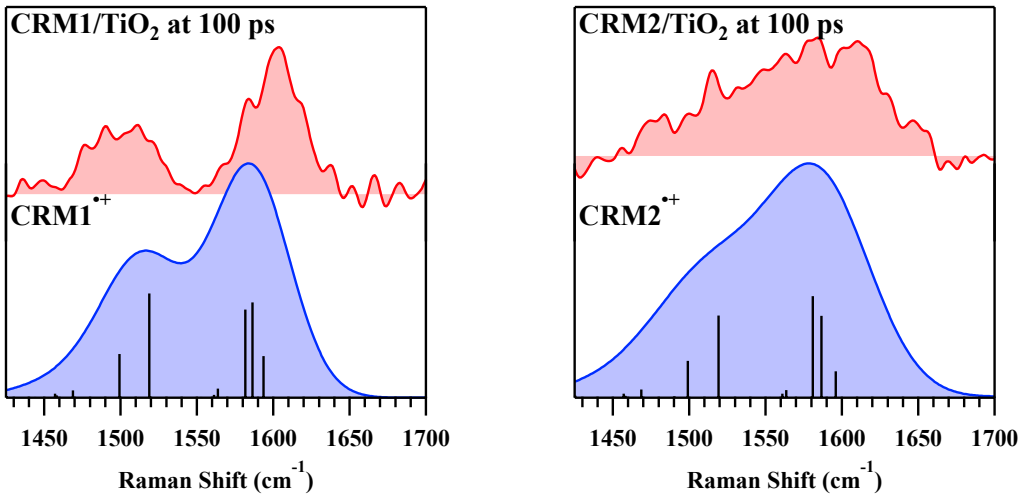

Figure D.7: A comparison of the 100 ps spectra of conjugated TPAC1 (left) and TPAC2 (right) with the Gaussian predicted Raman cross sections of the radical cations (shown as sticks) and spectra simulated by 30 and 40 cm^{-1} FWHM Gaussian line shape functions for TPAC1 and TPAC2, respectively.

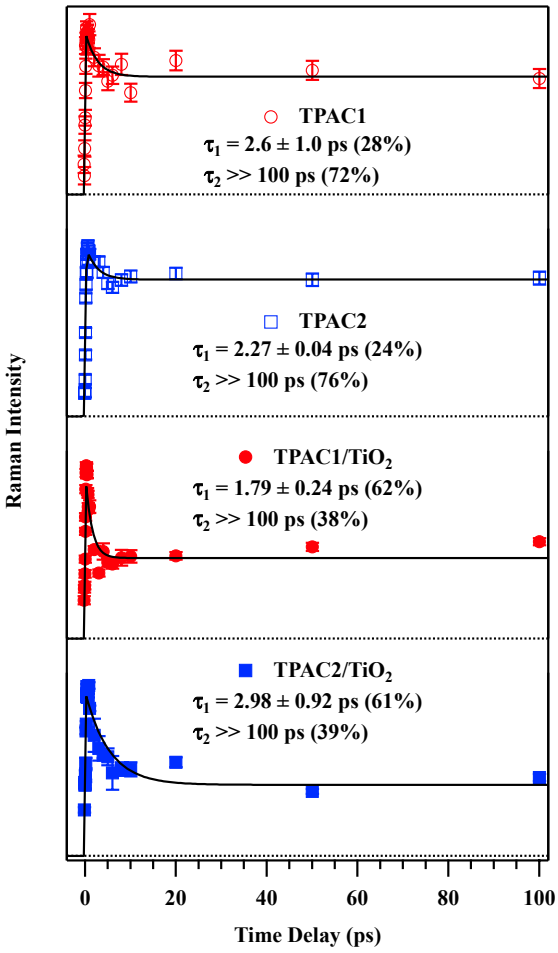

Figure D.8: Kinetic analysis of the delocalized 1590 cm^{-1} C=C stretch for TPAC1 (top), TPAC2 (second from top), TPAC1/TiO_2 (second from bottom) and conjugated TPAC2/TiO_2 (bottom). The dotted lines show zero. Multiexponential fits are shown as black lines and the extracted time constants are shown in the legend.

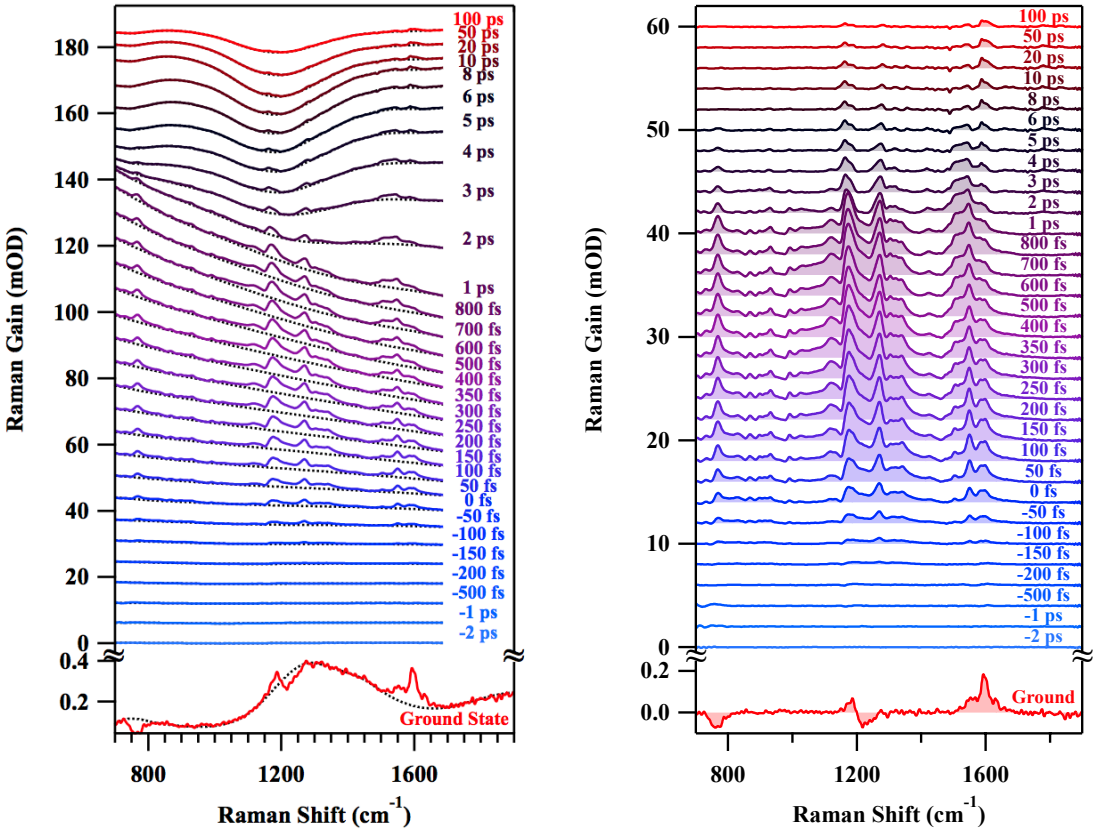

Figure D.9: Complete Raman spectra of TPAC3. Raw data is shown on the left and baseline subtracted data is shown on the right. Traces have been offset for clarity. Baselines, shown as dotted lines, were estimated by fitting a spline through hand chosen points.

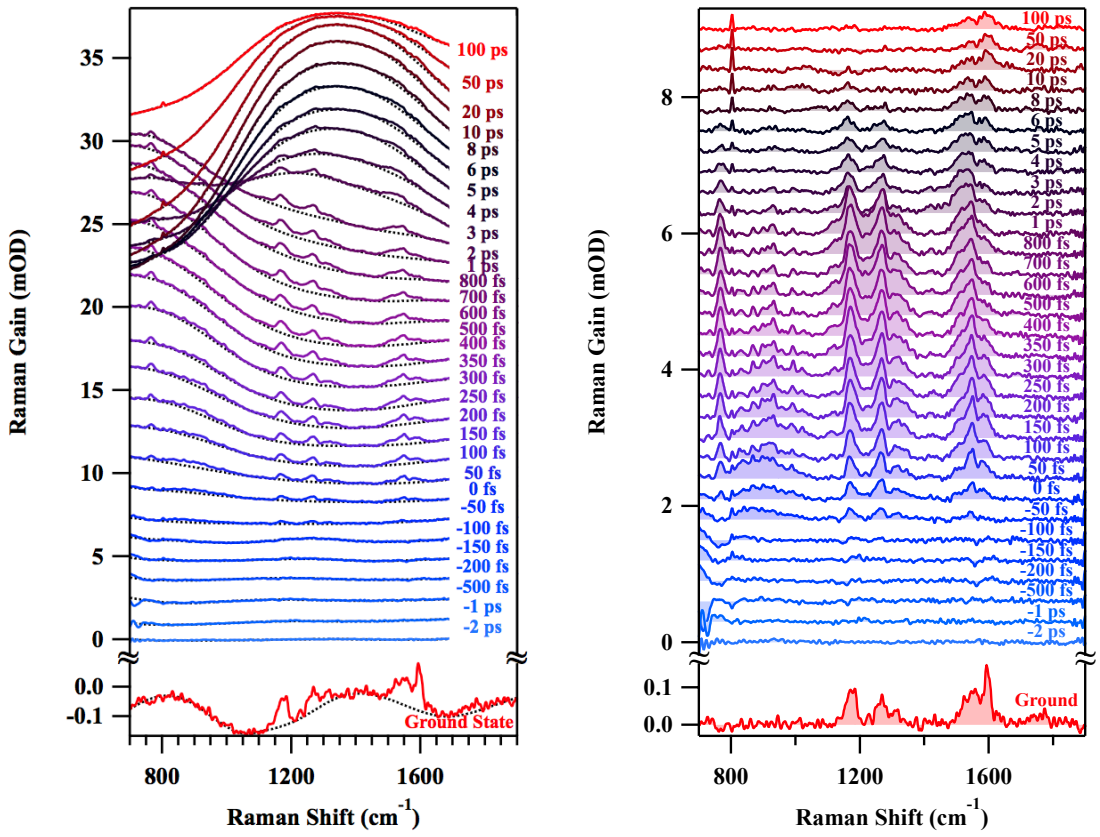

Figure D.10: Same as Figure D.9 but for conjugated TPAC3.

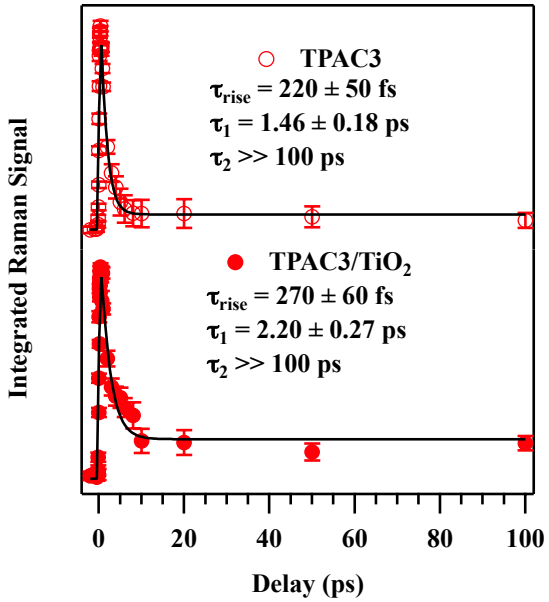

Figure D.11: Raman signal integrated between 700 and 1830 cm^{-1} for TPAC3 (top) and TPAC3/TiO$_2$ (bottom) are shown as markers. Multiexponential fits are shown as solid lines and the extracted time constants are indicated in the legend. These data agree well with those reported by Weigel and Ernsting for trans-stilbene.[23]

D.3 Synthetic Procedures

All commercially available reagents obtained from suppliers were used without further purification. Unless otherwise noted, all reactions were carried out under nitrogen with standard Schlenk techniques, and all glassware used in dry reactions were flame dried under high-vacuum prior to use. All organic extracts were dried over magnesium sulfate ($MgSO_4$) powder, and solvents were removed under reduced pressure with a rotary evaporator. Toluene, tetrahydrofuran (THF) and dimethylformamide (DMF) were purified and dried by passing through two columns of neutral alumina under nitrogen prior to use. Flash chromatography was performed using Silicycle SiliaFlash ® P60 (particle size 40-63 μm, 230-400 mesh) silica gel.

All ^{1}H and ^{13}C NMR spectra were obtained in chloroform-d, unless otherwise noted, with a Bruker AVB-400, AV-500 or AV-600 instrument. ^{13}C spectra were measured with a proton-decoupling pulse program. All chemical shifts (ppm) were calibrated to the residual peak of the deuterated solvent. Data from high-resolution mass spectrometry (HRMS) using electrospray ionization(ESI) were obtained by the UC Berkeley mass spectrometry facility. Elemental analysis (CHN) was performed by the UC Berkeley microanalysis laboratory.

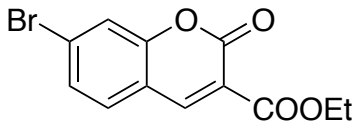

Ethyl 7-bromo-2-oxo-2H-chromene-3-carboxylate (1). To an 8-dram vial, 4-bromo-2-hydroxybenzaldehyde (1.00 g, 4.98 mmol) was added to diethyl malonate (0.796 g, 4.98 mmol) under ambient conditions, and the resulting suspension was stirred for 10 min at rt. Piperidine (0.846 g, 9.95 mmol) was added to the reaction mixture drop-wise. The reaction mixture turned from orange to red, and yellow solid formed after ~1 eq. was added. The remaining piperidine was added, and reaction mixture was stirred at rt for 16 h. Concentrated HCl (6 mL, 12 M) was slowly added in a drop-wise fashion to the reaction mixture, which appeared as orange, viscous oil. Pink precipitates formed, and the suspension was vigorously stirred in conc. HCl for 1 h until the solid flakes were evenly suspended. Water was then added to the reaction mixture to fill up the vial, and the solid flakes turned from pink to off-white. The suspension was stirred at rt for 2.5 h and was filtered through a Buchner funnel to collect the solid. The crude material was passed through a plug of silica gel with dichloromethane as the eluent, and the product was obtained as a white, powder (463 mg, 31 %). ^{1}H NMR (400 MHz, $CDCl_3$), δ (ppm) = 8.48 (s, 1H), 7.54 (ad, J = 0.4 Hz, 1H), 7.47 (ad, J = 0.8 Hz, 2H), 4.41 (q, J = 7.2 Hz, 2H), 1.41 (t, J = 7.2 Hz, 3H). ^{13}C (100 MHz, $CDCl_3$), δ (ppm) = 163.0, 156.0, 155.4, 148.0, 130.4, 129.0, 128.6, 120.3, 118.6, 116.0, 62.3, 14.4. HRMS (ESI, m/z): $[M]^+$ calcd for $C_{12}H_9O_4Br$ $[M]^+$: 295.9684; found, 295.9687.

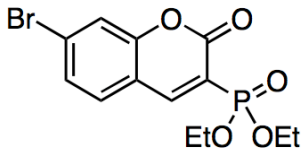

Diethyl (7-bromo-2-oxo-2H-chromen-3-yl)phosphonate (2). A dry 100mL RBF was charged with THF (35 mL) and CCl_4 (5 mL). To this flask, $TiCl_4$ (3.76 g, 19.8 mmol, 2.16 mL, 2 equiv.) was added at 0 °C dropwise via syringe, where upon addition generated an opaque yellow solution. A solution of 4-bromo-2-hydroxybenzaldehyde (2.0 g, 9.9 mmol, 1 equiv.) and triethyl phosphonoacetate (2.23 g, 9.9 mmol, 1.97 mL, 1 equiv.) in THF (5 mL) was then added dropwise. Lastly, a solution of pyridine (3.13 g, 39.6 mmol, 3.2 mL, 4 equiv.) in THF (7.5 mL) was slowly added, and the reaction was allowed to warm up to rt and stir overnight. Upon reaction completion, the mixture was quenched with H_2O (50mL). The aqueous layer was extracted three times with Et_2O, dried on Mg_2SO_4, and rotovapped to dryness. The residue was purified by SiO_2 column chromatography (3:97 MeOH:CH_2Cl_2) to obtain a clear solid (2.2 g, 6.09 mmol, 62 yield). ^{1}H NMR (600 MHz, $CDCl_3$): δ (ppm) = 8.44 (d, J = 16.8 Hz, 1H), 7.51 (s, 1H), 7.45-7.42 (m, 2H), 4.30-4.19 (m, 4H), 1.35 (t, J = 7.2 Hz, 6H). ^{13}C NMR (150 MHz, $CDCl_3$): δ 157.44, 157.34, 155.3, 152.5, 152.4, 130.1, 128.5, 128.4, 120.1, 116.8, 116.7, 63.5, 63.4, 16.32, 16.28. HRMS (ESI, m/z) calcd. for $C_{13}H_{15}BrO_5P$ $[M+H]^+$: 360.9835; found: 360.9847.

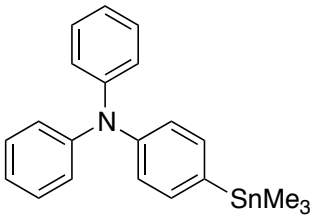

N,N-Diphenyl-4-(trimethylstannyl)aniline (3). 4-Bromotriphenylamine (500 mg, 1.54 mmol) was added to a 100 mL 3-neck flask and degassed with N_2. 30 mL of dry THF was added to the flask, and the resulting solution was cooled to -78 °C for 10 min. *n*-BuLi (2.5 M in hexanes, 1.70 mmol, 0.680 mL) was added to the reaction mixture dropwise at -78 °C and then stirred at -78 °C for 1.5 h. Trimethyltin chloride (372 mg, 1.77 mmol) was added to the reaction mixture in one shot at -78 °C. The reaction mixture was stirred for 30 minutes before warming up to rt and stirring for 12 h. The reaction mixture was diluted with diethyl ether and washed with H_2O three times. The organic layer was dried over $MgSO_4$ and filtered. Removal of solvent under reduced pressure yielded the product as brown oil. The crude material was used in the subsequent reaction without further purification.

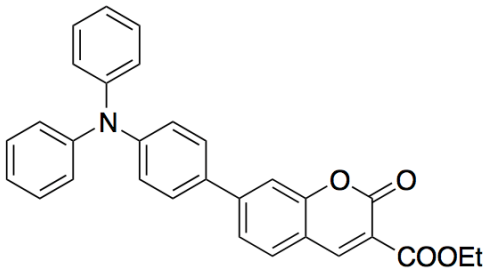

Ethyl 7-(4-(diphenylamino)phenyl)-2-oxo-2H-chromene-3-carboxylate (4). A 25-mL 3-neck flask connected to a condenser was charged with 1 (243 mg, 0.817 mmol), 2 (400 mg, 0.980 mmol), *tris*(dibenzylideneacetone)dipalladium(0) (Pd_2dba_3, 2 mol%, 15.0 mg, 16.3 μmol) and tri(*o*-tolyl)phosphine (P(*o*−tol)$_3$, 8 mol%, 19.9 mg, 65.3 μmol), and degassed with N_2. Toluene (2.7 mL) and DMF (0.54 mL) were added to the flask, and the reaction mixture was immediately heated at 100 ° for 16 h. The reaction mixture was then cooled to rt and diluted with diethyl ether. The ether layer was washed with H_2O three times, dried over $MgSO_4$ and filtered. The crude mixture was purified by flash chromatography (silica gel, $CHCl_3$), and the product was recrystallized in absolute ethanol. The product was collected as yellow needles after vacuum filtration (1 crop, 230 mg, 61 %) ^{1}H NMR (600 MHz, $CDCl_3$), δ (ppm) = 8.55 (s, 1 H), 7.62 (d, J = 7.8 Hz, 1H), 7.55–7.51 (m, 4H), 7.30 (t, J = 8.1 Hz, 4H), 7.16–7.13 (m, 6H), 7.09 (t, J = 7.2 Hz, 2H), 4.43 (q, J = 7.2 Hz, 2H), 1.42 (t, J = 7.2 Hz, 3H). ^{13}C (150 MHz, $CDCl_3$), δ (ppm) = 163.4, 157.1, 156.0, 149.2, 148.6, 147.3, 147.2, 131.5, 129.9, 129.6, 128.1, 125.3, 123.9, 123.2, 122.8, 117.2, 116.5, 113.9, 62.0, 14.4. HRMS (ESI, m/z) calcd. for $C_{30}H_{23}NO_4Na$ $[M+Na]^+$: 484.1519; found: 484.1521.

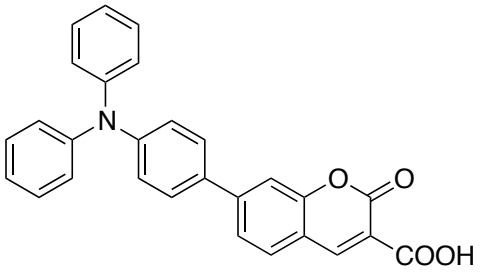

7-(4-(Diphenylamino)phenyl)-2-oxo-2H-chromene-3-carboxylic acid (TPAC1). To a 100-mL RBF attached to a condenser, added 3 (200 mg, 0.434 mmol), lithium hydroxide monohydrate (911 mg, 21.7 mmol), absolute ethanol (22 mL) and distilled water (11 mL). The reaction mixture was heated at reflux for 2 h. The reaction mixture was then cooled to rt, acidified with 2M HCl to pH = 0 and diluted with chloroform. The reaction mixture was extracted with chloroform three times, and the organic layer was dried over $MgSO_4$ and filtered. The crude mixture was purified by recrystallized in absolute ethanol. The product was collected as small orange plates after vacuum filtration (1 crop, 130 mg, 69 %). ^{1}H NMR (500 MHz, $CDCl_3$), δ (ppm) = 12.29 (broad s, 1H), 8.93 (s, 1H), 7.76 (d, J = 8.5 Hz, 1 H), 7.68 (dd, J = 4.0 Hz, 1.5 Hz, 1H), 7.64 (s, 1H), 7.54 (d, J = 9.0 Hz, 2H), 7.32 (t, J = 8.0 Hz, 4H), 7.18–7.14 (m, 6H), 7.12 (t, J = 7.5 Hz, 2H). ^{13}C (150 MHz,

$CDCl_3$), δ (ppm) = 164.6, 162.9, 155.5, 151.2, 149.7, 148.8, 147.1, 130.8, 130.6, 129.7, 128.3, 125.5, 124.4, 124.2, 122.5, 116.9, 114.0, 113.5. HRMS (ESI, m/z) calcd. for $C_{28}H_{18}NO_4$ [M-H]$^-$: 432.1241; found: 432.1234. Anal. calcd for $C_{28}H_{19}NO_4$: C, 77.59; H, 4.42; N, 3.23; found: C, 77.53; H, 4.50; N, 3.24.

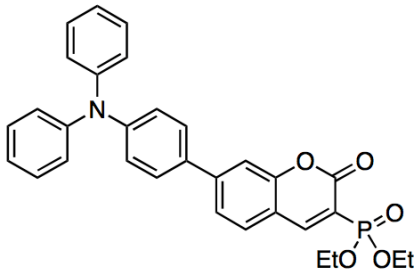

Diethyl (7-(4-(diphenylamino)phenyl)-2-oxo-2H-chromen-3-yl)phosphonate (5). A dry 100 mL RBF was charged with N,N-diphenyl-4-(trimethylstannyl)aniline 2 (3.0 g, 7.40 mmol, 1.1 equiv.), coumarin phosphonate 3 (2.0 g, 6.73 mmol, 1 equiv.), Pd_2dba_3 (123 mg, 0.13 mmol, 2 mol%) and P($o-$tolyl)$_3$ (164 mg, 0.54 mmol, 8 mol%). The flask was then evacuated and back-filled with nitrogen three times. Lastly, toluene (30 mL) and DMF (6 mL) were added to the flask and the reaction was allowed to stir at 110 °C overnight. Upon completion, the reaction mixture was poured into H_2O (80 mL) and extracted three times with CH_2Cl_2. The organic layers were combined, dried on $MgSO_4$ and rotovapped to dryness. The residue was purified by SiO_2 column chromatography (2:3 EtOAc:CH_2Cl_2) to obtain an orange-yellow solid (1.8 g, 3.43 mmol, 51% yield). ^{1}H NMR (300 MHz, $CDCl_3$): δ 8.52 (d, J = 17.1 Hz, ^{1}H), 7.62-7.49 (m, 5H), 7.33-7.26 (m, 4H), 7.17-7.06 (m, 8H), 4.37-4.19 (m, 4H), 1.39 (t, J = 6.9 Hz, 6H). ^{13}C NMR (100 MHz, $CDCl_3$): δ 158.4, 158.2, 155.7, 153.0, 152.9, 148.7, 146.9, 146.7, 131.1, 129.4, 129.3, 127.8, 124.9, 123.6, 122.8, 122.5, 117.0, 116.2, 116.1, 115.1, 113.6, 63.2, 63.1, 16.24, 16.17. HRMS (ESI, m/z) calcd. for $C_{31}H_{29}NO_5P$ [M+H]+: 526.1778; found: 526.1791.

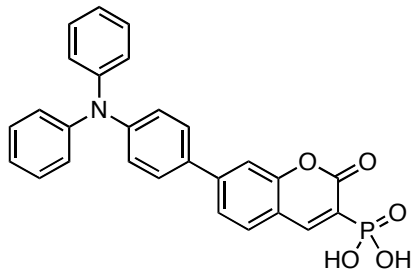

(7-(4-(Diphenylamino)phenyl)-2-oxo-2H-chromen-3-yl)phosphonic acid (TPAC2). A dry 100 mL RBF was charged with compound 2 (300 mg, 0.57 mmol, 1 equiv.) and 20 mL of CH_2Cl_2. To this stirring solution, bromotrimethylsilane (523.6 mg, 3.42 mmol, 0.45 mL, 6 equiv.) was added dropwise via syringe at rt and allowed to stir overnight. Upon consumption of starting material, determined by thin layer chromatography, the mixture was rotovapped to dryness. The resultant orange residue was then solvated in MeOH, to which CH_2Cl_2 and petroleum ether were slowly

added to precipitate a fluffy solid from solution. The solids were filtered off and washed with petroleum ether to provide a bright yellow solid (108 mg, 0.23 mmol, 40% yield). ^{1}H NMR (600 MHz, CD_3OD): δ 8.45 (d, J = 16.2 Hz, 1 H), 7.76 (d, J = 8.4 Hz, 1 H), 7.66-7.60 (m, 4H), 7.32-7.29 (m, 4 H), 7.11-7.07 (m, 8 H). ^{13}C NMR (150 MHz, $CDCl_3$): δ 160.8, 160.7, 157.0, 151.6, 151.5, 150.3, 148.7, 147.8, 133.1, 131.1, 130.6, 129.1, 126.2, 124.9, 124.1, 123.8, 121.3, 120.0, 118.1, 118.0, 114.5. HRMS (ESI, m/z) calcd. for $C_{27}H_{19}NO_5P$ [M-H]$^-$: 468.1006; found: 468.1011. Anal. calcd. for $C_{27}H_{20}NO_5P$ + H_2O: C, 66.53; H, 4.55; N, 2.87; found: C, 66.75; H, 4.50; N, 2.84.

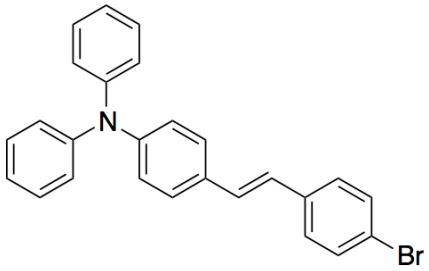

(E)-4-(4-Bromostyryl)-N,N-diphenylaniline (6). Synthesized according to reported procedures.[162]

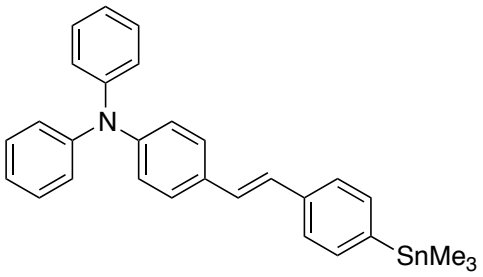

(E)-N,N-Diphenyl-4-(4-(trimethylstannyl)styryl)aniline (7). To a 50-mL 2-neck flask, added 6 (400 mg, 0.938 mmol) and degassed the content with N_2. Dry THF (15 mL) was added to the flask, and the resulting solution was cooled to -78 °C for 10 min. *n*-BuLi (2.5 M in hexanes, 1.03 mmol, 0.41 mL) was added to the reaction mixture dropwise and stirred for 2 h at -78 °C. Trimethyltin chloride (215 mg, 1.08 mmol) was added to the reaction mixture at -78 °C. The reaction mixture was stirred for 15 minutes before warming up to rt and stirring for 1.5 h. The reaction mixture was diluted with diethyl ether and washed with H_2O three times. The organic layer was dried over $MgSO_4$ and filtered. Removal of solvent under reduced pressure yielded the product as yellow oil. The crude material was used in the subsequent reaction without further purification.

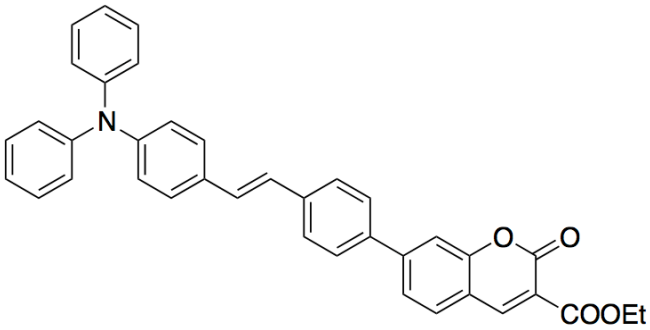

(E)-Ethyl 7-(4-(4-(diphenylamino)styryl)phenyl)-2-oxo-2H-chromene-3-carboxy-late (8). A 50-mL Schlenk tube was charged with 1 (232 mg, 0.782 mmol), 7 (478 mg, 0.938 mmol), Pd_2dba_3 (2 mol%, 14.3 mg, 15.6 μmol) and P($o-$tol)$_3$ (8 mol%, 19.0 mg, 62.5 μmol), and degassed with N_2. Toluene (2.6 mL) and DMF (0.50 mL) were added to the flask, and the reaction mixture was immediately heated at 90 °C for 16 h. The reaction mixture was then cooled to rt and diluted with chloroform. The organic layer was washed with H_2O three times, dried over $MgSO_4$ and filtered. The crude mixture was purified by flash chromatography (silica gel, $CHCl_3$); the column was eluted with increasing solvent polarity: from $CHCl_3$ to 5 % acetone in $CHCl_3$ and then to 10 % acetone in $CHCl_3$. The product was dissolved in chloroform and recrystallized by layering with methanol. The product was collected as orange, plate-like crystals after vacuum filtration (1 crop, 361 mg, 82 %). ^{1}H NMR (600 MHz, $CDCl_3$), δ (ppm) = 8.56 (s, 1 H), 7.67–7.59 (m, 7 H), 7.41 (d, J = 9.0 Hz, 2 H), 7.27 (t, J = 8.4 Hz, 4 H), 7.15 (d, J = 16.8 Hz, 1 H), 7.12 (d, J = 7.8 Hz, 4 H), 7.07–7.02 (m, 5 H), 4.43 (q, J = 7.2 Hz, 2 H), 1.43 (t, J = 7.2 Hz, 3 H). ^{13}C (150 MHz, $CDCl_3$), δ (ppm) = 163.4, 157.0, 155.9, 148.5, 147.9, 147.6, 147.2, 138.8, 137.3, 131.1, 130.0, 129.7, 129.5, 127.7, 127.2, 126.0, 124.8, 123.6, 123.5, 123.4, 117.7, 116.9, 114.5, 62.1, 14.4. HRMS (ESI, m/z) calcd. for $C_{38}H_{30}NO_4$ [M+H]$^+$: 564.2169; found: 564.2172.

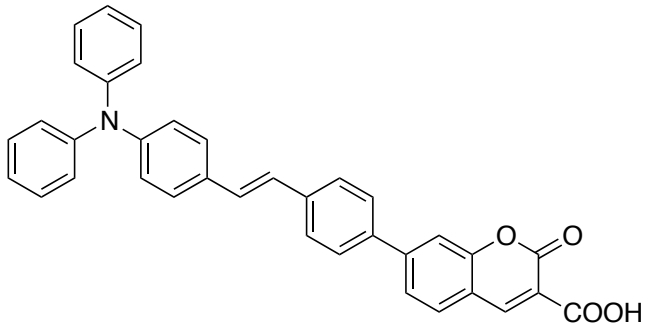

(E)-7-(4-(4-(Diphenylamino)styryl)phenyl)-2-oxo-2H-chromene-3-carboxylic acid (TPAC3). A 100-mL RBF attached to a condenser was charged with 8 (143 mg, 0.254 mmol), lithium hydroxide monohydrate (533 mg, 12.7 mmol), absolute ethanol (25 mL) and distilled water (6.3 mL). The reaction mixture was heated at reflux for 2 h and then cooled to rt. It was subsequently diluted with diethyl ether and extracted with 10 % NaOH solution three times. The aqueous layer was acidified with 2M HCl to pH = 0 and extracted with chloroform five times. The organic layer was

dried over $MgSO_4$ and filtered. Removal of the solvent yielded an orange solid. The crude material was purified by recrystallization in $CHCl_3$/MeOH. The product was collected as red needles after vacuum filtration (1 crop, 54 mg, 40 %). ^{1}H NMR (600 MHz, $CDCl_3$), δ (ppm) = 12.27 (broad s, 1 H), 8.96 (s, 1 H), 7.80 (d, J = 7.8 Hz, 1 H), 7.74 (d, J = 7.8 Hz, 1 H), 7.72 (s, 1 H), 7.67 (d, J = 8.4 Hz, 2 H), 7.63 (d, J = 8.4 Hz, 2 H), 7.42 (d, J = 8.4 Hz, 2 H), 7.28 (t, J = 7.8 Hz, 4 H), 7.17 (d, J = 16.2 Hz, 1 H), 7.13 (d, J = 7.8 Hz, 4 H), 7.07–7.02 (m, 5 H). ^{13}C (MHz, $CDCl_3$), δ (ppm) = 164.5, 162.8, 155.4, 151.1, 148.8, 147.6, 139.4, 136.6, 130.9, 130.1, 129.5, 127.82, 127.75, 127.3, 125.7, 124.9, 123.5, 123.4, 117.4, 114.7, 114.1. HRMS (ESI, m/z) calcd. for $C_{36}H_{24}NO_4$ [M-H]$^-$: 534.1711; found: 534.1706. Anal. calcd for $C_{36}H_{25}NO_4$: C, 80.73; H, 4.70; N, 2.62; found: C, 80.45; H, 4.78; N, 2.64

TiO_2 nanoparticles. A 250-mL RBF containing a stir bar was charged with 100 mL MeOH (spectroscopic grade), 0.250 mL Nanopure water and anhydrous LiOH (2.63 mmol, 63 mg, Fisher Scientific, anhydrous LiOH powder was recrystallized from water and flame-dried under high vacuum at 100 mTorr). The mixture was sonicated (Branson 1210) for 2 h or until LiOH was completely dissolved. At room temperature, titania isopropoxide (1.823 mmol, 0.540 mL, 99.999%, Aldrich) was added dropwise to the LiOH solution. After final addition of the titania precursor, stirring was continued for an additional 3 min and then sonicated for an additional 10 min. Based on theoretical mass calculations, the crude reaction mixture had a concentration of 1.47 mg/mL (~10 mg/7mL). For a 90-nm anatase titania particle, footprint calculations yields 4.1×104 TPAC ligands/particle, and the molecular weight of these nanoparticles are calculated to be 9.4×108 g/mol based on unit cells.

Typical preparation for dye-TiO_2 conjugates. A solution of TPAC1 is first prepared. In a 1-dram vial, dissolved TPAC1 (16.8 mg, 89 equiv, 433.45 mg/mmol) in 1.7 mL of 5:1 $CHCl_3$:MeOH mixture to make a 10 mg/mL solution. Seven 1 mL aliquots of TiO2 nanoparticles were centrifuged at 8000 rpm for 5 min to collect 10 mg of the particles (microcentrifuge tubes, Molecular BioProducts, Cat#3444). The supernatant was removed, and the white pellets were resuspended in 400 μL of the TPAC1 solution. The nanoparticle suspension was transferred to a 1-dram glass vial, sealed, and heated at 50 °C in an aluminum heating block. After 16 h, the vials were cooled to room temperature and divided the solution into 2×1.5 mL centrifuge tubes. To precipitate the nanoparticle conjugates, 400 μL of MeOH was added to each tube, and then the mixtures were centrifuged at 8000 rpm for 5 min. The supernatant was removed again, and the pellets resuspended in 400 μL MeOH/100 μL $CHCl_3$. Particles were then vortexed and sonicated for 1 min to disperse the particles evenly. This washing procedure was repeated 4-5 times (with 400 μL MeOH/100 μL $CHCl_3$, and 450 μL MeOH/50 μL $CHCl_3$ for the last wash) until the supernatant became relatively colorless. After the final wash, each pellet was resuspended in 500 μL of $CHCl_3$, and two aliquots were combined and passed through a 0.45 μm PTFE syringe filter. This stock solution was diluted with $CHCl_3$ to an appropriate concentration for subsequent photophysical and Raman studies. If unused, the stock solution was stored at room temperature and in the dark.

For the preparation of TPAC2 conjugates. 18.2 mg of TPAC2 (89 equiv, 469.43 mg/mmol)

was dissolved in 1.8 mL of 5:1 $CHCl_3$:MeOH mixture for 10 mg TiO2. Unbound dye was removed by successive washing as described above. Here, 300 μL MeOH/200 μL $CHCl_3$ was used to clean the conjugates, except for the last wash, which used a mixture of 400 μL MeOH/100 μL $CHCl_3$. The TPAC2 conjugates formed relatively large aggregates during the washes, and the final sample in $CHCl_3$ could not be filtered. The data were obtained with the washed but unfiltered conjugates.

For the preparation of TPAC3 conjugates. 20.8 mg of TPAC3 (89 equiv, 535.59 mg/mmol) was dissolved in 2.1 mL of 5:1 $CHCl_3$:MeOH mixture for 10 mg TiO_2. Here, 200 μL MeOH/300 μL $CHCl_3$ was used to remove unbound dye from the particle suspension. For the final wash, 300 μL MeOH/200 μL $CHCl_3$ was used before resuspending the final pellet in pure $CHCl_3$ and passed through a 0.45 μm PTFE syringe filter.

Appendix E

Supporting Information for the Manuscript: Characterization of a Conical Intersection in a Charge Transfer Dimer with Two-Dimensional Time Resolved Stimulated Raman Spectroscopy

E.1 JUSTIFICATION OF EQUATION 7.4

As mentioned in the main text, eq. 7.4 was used to scale the oscillatory magnitudes presented in Figures 7.3 and 7.8. Figure E.1 presents the exact numerical convolution of a Gaussian with eq. 7.3 (black line) and an approximate analytical function, eq. E.1, (red dashed line).

$$e^{-\frac{1}{2}\sigma^2\omega^2} \times \left\{ \frac{1}{2} e^{-\frac{1}{\tau}\left(t-\frac{\sigma^2}{2\tau}\right)} \left[\mathrm{erf}\left(\frac{1}{\sqrt{2}\sigma} \left(t - \frac{\sigma^2}{\tau} \right) \right) + 1 \right] \right\} \times \cos\left(\omega \left(t - \frac{\sigma^2}{\tau} \right) \right) \tag{E.1}$$

Here the first term is the damping of a cosinusoid of angular frequency ω due to convolution with a Gaussian of standard deviation σ, the term in the curly braces is the analytical convolution of a Gaussian of standard deviation σ with an exponential decay of decay constant τ, the final term is a cosinusoid with a phase shift. The phase shift, which is equivalent to a time shift of σ^2/τ, is necessary in order for eq. E.1 to match the exact numerical convolution. This time shift is suggested by the equivalent shift in the error function component of the term in the curly braces. The excellent agreement between the approximate analytical formula and the exact numerical convolution for time delays longer than 2.5σ (~FWHM) justifies the use of eq. 7.4 for scaling the oscillatory magnitudes in Figures 7.3 and 7.8. Note that the form of eq. E.1 suggests that the observed oscillatory phases are shifted from the intrinsic phases by an amount equal to $\omega\sigma^2/\tau$.

E.2 PEAK ASSIGNMENTS

There are a total of eight peaks observed below 500 cm^{-1} in Figure 7.3, with the exception of the 27 cm^{-1} mode, they can all be assigned to the D_{2h} point group of the monomers. The 27 cm^{-1} mode is an inter-dimer mode where the monomers move to overlap each other. Two modes are obscured by the solvent and/or excess TMB in the RR but are readily observed in the TA: the 354 cm^{-1} mode which is attributed to a B_{2g} out-of-plane deformation mode where the TMB benzene ring rotates about the y axis and the methyls wag to compensate; and the 284 cm^{-1} mode is characterized by a TMB B_{1g} motion where the benzene ring rotates about the z-axis and a TCNQ B_{2g} out-of-plane distortion in which the benzene ring twists about the y-axis and the end groups wag to compensate. Two ungerade modes gain intensity because of relaxed selection rules due to mixing with the inter-dimer degrees of freedom; the 221 (221) cm^{-1} mode corresponds to a B_{3u} out-of-plane TCNQ deformation and the 186 (187) cm^{-1} mode corresponds to B_{3u} methyl twisting motion on the TMB. The 151 (151) cm^{-1} mode is a TCNQ B_{3g} motion where the phenyl ring rocks about the x-axis and the NCC groups rock opposite. The 105 (136) cm^{-1} mode corresponds to an A_g $C_1C_2C_3$ and C_2C_1N bend on the TCNQ. There are three peaks above 400 cm^{-1} which can be observed only in the RR spectrum: the 433 cm^{-1} mode is a B_{3g} distortion of the TMB benzene ring; the 450 is a B_{3u} out-of-plane deformation where the TMB benzene ring bends along the z-axis and the methyl groups wag opposite; and the 464 cm^{-1} mode is a B_{3u} motion in which the TCNQ benzene ring bends along the y-axis and the hydrogens wag opposite.

E.3 5TH ORDER VS 3RD ORDER SIGNALS

This article reports the successful implementation of 2D-FSRS. There have been previous attempts,[231,232] but these have focused on the observation of side-bands, peaks shifted from the fundamentals by an amount equal to low frequencies, due to *ground* state wave packets. Side-bands have two potential origins, real anharmonic coupling between different modes within the same molecule–a true 5th order signal–or the result of a parallel 3rd order cascade, i.e. one 3rd order process involving one molecule generates a field that then participates as the third interaction in another 3rd order process with a different molecule and therefore yields no relevant information about vibrational coupling. McCammant and co-workers[192–194] have shown that for off resonance impulsive excitation of neat solvents the cascade signal is expected to be roughly three orders of magnitude larger than the 5th order signal making the experimental observation of side-bands due to anharmonic couplings difficult. In this report, a time dependent shift in the central frequency of a high-energy normal mode, not a side-band, is observed. Indeed, Mehlenbacher et al. have demonstrated that *sequential* cascades, i.e. cascades in which the photon generated in the first 3rd order process initiates the second one, can result in an oscillatory peak frequency in addition to the expected 5th order signal.[193] Our analysis of that work, outlined below, predicts that the 5th order signal will be independent of actinic pump intensity while the 3rd order signal will be approximately proportional to it. This result is intuitively expected because the change in frequency should be an intensive property for a true 5th order signal while one would expect it to be an extensive for a 3rd order cascade.

The following analysis builds off work by McCamant and co-workers who have shown that both 5th and 3rd order signals can result in a dispersive Lorentzian line-shape centered at the high frequency mode. The amplitude of this dispersive feature oscillates in time with a cosine phase for the 5th order signal and a sine phase for the 3rd order signal. A general equation for the total measured lineshape is shown in eq. E.2.

$$S(x, \Delta t) = \frac{A + B(\Delta t)x}{1 + x^2} \tag{E.2}$$

Where A is the magnitude of the regular FSRS signal, B is the time dependent magnitude of the 3rd or 5th order signal and x is defined by eq. E.3.

$$x = \frac{\omega - (\omega_{Rpu} - \omega_0)}{\Gamma/2} \tag{E.3}$$

Where ω is the measured frequency, ω_{Rpu} is the frequency of the Raman pump, ω_0 is the central frequency of the peak and Γ is the FWHM of the transition. The magnitudes of the dispersive features can be written as

$$B = B_{3^{rd},0} \sin(\omega_l \Delta t) \tag{E.4}$$

for the 3rd order signal or

$$B = B_{5^{th},0} \cos(\omega_l \Delta t) \tag{E.5}$$

for the 5th order signal where ω_l is the frequency of the low energy mode and the B's are given in reference.[193] The maximum of S is found at

$$x_{max} = \frac{R}{1 + \sqrt{1 + R^2}} \approx \frac{R}{2} \tag{E.6}$$

Where $R = B/A$ and we have assumed R to be small and only retained the first order of the Taylor expansion. Equation E.6 indicates that

$$\Delta\omega(\Delta t) = \frac{\Gamma}{4}\frac{B(\Delta t)}{A} \tag{E.7}$$

Where $\Delta\omega$ is the time dependent shift in the central frequency, which is what has been measured in this experiment. Therefore the total shift in frequency, that is the sum of the 5th and 3rd order contributions can be written as

$$\Delta\omega_{tot}(\Delta t) = \frac{\Gamma}{4A}\left(B_{5^{th},0}\cos(\omega_l\Delta t) + B_{3^{rd},0}\sin(\omega_l\Delta t)\right) = \frac{\Gamma B_{5^{th},0}}{4A}\sqrt{1+\beta^2}\cos(\omega_l\Delta t - \alpha) \tag{E.8}$$

Where α is defined as

$$\alpha = \arctan(\beta) \tag{E.9}$$

and $\beta = B_{3^{rd},0}/B_{5^{th},0}$. Furthermore Mehlenbacher et al. have shown that,

$$\beta \propto N\alpha_l \tag{E.10}$$

Where N is the number of molecules and α_l is the polarizability of the low wavenumber mode. The measurements made here are on an excited state species; therefore N is directly proportional to the intensity of the actinic pump, I_{Apu}. This means that if the 3rd order cascade is dominant the signal will increase roughly in proportion to N, or I_{Apu}. On the other hand, if the 5th order signal is dominant the signal will have no dependence on I_{Apu}.

Figure E.7 presents results from experiments with actinic pump intensities of 135 (red), 270 (black) and 405 (blue) GW/cm^2. Clearly that the magnitude of the frequency oscillations do not depend, within experimental error, on actinic pump intensity demonstrating that the data presented in the main text are indeed due to a 5th order process. The reason this experiment is successful and previous attempts failed is because N is orders of magnitude smaller than for neat solvents and β is linearly proportional to N. The key here is that while β is linearly proportional to α_l the FSRS signal is proportional α_l^2. This means that the same signal-to-noise can be maintained while drastically reducing the 3rd order cascade signal. For instance, if N is reduced 10,000 fold but α_l is increased 100 fold the overall FSRS signal strength will be unaffected but the contribution of the 3rd order cascade will be reduced by 100 fold.

E.4 2D-FSRS and Sliding Window Fourier Transforms

Two-dimensional FSRS experiments are limited by Fourier uncertainty. In other words, the better the Raman resolution–which determines how well the peak centers can be localized–the smaller

the observed magnitude of the central peak oscillations. Note that the Raman resolution is determined *both* by the Raman pump pulse shape and the intrinsic properties of the molecular system under study. This is shown by eq. 7.7 in the main text which demonstrates that FSRS is the experimental analog of a sliding window Fourier transform in which the sliding window function is an exponential decay, i.e. a single sided Poisson Window. Faster dephasing, as in the case of the 1271 cm^{-1} mode, means a shorter window (less averaging) and thus a larger observed oscillatory magnitude. This insight suggests that a Gaussian shaped Raman pump might be preferable for 2D-FSRS as a Gaussian window has the minimum Fourier uncertainty. Of course, Gaussian shaped Raman pump pulses have drawbacks that have been outlined before.[197] Finally, in systems where there are only a few well-separated Raman active peaks it will be advantageous to artificially reduce the experimental resolution in order to increase the measured oscillatory magnitude.

E.5 Derivation of Equation 7.10

We can derive eq. 7.10 in the main text by assuming that the force constant of the high frequency mode's potential depends linearly on the low frequency mode as shown in eq. E.11. A cartoon of this model is presented in Figure E.8.

$$k_h(t) = k_{h,0}\left(1 + \chi(q_l(t) - \Delta)\right) \tag{E.11}$$

Where $k_{h,0}$ is the force constant of the excited state potential energy surface along the high frequency mode when the low frequency normal coordinate is at its equilibrium position in the excited state, χ is the dimensionless linear coupling constant, $q_l(t)$ is the time dependent dimensionless displacement of the low frequency mode from its ground equilibrium position and Δ is the dimensionless displacement between the equilibrium geometries of the excited and ground states. Equation E.11 implies that

$$\omega_h(t) = \omega_{h,0}\sqrt{1 + \chi(q_l(t) - \Delta)} \tag{E.12}$$

We can Taylor expand the square root term and use the fact that $q_l(t) = \Delta(1 - \cos(\omega_l t))$ to arrive at eq. 7.10. When χ is large the higher order terms in the Taylor series result in oscillations at overtone frequencies albeit with much reduced magnitudes. For instance, for the values of χ that are observed here the first and second overtones are four and eight orders of magnitude weaker than the fundamental, respectively.

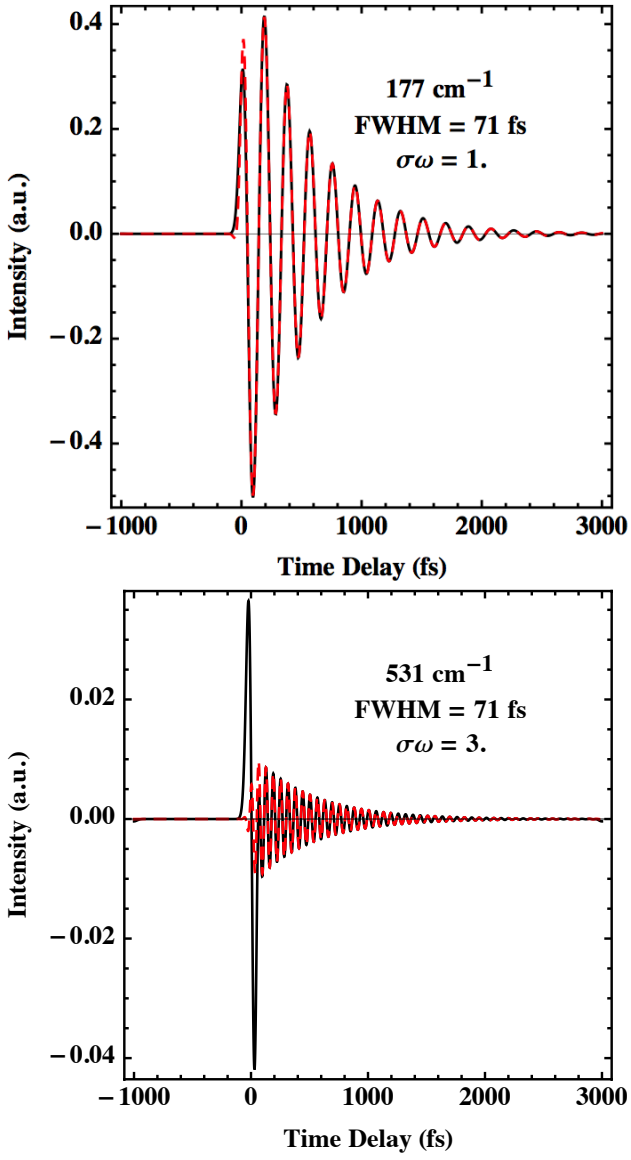

Figure E.1: A comparison of the approximate analytical convolution (red dashed line) and the exact numerical convolution (solid black line) for two different values of $\sigma\omega$; 1 (top) and 3 (bottom). When $\sigma\omega$ is small the approximation is excellent for all times, when $\sigma\omega$ is large the approximation fails at short delays but is still excellent for delays larger than the FWHM of the Gaussian function, which is analogous to the experimental cross correlation between the actinic pump and the probe.

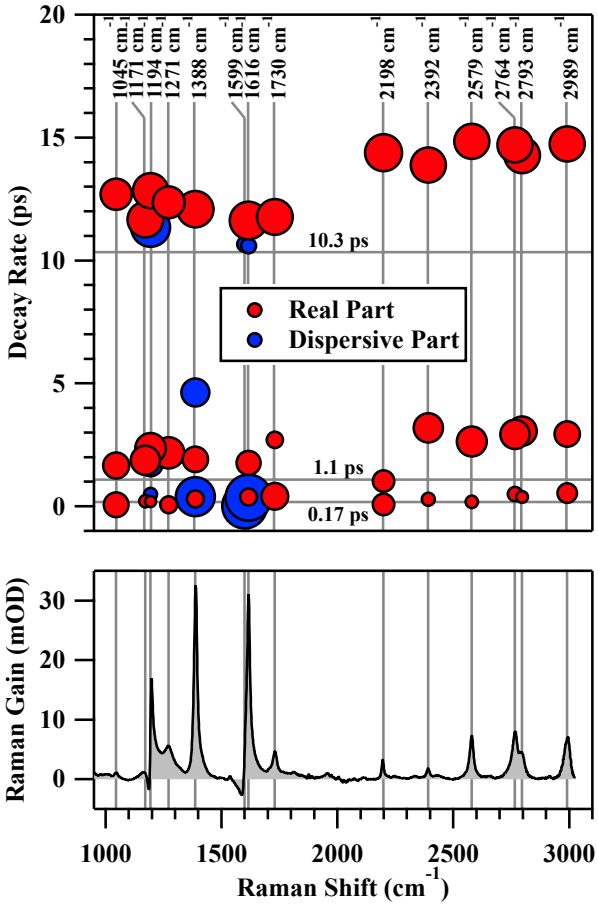

Figure E.2: Analysis of peak specific excited state amplitude decay kinetics for the TMB:TCNQ complex. The excited state complex spectrum 2 ps after excitation is shown at the bottom for reference. Each peak has been fit to a lorentzian lineshape (NB: peaks at 1194, 1388 and 1599 cm^{-1} include a dispersive component as discussed in Chapter 7) and the amplitudes are fit to a three component exponential decay. The decay components are presented as circles at the top where the ordinate, abscissa and area indicate the exponential time constant, peak frequency and fractional amplitude, respectively. Horizontal lines indicate the decay kinetics of the transient absorption as shown in Figure 7.2. There is relatively good agreement between the fundamentals' decay kinetics and those of transient absorption.

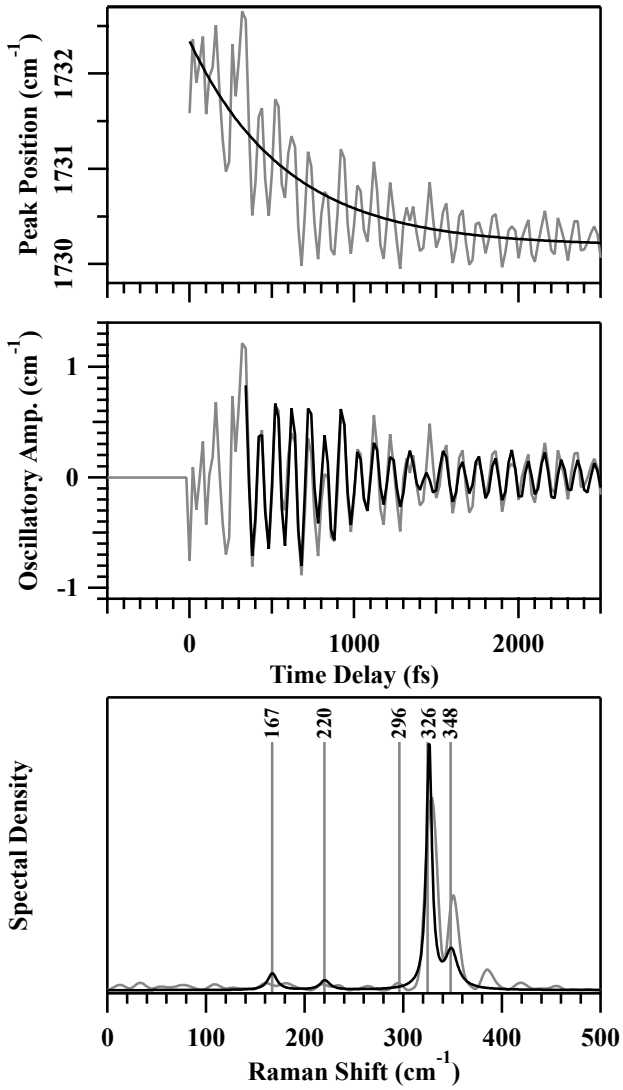

Figure E.3: Same as Figure 7.7 in the main text but for the 1730 cm^{-1} peak.

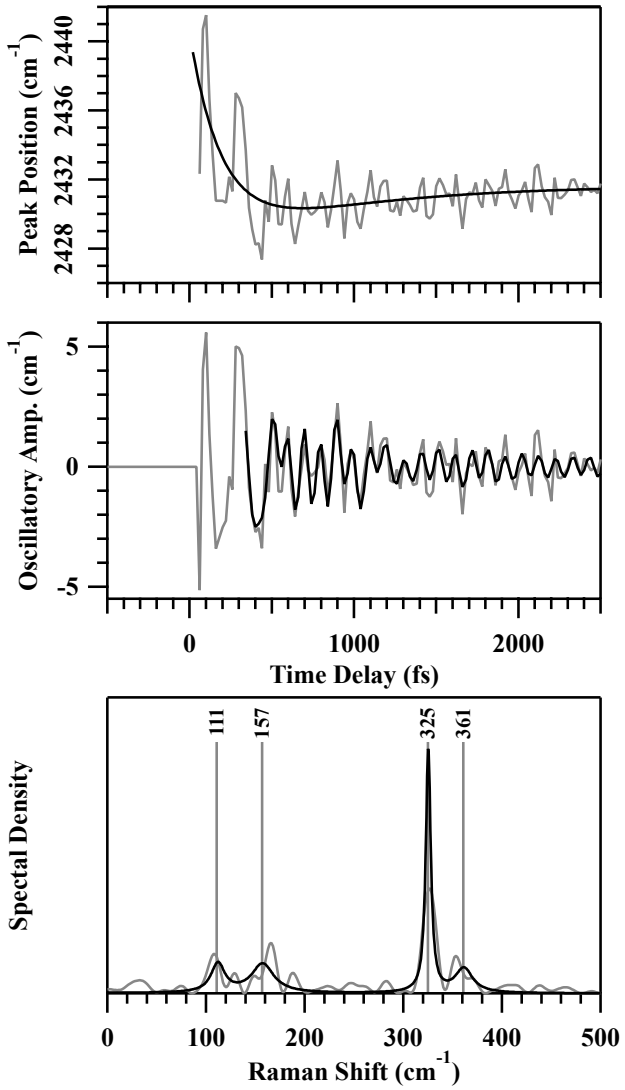

Figure E.4: Same as Figure 7.7 in the main text but for the 2431 cm^{-1} peak.

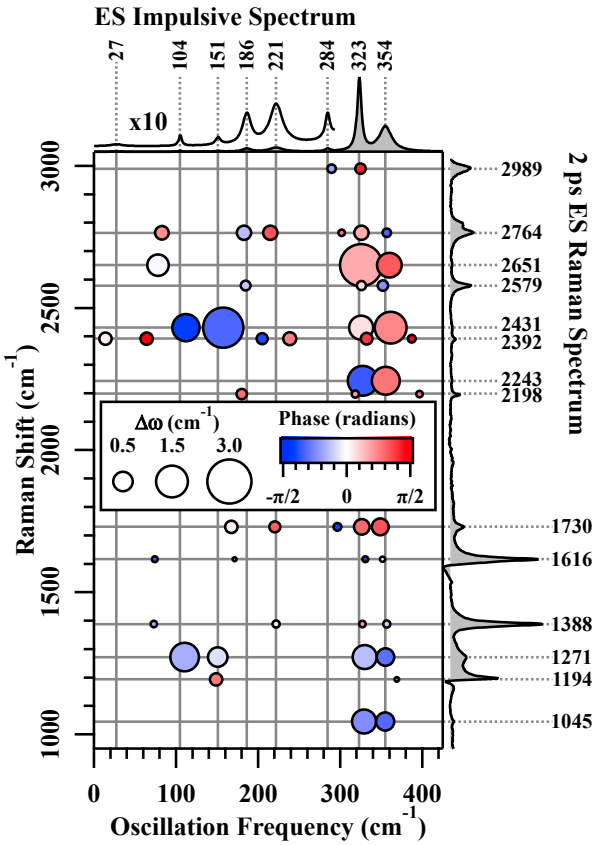

Figure E.5: Same as Figure 7.8 in Chapter 7 except with phases and without any scaling. Amplitudes and phases have been extrapolated back to $t = 0$.

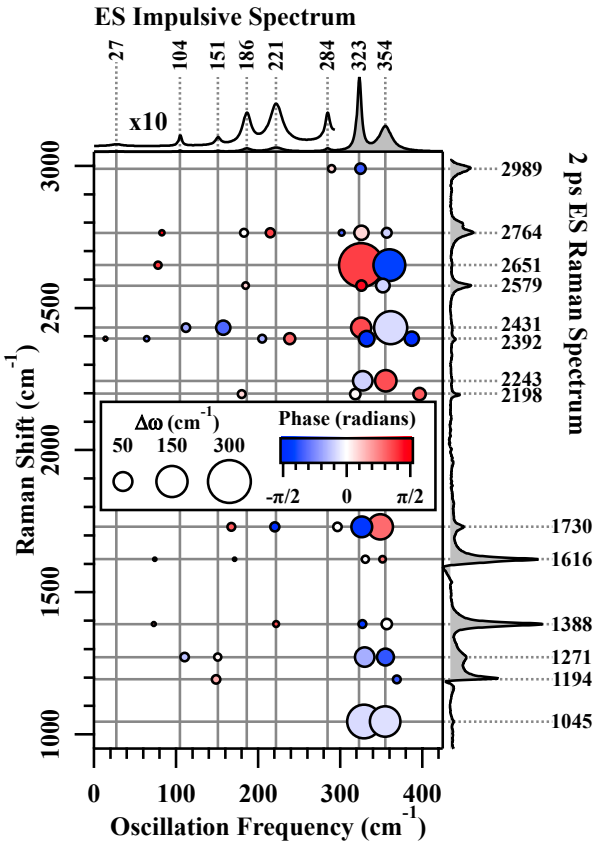

Figure E.6: Same as Figure 7.8 in Chapter 7 but showing the corrected estimated intrinsic phases and oscillatory magnitudes.

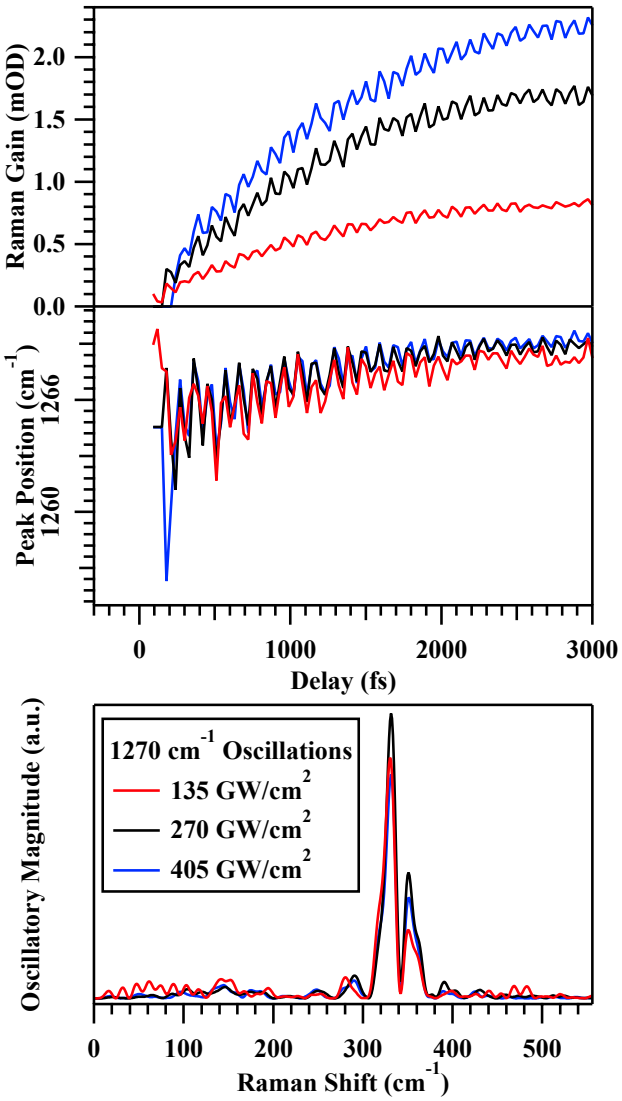

Figure E.7: Extracted peak parameters as a function of time for the 1271 cm^{-1} mode for three different actinic pump intensities. The Raman intensities are shown at the top, the peak frequencies in the middle and the Fourier transforms of the frequency oscillations after removal of the background population kinetics at the bottom. The oscillations in the center frequencies are clearly independent of the actinic pump intensity as expected for a 5^{th} order process.

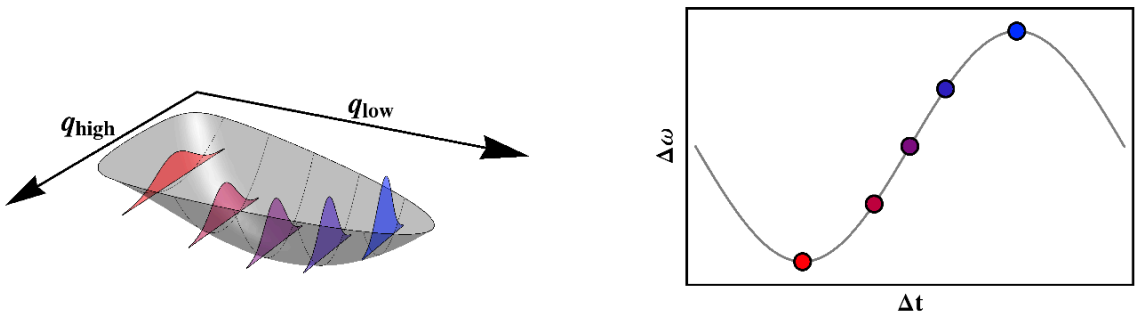

Figure E.8: A schematic potential energy surface (left) in which the force constant along the high frequency mode depends linearly upon the position of the low frequency mode. Wave functions for the lowest vibrational state of the high frequency mode are depicted for different displacements of the low frequency mode. If the low frequency mode can be treated classically and is oscillating it will modulate the frequency of the high-energy mode. This modulation is shown on the right as a function of time.

References

(1) Zewail, A. H. *J. Phys. Chem. A* **2000**, *104*, 5660–5694, DOI: 10.1021/jp001460h.

(2) Zewail, A. H. *Pure Appl. Chem.* **2000**, *72*, DOI: 10.1351/pac200072122219.

(3) Baskin, J. S.; Zewail, A. H. *J. Chem. Educ.* **2001**, *78*, 737, DOI: 10.1021/ed078p737.

(4) Birge, R. R. *Annu. Rev. Biophys. Bioeng.* **1981**, *10*, 315–354, DOI: 10.1146/annurev.bb.10.060181.001531.

(5) Blankenship, R. E., *Molecular mechanisms of photosynthesis*; Blackwell Science: Oxford ; Malden, MA, 2002.

(6) Klessinger, M.; Michl, J., *Excited states and photochemistry of organic molecules*; VCH: New York, 1995.

(7) *Conical intersections: electronic structure, dynamics & spectroscopy*; Domcke, W., Yarkony, D., Köppel, H., Eds.; Advanced series in physical chemistry v.15; World Scientific: River Edge, NJ, 2004.

(8) Worth, G. A.; Cederbaum, L. S. *Annu. Rev. Phys. Chem.* **2004**, *55*, 127–158, DOI: 10.1146/annurev.physchem.55.091602.094335.

(9) Shank, C. V. *Science* **1986**, *233*, 1276–1280.

(10) Huang, C.-P.; Asaki, M. T.; Backus, S.; Murnane, M. M.; Kapteyn, H. C.; Nathel, H. *Opt. Lett.* **1992**, *17*, 1289–1291, DOI: 10.1364/OL.17.001289.

(11) Bucksbaum, P. H. *Science* **2007**, *317*, 766–769, DOI: 10.1126/science.1142135.

(12) Siwick, B. J.; Dwyer, J. R.; Jordan, R. E.; Miller, R. J. D. *Science* **2003**, *302*, 1382–1385, DOI: 10.1126/science.1090052.

(13) Chen, L. X. *Annu. Rev. Phys. Chem.* **2005**, *56*, 221–254, DOI: 10.1146/annurev.physchem.56.092503.141310.

(14) Rose, T. S.; Rosker, M. J.; Zewail, A. H. *J. Chem. Phys.* **1988**, *88*, 6672–6673, DOI: 10.1063/1.454408.

(15) *Ultrafast infrared vibrational spectroscopy*; Fayer, M. D., Ed.; Taylor & Francis: Boca Raton, 2013.

(16) Mukamel, S.; Biggs, J. D. *J. Chem. Phys.* **2011**, *134*, 161101, DOI: 10.1063/1.3581889.

(17) Dorfman, K. E.; Fingerhut, B. P.; Mukamel, S. *Phys. Chem. Chem. Phys.* **2013**, *15*, 12348–12359, DOI: 10.1039/C3CP51117K.

(18) Fingerhut, B. P.; Dorfman, K. E.; Mukamel, S. *J. Chem. Theory Comput.* **2014**, DOI: 10.1021/ct401012u.

(19) Kukura, P.; McCamant, D. W.; Yoon, S.; Wandschneider, D. B.; Mathies, R. A. *Science* **2005**, *310*, 1006–1009, DOI: 10.1126/science.1118379.

(20) Fang, C.; Frontiera, R. R.; Tran, R.; Mathies, R. A. *Nature* **2009**, *462*, 200–204, DOI: 10.1038/nature08527.

(21) Kukura, P.; McCamant, D. W.; Mathies, R. A. *Annu. Rev. Phys. Chem.* **2007**, *58*, 461–488, DOI: 10.1146/annurev.physchem.58.032806.104456.

(22) Dasgupta, J.; Frontiera, R. R.; Taylor, K. C.; Lagarias, J. C.; Mathies, R. A. *P. Natl. Acad. Sci. USA* **2009**, *106*, 1784–1789, DOI: 10.1073/pnas.0812056106.

(23) Weigel, A.; Ernsting, N. *J. Phys. Chem. B* **2010**, *114*, 7879–7893, DOI: 10.1021/jp100181z.

(24) Hoffman, D. P.; Mathies, R. A. *Phys. Chem. Chem. Phys.* **2012**, *14*, 6298–6306, DOI: 10.1039/c2cp23468h.

(25) Rhinehart, J. M.; Challa, J. R.; McCamant, D. W. *J. Phys. Chem. B* **2012**, *116*, 10522–10534, DOI: 10.1021/jp3020645.

(26) Hoffman, D. P.; Lee, O. P.; Millstone, J. E.; Chen, M. S.; Su, T. A.; Creelman, M.; Fréchet, J. M. J.; Mathies, R. A. *J. Phys. Chem. C* **2013**, *117*, 6990–6997, DOI: 10.1021/jp400369b.

(27) Young, R. M.; Dyar, S. M.; Barnes, J. C.; Juríček, M.; Stoddart, J. F.; Co, D. T.; Wasielewski, M. R. *J. Phys. Chem. A* **2013**, DOI: 10.1021/jp409883a.

(28) Creelman, M.; Kumauchi, M.; Hoff, W. D.; Mathies, R. A. *J. Phys. Chem. B* **2014**, *118*, 659–667, DOI: 10.1021/jp408584v.

(29) Rau, H.; Lueddecke, E. *J. Am. Chem. Soc.* **1982**, *104*, 1616–1620, DOI: 10.1021/ja00370a028.

(30) Lednev, I. K.; Ye, T.-Q.; Hester, R. E.; Moore, J. N. *J. Phys. Chem.* **1996**, *100*, 13338–13341, DOI: 10.1021/jp9610067.

(31) Wachtveitl, J.; Nägele, T.; Puell, B.; Zinth, W.; Krüger, M.; Rudolph-Böhner, S.; Oesterhelt, D.; Moroder, L. *J. Photoch. Photobio. A* **1997**, *105*, 283–288, DOI: 10.1016/S1010-6030(96)04572-8.

(32) Azuma, J.; Tamai, N.; Shishido, A.; Ikeda, T. *Chem. Phys. Lett.* **1998**, *288*, 77–82, DOI: 10.1016/S0009-2614(98)00251-6.

(33) Saito, T.; Kobayashi, T. *J. Phys. Chem. A* **2002**, *106*, 9436–9441, DOI: 10.1021/jp0261408.

(34) Schmidt, B.; Sobotta, C.; Malkmus, S.; Laimgruber, S.; Braun, M.; Zinth, W.; Gilch, P. *J. Phys. Chem. A* **2004**, *108*, 4399–4404, DOI: 10.1021/jp0495747.

(35) Koller, F.; Sobotta, C.; Schrader, T.; Cordes, T.; Schreier, W.; Sieg, A.; Gilch, P. *Chem. Phys.* **2007**, *341*, 258–266, DOI: 10.1016/j.chemphys.2007.06.048.

(36) Hamm, P.; Ohline, S. M.; Zinth, W. *J. Chem. Phys.* **1997**, *106*, 519, DOI: 10.1063/1.473392.

(37) Fujino, T.; Tahara, T. *J. Phys. Chem. A* **2000**, *104*, 4203–4210, DOI: 10.1021/jp992757m.

(38) Schultz, T.; Quenneville, J.; Levine, B.; Toniolo, A.; Martínez, T. J.; Lochbrunner, S.; Schmitt, M.; Shaffer, J. P.; Zgierski, M. Z.; Stolow, A. *J. Am. Chem. Soc.* **2003**, *125*, 8098–8099, DOI: 10.1021/ja021363x.

(39) Chang, C.-W.; Lu, Y.-C.; Wang, T.-T.; Diau, E. W.-G. *J. Am. Chem. Soc.* **2004**, *126*, 10109–10118, DOI: 10.1021/ja049215p.

(40) Stuart, C. M.; Frontiera, R. R.; Mathies, R. A. *J. Phys. Chem. A* **2007**, *111*, 12072–12080, DOI: 10.1021/jp0751460.

(41) Cembran, A.; Bernardi, F.; Garavelli, M.; Gagliardi, L.; Orlandi, G. *J. Am. Chem. Soc.* **2004**, *126*, 3234–3243, DOI: 10.1021/ja038327y.

(42) Tiago, M. L.; Ismail-Beigi, S.; Louie, S. G. *J. Chem. Phys.* **2005**, *122*, 094311–094311, DOI: 10.1063/1.1861873.

(43) Crecca, C. R.; Roitberg, A. E. *J. Phys. Chem. A* **2006**, *110*, 8188–8203, DOI: 10.1021/jp057413c.

(44) Conti, I.; Garavelli, M.; Orlandi, G. *J. Am. Chem. Soc.* **2008**, *130*, 5216–5230, DOI: 10.1021/ja710275e.

(45) Tiberio, G.; Muccioli, L.; Berardi, R.; Zannoni, C. *ChemPhysChem* **2010**, *11*, 1018–1028, DOI: 10.1002/cphc.200900652.

(46) Böckmann, M.; Doltsinis, N. L.; Marx, D. *J. Phys. Chem. A* **2010**, *114*, 745–754, DOI: 10.1021/jp910103b.

(47) Cusati, T.; Granucci, G.; Persico, M. *J. Am. Chem. Soc.* **2011**, *133*, 5109–5123, DOI: 10.1021/ja1113529.

(48) Gámez, J. A.; Weingart, O.; Koslowski, A.; Thiel, W. *Phys. Chem. Chem. Phys.* **2013**, *15*, 11814–11821, DOI: 10.1039/C3CP51316E.

(49) Fujisawa, T.; Creelman, M.; Mathies, R. A. *J. Phys. Chem. B* **2012**, DOI: 10.1021/jp3001306.

(50) Einstein, A. *Ann. Phys.* **1905**, *322*, 132–148, DOI: 10.1002/andp.19053220607.

(51) Davisson, C.; Germer, L. H. *Phys. Rev.* **1927**, *30*, 705–740, DOI: 10.1103/PhysRev.30.705.

(52) Cohen-Tannoudji, C.; Diu, B.; Laloë, F., *Quantum mechanics*; Wiley: New York, 1977.

(53) Fayer, M. D., *Elements of quantum mechanics*; Oxford University Press: New York, 2001.

(54) Harris, D. C.; Bertolucci, M. D., *Symmetry and spectroscopy: an introduction to vibrational and electronic spectroscopy*; Dover Publications: New York, 1989.

(55) Herzberg, G., *Molecular Spectra and Molecular Structure: I. Spectra of Diatomic Molecules*, 2nd ed; R.E. Krieger Pub. Co: Malabar, Fla, 1989.

(56) Herzberg, G., *Molecular Spectra and Molecular Structure: II. Infrared and Raman Spectra of Polyatomic Molecules*; Krieger: Malabar, Fla., 1991.

(57) Herzberg, G., *Molecular Spectra and Molecular Structure: III. Electronic Spectra and Electronic Structure of Polyatomic Molecules*; Krieger Publ.: Malabar, Fla, 1991.

(58) Huber, K.-P.; Herzberg, G., *Molecular Spectra and Molecular Structure: IV. Constants of Diatomic Molecules*; Van Nostrand Reinhold: New York; London [etc.], 1979.

(59) McHale, J. L., *Molecular spectroscopy*, 1st ed; Prentice Hall: Upper Saddle River, N.J, 1999.

(60) Cotton, F. A., *Chemical applications of group theory*, 3rd ed; Wiley: New York, 1990.

(61) Kleppner, D.; Kolenkow, R. J., *An introduction to mechanics*; McGraw-Hill: New York, 1973.

(62) Wilson, E. B.; Decius, J. C.; Cross, P. C., *Molecular vibrations: the theory of infrared and Raman vibrational spectra*; Dover Publications: New York, 1980.

(63) Shen, Y. R., *The principles of nonlinear optics*; J. Wiley: New York, 1984.

(64) Mills, D. L., *Nonlinear optics: basic concepts*, 2nd, enl. ed; Springer: Berlin ; New York, 1998.

(65) Boyd, R. W., *Nonlinear optics*, 3rd ed; Academic Press: Amsterdam ; Boston, 2008.

(66) Franken, P. A.; Hill, A. E.; Peters, C. W.; Weinreich, G. *Phys. Rev. Lett.* **1961**, *7*, 118–119, DOI: 10.1103/PhysRevLett.7.118.

(67) Mukamel, S., *Principles of nonlinear optical spectroscopy*; Oxford Univ. Press: New York, 1995.

(68) Lee, D.; Albrecht, A. C. In *Advances in infrared and Raman spectroscopy*, Clark, R. J. H., Hester, R. E., Eds.; Heyden: London, 1985; Vol. 12, pp 179–213.

(69) McCamant, D. W.; Kukura, P.; Mathies, R. A. *J. Phys. Chem. B* **2005**, *109*, 10449–10457, DOI: 10.1021/jp050095x.

(70) Frontiera, R. R.; Shim, S.; Mathies, R. A. *J. Chem. Phys.* **2008**, *129*, 064507–6, DOI: 10.1063/1.2966361.

(71) Weigel, A.; Dobryakov, A.; Klaumünzer, B.; Sajadi, M.; Saalfrank, P.; Ernsting, N. P. *J. Phys. Chem. B* **2011**, *115*, 3656–3680, DOI: 10.1021/jp1117129.

(72) Lee, S.-Y.; Zhang, D.; McCamant, D. W.; Kukura, P.; Mathies, R. A. *J. Chem. Phys.* **2004**, *121*, 3632–3642, DOI: 10.1063/1.1777214.

(73) Sun, Z.; Jin, Z.; Lu, J.; Zhang, D. H.; Lee, S.-Y. *J. Chem. Phys.* **2007**, *126*, 174104–10, DOI: 10.1063/1.2715593.

(74) Sun, Z.; Qiu, X. Q.; Lu, J.; Zhang, D. H.; Lee, S.-Y. *J. Raman Spectrosc.* **2008**, *39*, 1568–1577, DOI: 10.1002/jrs.2040.

(75) Sun, Z.; Lu, J.; Zhang, D. H.; Lee, S.-Y. *J. Chem. Phys.* **2008**, *128*, 144114–13, DOI: 10.1063/1.2888551.

(76) Niu, K.; Cong, S.; Lee, S.-Y. *J. Chem. Phys.* **2009**, *131*, 054311–14, DOI: 10.1063/1.3198473.

(77) McCamant, D. W. **2011**, *115*, 9299–9305, DOI: 10.1021/jp2028164.

(78) Mathies, R.; Yu, N. *J. Raman Spectrosc.* **1978**, *7*, 349–352, DOI: 10.1002/jrs.1250070613.

(79) Shim, S.; Mathies, R. A. *Appl. Phys. Lett.* **2006**, *89*, 121124, DOI: 10.1063/1.2356318.

(80) McCamant, D. W.; Kukura, P.; Yoon, S.; Mathies, R. A. *Rev. Sci. Instrum.* **2004**, *75*, 4971–4980, DOI: 10.1063/1.1807566.

(81) Diels, J.-C.; Rudolph, W., *Ultrashort laser pulse phenomena: fundamentals, techniques, and applications on a femtosecond time scale*, 2nd ed; Optics and photonics; Elsevier / Academic Press: Amsterdam ; Boston, 2006.

(82) Diels, J.-C.; Rudolph, W. In *Ultrashort Laser Pulse Phenomena (Second Edition)*; Academic Press: Burlington, 2006, pp 277–339.

(83) Diels, J.-C.; Rudolph, W. In *Ultrashort Laser Pulse Phenomena (Second Edition)*, Diels, J.-C., Rudolph, W., Eds.; Academic Press: Burlington, 2006, pp 61–142.

(84) Zadoyan, R., *Prism Compressor for Ultrashort Laser Pulses*; Application Note 29: Technology and Applications Center, Newport Corporation, 2006.

(85) Cerullo, G.; De Silvestri, S. *Rev. Sci. Instrum.* **2003**, *74*, 1, DOI: 10.1063/1.1523642.

(86) Kovalenko, S. A.; Dobryakov, A. L.; Ruthmann, J.; Ernsting, N. P. *Phys. Rev. A* **1999**, *59*, 2369–2384, DOI: 10.1103/PhysRevA.59.2369.

(87) Kumar, V.; Osellame, R.; Ramponi, R.; Cerullo, G.; Marangoni, M. *Opt. Express* **2011**, *19*, 15143–15148, DOI: 10.1364/OE.19.015143.

(88) Stauffer, H. U.; Miller, J. D.; Roy, S.; Gord, J. R.; Meyer, T. R. *J. Chem. Phys.* **2012**, *136*, pages, DOI: doi:10.1063/1.3693669.

(89) Lagutchev, A.; Hambir, S. A.; Dlott, D. D. *J. Phys. Chem. C* **2007**, *111*, 13645–13647, DOI: 10.1021/jp075391j.

(90) Stiopkin, I. V.; Jayathilake, H. D.; Weeraman, C.; Benderskii, A. V. *J. Chem. Phys.* **2010**, *132*, pages, DOI: doi:10.1063/1.3432776.

(91) Brown, K. E.; Veldkamp, B. S.; Co, D. T.; Wasielewski, M. R. *J. Phys. Chem. Lett.* **2012**, 2362–2366, DOI: 10.1021/jz301107c.

(92) Hamm, P.; Lim, M.; Hochstrasser, R. M. *J. Phys. Chem. B* **1998**, *102*, 6123–6138, DOI: 10.1021/jp9813286.

(93) Jonas, D. M. *Annu. Rev. Phys. Chem.* **2003**, *54*, 425–463, DOI: 10.1146/annurev.physchem.54.011002.103907.

(94) Born, M., *Principles of optics: electromagnetic theory of propagation, interference and diffraction of light*, 7th expanded ed; Cambridge University Press: Cambridge ; New York, 1999.

(95) Pontecorvo, E.; Kapetanaki, S. M.; Badioli, M.; Brida, D.; Marangoni, M.; Cerullo, G.; Scopigno, T. *Opt. Express* **2011**, *19*, 1107–1112, DOI: 10.1364/OE.19.001107.

(96) Pontecorvo, E.; Ferrante, C.; Elles, C. G.; Scopigno, T. *Opt. Express* **2013**, *21*, 6866–6872, DOI: 10.1364/OE.21.006866.

(97) Yoon, S.; McCamant, D. W.; Kukura, P.; Mathies, R. A.; Zhang, D.; Lee, S.-Y. *J. Chem. Phys.* **2005**, *122*, 024505–9, DOI: 10.1063/1.1828044.

(98) Hoffman, D. P. FSRS-LabVIEW., GitHub, https://github.com/david-hoffman/FSRS-LabVIEW (accessed 07/15/2013).

(99) Muraoka, T.; Kinbara, K.; Aida, T. *Nature* **2006**, *440*, 512–515, DOI: 10.1038/nature04635.

(100) Yu, Y.; Nakano, M.; Ikeda, T. *Nature* **2003**, *425*, 145, DOI: 10.1038/425145a.

(101) Natansohn, A.; Rochon, P. *Chem. Rev.* **2002**, *102*, 4139–4176, DOI: 10.1021/cr970155y.

(102) Natansohn, A.; Rochon, P.; Ho, M.-S.; Barrett, C. *Macromolecules* **1995**, *28*, 4179–4183, DOI: 10.1021/ma00116a019.

(103) Gorostiza, P.; Volgraf, M.; Numano, R.; Szobota, S.; Trauner, D.; Isacoff, E. Y. *P. Natl. Acad. Sci. USA* **2007**, *104*, 10865–10870, DOI: 10.1073/pnas.0701274104.

(104) Dugave, C.; Demange, L. *Chem. Rev.* **2003**, *103*, 2475–2532, DOI: 10.1021/cr0104375.

(105) Yamashita, S.; Ono, H.; Toyama, O. *B. Chem. Soc. Jpn.* **1962**, *35*, 1849–1853, DOI: 10.1246/bcsj.35.1849.

(106) Rau, H. *J. Photochem.* **1984**, *26*, 221–225, DOI: 10.1016/0047-2670(84)80041-6.

(107) Nägele, T.; Hoche, R.; Zinth, W.; Wachtveitl, J. *Chem. Phys. Lett.* **1997**, *272*, 489–495, DOI: 10.1016/S0009-2614(97)00531-9.

(108) Lednev, I.; Ye, T.-Q.; Matousek, P.; Towrie, M.; Foggi, P.; Neuwahl, F.; Umapathy, S.; Hester, R.; Moore, J. *Chem. Phys. Lett.* **1998**, *290*, 68–74, DOI: 10.1016/S0009-2614(98)00490-4.

(109) Fujino, T.; Arzhantsev, S. Y.; Tahara, T. *J. Phys. Chem. A* **2001**, *105*, 8123–8129, DOI: 10.1021/jp0110713.

(110) Yager, K. G.; Barrett, C. J. *J. Chem. Phys.* **2007**, *126*, 094908, DOI: 10.1063/1.2538787.

(111) Poprawa-Smoluch, M.; Baggerman, J.; Zhang, H.; Maas, H. P. A.; De Cola, L.; Brouwer, A. M. *J. Phys. Chem. A* **2006**, *110*, 11926–11937, DOI: 10.1021/jp054982b.

(112) Hagiri, M.; Ichinose, N.; Zhao, C.; Horiuchi, H.; Hiratsuka, H.; Nakayama, T. *Chem. Phys. Lett.* **2004**, *391*, 297–301, DOI: 10.1016/j.cplett.2004.04.093.

(113) Frontiera, R. R.; Dasgupta, J.; Mathies, R. A. *J. Am. Chem. Soc.* **2009**, *131*, 15630–15632, DOI: 10.1021/ja907188b.

(114) Shim, S.; Mathies, R. A. *J. Phys. Chem. B* **2008**, *112*, 4826–4832, DOI: 10.1021/jp710518y.

(115) Gille, K.; Knoll, H.; Quitzsch, K. *Int. J. Chem. Kinet.* **1999**, *31*, 337–350, DOI: 10.1002/(SICI)1097-4601(1999)31:5<337::AID-KIN3>3.0.CO;2-E.

(116) Biswas, N.; Umapathy, S. *J. Phys. Chem. A* **2000**, *104*, 2734–2745, DOI: 10.1021/jp9929263.

(117) Frisch, M. J. et al. Gaussian 09 Revision A.1.

(118) Satzger, H.; Spörlein, S.; Root, C.; Wachtveitl, J.; Zinth, W.; Gilch, P. *Chem. Phys. Lett.* **2003**, *372*, 216–223, DOI: 16/S0009-2614(03)00364-6.

(119) Yamada, M.; Kondo, M.; Mamiya, J.-i.; Yu, Y.; Kinoshita, M.; Barrett, C. J.; Ikeda, T. *Angew. Chem. Int. Ed.* **2008**, *47*, 4986–4988, DOI: 10.1002/anie.200800760.

(120) Spörlein, S.; Carstens, H.; Satzger, H.; Renner, C.; Behrendt, R.; Moroder, L.; Tavan, P.; Zinth, W.; Wachtveitl, J. *P. Natl. Acad. Sci. USA* **2002**, *99*, 7998–8002, DOI: 10.1073/pnas.122238799.

(121) Mourot, A.; Fehrentz, T.; Feuvre, Y. L.; Smith, C. M.; Herold, C.; Dalkara, D.; Nagy, F.; Trauner, D.; Kramer, R. H. *Nat. Meth.* **2012**, *9*, 396–402, DOI: 10.1038/nmeth.1897.

(122) Yan, Y.; Chen, J. I. L.; Ginger, D. S. *Nano Lett.* **2012**, *12*, 2530–2536, DOI: 10.1021/nl300739n.

(123) Gustafson, T. L.; Roberts, D. M.; Chernoff, D. A. *J. Chem. Phys.* **1983**, *79*, 1559–1564, DOI: doi:10.1063/1.446027.

(124) Yan, Y.-X.; Nelson, K. A. *J. Chem. Phys.* **1987**, *87*, 6257–6265, DOI: doi:10.1063/1.453454.

(125) Dhar, L.; Rogers, J. A.; Nelson, K. A. *Chem. Rev.* **1994**, *94*, 157–193, DOI: 10.1021/cr00025a006.

(126) Pollard, W. T.; Cruz, C. H. B.; Shank, C. V.; Mathies, R. A. *J. Chem. Phys.* **1989**, *90*, 199–208, DOI: doi:10.1063/1.456658.

(127) Pollard, W. T.; Mathies, R. A. *Annu. Rev. Phys. Chem.* **1992**, *43*, 497–523, DOI: 10.1146/annurev.pc.43.100192.002433.

(128) Banin, U.; Bartana, A.; Ruhman, S.; Kosloff, R. *J. Chem. Phys.* **1994**, *101*, 8461–8481, DOI: doi:10.1063/1.468108.

(129) Rosca, F.; Kumar, A. T. N.; Ye, X.; Sjodin, T.; Demidov, A. A.; Champion, P. M. *J. Phys. Chem. A* **2000**, *104*, 4280–4290, DOI: 10.1021/jp993617f.

(130) Gruia, F.; Kubo, M.; Ye, X.; Ionascu, D.; Lu, C.; Poole, R. K.; Yeh, S.-R.; Champion, P. M. *J. Am. Chem. Soc.* **2008**, *130*, 5231–5244, DOI: 10.1021/ja7104027.

(131) Wand, A.; Kallush, S.; Shoshanim, O.; Bismuth, O.; Kosloff, R.; Ruhman, S. *Phys. Chem. Chem. Phys.* **2010**, *12*, 2149–2163, DOI: 10.1039/B920356G.

(132) Karunakaran, V.; Benabbas, A.; Youn, H.; Champion, P. M. *J. Am. Chem. Soc.* **2011**, *133*, 18816–18827, DOI: 10.1021/ja206152m.

(133) Loppnow, G.; Mathies, R. *Biophys. J.* **1988**, *54*, 35–43, DOI: 10.1016/S0006-3495(88)82928-X.

(134) Myers, A. B.; Mathies, R. A. *J. Chem. Phys.* **1984**, *81*, 1552–1558, DOI: doi:10.1063/1.447884.

(135) Tufts, D.; Kumaresan, R. *IEEE T. Acoust. Speech* **1982**, *30*, 671–675, DOI: 10.1109/TASSP.1982.1163927.

(136) Barkhuijsen, H.; de Beer, R.; Bovée, W. M. M. J.; van Ormondt, D. *J. Magn. Reson.* **1985**, *61*, 465–481, DOI: 10.1016/0022-2364(85)90187-8.

(137) Barkhuijsen, H.; de Beer, R.; van Ormondt, D. *J. Magn. Reson.* **1986**, *67*, 371–375, DOI: 10.1016/0022-2364(86)90446-4.

(138) Hoffman, D. P. Igor-Data-Analysis., GitHub, https://github.com/david-hoffman/Igor-Data-Analysis (accessed 07/15/2013).

(139) Martens, W. N.; Frost, R. L.; Kristof, J.; Kloprogge, J. T. *J. Raman Spectrosc.* **2002**, *33*, 84–91, DOI: 10.1002/jrs.827.

(140) Myers, A. B.; Mathies, R. A. In *Biological applications of Raman spectroscopy*, Spiro, T. G., Ed.; Wiley: New York, 1987; Vol. 2, pp 1–58.

(141) Kumar, A. T. N.; Rosca, F.; Widom, A.; Champion, P. M. *J. Chem. Phys.* **2001**, *114*, 701–724, DOI: doi:10.1063/1.1329640.

(142) Kumar, A. T. N.; Rosca, F.; Widom, A.; Champion, P. M. *J. Chem. Phys.* **2001**, *114*, 6795–6815, DOI: doi:10.1063/1.1356011.

(143) Johnson, A. E.; Myers, A. B. *J. Chem. Phys.* **1996**, *104*, 2497–2507, DOI: doi:10.1063/1.470998.

(144) Youngblood, W. J.; Lee, S.-H. A.; Maeda, K.; Mallouk, T. E. *Acc. Chem. Res.* **2009**, *42*, 1966–1973, DOI: 10.1021/ar9002398.

(145) Hagfeldt, A.; Boschloo, G.; Sun, L.; Kloo, L.; Pettersson, H. *Chem. Rev.* **2010**, *110*, 6595–6663, DOI: 10.1021/cr900356p.

(146) Gaal, D. A.; Hupp, J. T. *J. Am. Chem. Soc.* **2000**, *122*, 10956–10963, DOI: 10.1021/ja0024744.

(147) Watson, D. F.; Meyer, G. J. *Annu. Rev. Phys. Chem.* **2005**, *56*, 119–156, DOI: 10.1146/annurev.physchem.56.092503.141142.

(148) Anderson, N. A.; Lian, T. *Annu. Rev. Phys. Chem.* **2005**, *56*, 491–519, DOI: 10.1146/annurev.physchem.55.091602.094347.

(149) Duncan, W. R.; Prezhdo, O. V. *Annu. Rev. Phys. Chem.* **2007**, *58*, 143–184, DOI: 10.1146/annurev.physchem.58.052306.144054.

(150) Schwarzburg, K.; Ernstorfer, R.; Felber, S.; Willig, F. *Coordin. Chem. Rev.* **2004**, *248*, 1259–1270, DOI: 10.1016/j.ccr.2004.03.027.

(151) Myllyperkiö, P.; Manzoni, C.; Polli, D.; Cerullo, G.; Korppi-Tommola, J. *J. Phys. Chem. C* **2009**, *113*, 13985–13992, DOI: 10.1021/jp902226y.

(152) Willig, F.; Zimmermann, C.; Ramakrishna, S.; Storck, W. *Electrochim. Acta* **2000**, *45*, 4565–4575, DOI: 10.1016/S0013-4686(00)00608-3.

(153) Ziółek, M.; Tacchini, I.; Martínez, M. T.; Yang, X.; Sun, L.; Douhal, A. *Phys. Chem. Chem. Phys.* **2011**, *13*, 4032–4044, DOI: 10.1039/C0CP01898H.

(154) Ziółek, M.; Cohen, B.; Yang, X.; Sun, L.; Paulose, M.; Varghese, O. K.; Grimes, C. A.; Douhal, A. *Phys. Chem. Chem. Phys.* **2012**, *14*, 2816–2831, DOI: 10.1039/C2CP23825J.

(155) Wiberg, J.; Marinado, T.; Hagberg, D. P.; Sun, L.; Hagfeldt, A.; Albinsson, B. *J. Phys. Chem. C* **2009**, *113*, 3881–3886, DOI: 10.1021/jp8101139.

(156) Wiberg, J.; Marinado, T.; Hagberg, D. P.; Sun, L.; Hagfeldt, A.; Albinsson, B. *J. Phys. Chem. B* **2010**, *114*, 14358–14363, DOI: 10.1021/jp1002963.

(157) Li, R.; Lv, X.; Shi, D.; Zhou, D.; Cheng, Y.; Zhang, G.; Wang, P. *J. Phys. Chem. C* **2009**, *113*, 7469–7479, DOI: 10.1021/jp900972v.

(158) She, C.; Guo, J.; Irle, S.; Morokuma, K.; Mohler, D. L.; Zabri, H.; Odobel, F.; Youm, K.-T.; Liu, F.; Hupp, J. T.; Lian, T. *J. Phys. Chem. A* **2007**, *111*, 6832–6842, DOI: 10.1021/jp0709003.

(159) Ghosh, H. N.; Asbury, J. B.; Weng, Y.; Lian, T. *J. Phys. Chem. B* **1998**, *102*, 10208–10215, DOI: 10.1021/jp983502w.

(160) Mishra, A.; Fischer, M. K. R.; Bäuerle, P. *Angew. Chem. Int. Ed.* **2009**, *48*, 2474–2499, DOI: 10.1002/anie.200804709.

(161) Lockard, J. V.; Butler Ricks, A.; Co, D. T.; Wasielewski, M. R. *J. Phys. Chem. Lett.* **2010**, *1*, 215–218, DOI: 10.1021/jz900136a.

(162) Jiang, X.; Yang, X.; Zhao, C.; Jin, K.; Sun, L. *J. Phys. Chem. C* **2007**, *111*, 9595–9602, DOI: 10.1021/jp071015n.

(163) Yoshihara, T.; Katoh, R.; Furube, A.; Tamaki, Y.; Murai, M.; Hara, K.; Murata, S.; Arakawa, H.; Tachiya, M. *J. Phys. Chem. B* **2004**, *108*, 3817–3823, DOI: 10.1021/jp031305d.

(164) Tamaki, Y.; Furube, A.; Murai, M.; Hara, K.; Katoh, R.; Tachiya, M. *Phys. Chem. Chem. Phys.* **2007**, *9*, 1453–1460, DOI: 10.1039/b617552j.

(165) Huber, R.; Spörlein, S.; Moser, J. E.; Grätzel, M.; Wachtveitl, J. *J. Phys. Chem. B* **2000**, *104*, 8995–9003, DOI: 10.1021/jp9944381.

(166) Waldeck, D. H. *Chem. Rev.* **1991**, *91*, 415–436, DOI: 10.1021/cr00003a007.

(167) Gegiou, D.; Muszkat, K. A.; Fischer, E. *J. Am. Chem. Soc.* **1968**, *90*, 12–18, DOI: 10.1021/ja01003a003.

(168) Gegiou, D.; Muszkat, K. A.; Fischer, E. *J. Am. Chem. Soc.* **1968**, *90*, 3907–3918, DOI: 10.1021/ja01017a002.

(169) Zuleta, M.; Edvinsson, T.; Yu, S.; Ahmadi, S.; Boschloo, G.; Göthelid, M.; Hagfeldt, A. *Phys. Chem. Chem. Phys.* **2012**, *14*, 10780–10788, DOI: 10.1039/C2CP41010A.

(170) El-Zohry, A.; Orthaber, A.; Zietz, B. *J. Phys. Chem. C* **2012**, *116*, 26144–26153, DOI: 10.1021/jp306636w.

(171) Lin, Y.-D.; Chow, T. J. *J. Mater. Chem.* **2011**, *21*, 14907–14916, DOI: 10.1039/C1JM11623A.

(172) Teng, C.; Yang, X.; Yang, C.; Li, S.; Cheng, M.; Hagfeldt, A.; Sun, L. *J. Phys. Chem. C* **2010**, *114*, 9101–9110, DOI: 10.1021/jp101238k.

(173) Hagberg, D. P.; Yum, J.-H.; Lee, H.; De Angelis, F.; Marinado, T.; Karlsson, K. M.; Humphry-Baker, R.; Sun, L.; Hagfeldt, A.; Grätzel, M.; Nazeeruddin, M. K. *J. Am. Chem. Soc.* **2008**, *130*, 6259–6266, DOI: 10.1021/ja800066y.

(174) Tian, H.; Yang, X.; Chen, R.; Zhang, R.; Hagfeldt, A.; Sun, L. *J. Phys. Chem. C* **2008**, *112*, 11023–11033, DOI: 10.1021/jp800953s.

(175) Tisdale, W. A.; Williams, K. J.; Timp, B. A.; Norris, D. J.; Aydil, E. S.; Zhu, X.-Y. *Science* **2010**, *328*, 1543–1547, DOI: 10.1126/science.1185509.

(176) Nozik, A. J. *Annu. Rev. Phys. Chem.* **2001**, *52*, 193–231, DOI: 10.1146/annurev.physchem.52.1.193.

(177) Shah, J., *Ultrafast Spectroscopy of Semiconductors and Semiconductor Nanostructures*; Springer: Berlin; New York, 1996.

(178) Rosspeintner, A.; Lang, B.; Vauthey, E. *Annu. Rev. Phys. Chem.* **2013**, *64*, 247–271, DOI: 10.1146/annurev-physchem-040412-110146.

(179) Kulinowski, K.; Gould, I. R.; Myers, A. B. *J. Phys. Chem.* **1995**, *99*, 9017–9026, DOI: 10.1021/j100022a012.

(180) Thompson, B. C.; Fréchet, J. M. J. *Angew. Chem. Int. Ed.* **2008**, *47*, 58–77, DOI: 10.1002/anie.200702506.

(181) Smith, M. L.; McHale, J. L. *J. Phys. Chem.* **1985**, *89*, 4002–4007, DOI: 10.1021/j100265a015.

(182) McHale, J. L.; Merriam, M. J. *J. Phys. Chem.* **1989**, *93*, 526–529, DOI: 10.1021/j100339a008.

(183) Markel, F.; Ferris, N. S.; Gould, I. R.; Myers, A. B. *J. Am. Chem. Soc.* **1992**, *114*, 6208–6219, DOI: 10.1021/ja00041a045.

(184) Myers, A. B. *Chem. Phys.* **1994**, *180*, 215–230, DOI: 10.1016/0301-0104(93)E0420-Z.

(185) Kulinowski, K.; Gould, I. R.; Ferris, N. S.; Myers, A. B. *J. Phys. Chem.* **1995**, *99*, 17715–17723, DOI: 10.1021/j100050a008.

(186) Britt, B. M.; McHale, J. L.; Friedrich, D. M. *J. Phys. Chem.* **1995**, *99*, 6347–6355, DOI: 10.1021/j100017a014.

(187) Myers, A. B. *Chem. Rev.* **1996**, *96*, 911–926, DOI: 10.1021/cr950249c.

(188) Wynne, K.; Galli, C.; Hochstrasser, R. M. *J. Chem. Phys.* **1994**, *100*, 4797–4810, DOI: 10.1063/1.467201.

(189) Rubtsov, I. V.; Yoshihara, K. *J. Phys. Chem. A* **1999**, *103*, 10202–10212, DOI: 10.1021/jp991998r.

(190) Chiu, C.-C.; Hung, C.-C.; Chen, C.-L.; Cheng, P.-Y. *J. Phys. Chem. B* **2013**, *117*, 9734–9756, DOI: 10.1021/jp404615u.

(191) Cina, J. A.; Kovac, P. A. *J. Phys. Chem. A* **2013**, *117*, 6084–6095, DOI: 10.1021/jp312878t.

(192) Wilson, K. C.; Lyons, B.; Mehlenbacher, R.; Sabatini, R.; McCamant, D. W. *J. Chem. Phys.* **2009**, *131*, 214502–15, DOI: 10.1063/1.3263909.

(193) Mehlenbacher, R. D.; Lyons, B.; Wilson, K. C.; Du, Y.; McCamant, D. W. *J. Chem. Phys.* **2009**, *131*, 244512, DOI: 10.1063/1.3276684.

(194) Dunlap, B.; Wilson, K. C.; McCamant, D. W. *J. Phys. Chem. A* **2013**, *117*, 6205–6216, DOI: 10.1021/jp400484w.

(195) Zhao, B.; Sun, Z.; Lee, S.-Y. *J. Chem. Phys.* **2011**, *134*, 024307, DOI: 10.1063/1.3525100.

(196) Webster, O.; Mahler, W.; Benson, R. *J. Org. Chem.* **1960**, *25*, 1470–1470, DOI: 10.1021/jo01078a037.

(197) Hoffman, D. P.; Valley, D.; Ellis, S. R.; Creelman, M.; Mathies, R. A. *Opt. Express* **2013**, *21*, 21685–21692, DOI: 10.1364/OE.21.021685.

(198) Benesi, H. A.; Hildebrand, J. H. *J. Am. Chem. Soc.* **1949**, *71*, 2703–2707, DOI: 10.1021/ja01176a030.

(199) Jeanmaire, D. L.; Van Duyne, R. P. *J. Am. Chem. Soc.* **1976**, *98*, 4029–4033, DOI: 10.1021/ja00430a001.

(200) Horng, M. L.; Gardecki, J. A.; Papazyan, A.; Maroncelli, M. *J. Chem. Phys.* **1995**, *99*, 17311–17337, DOI: 10.1021/j100048a004.

(201) Girlando, A.; Pecile, C. *Spectrochim. Acta A-M* **1973**, *29*, 1859–1878, DOI: 10.1016/0584-8539(73)80170-9.

(202) Khatkale, M. S.; Devlin, J. P. *J. Chem. Phys.* **1979**, *70*, 1851–1859, DOI: 10.1063/1.437662.

(203) Eldridge, J. E.; Lin, Y.; Mayadunne, T. C.; Montgomery, L. K.; Kaganov, S.; Miebach, T. *Solid State Commun.* **1998**, *105*, 427–431, DOI: 10.1016/S0038-1098(97)10161-2.

(204) Pawlukojć, A.; Natkaniec, I.; Bator, G.; Sobczyk, L.; Grech, E.; Nowicka-Scheibe, J. *Spectrochim. Acta A* **2006**, *63*, 766–773, DOI: 10.1016/j.saa.2005.06.030.

(205) Niu, K.; Zhao, B.; Sun, Z.; Lee, S.-Y. *J. Chem. Phys.* **2010**, *132*, 084510, DOI: 10.1063/1.3330818.

(206) Patuwo, M. Y.; Lee, S.-Y. *J. Chem. Phys.* **2013**, *139*, 234101, DOI: 10.1063/1.4843395.

(207) Zhang, Y.; Improta, R.; Kohler, B. *Phys. Chem. Chem. Phys.* **2013**, DOI: 10.1039/C3CP53815J.

(208) Heider, N.; Fischer, S. F. *Chem. Phys.* **1984**, *88*, 209–220, DOI: 10.1016/0301-0104(84)85280-5.

(209) Dobryakov, A. L.; Kovalenko, S. A.; Weigel, A.; Pérez-Lustres, J. L.; Lange, J.; Müller, A.; Ernsting, N. P. *Rev. Sci. Instrum.* **2010**, *81*, 113106, DOI: 10.1063/1.3492897.

(210) Saar, B. G.; Freudiger, C. W.; Reichman, J.; Stanley, C. M.; Holtom, G. R.; Xie, X. S. *Science* **2010**, *330*, 1368–1370, DOI: 10.1126/science.1197236.

(211) Min, W.; Freudiger, C. W.; Lu, S.; Xie, X. S. *Annu. Rev. Phys. Chem.* **2011**, *62*, 507–530, DOI: 10.1146/annurev.physchem.012809.103512.

(212) Ozeki, Y.; Umemura, W.; Otsuka, Y.; Satoh, S.; Hashimoto, H.; Sumimura, K.; Nishizawa, N.; Fukui, K.; Itoh, K. *Nat. Photon.* **2012**, *6*, 845–851, DOI: 10.1038/nphoton.2012.263.

(213) Freudiger, C. W.; Yang, W.; Holtom, G. R.; Peyghambarian, N.; Xie, X. S.; Kieu, K. Q. *Nat. Photon.* **2014**, *8*, 153–159, DOI: 10.1038/nphoton.2013.360.

(214) Schulze, G.; Jirasek, A.; Yu, M. M. L.; Lim, A.; Turner, R. F. B.; Blades, M. W. *Appl. Spectrosc.* **2005**, *59*, 545–574.

(215) Cao, A.; Pandya, A. K.; Serhatkulu, G. K.; Weber, R. E.; Dai, H.; Thakur, J. S.; Naik, V. M.; Naik, R.; Auner, G. W.; Rabah, R.; Freeman, D. C. *J. Raman Spectrosc.* **2007**, *38*, 1199–1205, DOI: 10.1002/jrs.1753.

(216) Liland, K. H.; Almøy, T.; Mevik, B.-H. *Appl. Spectrosc.* **2010**, *64*, 1007–1016.

(217) Peng, J.; Peng, S.; Jiang, A.; Wei, J.; Li, C.; Tan, J. *Anal. Chim. Acta* **2010**, *683*, 63–68, DOI: 10.1016/j.aca.2010.08.033.

(218) Zhang, Z.-M.; Chen, S.; Liang, Y.-Z. *Analyst* **2010**, *135*, 1138–1146, DOI: 10.1039/B922045C.

(219) Zhang, Z.-M.; Chen, S.; Liang, Y.-Z.; Liu, Z.-X.; Zhang, Q.-M.; Ding, L.-X.; Ye, F.; Zhou, H. *J. Raman Spectrosc.* **2010**, *41*, 659–669, DOI: 10.1002/jrs.2500.

(220) Rowlands, C.; Elliott, S. *J. Raman Spectrosc.* **2011**, *42*, 363–369, DOI: 10.1002/jrs.2691.

(221) Schulze, H. G.; Foist, R. B.; Okuda, K.; Ivanov, A.; Turner, R. F. B. *Appl. Spectrosc.* **2011**, *65*, 75–84.

(222) Weakley, A. T.; Griffiths, P. R.; Aston, D. E. *Appl. Spectrosc.* **2012**, *66*, 519–529.

(223) De Beer, A. G. F.; Chen, Y.; Scheu, R.; Conboy, J. C.; Roke, S. *J. Phys. Chem. C* **2013**, DOI: 10.1021/jp406161n.

(224) Boyd, S. P.; Vandenberghe, L., *Convex optimization*; Cambridge University Press: Cambridge, UK ; New York, 2004.

(225) Candès, E. J.; Li, X.; Ma, Y.; Wright, J. *J. ACM* **2011**, *58*, 11:1–11:37, DOI: 10.1145/1970392.1970395.

(226) Schomacker, K. T.; Delaney, J. K.; Champion, P. M. *J. Chem. Phys.* **1986**, *85*, 4240–4247, DOI: doi:10.1063/1.451795.

(227) Okamoto, H.; Hamaguchi, H.-o.; Tasumi, M. *Chem. Phys. Lett.* **1986**, *130*, 185–189, DOI: 10.1016/0009-2614(86)80451-1.

(228) Biswas, N.; Umapathy, S. *J. Chem. Phys.* **2003**, *118*, 5526, DOI: 10.1063/1.1555628.

(229) Yoon, S.; Kukura, P.; Stuart, C. M.; Mathies, R. A. *Mol. Phys.* **2006**, *104*, 1275–1282, DOI: 10.1080/00268970500525846.

(230) Kuramochi, H.; Takeuchi, S.; Tahara, T. *J. Phys. Chem. Lett.* **2012**, *3*, 2025–2029, DOI: 10.1021/jz300542f.

(231) Kukura, P.; Frontiera, R.; Mathies, R. A. *Phys. Rev. Lett.* **2006**, *96*, DOI: 10.1103/PhysRevLett.96.238303.

(232) Frontiera, R. R.; Mathies, R. A. *J. Chem. Phys.* **2007**, *127*, DOI: 10.1063/1.2780843.